OPTICAL CEREBRAL BLOOD FLOW MONITORING OF MICE TO MEN

Wesley Boehs Baker

A DISSERTATION

in

Physics and Astronomy

Presented to the Faculties of the University of Pennsylvania in Partial

Fulfillment of the Requirements for the Degree of Doctor of Philosophy

2015

Supervisor of Dissertation

_____

Arjun G. Yodh

Professor of Physics and Astronomy

Graduate Group Chairperson

_____

Marija Drndic

Professor of Physics and Astronomy

Dissertation Committee

Philip Nelson, Professor of Physics

Alison Sweeney, Assistant Professor of Physics

Mark Goulian, Professor of Physics

Joel Greenberg, Research Professor of Neurology

Dedication

To my parents, Kent and Cindy Baker, and my brother, Ross.

Acknowledgements

If one of my undergraduate classmates from Bucknell University were to interact with me now, he would have a hard time believing that I'm the same person he knew from Bucknell. I've matured greatly during my graduate school years, both professionally and socially, and I have many people to thank for this.

I will begin with my initial research mentors, Turgut Durduran and Joel Greenberg. When I started graduate school, there was much to be improved with my communication skills and critical thinking skills. I cannot thank Turgut and Joel enough for their heroic patience while training me. In addition to providing research guidance, they showed me how to be effective as part of a team, and how to actively take ownership of a project. I was very lucky to have Joel and Turgut as research mentors, and I'm very lucky now for their friendship. Joel also devoted considerable time to helping me with writing my first paper.

I further owe a great deal to my research advisor, Arjun Yodh. Most of my successful research ideas orginated from discussions with Arjun. Arjun also spent a lot of time carefully editing my papers and reviewing my oral presentations. My professional writing and public speaking have improved by orders of magnitude during my graduate school years, in large part due to Arjun's efforts.

I also acknowledge my clinical collaborators Dan Licht, David Kung, Emile Mohler, John Detre, Janos Luckl, Zhenghui Sun, and Teruyuki Hiraki, who were all very responsive to my questions and requests and pleasant to work with. I further thank Marion Knauss and Victoria Pallet for their crucial help with my pig experiments.

My friends from graduate school are fantastic!! Not only have they been invaluable to my thesis, but they have dramatically improved the quality of my life. I'm very grateful to Peter Yunker, Erin Buckley, Ashwin Parthasarathy, Tiffany Ko, John Alison, Dominick Olivito, Anton Souslov, Han Ban, Meeri Kim, Jennifer Lynch, Rickson Mesquita, Venki Kavuri, Steve Schenkel, Maddie Winters, David Busch, ShihYu Tzeng, Detian Wang, Zhe Li, Sophie Chung, Bryan Chong, Jeff Cochran, Julien Menko, Ken Abramson, Mike Herbst, Ryan Reece, Joseph Clampitt, and Mark Skandera. I will always treasure the wonderful memories from our many great times together.

Without the love and support of my family, I never would have made it to graduate school in the first place. I could not ask for more loving and supportive parents than my Mom and Dad. They've always made time to attend my concerts, help me with my problems, and unconditionally accept me for who I am. I'm also deeply grateful to my brother Ross. His tough love has on numerous occasions put me back on the right track, and he has always stood up for my interests, even when we were in elementary school together.

Finally, I want to thank my dog Harley. Our relationship consists of Harley doing what she wants while I deal with the consequences. Harley often gets me in trouble, but she is a very loving dog and a wonderful companion at home.

ABSTRACT

OPTICAL CEREBRAL BLOOD FLOW MONITORING OF MICE TO MEN

Wesley Boehs Baker
Arjun G. Yodh

This thesis describes cerebral hemodynamic monitoring with the optical techniques of diffuse optical spectroscopy (DOS) and diffuse correlation spectroscopy (DCS). DOS and DCS both employ near-infrared light to investigate tissue physiology millimeters to centimeters below the tissue surface. DOS is a static technique that analyzes multispectral tissue-scattered light intensity signals with a photon diffusion approach (Chapter 2) or a Modified Beer-Lambert law approach (Chapter 3) to derive tissue oxy- and deoxy-hemoglobin concentrations, which are in turn used to compute tissue oxygen saturation and blood volume (Section 2.13). DCS is a qualitatively different dynamic technique that analyzes rapid temporal fluctuations in tissue-scattered light with a correlation diffusion approach to derive tissue blood flow (Chapter 4). Further, in combination these measurements of blood flow and blood oxygenation provide access to tissue oxygen metabolism (Section 7.6).

The new contributions of my thesis to the diffuse optics field are a novel analysis technique for the DCS signal (Chapter 5), and a novel approach for separating cerebral hemodynamic signals from extra-cerebral artifacts (Chapter 6). The DCS analysis technique extends the Modified Beer-Lambert approach for DOS to the DCS measurement. This new technique has some useful advantages compared to the correlation diffusion approach. It facilitates real-time flow monitoring in complex tissue geometries, provides a novel route for increasing DCS measurement speed, and can be used to probe tissues wherein light transport is non-diffusive (Chapter 5). It also can be used to filter signals from superficial tissues. For separation of cerebral hemodynamic signals from extra-cerebral artifacts, the Modified Beer-Lambert approach is employed in a pressure modulation scheme, which determines subject-specific contributions of extra-cerebral and cerebral tissues to the DCS/DOS signals by utilizing probe pressure modulation to induce variations

in extra-cerebral hemodynamics while cerebral hemodynamics remain constant (Chapter 6).

In another novel contribution, I used optical techniques to characterize neurovascular coupling at several levels of cerebral ischemia in a rat model (Chapter 7). Neurovascular coupling refers to the relationship between increased blood flow and oxygen metabolism and increased neuronal activity in the brain. In the rat, localized neuronal activity was increased from functional forepaw stimulation. Under normal flow levels, I (and others) observed that the increase in cerebral blood flow (surrogate for oxygen delivery) from forepaw stimulation exceeded the increase in cerebral oxygen metabolism by about a factor of 2. My measurements indicate that this mismatch between oxygen delivery and consumption are more balanced during ischemia (Chapter 7).

In Chapters 2 and 3, I review the underlying theory for the photon diffusion model and the Modified Beer-Lambert law for DOS analysis. I also review the correlation diffusion approach for analyzing DCS signals in Chapter 4. My hope is that readers new to the field will find these background chapters helpful.

Contents

List of Tables

List of Figures

Chapter 1

Introduction

Diffuse correlation spectroscopy [37, 79, 84, 182, 269] (DCS) and diffuse optical spectroscopy [99, 115, 166, 175, 193, 219, 231, 248] (DOS) are optical techniques that employ near-infrared light (NIR) to monitor cerebral blood flow, oxygen saturation, and blood volume continuously and non-invasively at the bedside. In adults, the surface of the cerebral cortex is about 1-1.5 cm below the surface of the scalp, which is optically deep tissue. To investigate tissue physiology centimeters below the tissue surface, DCS/DOS relies on the NIR spectral window ($\sim 650-950$ nm) wherein light absorption from water and hemoglobin is relatively low (Figure 1.1). Although the overall low light absorption enables NIR photons to travel deep in tissue, the spectra of dominant NIR tissue chromophores, i.e., oxy-hemoglobin (HbO or HbO_2), deoxy-hemoglobin (HbR or Hb), and water, still differ significantly across the spectral window (Figure 1.1). Thus, these tissue chromophore concentrations can be separated from one another and quantitatively resolved with multi-spectral spectroscopy measurements.

Conversely, tissue scattering is high in the NIR window, and photons will scatter thousands of times before they are absorbed. While most traditional optical spectroscopy techniques sample optically thin media where photons scatter no more than once, cerebral tissue measurements are in the opposite, optically thick regime. In the high multiple scattering limit, light transport through tissue is very well approximated as a diffusive process (Chapter 2). The photon diffusion model of light makes the inverse problem of determining tissue absorption, scattering, and blood flow from measurements of light intensity tractable (Chapters 2, 4).

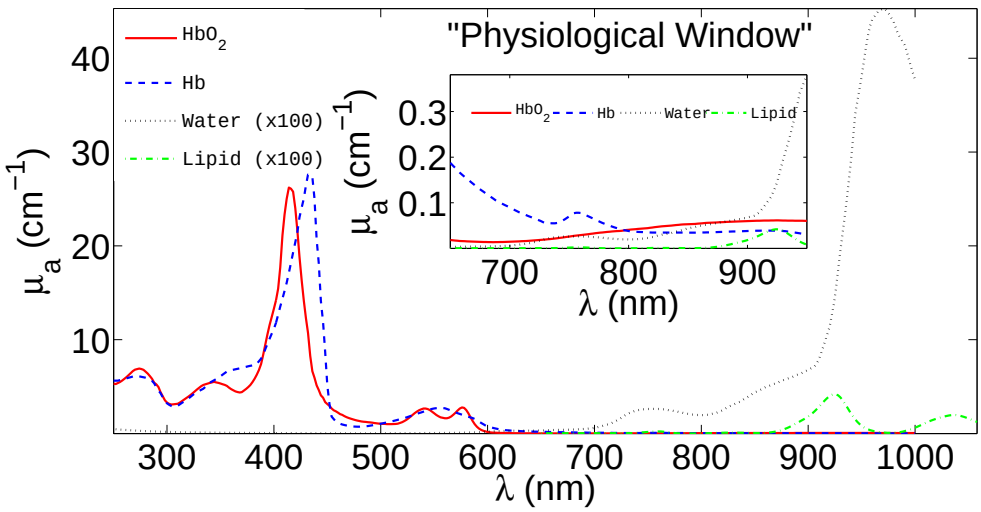

Figure 1.1: Absorption (μ_a) spectra of main tissue chromophores over a large wavelength range. The inset shows the so-called "physiological window" in the near-infrared where water and hemoglobin absorption are relatively low. Notice in the inset that the water and lipid absorption are not multiplied by 100. In this NIR spectral window, light can penetrate several centimeters into tissue. Furthermore, there are clear features in the spectra which enable estimation of chromophore concentration from diffuse optical measurements at several wavelengths. This figure is a reprint of [79, Figure 1]

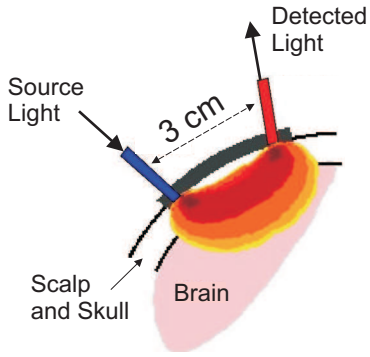

Figure 1.2: A single DCS/DOS source-detector pair (separation $\rho = 3$ cm) in the remission geometry for brain tissue measurements.

A very basic DCS/DOS cerebral measurement with a single source-detector pair is depicted in Figure 1.2. NIR light delivered to a point on the scalp diffuses through tissue randomly in all directions. A fraction of this diffusing light emerges at the light detector located a few centimeters away from the source point. This detected light has probed (i.e., interacted with) a "banana shaped" volume of tissue that spans millimeters to a couple centimeters below the scalp surface (Section 2.12).

The DOS and DCS techniques use the same measurement geometry, but they measure the detected light intensity on different time scales (Figure 1.3). DOS is a static technique that measures slow ($0.1 - 1$ s) variations in the detected light intensity induced by tissue absorption (μ_a) and scatttering (μ_s') changes. DCS is a qualitatively different dynamic technique that measures the rapid (microsecond scale) speckle light intesity fluctuations induced by blood flow (F). Tissue absorption in the NIR spectral window depends predominantly on HbO_2, Hb, water, and lipids. Multispectral DOS measurements can quantitatively resolve the concentrations of these chromophores through using the photon diffusion model to separate absorption from scattering (Section 2.13). The primary chromophores of interest are oxy- and deoxy-hemoglobin, from which the tissue oxygen saturation, i.e., $StO_2 = HbO_2/(HbO_2+Hb)$, and tissue blood volume, i.e., $BV \propto (HbO_2 + Hb)$, can be calculated (see Section 2.13).

DCS obtains a tissue blood flow index, F, that is directly proportional to tissue blood flow, from the decay of the intensity autocorrelation function of the speckle intensity fluctuations (Section 4.9). Further, a tissue compartment model (Section 7.6) can be employed to compute an index of tissue oxygen metabolism (or oxygen consumption rate) from measurements of F and StO_2.

As might be anticipated, this information about cerebral blood flow, blood oxygenation and oxygen metabolism has clinical value. All three parameters, for example, are important biomarkers for brain diseases such as ischemic stroke [127, 229].

1.1 Ischemic Stroke

Ischemic stroke is among the leading causes of death and morbidity, and occurs in $\tilde{7}$00 thousand people each year in the U.S. alone [110]. In an ischemic stroke, a blood clot blocks a cerebral

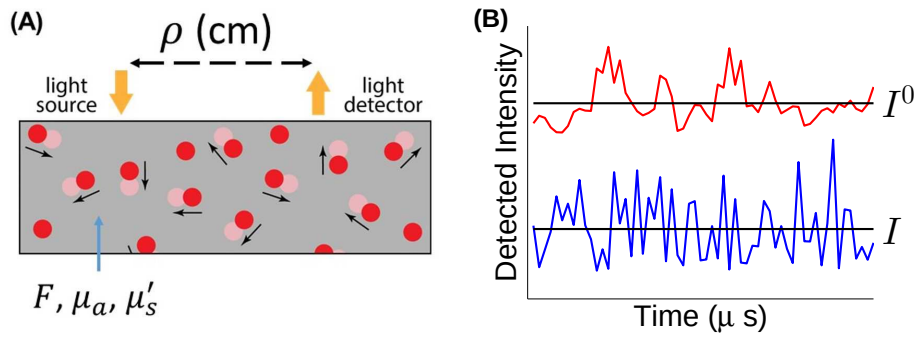

Figure 1.3: **(A)** Schematic for a homogeneous tissue model of the head with a blood flow index, absorption coefficient, and reduced scattering coefficient of F, μ_a, and μ_s', respectively. The incident source intensity, I_s, remains constant over time. Blood cell motion (e.g., red disks at time t and light-red disks at time $t+\tau$) induces fast temporal fluctuations (i.e., speckle intensity fluctuations) in the detected light intensity on the time scale of μs, while absorption and scattering changes modify mean light intensities (e.g., averaged on time scales of ms or greater). **(B)** Schematic of detected intensity fluctuations for a baseline tissue state (red curve) and a perturbed state from baseline with higher blood flow and absorption (blue curve). The horizontal black lines are the mean intensities for the two states, denoted as I^0 and I.

artery (e.g., middle cerebral artery (MCA)), causing an interruption in blood flow supply to a localized region of the brain (Figure 1.4). The stroke lesion is comprised of a core and a penumbra [11, 127, 229]. The core is almost entirely dependent on the blocked artery for blood flow supply, and consequentially, blood flow in the core is very low ($< 20\%$ of normal flow). This tissue region does not remain viable long, and is usually doomed. Surrounding the core is the penumbra, which is partially dependent on the blocked artery for blood flow supply. Thus, blood flow in the penumbra is low ($< 50\%$ of normal flow), but substantially higher than the core due to perfusion from collateral vessels. Therefore, the penumbra remains viable on a longer time scale than the core.

The volume of stroke-related dead tissue is the infarct. On short time scales, the infarct mostly consists of the core, but on longer time scales, the penumbra will also succumb to low blood flow conditions (Figure 1.4). Importantly, the penumbra tissue does not die all at once, but is recruited in a complex infarction process that results in gradual infarct growth until well perfused tissue is encountered (Figure 1.4).

Since the recruitment of penumbra tissue into the infarct takes time, an acute therapeutic

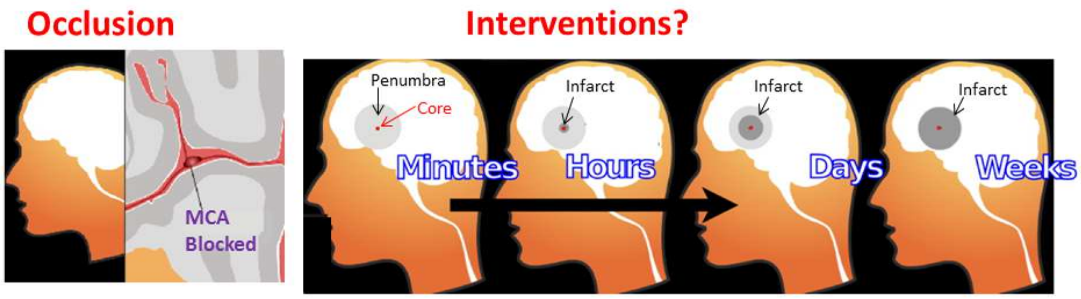

Figure 1.4: Exemplar schematic of acute ischemic stroke progression. Blood flow supply is interrupted to a localized region of the brain (i.e., the stroke lesion) by occlusion of the middle cerebral artery (MCA) (left). The ischemic stroke lesion consists of a core that depends almost entirely on the MCA for blood flow supply, and a surrounding penumbra that is partially perfused by collateral vessels. On short time scales, the infarct largely consists of the core. At longer time scales, the infarct expands into the penumbra until well perfused tissue is encountered. Since the recruitment of penumbra tissue into the infarct takes time, there is an acute therapeutic window in which interventions can be prescribed to reduce the infarct growth by maximizing perfusion. DCS is a promising technique for determining the efficacy of an intervention's ability to increase penumbra blood flow. This figure is courtesy of Turgut Durduran.

window should exist where effective treatment interventions can halt infarct growth. Thus, treatments for acute ischemic stroke aim to minimize neurological damage by maximizing perfusion to the brain lesion [86,97,259]. Of course, the most obvious way restore blood flow is to remove the clot blocking the cerebral artery. Indeed, on short time scales within a few hours of stroke onset, rtPA infusion is typically prescribed, which is a drug that dissolves the clot.

However, on longer time scales after stroke onset, rtPA infusion can be harmful. If the core has been dead long enough, the vasculature in the core is often no longer intact. In these cases, a sudden restoration of blood flow to the core results in heavy bleeding that leads to death. Paradoxically, restoration of blood flow to the core hours after stroke onset can also exacerbate tissue damage through mechanisms such as increased edema (e.g., brain swelling from a leaky vasculature) and the production of injurious free oxygen radicals [229]. Thus, on time scales of several hours to days following stroke onset, the treatment strategy is to maximize perfusion to the penumbra to halt infarct growth without restoring flow to the core.

Numerous acute treatment interventions for stroke are available, but variability in response-to-treatment has been observed [86, 97, 155], and an effective treatment for one patient may be ineffective, or even harmful, for another patient. Thus, a promising clinical application for DCS

and DOS is rapid patient-specific assessment of treatment efficacy. An effective treatment will increase perfusion to the penumbra, which DCS and DOS/NIRS can measure in real time. Indeed, DCS and DOS enable detection of hemodynamic changes before new neurological symptoms emerge [84, 192, 277]. Crucially, DCS and DOS/NIRS can detect an ineffective treatment on a faster time scale than the time it takes for new neurological symptoms from an ineffective treatment to develop.

1.2 Thesis organization

Although DCS and DOS show strong potential for ischemic stroke treatment management, a well-known drawback for optical monitoring of cerebral tissue is its significant sensitivity to blood flow and oxygenation in the *extra-cerebral* tissues (scalp and skull) [26, 184, 221, 237, 238]. Traditional diffuse optics analyses approximate the head as a homogeneous medium (Figure 1.3A). The homogenous model is simple and does not require *a priori* anatomical information, but it ignores differences between extra-cerebral hemodynamics and cerebral hemodynamics in the brain. Because extra-cerebral blood flow and blood oxygenation are non-negligible, their responses contaminate the DCS and DOS signals. Specifically, extra-cerebral contributions can lead experimenters to incorrectly assign cerebral physiological responses [64, 237, 239], which raises questions about the accuracy of optical cerebral monitoring.

A big part of my thesis was the development of a new analysis approach for filtering extra-cerebral contamination in the DCS measurements of cerebral blood flow. This approach utilizes a novel DCS Modified Beer-Lambert law for analysis of DCS signals (Chapter 5), and employs a two-layer model of the head with pressure modulation to separate the cerebral and extra-cerebral contributions to the DCS signal (Chapter 6). Importantly, this algorithm does not require *a priori anatomical information* (though it's helpful if available), and can be implemented in real-time. Further, this algorithm extends to the DOS measurement of cerebral blood oxygenation and blood volume (Chapter 6). My hope is that this algorithm when implemented in clinical settings will lead to more reliable cerebral hemodynamic monitoring.

In another major part of my thesis, I utilized optical techniques to assess neurovascular coupling at different levels of cerebral ischemia, including penumbral levels and core levels, in a

rat model (Chapter 7). Neurovascular coupling is the quantification of hemodynamics due to increase neuronal activity. To increase neuronal activity, the forepaw of the rat was stimulated. For normal flow, this resulted in a localized blood flow increase (which is a surrogate for oxygen delivery) that substantially exceeded the localized oxygen consumption increase by about a factor of 2 (Chapter 7). If forepaw stimulation continues to increase oxygen delivery more than oxygen consumption during ischemia, then stimulation could be an effective treatment for locally increasing oxygen to the penumbral region of the stroke region. The oxygen delivery and consumption increases from functional stimulation are more balanced at the penumbral levels of ischemia, but the oxygen delivery increase is still slightly higher. This suggests that functional stimulation may be neuroprotective in the penumbra.

Additionally, I have extensively reviewed the underlying theory for the photon diffusion and Modified Beer-Lambert law approaches for analyzing DOS signals in Chapters 2 and 3, respectively. I also have reviewed the underlying theory for the correlation diffusion approach for analyzing DCS signals in Chapter 4. My hope is that readers new to the field will find these background chapters helpful.

Chapter 2

Diffuse Optical Spectroscopy (DOS): Photon Diffusion Approach

2.1 Introduction

Light in the near-infrared (NIR) spectral window (650-950 nm) interacts with tissue via two fundamental processes: absorption and scattering (Figure 2.1). Absorption is the light interaction with matter resulting in the conversion of light energy to other forms of energy (e.g., thermal energy). Thus, absorption irretrievably removes light from tissue via the destruction of photons. The energy of these vanished photons is not lost, but transferred to tissue in the form of heat. Scattering is the light interaction with matter where light is taken up by matter and re-emitted. The re-emitted, or scattered, light may have both a different energy and momentum than the original light. As illustrated in Figure 2.1B, $\mathbf{k_i} = 2\pi/\lambda_i \hat{k_i}$ and $\mathbf{k_s} = 2\pi/\lambda_s \hat{k_s}$ are the wave vectors and λ_i and λ_s are the wavelengths of the incident and scattered light, respectively. The scattering interaction in principle could impart both an energy change ($\hbar\omega = \hbar v(|\mathbf{k_s}| - |\mathbf{k_i}|)$; v is the speed of light through matter) and a momentum change ($\hbar\mathbf{q} = \hbar(\mathbf{k_s} - \mathbf{k_i})$) between the scattered and incident light.

Elastic (or Rayleigh) scattering is a commonly used term describing scattering interactions where light energy is conserved (i.e., $\lambda_s = \lambda_i$), but light momentum is not necessary conserved (i.e., the directions of $\mathbf{k_i}$ and $\mathbf{k_s}$ are different). In Raman scattering and fluorescence, the energy

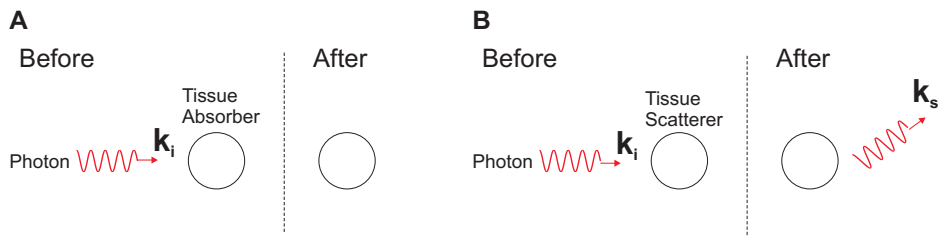

Figure 2.1: Photon absorption (A) and scattering (B) interactions within tissue. A tissue absorber completely transforms the photon's energy into internal thermal energy, thus halting any further propagation of the photon through tissue. A tissue scatterer takes up the incident photon with wave vector $\mathbf{k_i}$ and reemits a scattered photon with wave vector $\mathbf{k_s}$. The scattering interaction can induce changes in both the magnitude and direction between $\mathbf{k_s}$ and $\mathbf{k_i}$.

of the scattered light is different from the incident light. The energy shifts in Raman scattering are caused by photon interactions with vibrational and rotational degrees of freedom in matter, while the energy shifts in fluorescence are caused by photon interactions with electronic degrees of freedom in matter. Energy shifts in fluorescense are typically much larger, and thus easier to detect, than energy shifts in Raman scattering. For near-infrared light propagating in endogenous tissue, elastic scattering is dominant. However, if exogenous contrast agents such as fluorescent dyes (e.g., Indocyanine Green) are added to tissue to improve contrast, fluorescent scattering will obviously need to be considered as well [59].

Elastic light scattering in tissue reveals structural information about cells and surrounding fluids [74, 189, 248]. This is because light scattering originates from spatial variations in the refractive index on the length scale of the light wavelength [18]. In most cases, the refractive index is directly proportional to the molecule number density [100], and light scattering measurements therefore provide information on the spatial heterogeneity of molecule density. Pure water is a non-scattering medium because the number density of water molecules is homogeneous on the length scale of λ. Tissue, in contrast, is a highly scattering medium for near-infrared light because it has heterogeneous regions of greater and lesser density on a length scale comparable to NIR wavelengths. Examples of these heterogeneous regions include interfaces between cells and extracellular space and interfaces between cellular cytoplasm and cellular organelles.

Tissue light absorption measurements provide complementary information on the concentrations of various tissue chromophores. In the near-infrared spectral region, the strongest

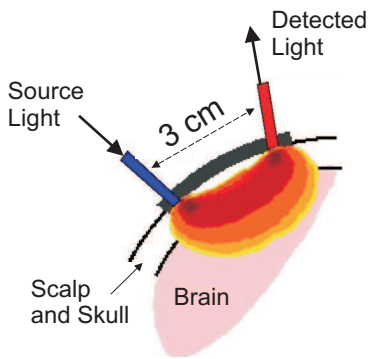

Figure 2.2: A single DOS source-detector pair (separation $\rho = 3$ cm) in the remission geometry for brain tissue measurements. Detected light travels over a distribution of pathlengths between source and detector to probe a "banana shaped" volume of tissue [200]. As a rough rule of thumb, the mean penetration depth is of order $\rho/3 = 1$ cm.

absorbing endogeneous tissue chromophores are oxy- and deoxy-hemoglobin and water (Figure 2.20) [144]. From using the well-known spectra of these chromophores [207], tissue absorption measurements at multiple wavelengths permits the direct calculation of the chromophore concentrations (Section 2.13) [79, Section 2.8].

Diffuse optical spectroscopy (DOS) uses near-infrared light to measure absorption and scattering in tissue. For example, a very basic DOS measurement probing brain tissue is depicted in Figure 2.2. Near-infrared source light is delivered to a point on the scalp surface via an optical fiber. Another optical fiber is employed to detect the backscattered component of the source light emerging from tissue at a different point on the scalp surface. This detected light has probed (i.e., interacted with) a "banana shaped" volume of tissue that spans millimeters to a couple centimeters below the scalp surface (Section 2.12) [200]. It is important to recognize, though, that the attenuation in the detected light relative to the source depends on both the absorption and scattering properties of tissue. In order to separate scattering effects from absorption effects in the detected light signals, a quantitative model of light transport through tissue is required.

In this chapter, I will first show that light transport over long distances in tissue is well approximated as a diffusive process [123, 266]. Then, I will discuss in detail how to use the diffusion model of light transport in practice to separate tissue absorption from tissue scattering in DOS measurements [10, 79].

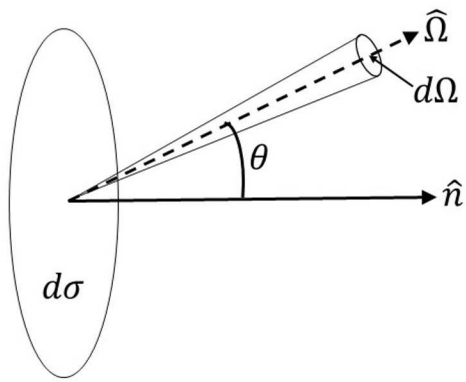

Figure 2.3: The light radiance L is defined such that the radiant power transported across an element of area $d\sigma$ at position $\mathbf{r}$ and time t in directions confined to an element of solid angle $d\Omega$ centered around the $\hat{\Omega}$ direction is $L(\mathbf{r}, \hat{\Omega}, t, \lambda) \cos\theta d\sigma d\Omega$.

2.2 Radiative Transport Theory

Maxwell's equations correctly describe light transport through all media, including tissue. However, because of their complexity, solving Maxwell's equations over long distances in tissue is an intractable problem that must be addressed numerically. From numerical solutions, it is very difficult to gain physical insight on light transport through tissue. For these reasons, I will use radiative transport theory as the starting point for the theoretical description of diffuse optics, which is an excellent approximation of Maxwell's equations for describing light transport through tissue [46, 51, 142]. The notation for important light transport parameters is shown in Table 2.1.

In radiative transport theory, light with wavelength λ propagating through tissue with refractive index n is characterized by its light radiance, $L(\mathbf{r}, \hat{\Omega}, t, \lambda)$ [Wcm^{-2}sr^{-1}], which is the light power per unit area traveling in the $\hat{\Omega}$ direction at position $\mathbf{r}$ and time t. The amount of radiant power, $W(\hat{\Omega})$ [W], which is transported across an element of area $d\sigma$ in directions confined to an element of solid angle $d\Omega$ (see Figure 2.3) is

$$W(\hat{\Omega}) = L \cos\theta d\sigma d\Omega, \tag{2.1}$$

where θ is the angle between $\hat{\Omega}$ and the area element's normal vector, $\hat{n}$.

The interactions of light with tissue are in turn characterized by an absorption coefficient, $\mu_a(\hat{\Omega}, \mathbf{r}, t, \lambda)$ [$1/$cm], and a scattering phase function, $p(\hat{\Omega}, \hat{\Omega}', \mathbf{r}, t, \lambda)$ [$1/$cm]. These parameters

are wavelength-dependent probability densities for light absorption in the $\hat{\Omega}$ direction and for light scattering into the direction $\hat{\Omega}$ given the incident direction $\hat{\Omega}'$ at $(\mathbf{r}, t)$, respectively. To understand their physical meanings, consider a radiance $L(\mathbf{r}, \hat{\Omega}, t, \lambda)$ incident on an infinitesimal spherical volume of diameter $|d\mathbf{r}|$ (Figure 2.4). The amount of the incident radiance absorbed by this volume is $\mu_a(\hat{\Omega}, \mathbf{r}, t, \lambda)L(\mathbf{r}, \hat{\Omega}, t, \lambda)|d\mathbf{r}|$, and the amount of the incident radiance scattered into the $\hat{\Omega}'$ direction is $p(\hat{\Omega}', \hat{\Omega}, \mathbf{r}, t, \lambda)L(\mathbf{r}, \hat{\Omega}, t, \lambda)|d\mathbf{r}|$.

Often of interest is the total amount of incident radiance scattered by the tissue volume in all directions. This is determined by a tissue scattering coefficient, $\mu_s(\hat{\Omega}, \mathbf{r}, t, \lambda)$ [$1/$cm], which is simply the integral of the scattering phase function over all 4π steradians of space[1]:

$$\mu_s(\hat{\Omega}, \mathbf{r}, t, \lambda) = \int_{4\pi} p(\hat{\Omega}', \hat{\Omega}, \mathbf{r}, t, \lambda)\mathrm{d}\Omega'. \tag{2.2}$$

From the definition of the scattering phase function p, $\mu_s(\hat{\Omega}, \mathbf{r}, t, \lambda)L(\mathbf{r}, \hat{\Omega}, t, \lambda)|d\mathbf{r}|$ is the total amount of incident radiance scattered by the infinitesimal tissue volume, and μ_s is the probability density for tissue scattering in any direction[2].

The typical light transport length scales between absorption and scattering events are the multiplicative inverses of μ_a and μ_s, respectively. To understand why, let us use the particle description of light as a packet of N_0 photons propagating through a homogeneous medium. Let $N(r)$ be the number of photons that have *not* been scattered after traveling a distance r inside the medium. The probability of a single photon being scattered in distance dr is $\mu_s dr$. Therefore, since $N(r + dr)$ is less than $N(r)$ by the number of photons that have scattered in dr, we have the equation

$$N(r + dr) = N(r) - N(r)\mu_s dr,$$

which is a differential equation:

$$\frac{dN(r)}{dr} = -\mu_s N(r).$$

The above equation describes exponential decay, and has the well known solution [100, Section

[1] In spherical coordinates, $\int_{4\pi} f(\hat{\Omega})\mathrm{d}\Omega = \int_0^{\pi}\int_0^{2\pi} f(\theta, \phi)\sin\theta\mathrm{d}\theta\mathrm{d}\phi$ [240, Section 14.4].

[2] If the tissue volume consists of discrete scattering particles with number density ϱ and a scattering cross section of σ_s [cm^2], then $\mu_s = \varrho\sigma_s$ [240, Section 14.2]. Here, the total scattered light power from a single particle is the product of σ_s and the incident radiance on the particle. Thus, a particle occupies an effective area σ_s where light impinging on this area is scattered. Similarly, the scattering phase function, p, is related to the particle differential scattering cross-section, σ_D, via $p = \varrho\sigma_D$ [240, Section 14.4]

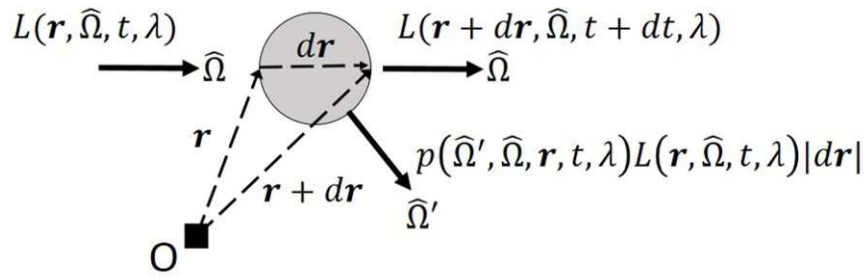

Figure 2.4: The radiance $L(\mathbf{r} + d\mathbf{r}, \hat{\Omega}, t + dt, \lambda)$ emerging from an infinitesimal spherical volume of tissue is different from the radiance $L(\mathbf{r}, \hat{\Omega}, t, \lambda)$ incident on the volume because of the interactions between light and tissue. The portion of the incident radiance absorbed by the tissue volume is $\mu_a(\hat{\Omega}, \mathbf{r}, t, \lambda) L(\mathbf{r}, \hat{\Omega}, t, \lambda)|d\mathbf{r}|$. The portion of the incident radiance scattered by the tissue volume into the $\hat{\Omega}'$ direction is $p(\hat{\Omega}', \hat{\Omega}, \mathbf{r}, t, \lambda) L(\mathbf{r}, \hat{\Omega}, t, \lambda)|d\mathbf{r}|$. Here, $|d\mathbf{r}|$ denotes the magnitude of the vector $d\mathbf{r}$, i.e., $|d\mathbf{r}| = v dt$, where $v = c/n$ is the speed of light through the volume element.

43-1]

$$N(r) = N_0 \exp[-\mu_s r] = N_0 \exp[-r/\ell_s],$$

where $\ell_s \equiv 1/\mu_s$ is the scattering length. Note that the probability density function for a photon to scatter after traveling a distance r without scattering, i.e., $P_s(r)dr$, is equal to the probability that a photon travels a distance r without scattering (i.e., $N(r)/N_0$) multiplied by the probability of scattering in distance dr (i.e., $\mu_s dr$):

$$P_s(r)dr = \frac{N(r)}{N_0}\mu_s dr = \mu_s \exp[-\mu_s r]dr.$$

Consequentially, the mean distance a photon travels between scattering events is the scattering length, i.e.,

$$\langle r \rangle = \int_0^\infty r P_s(r) \mathrm{d}r = \int_0^\infty r \mu_s \exp[-\mu_s r] \mathrm{d}r = \frac{1}{\mu_s} = \ell_s. \tag{2.3}$$

Using exactly the same logic, the absorption length, $\ell_a \equiv 1/\mu_a$, is the mean distance photons travel before they are absorbed.

Transport theory is valid when the characteristic scattering and absorption lengths, ℓ_s and ℓ_a, are much greater than the light wavelength. In other words, photons travel distances of many wavelengths between interactions with tissue. This is true for near-infrared light, where typical values for ℓ_s and ℓ_a are on the order of 0.1 and 10 cm, respectively. Under these conditions, light transport is adequately described by the geometrical optics (or small wavelength) limit of

Table 2.1: Parameters affecting light transport through tissue

Quantity	Symbol	Units
Light radiance (Equation 2.4)	L	W cm^{-2} sr^{-1}
Scattering phase function (Figure 2.4)	p	$1/\text{cm}$
Absorption coefficient (Figure 2.4)	μ_a	$1/\text{cm}$
Absorption length	$\ell_a \equiv 1/\mu_a$	cm
Scattering coefficient (Equation 2.2)	μ_s	$1/\text{cm}$
Scattering length	$\ell_s \equiv 1/\mu_s$	cm
Total transport coefficient	$\mu_t \equiv \mu_a + \mu_s$	$1/\text{cm}$
Normalized scattering phase function	$f \equiv p/\mu_s$	dimensionless
Refractive index	n	dimensionless
Speed of light in tissue	$v = c/n$	cm/s
Radiant source power per volume (Equation 2.7)	Q	W cm^{-3} sr^{-1}

Maxwell's equations [31, Chapter 3], where the light electric field propagates in straight lines between tissue interactions as a local quasi plane wave. The light radiance in terms of these propagating electric fields is[3] [116, Section 9.3.1]:

$$L(\mathbf{r}, \hat{\Omega}, t) = \begin{cases} \left|E_{\parallel}(\mathbf{r}, \hat{\Omega}, t)\right|^2 + \left|E_{\perp}(\mathbf{r}, \hat{\Omega}, t)\right|^2 & \text{, unpolarized light} \\ \left|\mathbf{E}(\mathbf{r}, \hat{\Omega}, t)\right|^2 & \text{, polarized light,} \end{cases} \tag{2.4}$$

where $\mathbf{E}(\mathbf{r}, \hat{\Omega}, t)$ is the complex representation of the electric field at $(\mathbf{r}, t)$ that is transported as a quasi plane wave with wave vector $\mathbf{k}_\Omega = (2\pi n/\lambda)\hat{\Omega}$, amplitude $\mathbf{E_0}$, and angular frequency ω, i.e.,

$$\mathbf{E}(\mathbf{r}, \hat{\Omega}, t) = \mathbf{E_0}(\mathbf{r}, t) \exp\left[i(\mathbf{k}_\Omega \cdot \mathbf{r} - \omega t)\right]. \tag{2.5}$$

For unpolarized light, the light radiance is the sum over the intensities of the two orthogonal polarization components, i.e., $|E_{\parallel}|^2 = E_{\parallel}E_{\parallel}^*$ and $|E_{\perp}|^2 = E_{\perp}E_{\perp}^*$. Another key result from geometrical optics is that light interference effects are negligible, which results in additive light intensities.

Changes in the light radiance are described by the radiative transport equation, which is a conservation equation for the radiance in each infinitesimal volume element within the tissue. Referring again to Figure 2.4, the change in radiance as it moves across an infinitesimal tissue volume element in the $\hat{\Omega}$ direction is given by a convective (or material) derivative of the

[3]Here and in some of the remaining equations, the λ dependence of L is implict to make the notation less cumbersome.

radiance [240, Section 16.12]:

$$dL \equiv L(\mathbf{r}+d\mathbf{r},\hat{\Omega},t+dt) - L(\mathbf{r},\hat{\Omega},t) = \frac{\partial L(\mathbf{r},\hat{\Omega},t)}{\partial t}dt + d\mathbf{r}\cdot\nabla L(\mathbf{r},\hat{\Omega},t)$$
$$= \frac{\partial L(\mathbf{r},\hat{\Omega},t)}{\partial t}dt + vdt\hat{\Omega}\cdot\nabla L(\mathbf{r},\hat{\Omega},t). \tag{2.6}$$

Because interference effects are negligible, this change in radiance dL also must be equal to

$$dL = -\mu_a(\hat{\Omega},\mathbf{r},t)L(\mathbf{r},\hat{\Omega},t)|d\mathbf{r}| - L(\mathbf{r},\hat{\Omega},t)\int\limits_{\hat{\Omega}'\neq\hat{\Omega}} p(\hat{\Omega}',\hat{\Omega},\mathbf{r},t)\mathrm{d}\Omega'|d\mathbf{r}|+$$
$$\int\limits_{\hat{\Omega}'\neq\hat{\Omega}} p(\hat{\Omega},\hat{\Omega}',\mathbf{r},t)L(\mathbf{r},\hat{\Omega}',t)\mathrm{d}\Omega'|d\mathbf{r}| + Q(\mathbf{r},\hat{\Omega},t)vdt. \tag{2.7}$$

Here, $Q(\mathbf{r},\hat{\Omega},t)$ [Wcm^{-3}sr^{-1}] is the light power per volume emitted by sources at position $\mathbf{r}$ and time t in the $\hat{\Omega}$ direction with wavelength λ. The change in radiance dL is decreased by the losses in the incident radiance due to absorption (first term, right-hand side) and due to scattering in all directions $\hat{\Omega}'$ different than $\hat{\Omega}$ (second term, right-hand side). dL is also increased by the gains in radiance scattered into $\hat{\Omega}$ from all incident directions $\hat{\Omega}'$ different than $\hat{\Omega}$ (third term, right-hand side) and the gains from light sources inside the volume element (fourth term, right-hand side)[4]. Substituting vdt for $|d\mathbf{r}|$, and adding zero, i.e., $-p(\hat{\Omega},\hat{\Omega},\mathbf{r},t,\lambda)L(\mathbf{r},\hat{\Omega},t,\lambda)|d\mathbf{r}| + p(\hat{\Omega},\hat{\Omega},\mathbf{r},t,\lambda)L(\mathbf{r},\hat{\Omega},t,\lambda)|d\mathbf{r}|$, to the right-hand side of Equation 2.7, we obtain

$$dL = -\left[\mu_a(\hat{\Omega},\mathbf{r},t) + \mu_s(\hat{\Omega},\mathbf{r},t)\right]L(\mathbf{r},\hat{\Omega},t)vdt+$$
$$\int_{4\pi} p(\hat{\Omega},\hat{\Omega}',\mathbf{r},t)L(\mathbf{r},\hat{\Omega}',t)\mathrm{d}\Omega' vdt + Q(\mathbf{r},\hat{\Omega},t)vdt, \tag{2.8}$$

where μ_s is given by Equation 2.2. Combining Equations 2.6 and 2.8 results in the radiative transport equation (RTE) [46, Section 1.3],

$$\frac{1}{v}\frac{\partial L(\mathbf{r},\hat{\Omega},t,\lambda)}{\partial t} = -\hat{\Omega}\cdot\nabla L(\mathbf{r},\hat{\Omega},t,\lambda) - \mu_t(\hat{\Omega},\mathbf{r},t,\lambda)L(\mathbf{r},\hat{\Omega},t,\lambda) + Q(\mathbf{r},\hat{\Omega},t,\lambda)+$$
$$\mu_s(\hat{\Omega},\mathbf{r},t,\lambda)\int_{4\pi} L(\mathbf{r},\hat{\Omega}',t)f(\hat{\Omega},\hat{\Omega}',\mathbf{r},t,\lambda)\mathrm{d}\Omega'. \tag{2.9}$$

[4]To understand the gain in radiance from light sources, note that $Q(\mathbf{r},\hat{\Omega},t,\lambda)dt$ is the light energy per volume generated in time dt that is propagating in the $\hat{\Omega}$ direction. The increase in the light radiance emerging from the volume element due to sources is then the product of this generated light energy with the speed of light through the volume element.

Here, I have introduced a total transport coefficient, μ_t [$1/\text{cm}$], and a normalized scattering phase function, f, which are defined as:

$$\mu_t(\hat{\Omega}, \mathbf{r}, t, \lambda) \equiv \mu_a(\hat{\Omega}, \mathbf{r}, t, \lambda) + \mu_s(\hat{\Omega}, \mathbf{r}, t, \lambda) \tag{2.10}$$

$$f(\hat{\Omega}, \hat{\Omega}', \mathbf{r}, t, \lambda) = \frac{p(\hat{\Omega}, \hat{\Omega}', \mathbf{r}, t, \lambda)}{\mu_s(\hat{\Omega}, \mathbf{r}, t, \lambda)}. \tag{2.11}$$

Note from Equations 2.2 and 2.11 that

$$\int_{4\pi} f(\hat{\Omega}, \hat{\Omega}', \mathbf{r}, t, \lambda) \mathrm{d}\Omega' = 1. \tag{2.12}$$

The RTE (Equation 2.9) is the main result of this section, which I derived using the geometrical optics limit of Maxwell's equations[5]. A hidden assumption in this derivation of the RTE is that the radiation field propagating through matter is unpolarized. In principle, both the absorption coefficient and scattering phase function depend on the polarization state of the radiation field, and a *vector* radiative transport equation is required to account for polarization effects [188]. In the vector RTE, L is replaced by a 4×1 vector of the four Stokes parameters describing the intensity and polarization of the light field, i.e.,

$$\tilde{L} = \begin{pmatrix} L \\ p_E L \\ \epsilon\langle -E_\parallel E_\perp^* - E_\perp E_\parallel^* \rangle \\ \epsilon\langle i(E_\perp E_\parallel^* - E_\parallel E_\perp^*) \rangle \end{pmatrix},$$

where p_E is the degree of polarization, ϵ is a proportionality constant, $E_\parallel$ and $E_\perp$ denote the orthogonal polarization states of the electric field (see Equation 2.4), and the angle brackets denote time averages [51, 188]. Additionally, μ_t, μ_s, and f are replaced by 4×4 tensors. The vector RTE simplifies to the scalar RTE (Equation 2.9) when the light field is completely unpolarized, i.e., $p_E = 0$. In many practical DOS tissue measurements, the light field is unpolarized because of the rapid depolarization of light via multiple scattering [18, Chapter 14].

To summarize, the scalar RTE is valid when

[5] In a more rigorous approach, Jorge Ripoll also recently presented a step by step derivation of the RTE directly from Maxwell's equations [211].

- The characteristic scattering length, $\ell_s \equiv 1/\mu_s$, and the characteristic absorption length, $\ell_a \equiv 1/\mu_a$, are both much greater than the light wavelength λ. The photon propagation distances within the medium also need to be much greater than λ.

- The light field propagating through tissue is unpolarized.

- The tissue refractive index is homogeneous, meaning that between tissue interactions, the light field travels with constant velocity $v = c/n$. This condition can be relaxed by replacing v with $v(\mathbf{r}, \hat{\Omega}, t, \lambda)$ in the RTE (Equation 2.9).

Though it is considerably simpler than Maxwell's equations, the RTE is still complex enough that it must be solved numerically in most cases of interest [9, 162]. Numerical schemes to solve the RTE are computationally time consuming and difficult to implement in data fitting algorithms. Fortunately, for many cases of practical importance, near-infrared light transport through tissue is well approximated as a diffusive process, which reduces the complexity of the RTE significantly.

2.3 Photon Diffusion Equation

Under diffusive light transport, individual photons execute random walks through tissue, wandering about in all directions without having a preferential direction of travel. As with Brownian motion of diffusing particles in general, the net movement of large numbers of photons through tissue is driven by the concentration gradient of these photons. Macroscopically, the concentration of photons is directly proportional to the photon energy concentration (also called the light energy density), $\Gamma(\mathbf{r}, t)$ [Jcm^{-3}], which is the light energy per volume at $(\mathbf{r}, t)$. The photon energy concentration is in turn dependent on the light radiance, L (Table 2.1).[6] To understand how, note that $L(\mathbf{r}, \hat{\Omega}, t)/v$, where v is the speed of light, is the component of the photon energy concentration traveling in the $\hat{\Omega}$ direction [100, Section 43-5]. The total photon energy

[6] To make the notation less cumbersome in this section, I will no longer explicitly label the wavelength dependence (i.e., λ) in L, μ_a, μ_s, and f. The wavelength dependence is not important in the derivation of the photon diffusion equation, but it will be very important later on when I discuss diffuse optical spectroscopy.

concentration is thus the integral of L/v over all solid angles, i.e.,

$$\Gamma(\mathbf{r},t) = \frac{1}{v}\int_{4\pi} L(\mathbf{r},\hat{\Omega},t)\mathrm{d}\Omega = \frac{1}{v}\Phi(\mathbf{r},t). \tag{2.13}$$

In Equation 2.13, I have introduced the photon fluence rate, $\Phi(\mathbf{r},t)$ [Wcm^{-2}], which is defined as the total light power per area moving radially outward from the infinitesimal volume element centered at $(\mathbf{r},t)$:

$$\Phi(\mathbf{r},t) \equiv \int_{4\pi} L(\mathbf{r},\hat{\Omega},t)\mathrm{d}\Omega. \tag{2.14}$$

Clearly, the photon energy concentration and fluence rate are directly proportional to each other (Equation 2.13). The rest of this section presents a detailed derivation of the diffusion model for the photon fluence rate (Equation 2.46). A summary of important optical parameters in this diffusion model are given in Table 2.2.

2.3.1 Continuity relation between the photon fluence rate and the photon flux

The transport of the fluence rate through tissue is described by a continuity equation obtained from integrating the radiative transport equation (Equation 2.9) over all solid angles:[7]

$$\begin{aligned}\frac{1}{v}\frac{\partial}{\partial t}\int_{4\pi} L(\mathbf{r},\hat{\Omega},t)\mathrm{d}\Omega = -\int_{4\pi}\nabla\cdot\left(L(\mathbf{r},\hat{\Omega},t)\hat{\Omega}\right)\mathrm{d}\Omega - \\ \int_{4\pi}\mu_t(\hat{\Omega},\mathbf{r},t)L(\mathbf{r},\hat{\Omega},t)\mathrm{d}\Omega + \int_{4\pi} Q(\mathbf{r},\hat{\Omega},t)\mathrm{d}\Omega + \\ \int_{4\pi}\mu_s(\hat{\Omega},\mathbf{r},t)\int_{4\pi} L(\mathbf{r},\hat{\Omega}',t)f(\hat{\Omega},\hat{\Omega}',\mathbf{r},t)\mathrm{d}\Omega'\mathrm{d}\Omega.\end{aligned} \tag{2.15}$$

The photon diffusion model is only applicable in isotropic media, wherein the scattering and absorption coefficients do not depend on the direction of light travel:

$$\textbf{assumption 1: } \mu_s(\hat{\Omega},\mathbf{r},t) = \mu_s(\mathbf{r},t), \quad \mu_a(\hat{\Omega},\mathbf{r},t) = \mu_a(\mathbf{r},t). \tag{2.16}$$

Physically, Equation 2.16 means that on both the scattering and absorption length scales, $\ell_s \equiv 1/\mu_s$ and $\ell_a \equiv 1/\mu_a$, respectively, the medium looks the same to incident photons from every

[7] Because $\hat{\Omega}$ is a constant direction vector, $\hat{\Omega}\cdot\nabla L(\mathbf{r},\hat{\Omega},t) = \nabla\cdot\left(L(\mathbf{r},\hat{\Omega},t)\hat{\Omega}\right)$ [116, Section 1.2.6]

direction. Under this condition, Equation 2.15 simplifies to

$$\frac{1}{v}\frac{\partial\Phi(\mathbf{r},t)}{\partial t} = -\nabla\cdot\int_{4\pi} L(\mathbf{r},\hat{\Omega},t)\hat{\Omega}\mathrm{d}\Omega - \mu_t(\mathbf{r},t)\Phi(\mathbf{r},t) + S(\mathbf{r},t) + \mu_s(\mathbf{r},t)\int_{4\pi}\left[\int_{4\pi} f(\hat{\Omega},\hat{\Omega}',\mathbf{r},t)\mathrm{d}\Omega\right] L(\mathbf{r},\hat{\Omega}',t)\mathrm{d}\Omega'. \tag{2.17}$$

Here, $S(\mathbf{r},t)$ [Wcm^{-3}] is the concentration of radiant source power, or the total power per volume emitted radially outward from position $\mathbf{r}$ at time t, i.e.,

$$S(\mathbf{r},t) \equiv \int_{4\pi} Q(\mathbf{r},\hat{\Omega},t)\mathrm{d}\Omega. \tag{2.18}$$

Another assumption of photon diffusion theory is that the normalized scattering phase function, f, is rotationally symmetric. Mathematically, this means that f depends only on the angle between incident and outgoing scattering wave vectors:

$$\textbf{assumption 2: } f(\hat{\Omega},\hat{\Omega}',\mathbf{r},t) = f(\hat{\Omega}',\hat{\Omega},\mathbf{r},t) = f(\hat{\Omega}\cdot\hat{\Omega}',\mathbf{r},t). \tag{2.19}$$

Assumptions 1 (Equation 2.16) and 2 (Equation 2.19) go hand in hand in that they are generally either both true or both false. Applying Equations 2.10 and 2.12 to Equation 2.17, along with using assumption 2, results in a continuity equation for the fluence rate,

$$\frac{1}{v}\frac{\partial\Phi(\mathbf{r},t)}{\partial t} + \nabla\cdot\mathbf{J}(\mathbf{r},t) + \mu_a(\mathbf{r},t)\Phi(\mathbf{r},t) = S(\mathbf{r},t), \tag{2.20}$$

where the photon flux, $\mathbf{J}(\mathbf{r},t)$ [Wcm^{-2}], is the vector sum of the radiance emerging from the infinitesimal volume element centered at $(\mathbf{r},t)$, i.e.,

$$\mathbf{J}(\mathbf{r},t) \equiv \int_{4\pi} L(\mathbf{r},\hat{\Omega},t)\hat{\Omega}\mathrm{d}\Omega. \tag{2.21}$$

Note that $\mathbf{J}(\mathbf{r},t)\cdot\hat{n}d\sigma$ [W] is the net light power crossing an element of area $d\sigma$ (with normal vector $\hat{n}$) in the $\hat{n}$ direction (see Figure 2.3). This physical meaning of the photon flux is understood from the definition of the light radiance (Equation 2.1). The light power crossing the area element $d\sigma$ from light traveling in the $\hat{\Omega}$ direction is

$$W(\hat{\Omega}) = L(\mathbf{r},\hat{\Omega},t)d\Omega d\sigma\cos\theta = L(\mathbf{r},\hat{\Omega},t)\hat{\Omega}\cdot\hat{n}d\sigma d\Omega.$$

Thus, the total net light power crossing $d\sigma$, i.e., $\int_{4\pi} W(\hat{\Omega})\mathrm{d}\Omega$, is $\mathbf{J}(\mathbf{r},t)\cdot\hat{n}d\sigma$.

2.3.2 Fick's law relation between the photon fluence rate and the photon flux

Another relation between the photon fluence rate and the photon flux is derived from approximating the light radiance, L, as a series expansion of spherical harmonics, $Y_{\ell m}$ (with coefficients $\tilde{\phi}_{\ell m}$), truncated at $\ell = N$:

$$L(\mathbf{r}, \hat{\Omega}, t) = \sum_{\ell=0}^{N} \sum_{m=-\ell}^{\ell} \sqrt{\frac{2\ell+1}{4\pi}} \tilde{\phi}_{\ell m}(\mathbf{r}, t) Y_{\ell m}(\hat{\Omega}). \tag{2.22}$$

Equation 2.22 is the so-called P_N approximation of the light radiance [46,134,142]. Substituting Equation 2.22 into Equation 2.14, and noting that spherical harmonics form an orthonormal set, we obtain

$$\begin{aligned}
\Phi(\mathbf{r}, t) &= \sum_{\ell=0}^{N} \sum_{m=-\ell}^{\ell} \tilde{\phi}_{\ell m}(\mathbf{r}, t) \int_{4\pi} \sqrt{\frac{2\ell+1}{4\pi}} Y_{\ell m}(\hat{\Omega}) \mathrm{d}\Omega \\
&= \sum_{\ell=0}^{N} \sum_{m=-\ell}^{\ell} \sqrt{2\ell+1} \tilde{\phi}_{\ell m}(\mathbf{r}, t) \int_{4\pi} Y_{00}^{*}(\hat{\Omega}) Y_{\ell m}(\hat{\Omega}) \mathrm{d}\Omega \\
&= \tilde{\phi}_{00}(\mathbf{r}, t).
\end{aligned} \tag{2.23}$$

Similarly, substituting Equation 2.22 into Equation 2.21 results in[8]

$$\begin{aligned}
\mathbf{J}(\mathbf{r}, t) &= \sum_{\ell=0}^{N} \sum_{m=-\ell}^{\ell} \sqrt{\frac{2\ell+1}{4\pi}} \tilde{\phi}_{\ell m}(\mathbf{r}, t) \int_{4\pi} Y_{\ell m}(\hat{\Omega}) \left[\sin\theta\cos\phi\hat{x} + \sin\theta\sin\phi\hat{y} + \cos\theta\hat{z}\right] \mathrm{d}\Omega \\
&= \sqrt{\frac{4\pi}{3}} \sum_{\ell=0}^{N} \sum_{m=-\ell}^{\ell} \sqrt{\frac{2\ell+1}{4\pi}} \tilde{\phi}_{\ell m}(\mathbf{r}, t) \int_{4\pi} Y_{\ell m}(\hat{\Omega}) \left[\sqrt{\frac{1}{2}} \left(Y_{1-1}^{*}(\hat{\Omega}) - Y_{11}^{*}(\hat{\Omega})\right) \hat{x} - \right. \\
&\quad \left. i\sqrt{\frac{1}{2}} \left(Y_{1-1}^{*}(\hat{\Omega}) + Y_{11}^{*}(\hat{\Omega})\right) \hat{y} + Y_{10}^{*}(\hat{\Omega})\hat{z}\right] \mathrm{d}\Omega \\
&= \sqrt{\frac{1}{2}} \left(\tilde{\phi}_{1-1}(\mathbf{r}, t) - \tilde{\phi}_{11}(\mathbf{r}, t)\right) \hat{x} - i\sqrt{\frac{1}{2}} \left(\tilde{\phi}_{1-1}(\mathbf{r}, t) + \tilde{\phi}_{11}(\mathbf{r}, t)\right) \hat{y} + \tilde{\phi}_{10}(\mathbf{r}, t)\hat{z}
\end{aligned} \tag{2.24}$$

[8] I wrote $\hat{\Omega}$ in terms of the Cartesian unit vectors (i.e., $\hat{x}$, $\hat{y}$, and $\hat{z}$), where θ and ϕ (not to be confused with $\tilde{\phi}_{\ell m}$) are the polar angle and azimuthal angle, respectively, in the spherical coordinate system [116, Section 1.4.1].

In terms of the coefficients $\tilde{\phi}_{\ell m}$, the net power per area traveling in the $\hat{\Omega}$ direction is

$$\begin{aligned}
\mathbf{J}\cdot\hat{\Omega} &= J_x \sin\theta\cos\phi + J_y \sin\theta\sin\phi + J_z\cos\theta \\
&= \frac{1}{\sqrt{2}}\left(\tilde{\phi}_{1-1} - \tilde{\phi}_{11}\right)\sin\theta\cos\phi - \frac{i}{\sqrt{2}}\left(\tilde{\phi}_{1-1} + \tilde{\phi}_{11}\right)\sin\theta\sin\phi + \tilde{\phi}_{10}\cos\theta \\
&= \tilde{\phi}_{10}\cos\theta + \frac{\sin\theta}{\sqrt{2}}(\cos\phi - i\sin\phi)\tilde{\phi}_{1-1} - \frac{\sin\theta}{\sqrt{2}}(\cos\phi + i\sin\phi)\tilde{\phi}_{11} \\
&= \tilde{\phi}_{10}\cos\theta + \frac{1}{\sqrt{2}}\sin\theta \mathrm{e}^{-i\phi}\tilde{\phi}_{1-1} - \frac{1}{\sqrt{2}}\sin\theta\mathrm{e}^{i\phi}\tilde{\phi}_{11} \\
&= \sqrt{\frac{4\pi}{3}}\left(\tilde{\phi}_{10}Y_{10}(\hat{\Omega}) + \tilde{\phi}_{1-1}Y_{1-1}(\hat{\Omega}) + \tilde{\phi}_{11}Y_{11}(\hat{\Omega})\right),
\end{aligned} \tag{2.25}$$

In Equation 2.25, there is still implicit position and time dependence in the coefficients $\tilde{\phi}_{\ell m}$ and $\mathbf{J}$.

For diffusive light transport, L is accurately described by the P_1 approximation, wherein the series expansion in Equation 2.22 is truncated at $N = 1$:

$$L(\mathbf{r},\hat{\Omega},t) = \frac{1}{4\pi}\tilde{\phi}_{00}(\mathbf{r},t) + \sqrt{\frac{3}{4\pi}}\left(\tilde{\phi}_{1-1}(\mathbf{r},t)Y_{1-1}(\hat{\Omega}) + \tilde{\phi}_{10}(\mathbf{r},t)Y_{10}(\hat{\Omega}) + \tilde{\phi}_{11}(\mathbf{r},t)Y_{11}(\hat{\Omega})\right) \tag{2.26}$$

From combining Equations 2.23, 2.25, and 2.26, we see that the P_1 approximation of the light radiance is a linear combination of the photon fluence rate and flux, i.e.,

$$L(\mathbf{r},\hat{\Omega},t) = \frac{1}{4\pi}\Phi(\mathbf{r},t) + \frac{3}{4\pi}\mathbf{J}(\mathbf{r},t)\cdot\hat{\Omega}. \tag{2.27}$$

A necessary condition for diffusive light transport is the validity of Equation 2.27. For nearly isotropic light, i.e.,

$$\textbf{assumption 3: } \Phi(\mathbf{r},t) \gg |\mathbf{J}(\mathbf{r},t)|, \tag{2.28}$$

the dominance of the isotropic fluence rate term in the P_N expansion ensures the accuracy of the P_1 approximation.

Substituting Equation 2.27 into the radiative transport equation (Equation 2.9), we have[9]

$$\begin{aligned}
\frac{1}{v}\frac{\partial\Phi}{\partial t} + \frac{3}{v}\frac{\partial}{\partial t}(\mathbf{J}\cdot\hat{\Omega}) = -\hat{\Omega}\cdot\nabla\Phi - 3\hat{\Omega}\cdot\nabla\left(\mathbf{J}\cdot\hat{\Omega}\right) - (\mu_t - \mu_s)\Phi - 3\mu_t\mathbf{J}\cdot\hat{\Omega} + \\
4\pi Q(\hat{\Omega}) + 3\mu_s\int_{4\pi} f(\hat{\Omega}\cdot\hat{\Omega}')\mathbf{J}\cdot\hat{\Omega}'\mathrm{d}\Omega'.
\end{aligned} \tag{2.29}$$

[9]For simplicity, the $\mathbf{r}$ and t dependence is implicit for Φ, $\mathbf{J}$, μ_t, μ_s, f, and Q.

The last term on the right-hand side in Equation 2.29 is further simplified by evaluating the integral in a spherical coordinate system defined such that $\hat{\Omega}$ is pointing in the $\hat{z}$ direction:

$$\begin{aligned}\int_{4\pi} f(\hat{\Omega}\cdot\hat{\Omega}')\mathbf{J}\cdot\hat{\Omega}'\mathrm{d}\Omega' &= \int_{4\pi} f(\cos\theta')\left[\sin\theta'\cos\phi'\hat{x}+\cos\theta'\cos\phi'\hat{y}+\cos\theta'\hat{z}\right]\mathrm{d}\Omega'\cdot\mathbf{J}\\ &= \int_{4\pi} f(\cos\theta')\cos\theta'\mathrm{d}\Omega'\hat{z}\cdot\mathbf{J}\\ &= \int_{4\pi} f(\hat{\Omega}\cdot\hat{\Omega}')\hat{\Omega}\cdot\hat{\Omega}'\mathrm{d}\Omega'\hat{\Omega}\cdot\mathbf{J}\\ &= \mathsf{g}\hat{\Omega}\cdot\mathbf{J}. \end{aligned} \tag{2.30}$$

Equation 2.30 introduces the scattering anisotropy factor, g, which is the ensemble average of the cosine of the scattering angle θ, i.e.,

$$\mathsf{g}(\mathbf{r},t) \equiv \int_{4\pi} f(\hat{\Omega}\cdot\hat{\Omega}',\mathbf{r},t)\hat{\Omega}\cdot\hat{\Omega}'\mathrm{d}\Omega' = \langle\cos\theta\rangle. \tag{2.31}$$

The closer g is to unity, the more probable it is for a photon to be scattered in the forward direction, i.e., $\theta = 0$. Reported near-infrared tissue measurements of g from the literature vary a lot, but in general, g is high (> 0.7) [144].

Substituting Equation 2.30 into Equation 2.29, we obtain

$$\frac{1}{v}\frac{\partial\Phi}{\partial t}+\frac{3}{v}\frac{\partial}{\partial t}(\mathbf{J}\cdot\hat{\Omega}) = -\hat{\Omega}\cdot\nabla\Phi-3\hat{\Omega}\cdot\nabla\left(\mathbf{J}\cdot\hat{\Omega}\right)-(\mu_t-\mu_s)\Phi-3(\mu_t-\mu_s\mathsf{g})\mathbf{J}\cdot\hat{\Omega}+4\pi Q(\hat{\Omega}). \tag{2.32}$$

Multiplying Equation 2.32 by $\hat{\Omega}$ and integrating over all solid angles results in a simpler relation between the fluence rate and flux:

$$\begin{aligned}\frac{1}{v}\frac{\partial\Phi}{\partial t}\int_{4\pi}\hat{\Omega}\mathrm{d}\Omega = -\frac{3}{v}\frac{\partial}{\partial t}\int_{4\pi}\hat{\Omega}\left[\mathbf{J}\cdot\hat{\Omega}\right]\mathrm{d}\Omega - \int_{4\pi}\hat{\Omega}\left[\hat{\Omega}\cdot\nabla\Phi\right] - 3\int_{4\pi}\hat{\Omega}\left[\hat{\Omega}\cdot\nabla(\mathbf{J}\cdot\hat{\Omega})\right]\mathrm{d}\Omega-\\ (\mu_t-\mu_s)\Phi\int_{4\pi}\hat{\Omega}\mathrm{d}\Omega - 3(\mu_t-\mu_s\mathsf{g})\int_{4\pi}\hat{\Omega}\left[\mathbf{J}\cdot\hat{\Omega}\right] + 4\pi\int_{4\pi}Q(\hat{\Omega})\hat{\Omega}\mathrm{d}\Omega\end{aligned} \tag{2.33}$$

Equation 2.33 is further simplified through noting that for any vector $\mathbf{A}$,

$$\int_{4\pi}\hat{\Omega}\left(\hat{\Omega}\cdot\mathbf{A}\right)\mathrm{d}\Omega = \frac{4\pi}{3}\mathbf{A} \tag{2.34}$$

$$\int_{4\pi}\hat{\Omega}\left[\hat{\Omega}\cdot\nabla\left(\mathbf{A}\cdot\hat{\Omega}\right)\right]\mathrm{d}\Omega = 0. \tag{2.35}$$

Equation 2.34 is derived through evaluating the integral in a spherical coordinate system defined such that $\mathbf{A}$ is pointing in the $\hat{z}$ direction,

$$\begin{aligned}\int_{4\pi} \hat{\Omega}\left(\hat{\Omega}\cdot\mathbf{A}\right)\mathrm{d}\Omega &= |\mathbf{A}|\int_{4\pi}\hat{\Omega}\cos\theta\mathrm{d}\Omega \\ &= 2\pi|\mathbf{A}|\hat{z}\int_0^{\pi}\cos^2\theta\sin\theta\mathrm{d}\theta \\ &= \frac{4\pi}{3}\mathbf{A}, \end{aligned} \tag{2.36}$$

To derive Equation 2.35, note that[10] [116, Section 1.2.6]

$$\begin{aligned}\hat{\Omega}\cdot\nabla(\hat{\Omega}\cdot\mathbf{A}) &= \hat{\Omega}\cdot\left(\hat{\Omega}\times(\nabla\times\mathbf{A})+\mathbf{A}\times(\nabla\times\hat{\Omega})+(\hat{\Omega}\cdot\nabla)\mathbf{A}+(\mathbf{A}\cdot\nabla)\hat{\Omega}\right) \\ &= \hat{\Omega}\cdot(\hat{\Omega}\cdot\nabla)\mathbf{A} = \frac{\partial A_r}{\partial r}, \end{aligned} \tag{2.37}$$

where the last line uses spherical coordinates; $\mathbf{A} = A_r\hat{r} + A_\theta\hat{\theta} + A_\phi\hat{\phi}$ and $\hat{\Omega} = \hat{r}$. From Equation 2.37,

$$\int_{4\pi}\hat{\Omega}\left[\hat{\Omega}\cdot\nabla\left(\mathbf{A}\cdot\hat{\Omega}\right)\right]\mathrm{d}\Omega = \frac{\partial A_r}{\partial r}\int_{4\pi}\hat{\Omega}\mathrm{d}\Omega = 0. \tag{2.38}$$

Substituting Equations 2.34 and 2.35 into 2.33, as well as noting that $\int_{4\pi}\hat{\Omega}\mathrm{d}\Omega = 0$, we have

$$\nabla\Phi = -\frac{3}{v}\frac{\partial\mathbf{J}}{\partial t} - 3(\mu_t - \mu_s\mathsf{g})\mathbf{J} + 3\int_{4\pi}\mathsf{Q}(\hat{\Omega})\hat{\Omega}\mathrm{d}\Omega. \tag{2.39}$$

For diffusive light transport, two additional assumptions are now made:

assumption 4: Light sources are isotropic, i.e., $Q(\hat{\Omega}) = Q$ (2.40)

assumption 5: Slow temporal photon flux variations, i.e., (2.41)

$$\frac{3}{v}\frac{\partial\mathbf{J}}{\partial t} + 3(\mu_t - \mu_s\mathsf{g})\mathbf{J} = 3(\mu_t - \mu_s\mathsf{g})\mathbf{J}. \tag{2.42}$$

Applying these two assumptions to Equation 2.39 results in the well known diffusive relation between the fluence rate and flux, i.e., Fick's first law of diffusion [17, Chapter 2]:

$$\begin{aligned}\mathbf{J}(\mathbf{r},t) &= -\frac{1}{3(\mu_s'(\mathbf{r},t)+\mu_a(\mathbf{r},t))}\nabla\Phi(\mathbf{r},t) \\ &= -\frac{D(\mathbf{r},t)}{v}\nabla\Phi(\mathbf{r},t) = -D(\mathbf{r},t)\nabla\Gamma(\mathbf{r},t) \end{aligned} \tag{2.43}$$

[10] Since $\hat{\Omega}$ is a constant unit vector, $(\mathbf{A}\cdot\nabla)\hat{\Omega} = 0$ and $\mathbf{A}\times(\nabla\times\hat{\Omega}) = 0$. Further, by the nature of cross products, $\hat{\Omega}$ and $\hat{\Omega}\times(\nabla\times\mathbf{A})$ are perpendicular vectors; thus their dot product is zero.

Table 2.2: Relevant optical parameters in diffusion model of light transport

Quantity	Symbol	Units
Speed of light in tissue	$v = c/n$	cm/s
Photon fluence rate (Equation 2.14)	Φ	W cm^{-2}
Photon energy concentration (Equation 2.13)	$\Gamma = \Phi/v$	J cm^{-3}
Absorption coefficient (Figure 2.4)	$\mu_a = 1/\ell_a$	$1/$cm
Scattering coefficient (Equation 2.2)	$\mu_s = 1/\ell_s$	$1/$cm
Scattering anisotropy factor (Equation 2.31)	g	dimensionless
Reduced scattering coefficient	$\mu_s' \equiv \mu_s(1 - \mathrm{g})$	$1/$cm
Photon transport mean-free path (random walk step)	$\ell_{tr} \equiv 1/(\mu_s' + \mu_a)$	cm
Photon diffusion coefficient	$D \equiv v\ell_{tr}/3$	cm^2/s
Photon flux (Equation 2.21)	$J = -D\nabla\Gamma$	W cm^{-2}
Concentration of radiant source power (Equation 2.18)	S	W cm^{-3}

Here, $\Gamma(\mathbf{r}, t)$ is the photon energy concentration, which is given in Equation 2.13, $\mu_s'(\mathbf{r}, t)$ [$1/$cm] is the reduced scattering coefficient, i.e.,

$$\mu_s'(\mathbf{r}, t) \equiv \mu_s(\mathbf{r}, t)\left[1 - \mathrm{g}(\mathbf{r}, t)\right], \tag{2.44}$$

and $D(\mathbf{r}, t)$ [cm^{2}s$^-1$] is the photon diffusion coefficient, i.e.,

$$D(\mathbf{r}, t) \equiv \frac{v}{3(\mu_s'(\mathbf{r}, t) + \mu_a(\mathbf{r}, t))} = \frac{1}{3}v\ell_{tr}. \tag{2.45}$$

The photon diffusion coefficient is directly proportional to the photon transport mean-free path, $\ell_{tr} \equiv 1/(\mu_s' + \mu_a)$ [cm], which is the random walk step of diffusing photons [17, Chapter 1].

2.3.3 Photon diffusion model

Substituting the diffusive relation between the fluence rate and flux (Equation 2.43) into the continuity relation (Equation 2.20) results in the photon diffusion equation for the photon fluence rate [123, 210]:

$$\nabla \cdot [D(\mathbf{r}, t)\nabla\Phi(\mathbf{r}, t)] - v\mu_a(\mathbf{r}, t)\Phi(\mathbf{r}, t) - \frac{\partial\Phi(\mathbf{r}, t)}{\partial t} = -vS(\mathbf{r}, t). \tag{2.46}$$

Microscopically, the photon diffusion equation (Equation 2.46) is a consequence of many individual photons executing random walks through tissue [17, 49]. In this random walk visualization, photons move in straight-line segments with sudden interruptions wherein either the propagation direction is randomly changed or the photon is absorbed. The average length of the

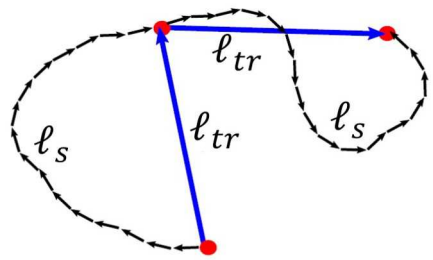

Figure 2.5: Schematic of a photon taking two random walk steps through tissue. Each random walk step involves many photon scattering events. This figure is adopted from Figure 2.2 in David Busch's thesis [39].

straight-line segments is the transport mean-free path, ℓ_{tr}. For near-infrared light propagating through tissue, the scattering anisotropy factor g (2.31) is typically close to unity, which means that $\mu_s' \ll \mu_s$ (Equation 2.44), which in turn means that the transport mean-free path, ℓ_{tr}, is much greater than the scattering length, $\ell_s \equiv 1/\mu_s$. Thus, photons scatter many times over the length scale of ℓ_{tr}, and each scattering event produces a "kink" in their paths through tissue (Figure 2.5). However, because of the high bias for forward scattering in tissue, the direction of travel of photons is not fully randomized until they have moved over a length scale of ℓ_{tr}. Thus, over large length scales, individual photon dynamics resemble random walks with step size ℓ_{tr} (Figure 2.5).

To summarize, the validity of the photon diffusion model (Equation 2.46) rests on the validity of several assumptions about the nature of light transport:

Light radiance is nearly isotropic (Equation 2.28): Nearly isotropic light radiance (i.e., $\Phi \gg |\mathbf{J}|$) is well modeled by the P_1 approximation (Equation 2.27). If $\mu_s' \gg \mu_a$ (i.e., a typical photon takes many random walk steps of length $\ell_{tr} \approx 1/\mu_s'$ before it is absorbed), and the photon propagation distances within the medium are large relative to ℓ_{tr}, then the light radiance will be nearly isotropic.

Rotational symmetry (Equations 2.16, 2.19)): The photon diffusion model assumes that the tissue optical properties μ_a, μ_s, and f are independent of the direction of light travel. Physically, this means that tissue should be rotationally symmetric on the absorption and scattering length scales of $\ell_a \equiv 1/\mu_a$ and $\ell_s \equiv 1/\mu_s$, respectively.

Radiative Transport Equation (Equation 2.9) is valid: As discussed at the end of Section 2.2, the RTE is valid for unpolarized light propagating in media wherein ℓ_s and ℓ_a are much greater than the light wavelength λ.

Slow temporal variations in photon flux (Equation 2.42): The implication of this assumption is that the variation in photon flux occurs on a time scale much larger than the time it takes photons to move one transport length, i.e., $t_{tr} \equiv \ell_{tr}/v$. The left-hand side of Equation 2.42 can be rewritten as

$$\begin{aligned}\frac{3}{v}\frac{\partial \mathbf{J}}{\partial t} + 3(\mu_t - \mu_s \mathsf{g})\mathbf{J} &= 3(\mu_s' + \mu_a)\left[\frac{\ell_{tr}}{v}\frac{\partial \mathbf{J}}{\partial t} + \mathbf{J}\right] \\ &\approx 3(\mu_s' + \mu_a)\left[t_{tr}\frac{\Delta \mathbf{J}}{(\Delta t)_J} + \mathbf{J}\right] \\ &= 3(\mu_s' + \mu_a)\mathbf{J}, \text{ if } t_{tr} \ll (\Delta t)_J. \end{aligned} \tag{2.47}$$

Here, $(\Delta t)_J$ is the time scale over which the change in flux, $\Delta\mathbf{J}$, becomes significant relative to $\mathbf{J}$. Equation 2.47 is valid provided that $t_{tr} \ll (\Delta t)_J$. For frequency space, i.e., $\mathbf{J} = \tilde{\mathbf{J}}\mathrm{e}^{i\omega t}$,

$$\begin{aligned}\frac{3}{v}\frac{\partial \mathbf{J}}{\partial t} + 3(\mu_t - \mu_s \mathsf{g})\mathbf{J} &= 3(\mu_s' + \mu_a)(t_{tr} i\omega + 1)\mathbf{J} \\ &= 3(\mu_s' + \mu_a)\sqrt{1 + (\omega t_{tr})^2}\mathrm{e}^{i\arctan(\omega t_{tr})}\mathbf{J} \\ &= 3(\mu_s' + \mu_a)\mathbf{J}, \text{ if } \omega t_{tr} \ll 1. \end{aligned} \tag{2.48}$$

For typical tissue properties of $\mu_a = 0.1$ 1/cm, $\mu_s' = 10$ 1/cm, and $n = 1.4$, $t_{tr} \approx 5$ ps. Thus, from Equation 2.48, the slowly varying flux condition is satisfied if the linear frequencies in the signal (i.e., $f = 2\pi\omega$), satisfy the condition $f \ll 32$ GHz.

Homogeneous refractive index: More precisely, this means that photons travel with constant velocity, v, between scattering events. If v depends on position and time, then this assumption is relaxed by replacing v with $v(\mathbf{r}, t)$ in the photon diffusion equation (Equation 2.46). In complex media where v also depends on the direction of light travel, $\hat{\Omega}$, the diffusion model is no longer valid.

Light sources are isotropic (Equation 2.40).

These assumptions are valid in the *near-infrared spectral window* ($\sim 650 - 950$ nm) for many tissues, wherein light transport is dominated by scattering ($\mu_s' \gg \mu_a$)[11]. For example, in brain and breast tissue, μ_s' is roughly two orders of magnitude greater than μ_a (see Table 2.3). Muscle, skin, fat, and a variety of other tissues are also highly scattering, low absorbing media in the near-infrared [144]. Many researchers have shown experimentally that the diffusion model is a good approximation of light transport in these tissues, e.g. [55, 80, 96, 201, 266].

The photon diffusion model (Equation 2.46) is a major simplification of the radiative transport model (Equation 2.9), and in several relevant tissue geometries, the diffusion model can be *solved analytically*. With analytical solutions in hand, it is much easier to gain physical insight and intuition on tissue light transport. The analytical solutions further facilitate the implementation of data fitting algorithms to extract tissue hemoglobin concentrations from fluence rate measurements. Even when numerical solutions are required, the photon diffusion model is considerably more tractable than the full radiative transport model.

Keep in mind, though, that the diffusion model also has limitations in tissue measurements. In anisotropic tissues such as axon fiber bundles, the rotational symmetry assumption may no longer be reasonable. To account for anisotropy, Heino *et al* proposed an anisotropic diffusion model that relaxes the isotropic assumption for the scattering phase function (Equation 2.19), but keeps the isotropic assumption for the scattering coefficient (Equation 2.16) [126]. Although this model is an improvement over the isotropic diffusion model (Equation 2.46), it is likely that in tissue where the phase function is anisotropic, the scattering coefficient will be anisotropic as well.

In tissues that contain very high concentrations of blood (i.e., high μ_a), as in the liver, or in applications wherein the photon propagation distances are comparable to ℓ_{tr} (e.g., finger joint measurements), the photon propagation directions do not fully randomize to create a nearly isotropic radiance. Further, some heterogenous tissues have both "diffusing regions" such as brain tissue, where the diffusion model assumptions hold, and "non-diffusing regions" such as cerebrospinal fluid, where the diffusion model assumptions break down [63, 196]. In all of these cases, approximations beyond the P_1 (Equation 2.27) are needed for optimal data analysis. One

[11]Recall that $\mu_s' \approx 1/\ell_{tr}$ (in diffusion regime) and μ_a are probability densities for isotropic light scattering and light absorption, respectively (see Figure 2.4, Equation 2.2, and Equation 2.45)

Table 2.3: Optical properties (mean $\pm$ SD) of brain and breast tissue at $\lambda = 780$ nm compiled from Tables 2 and 3 in Jacques' review of tissue optical properties [144].

Tissue	Brain	Breast	Number of samples (n)
μ_a (cm^{-1})	0.15 ± 0.04	0.05 ± 0.02	5
μ_s' (cm^{-1})	12 ± 8	11 ± 6	8

approach is to use the higher order P_3 approximation (Equation 2.22 with N = 3) of the light radiance in the radiative transport equation (Equation 2.9) to model the photon fluence rate [21, 135]. Another approach is to solve the radiative transport equation directly using numerical methods such as Monte Carlo simulations or finite element techniques [9, 79, 124, 162, 254]. Compared to the diffusion model, these more complex approaches are computationally time consuming.

The rest of this chapter mostly follows the tutorial approach taken in Durduran *et al* to present how the diffusion model is used in practice to probe tissue absorption and scattering with near-infrared light [79]. Section 2.13 then discusses how to convert measurements of μ_a at multiple wavelengths into measurements of oxygenated and de-oxygenated tissue hemoglobin concentrations.

2.4 Source Types

To apply the diffusion model for measuring tissue absorption and scattering, one typically detects light at known distances from point sources. Figure 2.6 shows two source-detector pairs; one in the reflection geometry and the other in the transmission geometry. In the reflection geometry (also see Figure 2.2), light injected into the tissue by a source fiber (usually coupled to a laser) is detected a distance ρ away with another fiber (usually coupled to a photomultiplier tube or avalanche photodiode). In the transmission geometry, light detection is facilitated using either a fiber or a lens/CCD camera system. At first glance, the directional light from a fiber violates the isotropic source assumption for the diffusion model (Equation 2.40). This light source, however, can be very well approximated by an isotropic light source at depth ℓ_{tr} inside the tissue [96]. In practice, the source-detector separations should exceed $3\ell_{tr}$ to apply the diffusion model and expect accurate ($\sim 5\%$) results [154].

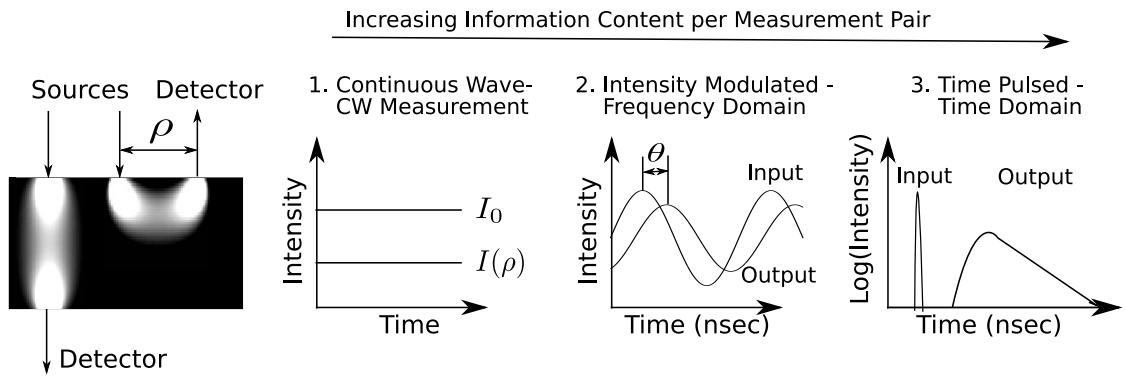

Figure 2.6: Three common types of sources are employed. On the far left are schematic "banana patterns" showing the sampled volumes in the reflection and transmission geometries. As a rough rule of thumb, the mean light penetration depth in the reflection geometry is $\rho/3$ (for a more precise relation, see [200]). For continuous wave (CW) sources (panel (1)), the input light intensity, I_0, remains constant, and slow ($0.1 - 1$ s) variations in the detected light intensity ($I(\rho)$) induced by changes in tissue absorption and tissue scattering are measured. For intensity modulated (FD) and time-resolved (TR) sources, the source (input) and detected (output) light intensities resemble panels (2) and (3), respectively. In the FD measurement, the amplitude and phase (θ) of the detected signal are related to the absolute tissue optical properties.

Three types of light sources commonly used in diffuse optics are (see Figure 2.6): continuous wave (CW), intensity modulated (FD), and time resolved (TR). The simplest source type is CW light, where the intensity remains constant over time [48, 61, 98, 228]. CW sources enable fast data acquisition and the use of simple detectors and detection electronics, but as I will discuss further, μ_a and μ_s' cannot be determined simultaneously from a single CW measurement (Sections 2.5).

Intensity modulated sources (the frequency-domain technique, FD) are more complex but also give more information about the medium [10, 47, 80, 113, 133, 253]. Here, the light intensity of the source is sinusoidally modulated with angular frequency ω (of order 100 MHz or larger, up to ~ 1 GHz), producing a diffusive wave in the medium oscillating at the same frequency (Section 2.5). At a given source-detector separation, both the amplitude and phase of the diffusing wave are measured. The additional information from the phase, in principle, permits simultaneous determination of μ_a and μ_s'.

Time resolved light sources (the time-domain technique, TR) deliver short light pulses ($<$ 100 ps) to the medium, which will temporally broaden as they propagate through the medium.

At the detector, the temporal pulse shape contains the necessary information to determine μ_a and D from a single source-detector pair. Time resolved light is related to intensity modulated light via a Fourier transform (Section 2.7), and it contains the same information content as intensity modulated sources scanned over the wide range of modulation frequencies present in the source light pulse [10, 16, 143, 201, 203].

2.5 Diffuse photon density waves

In the frequency-domain, the source is radio frequency modulated light delivered to the medium at position $\mathbf{r}_s$ such that $S(\mathbf{r}, t)$ in the diffusion model (2.46) is[12]

$$S(\mathbf{r}, t) = S_0 \left(1 + M\mathrm{e}^{i\omega t}\right) \delta(\mathbf{r} - \mathbf{r}_s), \tag{2.49}$$

where S_0 [W] is the time averaged power emitted by the source, M [dimensionless] is the depth of modulation of the source, $0 \leq M \leq 1$, ω is the angular frequency of modulation, i.e., $\omega = 2\pi f$ where f is the frequency of modulation in [Hz], and $\delta(\mathbf{r})$ [cm^{-3}] is the three-dimensional Dirac delta function. This light source produces a photon fluence rate with a continuous wave (CW) component and an oscillating ac component at the same angular frequency ω:

$$\begin{aligned} \Phi(\mathbf{r}, t) &= \Phi_{cw}(\mathbf{r}) + \Phi_{ac}(\mathbf{r}, t) \\ &= \Phi_{cw}(\mathbf{r}) + U(\mathbf{r})\mathrm{e}^{i\omega t}. \end{aligned} \tag{2.50}$$

Here, $U(\mathbf{r})e^{i\omega t}$ is the complex representation of the frequency-domain photon fluence rate. Both Φ_{cw} and U are described by diffusion equations obtained from substituting Equations 2.50 and 2.49 into Equation 2.46:

$$\nabla \cdot (D(\mathbf{r})\nabla\Phi_{cw}(\mathbf{r})) - v\mu_a(\mathbf{r})\Phi_{cw}(\mathbf{r}) = -vS_0\delta(\mathbf{r} - \mathbf{r}_s) \tag{2.51}$$

$$\nabla \cdot (D(\mathbf{r})\nabla U(\mathbf{r})) - (v\mu_a(\mathbf{r}) + i\omega)U(\mathbf{r}) = -vMS_0\delta(\mathbf{r} - \mathbf{r}_s). \tag{2.52}$$

For homogeneous media, these equations simplify to

$$\left(\nabla^2 - k_0^2\right) \Phi_{cw}(\mathbf{r}) = -\frac{vS_0}{D}\delta(\mathbf{r} - \mathbf{r}_s) \tag{2.53}$$

$$\left(\nabla^2 - k^2\right) U(\mathbf{r}) = -\frac{vMS_0}{D}\delta(\mathbf{r} - \mathbf{r}_s), \tag{2.54}$$

[12]For simplicity, I am employing the complex representation ($e^{i\omega t}$) for sinuosoidal oscillations in the source and fluence rate. The actual source and fluence rate will be the real parts of their complex representations.

where $k_0^2 \equiv v\mu_a/D$ and $k^2 \equiv (v\mu_a + i\omega)/D$.[13]

The general solution to Equation 2.54 is a damped wave-like fluence rate "disturbance" in the turbid medium, which is called a diffuse photon density wave.

2.5.1 Solutions in infinite, homogeneous turbid media

2.5.1.1 Frequency domain solution

Conceptually, diffuse photon density waves are easiest to understand in the infinite, homogeneous medium with a single intensity modulated point source at the origin (i.e., $\mathbf{r}_s = 0$ in Equation 2.49). In this geometry, the solution to Equation 2.54 given the boundary condition that the fluence rate falls to zero at infinity is well known [10, 45]. It has the form of a simple damped spherical wave with complex wave vector $k = k_r + ik_i$, i.e.,

$$U(\mathbf{r}) = \frac{vMS_0}{4\pi Dr}\exp(-kr), \tag{2.55}$$

where $r = |\mathbf{r}|$. To determine k_r and k_i, note that

$$k^2 \equiv \frac{v\mu_a + i\omega}{D} = \left(\frac{v^2\mu_a^2 + \omega^2}{D^2}\right)^{1/2} \exp\left[i\arctan\left(\frac{\omega}{v\mu_a}\right)\right], \tag{2.56}$$

and therefore

$$k_r = \left(\frac{v^2\mu_a^2 + \omega^2}{D^2}\right)^{1/4} \cos\left[\frac{1}{2}\arctan\left(\frac{\omega}{v\mu_a}\right)\right] = a\cos[b/2], \tag{2.57}$$

$$k_i = \left(\frac{v^2\mu_a^2 + \omega^2}{D^2}\right)^{1/4} \sin\left[\frac{1}{2}\arctan\left(\frac{\omega}{v\mu_a}\right)\right] = a\sin[b/2], \tag{2.58}$$

where $a \equiv ((v^2\mu_a^2 + \omega^2)/D^2)^{1/4}$, and $b \equiv \arctan(\omega/(v\mu_a))$. Equivalent expressions to Equations 2.57 and 2.58 are

$$k_r = \left(\frac{v\mu_a}{2D}\right)^{1/2} \left[\left(1 + \left[\frac{\omega}{v\mu_a}\right]^2\right)^{1/2} + 1\right]^{1/2} \tag{2.59}$$

$$k_i = \left(\frac{v\mu_a}{2D}\right)^{1/2} \left[\left(1 + \left[\frac{\omega}{v\mu_a}\right]^2\right)^{1/2} - 1\right]^{1/2}. \tag{2.60}$$

[13] Some authors use slightly different definitions for k^2 and U, e.g., $k^2 = (v\mu_a - i\omega)/D$ with $\Phi_{ac} = U\mathrm{e}^{-i\omega t}$; $k^2 = (-v\mu_a + i\omega)/D$ with $\Phi_{ac} = U\mathrm{e}^{-i\omega t}$; $k^2 = -(v\mu_a + i\omega)/D$ with $\Phi_{ac} = U\mathrm{e}^{i\omega t}$. The latter two definitions enable us to write Equation 2.54 in Helmholtz form, which has the advantage of more obvious analogies with waves. I chose the definitions used by Arridge *et al* in their classic paper deriving solutions to Equation 2.54 for several useful geometries [10], i.e., $k^2 = (v\mu_a + i\omega)/D$ with $\Phi_{ac} = U\mathrm{e}^{i\omega t}$. Of course, regardless of the way terms are defined, the solutions are the same.

The complete diffuse photon density wave is given by

$$\Phi_{ac}(\mathbf{r}, t) = A(\mathbf{r}) \exp\left[i(\omega t - \theta(\mathbf{r}))\right], \tag{2.61}$$

where $A(\mathbf{r})$ and $\theta(\mathbf{r})$ are the amplitude and phase of the diffuse photon density wave, respectively:

$$A(\mathbf{r}) = \frac{vMS_0}{4\pi Dr} \exp(-k_r r) \tag{2.62}$$

$$\theta(\mathbf{r}) = k_i r. \tag{2.63}$$

From measurements of A and θ at *one* source-detector separation r, Equations 2.62 and 2.63 can be solved for the optical properties μ_a and μ_s' only if v and the product MS_0 are known. We typically do assume a tissue index of refraction of $n = 1.4$ for calculating $v = c/n$ in the near-infrared spectral range [29, 144]. However, the product MS_0 is unknown in practice. Even if the modulation depth and power of the source laser are carefully measured initially, small changes in any elements of the fluence rate measurement (e.g., detector sensitivity, fiber coupling with tissue) will effectively change MS_0 [96]. I will discuss these fluence rate measurement effects in detail in Section 2.11.

The determination of optical properties with diffuse photon density waves, then, requires measurements of their amplitude and phase at *multiple* distances from the source. Figure 2.7 outlines the procedure for extracting μ_a and μ_s' from measured changes in wave amplitude and wave phase with distance from the source. Briefly, the slopes of $\log(Ar)$ vs. r and θ vs. r are $-k_r$ and k_i, respectively, from which μ_a and μ_s' can be calculated using Equations 2.57 and 2.58 [93].

Specifically, from using trigonometry relations,

$$\frac{k_r}{k_i} - \frac{k_i}{k_r} = \frac{1 + \cos b - 1 + \cos b}{\sin b} = \frac{2}{\tan b} = \frac{2v\mu_a}{\omega}, \tag{2.64}$$

and

$$k_r^2 - k_i^2 = a^2 \cos b = a^2 \frac{v\mu_a}{\sqrt{\omega^2 + (v\mu_a)^2}} = \frac{v\mu_a}{D}. \tag{2.65}$$

Rearranging Equations 2.64 and 2.65, we obtain

$$\mu_a = \frac{\omega}{2v}\left(\frac{k_r}{k_i} - \frac{k_i}{k_r}\right), \tag{2.66}$$

$$\mu_s' = \frac{2v}{3\omega} k_r k_i - \mu_a \approx \frac{2v}{3\omega} k_r k_i. \tag{2.67}$$

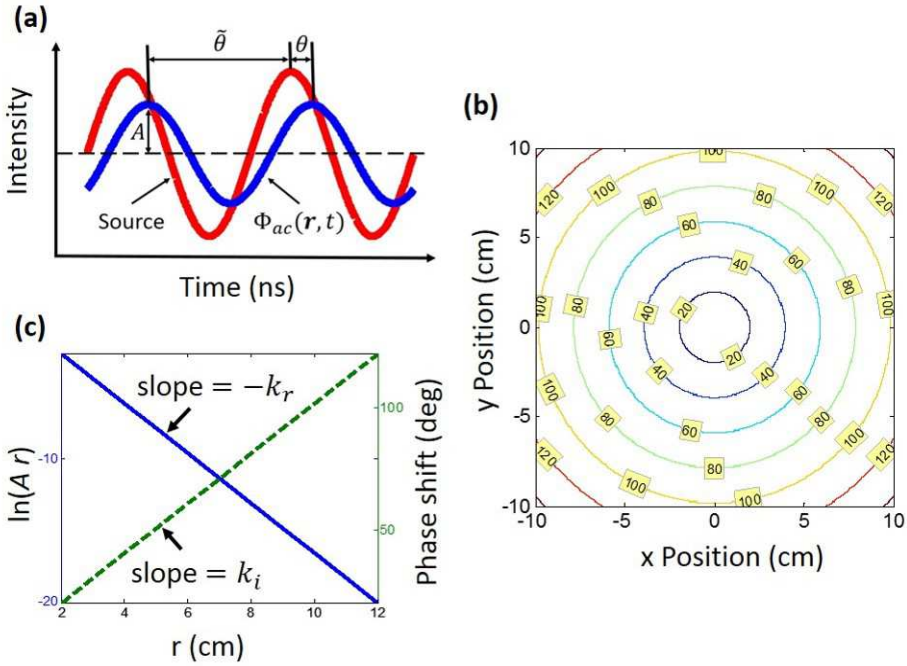

Figure 2.7: A radio-frequency modulated light source at $\mathbf{r}_s = 0$ induces a diffuse photon density wave, $\Phi_{ac}(\mathbf{r}, t)$ (Equation 2.61), which is characterized by its amplitude, A, and its phase shift from the source, θ **(a)**. Some researchers use $\tilde{\theta} = -\theta$ (also depicted in panel (a)) to characterize the phase shift of the diffuse photon density wave instead, i.e., $\Phi_{ac} = A \exp[i(\omega t + \tilde{\theta})]$. In the homogeneous infinite geometry, Φ_{ac} is a simple spherical wave. Panel **(b)** shows constant phase contours (θ in degrees) as a function of position for a typical set of parameters in tissue measurements: $\mu_a = 0.1$ 1/cm, $\mu_s' = 10$ 1/cm, $\omega = 2\pi \times (70$ MHz$)$ and an index of refraction $n = 1.4$. Note that the wavelength ($2\pi/k_i \sim 19$ cm) is roughly a factor of 20 greater than the attenuation length ($1/k_r \sim 1$ cm). For this same set of parameters, panel **(c)** plots $\log(Ar)$ (blue solid line) and θ (green dashed line) as a function of the radial distance from the source, r. The slopes reveal $-k_r$ and k_i (see Equations 2.62 and 2.63), from which μ_a and μ_s' can be calculated using Equations 2.66 and 2.67 (v is assumed). Note that the slope of $\tilde{\theta}$ vs. r is $-k_i$ instead of k_i. Therefore, phase measurements from instruments that report $\tilde{\theta}$ will show *decreasing* phase with increasing r.

The approximation in Equation 2.67 is equivalent to making the approximation $D \approx v/(3\mu_s')$.

Equations 2.59 and 2.60 reveal why frequency domain sources are radio-frequency modulated. If $\omega \ll v\mu_a$, then k_i is very close to zero, resulting in unmeasurable phase changes with increasing r. As ω increases, the instrument will have an improved sensitivity to phase changes with increasing r at the cost of higher attenuation in the amplitude. The modulation frequency should be chosen to balance the trade off between having a high sensitivity to phase with increasing r and having a large range of separations r over which the amplitude signal is above the noise floor of the detector. Thus, radio frequencies of order ~ 100 MHz up to $1GHz$ are used for modulating light sources in frequency domain measurements of tissue. Note that instrument measurements cannot differentiate between phase shifts of 0, 2π, 4π, etc. Source-detector separations in multiple distance measurements, then, should be chosen such that the phase does not change by more than 2π between adjacent separations. In practice this is not an issue for frequencies less than 1 GHz because the wavelength of the diffuse photon density wave ($2\pi/k_i$) is much greater than the attenuation length of the wave ($1/k_r$), as is evident from Figure 2.7. Therefore, at separations wherein the phase has changed by over a wavelength, the amplitude is essentially zero.

2.5.1.2 Continuous wave solution

The CW fluence rate is the solution to Equation 2.53 in the homogeneous infinite geometry, which is the special case of the ac solution (Equation 2.55)at $\omega = 0$:

$$\Phi_{cw}(\mathbf{r}) = \frac{vS_0}{4\pi Dr} \exp(-\left[v\mu_a/D\right]^{1/2} r). \tag{2.68}$$

The optical properties μ_a and μ_s' cannot be uniquely determined from measurements of $\Phi_{cw}(\mathbf{r})$ alone, regardless of the number of distances r that are measured. In a classic paper, Arridge and Lionheart theoretically proved that it is impossible to uniquely separate absorption from scattering with CW light [8]. Consequentially, in order to obtain μ_a from CW light measurements, D must be *assumed*, which is a major drawback. Errors in the assumed tissue scattering coefficient will result in systematic errors in the measured absorption coefficient.

Some frequency domain instruments, such as the ISS Imagent (ISS Medical, Urbana-Champaign, IL), measure both the ac and dc fluence rates. In the same manner as described in Figure 2.7,

μ_a and D can be determined from measurements of dc amplitude and phase at multiple source-detector separations. The dc amplitude (Equation 2.68) is less attenuated than the ac amplitude (Equation 2.62) at a given separation r, which in principle means the signal to noise ratio of the dc amplitude is higher than the ac amplitude. However, the ac amplitude and phase combination for determining optical properties is less sensitive to stray ambient light. In typical measurements, the phase is substantially noisier than the ac or dc amplitudes. This suggests that it may be best to bypass the phase measurements by using the ac and dc amplitudes to obtain the tissue optical properties. However, although the ac and dc signals are less noisy than the phase, the extracted optical properties from ac and dc amplitude measurements are very susceptible to instrument noise because of the similarity in changes of the ac and dc amplitudes with increasing r [93, Section 2D]. In practice, Equations 2.68 and 2.62 are not independent, meaning they cannot be uniquely solved for μ_a and μ_s'.

2.5.1.3 Time domain solution

The time-domain and frequency-domain solutions to Equation 2.46 are Fourier transform pairs (Section 2.7). Therefore, the inverse Fourier transform of Equation 2.55 gives the homogeneous infinite medium fluence rate solution to Equation 2.46 in the presence of a pulsed point source of the form $S(\mathbf{r}, t) = S_0\delta(\mathbf{r})\delta(t)$, where S_0 [J] is the total energy of the light pulse. The resulting fluence rate is

$$\Phi(\mathbf{r}, t) = \frac{vS_0}{(4\pi Dt)^{3/2}} \exp\left[-\frac{r^2}{4Dt} - \mu_a vt\right]. \tag{2.69}$$

Here, instead of using fluence rate measurements at multiple distances to derive optical properties, one measures the fluence rate at multiple times for a *single source-detector separation*. Equation 2.69 (convolved with an "instrument response function") is then fit to this measured time-domain data to extract D and μ_a [39, 191]. Alternatively, if it is only necessary to determine μ_a, the full nonlinear fit can be avoided by noting that $\partial \log \Phi(\mathbf{r}, t)/\partial t \to -\mu_a v$ as $t \to \infty$. Thus, μ_a is given by the slope of the natural log of the fluence rate at long times (i.e., typically only a few nanoseconds) [201].

The major advantage of using time-resolved pulsed sources compared to intensity modulated

sources is that only one source-detector separation is needed to measure absolute optical properties. Also, by employing time-gating and moments analysis at the detection end, it is possible to pathlength resolve the detected light in order to reject contributions from superficial tissue layers [172, 222]. However, time-resolved instrumentation is considerably more complex and expensive than frequency-domain instrumentation.

2.6 Boundary Conditions

While conceptually useful, the infinite homogeneous medium is not a good appoximation for practical tissue geometries. Most realistic geometries have interfaces between different media. For example, in the DOS measurement depicted in Figure 2.2, there is the interface between the scalp and the probe. A particularly useful geometry is the planar interface wherein a semi-infinite turbid tissue is bounded in the other half-space by air (Figure 2.8). Another commonly used geometry is the slab geometry wherein tissue is bounded by two planar interfaces (Figure 2.8). The diffusion model can still be applied near these interfaces provided appropriate boundary conditions on the fluence rate are used. In this section, I will derive the partial-flux boundary condition (also known as the Robin boundary condition) and the extrapolated-zero boundary condition on the photon fluence rate at the interface between a highly scattering medium (e.g., tissue) and a *non-scattering* medium (e.g., air) [7,123]. These boundary conditions are applicable at a given point $\mathbf{r}_i$ on any turbid-nonscattering interface. In this derivation, it is necessary to consider the light radiance (see Table 2.1) again.

2.6.1 Partial-Flux Boundary Condition

Photons escaping from the tissue into air will almost never re-enter the tissue medium because non-scattering media do not alter the direction of light travel. Therefore, if all light sources are inside the tissue, the incoming irradiance (i.e., total light power per area traveling into the diffuse medium at the boundary) at position $\mathbf{r}_i$ on the interface, i.e., $J_{in}(\mathbf{r}, t)$, is due to Fresnel reflections of the radiance in the diffuse medium that travels out toward the interface (see Figure 2.8):

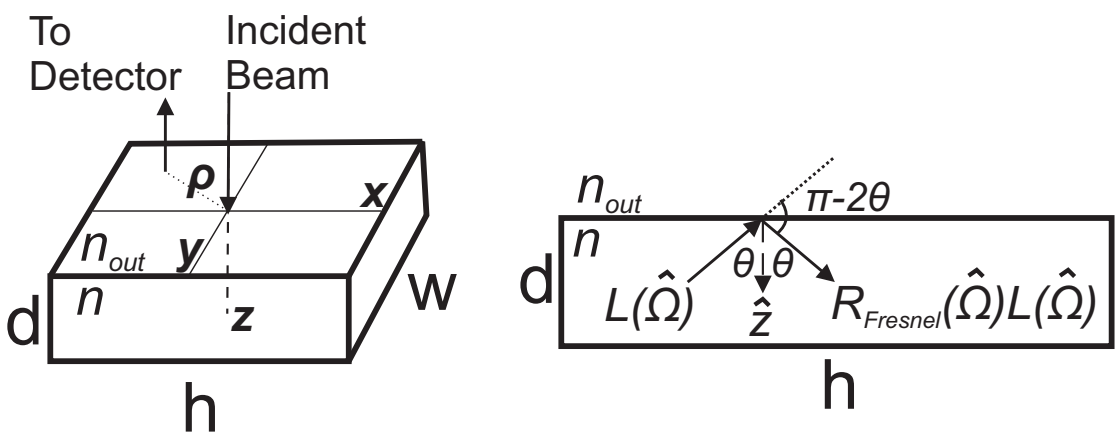

Figure 2.8: Common geometry used to model tissue with refractive index n that is bounded by a non-scattering medium with refractive index n_{out}. In the semi-infinite geometry, w, h, and d all go to infinity, while in the infinite slab geometry, w and h are infinite but d is finite. Both geometries have azimuthal symmetry about the z-axis, meaning the photon fluence rate only depends on the radial and axial cylindrical coordinates ρ and z. On the left, a single source-detector pair (with separation ρ) in the remission geometry is shown. Note that for the slab geometry, detectors can also be used for transmission measurements by being placed on the $z = d$ plane. On the right is a cross-section showing that the radiance moving into the turbid medium at a point $\mathbf{r}_i$ on the boundary is due to the Fresnel reflection of the radiance incident on the boundary.

$$J_{in}(\mathbf{r}_i, t) \equiv \int\limits_{\hat{\Omega}\cdot\hat{z}>0} L(\mathbf{r}_i, \hat{\Omega}, t)\hat{\Omega}\mathrm{d}\Omega \cdot \hat{z} \tag{2.70}$$

$$= \int\limits_{\hat{\Omega}\cdot\hat{z}<0} R_{Fresnel}(\hat{\Omega})L(\mathbf{r}_i, \hat{\Omega}, t)\hat{\Omega}\mathrm{d}\Omega \cdot (-\hat{z}). \tag{2.71}$$

$R_{Fresnel}(\hat{\Omega})$ is the familiar Fresnel reflection coefficient for light incident upon the boundary in a direction $\hat{\Omega}$ from within the tissue [116, Chapter 9], and $\mathbf{r}_i$ denotes a point on the boundary. Note that J_{in} is also called the partial flux because the integration in Equation 2.70 is over 2π steradians in the $z > 0$ hemisphere, whereas the integration in the full photon flux, $\mathbf{J}$ (Equation 2.21), is over all 4π steradians of space[14]. All of the light power crossing the boundary into the tissue is from Fresnel reflections, and consequentially the partial flux is the total reflected power into the tissue from light traveling inside the tissue towards the boundary (Equation 2.71).

To convert Equations 2.70 and 2.71 into a boundary condition on the fluence rate, we use the P_1 approximation of the radiance (Equation 2.27), which we also used to derive the photon diffusion equation. Substituting Equation 2.27 into Equation 2.70 and evaluating the integral in spherical coordinates results in

$$\begin{aligned} J_{in}(\mathbf{r}_i, t) &= \int_0^{\pi/2}\int_0^{2\pi}\left(\frac{1}{4\pi}\Phi + \frac{3}{4\pi}\mathbf{J}\cdot[\sin\theta\cos\phi\hat{x} + \sin\theta\sin\phi\hat{y} + \cos\theta\hat{z}]\right)\cos\theta\sin\theta\mathrm{d}\phi\mathrm{d}\theta \\ &= \frac{1}{2}\Phi(\mathbf{r}_i, t)\int_0^{\pi/2}\cos\theta\sin\theta\mathrm{d}\theta + \frac{3}{2}J_z(\mathbf{r}_i, t)\int_0^{\pi/2}\cos^2\theta\sin\theta\mathrm{d}\theta \\ &= \frac{\Phi(\mathbf{r}_i, t)}{4} + \frac{J_z(\mathbf{r}_i, t)}{2}, \end{aligned} \tag{2.72}$$

where $J_z(\mathbf{r}_i, t)$ is the $z-$component of the photon flux.

[14] $\mathbf{J}(\mathbf{r}_i, t)\cdot\hat{z}$ is the *net* light power per area crossing the boundary. The Fresnel reflections in Equation 2.71 determine the *total* light power per area crossing the boundary into the tissue, which is the partial flux.

Similarly, substituting Equation 2.27 into Equation 2.71 results in

$$\begin{aligned}
J_{in}(\mathbf{r}_i,t) &= \int_0^{\pi/2}\int_0^{2\pi} R_{Fresnel}(\theta)L(r_i,\pi-\theta,\phi,t)[-\cos(\pi-\theta)]\sin(\pi-\theta)\mathrm{d}\phi\mathrm{d}\theta \\
&= \int_0^{\pi/2}\int_0^{2\pi} R_{Fresnel}(\theta)\left(\frac{1}{4\pi}\Phi + \frac{3}{4\pi}\mathbf{J}\cdot[\sin(\pi-\theta)\cos\phi\hat{x}+\right. \\
&\qquad\qquad \left.\sin(\pi-\theta)\sin\phi\hat{y}+\cos(\pi-\theta)\hat{z}]\right)\cos\theta\sin\theta\mathrm{d}\phi\mathrm{d}\theta \\
&= \int_0^{\pi/2}\int_0^{2\pi} R_{Fresnel}(\theta)\left(\frac{1}{4\pi}\Phi - \frac{3}{4\pi}J_z\cos\theta\right)\cos\theta\sin\theta\mathrm{d}\phi\mathrm{d}\theta \\
&= R_\Phi\frac{\Phi(\mathbf{r}_i,t)}{4} - R_J\frac{J_z(\mathbf{r}_i,t)}{2} \qquad (2.73)
\end{aligned}$$

where

$$R_\Phi \equiv \int_0^{\pi/2} 2\sin\theta\cos\theta R_{Fresnel}(\theta)\mathrm{d}\theta \qquad (2.74)$$

$$R_J \equiv \int_0^{\pi/2} 3\sin\theta\cos^2\theta R_{Fresnel}(\theta)\mathrm{d}\theta. \qquad (2.75)$$

In arriving at Equation 2.73, we used the fact that $R_{Fresnel}(\hat{\Omega})$ depends on the polar angle θ (Figure 2.8) but not the azimuthal angle ϕ. For the case of unpolarized light with $n > n_{out}$, the reflection coefficient for light incident on the boundary from the tissue is [116, 123]

$$R_{Fresnel}(\theta) = \begin{cases} \frac{1}{2}\left(\frac{n\cos\theta' - n_{out}\cos\theta}{n\cos\theta' + n_{out}\cos\theta}\right)^2 + \frac{1}{2}\left(\frac{n\cos\theta - n_{out}\cos\theta'}{n\cos\theta + n_{out}\cos\theta'}\right)^2 & \text{if } 0 \le \theta \le \theta_c, \\ 1 & \text{if } \theta_c \le \theta \le \pi/2, \end{cases} \qquad (2.76)$$

where the angle of incidence θ and the refracted angle θ' satisfy Snell's law, i.e., $n\sin\theta = n_{out}\sin\theta'$, and the critical angle θ_c for total internal reflection is given by $n\sin\theta_c = n_{out}$.

Combining Equations 2.72 and 2.73, we obtain

$$\Phi(\mathbf{r}_i,t) = \frac{1+R_J}{1-R_\Phi}(-2J_z(\mathbf{r}_i,t)). \qquad (2.77)$$

Equation 2.77 is commonly rearranged in terms of an effective reflection coefficient, R_{eff}, to account for the refractive index mismatch between tissue and the non-scattering medium:

$$\Phi(\mathbf{r}_i,t) = \frac{1+R_{eff}}{1-R_{eff}}(-2J_z(\mathbf{r}_i,t)) \qquad (2.78)$$

with

$$R_{eff} \equiv \frac{R_\Phi + R_J}{2 - R_\Phi + R_J}. \qquad (2.79)$$

n	n_{out}	R_Φ	R_J	R_{eff}	$\lvert\Phi/J_z\rvert$
1.40	1.40	0	0	0	2.0
1.33	1.00	0.472	0.328	0.431	5.1
1.40	1.00	0.529	0.389	0.493	6.0

Table 2.4: Ratios of the fluence rate to the flux at the surface boundary, as given by Equation 2.77, for some typical index refraction

Given refractive indices n and n_{out}, $R_{eff} \approx -1.440\,(n/n_{out})^{-2} + 0.701\,(n/n_{out})^{-1} + 0.668 + 0.0636\,(n/n_{out})$ [88, 118]. However, it is best to solve the integrals for R_Φ (Equation 2.74) and R_J (Equation 2.75) numerically using Equation 2.76 for the Fresnel reflection coefficient. Table 2.4 lists the exact R_{eff} and ratio $|\Phi/J_z|$ for some typical index of refraction mismatches.

The partial flux boundary condition is obtained from substituting Fick's law of diffusion (Equation 2.43) in for J_z in Equation 2.78:

$$\Phi(\mathbf{r}_i, t) = z_b \frac{\partial \Phi(\mathbf{r}_i, t)}{\partial z}, \tag{2.80}$$

where

$$z_b \equiv \frac{2}{3}\ell_{tr}\frac{1 + R_{eff}}{1 - R_{eff}}. \tag{2.81}$$

2.6.2 Extrapolated-Zero Boundary Condition

The partial-flux boundary condition is exact, but it is difficult to use in practice, especially if analytical solutions to the diffusion equation with interfaces are desired. The extrapolated-zero boundary condition is an approximation of the partial-flux boundary condition that makes solving the diffusion equation more tractable. It is derived by Taylor expanding the fluence rate to first order around the boundary (at $z = 0$, with the first derivative term taken from the partial-flux boundary condition (Equation 2.80), i.e.,

$$\Phi(z) = \Phi(0) + \frac{\partial \Phi}{\partial z} z = \Phi(0) + \frac{\Phi(0)}{z_b} z. \tag{2.82}$$

As shown in Figure 2.9, if we use this line to approximate the fluence rate outside of the turbid medium ($z < 0$), then

$$\Phi(z = -z_b) = 0, \tag{2.83}$$

which is the extrapolated-zero boundary condition.

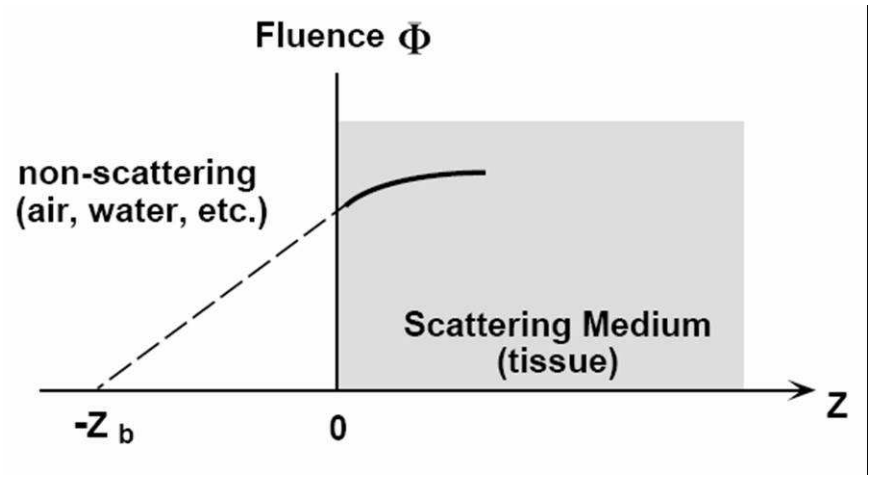

Figure 2.9: The fluence rate curve is approximated by its tangent line at $z = 0$, where the $\Phi = 0$ intercept of this curve is $z = -z_b$. This figure is adapted from Li [170, Fig. 1.6].

2.7 Green's function solutions

An age old strategy [6, 15] employed to solve the time-domain and frequency-domain diffusion equations (Equation 2.46 and Equation 2.52) is to first find their respective Green's functions, and then to use these Green's functions to construct more general solutions. We will first focus on the special case of homogeneous media. In the time-domain, the homogeneous photon diffusion equation is

$$\left(\nabla^2 - \frac{v\mu_a}{D} - \frac{1}{D}\frac{\partial}{\partial t}\right)\Phi(\mathbf{r}, t) = -\frac{v}{D}S(\mathbf{r}, t). \tag{2.84}$$

The homogeneous time-domain Green's function ($g(\mathbf{r}, \mathbf{r}_s, t, t_s)$ [cm^{-2}s^{-1}]) is defined as the solution of Equation 2.84 for a normalized infinitesimally narrow light pulse emitted at position $\mathbf{r}_s$ and time t_s, i.e.,

$$\left(\nabla^2 - \frac{v\mu_a}{D} - \frac{1}{D}\frac{\partial}{\partial t}\right) g(\mathbf{r}, \mathbf{r}_s, t, t_s) = -\frac{v}{D}\delta(\mathbf{r} - \mathbf{r}_s)\delta(t - t_s), \tag{2.85}$$

that satisfies the boundary condition (e.g., Equation 2.83) for the geometry of interest. For an arbitrary source distribution, $S(\mathbf{r}, t)$, the photon fluence rate solution to Equation 2.84 is the convolution of the Green's function with $S(\mathbf{r} + \mathbf{r}_s, t + t_s)$, i.e.,

$$\Phi(\mathbf{r}, t) = \int g(\mathbf{r}', \mathbf{r}_s, t', t_s) S(\mathbf{r} + \mathbf{r}_s - \mathbf{r}', t + t_s - t') \mathrm{d}^3 r' \mathrm{d}t', \tag{2.86}$$

where the spatial integration is done over the entire volume of tissue, and the temporal integration is from $-\infty$ to ∞. Notice that the photon fluence rate from a point source, i.e., $S(\mathbf{r},t) = S_0\delta(\mathbf{r}-\mathbf{r}_s, t-t_s)$, is $\Phi(\mathbf{r},t) = S_0 g(\mathbf{r},\mathbf{r}_s,t,t_s)$.

Similarly, the frequency-domain homogeneous Green's function ($G(\mathbf{r},\mathbf{r}_s)$ [cm^{-2}]) is the solution of Equation 2.54 for a normalized oscillating point source at position $\mathbf{r}_s$, i.e.,

$$\left(\nabla^2 - k^2\right) G(\mathbf{r},\mathbf{r}_s) = -\frac{v}{D}\delta(\mathbf{r}-\mathbf{r}_s), \tag{2.87}$$

that satisfies the boundary condition for the geometry of interest. The solution to the homogeneous frequency-domain photon diffusion equation (Equation 2.54) for an arbitrary distribution of oscillating point sources (i.e., $S_{ac}(\mathbf{r},t) = S(\mathbf{r})\mathrm{e}^{i\omega t}$) is

$$U(\mathbf{r}) = \int G(\mathbf{r}',\mathbf{r}_s)S(\mathbf{r}+\mathbf{r}_s-\mathbf{r}')\mathrm{d}^3r', \tag{2.88}$$

where the spatial integration again is over the entire volume of tissue. As with the time-domain, the frequency-domain fluence rate for a point source, $S(\mathbf{r}) = S_0\delta(\mathbf{r}-\mathbf{r}_s)$, is $U(\mathbf{r}) = S_0 G(\mathbf{r},\mathbf{r}_s)$.

Notice that Equation 2.86 can also be used to find the photon fluence rate, $\Phi_{ac}(\mathbf{r},t)$ (Equation 2.50), for the same arbitrary distribution of oscillating sources. Substituting S_{ac} into Equation 2.86, we obtain

$$\Phi_{ac}(\mathbf{r},t) = \mathrm{e}^{i\omega t}\int\left(\int_{-\infty}^{\infty} g(\mathbf{r}',\mathbf{r}_s,t',t_s)\mathrm{e}^{-i\omega(t'-t_s)}\mathrm{d}t'\right)S(\mathbf{r}+\mathbf{r}_s-\mathbf{r}')\mathrm{d}^3r'. \tag{2.89}$$

Recalling that $\Phi_{ac}(\mathbf{r},t) = U(\mathbf{r})\mathrm{e}^{i\omega t}$ (Equation 2.50), Equation 2.89 is equivalent to

$$U(\mathbf{r}) = \int\left(\int_{-\infty}^{\infty} g(\mathbf{r}',\mathbf{r}_s,t',t_s)\mathrm{e}^{-i\omega(t'-t_s)}\mathrm{d}t'\right)S(\mathbf{r}+\mathbf{r}_s-\mathbf{r}')\mathrm{d}^3r'. \tag{2.90}$$

Comparing Equation 2.90 with Equation 2.88, it is evident that the frequency-domain Green's function, $G(\mathbf{r},\mathbf{r}_s)$, is the Fourier transform of the time-domain Green's function, i.e.,

$$G(\mathbf{r},\mathbf{r}_s) = \int_{-\infty}^{\infty} g(\mathbf{r},\mathbf{r}_s,t,t_s)\mathrm{e}^{-i\omega(t-t_s)}\mathrm{d}t. \tag{2.91}$$

Correspondingly, the time-domain Green's function is the inverse Fourier transform of $G(\mathbf{r},\mathbf{r}_s)$:

$$g(\mathbf{r},\mathbf{r}_s,t,t_s) = \frac{1}{2\pi}\int_{-\infty}^{\infty} G(\mathbf{r},\mathbf{r}_s)\mathrm{e}^{i\omega(t-t_s)}\mathrm{d}\omega. \tag{2.92}$$

Importantly, Equations 2.91 and 2.92 can be utilized to convert a time-domain Green's function to its corresponding frequency-domain Green's function, and vice versa. The time-domain and frequency-domain fluence rates are then given by Equations 2.86 and 2.88, respectively.

Finally, the Green's function for a continuous-wave light source (i.e., $G_{cw}(\mathbf{r}, \mathbf{r}_s)$) is the special case of the frequency-domain Green's function for $\omega = 0$. The CW analogue of Equation 2.88 for the CW fluence rate is

$$\Phi_{cw}(\mathbf{r}) = \int G_{cw}(\mathbf{r}', \mathbf{r}_s) S(\mathbf{r} + \mathbf{r}_s - \mathbf{r}') \mathrm{d}^3 r'. \tag{2.93}$$

Exactly the same approach can be used for heterogeneous geometries as well. The key difference is that the definition of time-domain and frequency-domain Green's functions are the heterogeneous analogues of Equation 2.85 and Equation 2.87.

2.8 Semi-infinite Frequency-Domain Green's Function for Partial-Flux Boundary Condition

I will now utilize the method of images [35] to derive the frequency-domain Green's function of the photon diffusion equation for the semi-infinite geometry (Figure 2.8) and the partial-flux boundary condition (Equation 2.80). The method of images consists of adding infinite medium Green's functions (e.g., arising from a light source and "image sources") together in a way that satisfies the appropriate boundary condition.

First, recall from Section 2.4 that light from the incident beam in Figure 2.8 is well approximated as an isotropic point source at position (in cylindrical coordinates) $\mathbf{r}_s = (\rho_s = 0, z_s = \ell_{tr})$. The frequency-domain Green's function for this point source in the infinite geometry is (see Equation 2.55)

$$G_I([\rho, z], [\rho_s = 0, z_s = \ell_{tr}]) = \frac{v}{4\pi D r_1} \exp(-k r_1), \tag{2.94}$$

where $r_1 \equiv \sqrt{(z - \ell_{tr})^2 + \rho^2}$. The partial-flux Green's function for the semi-infinite geometry (i.e., G_S^{pf}) is the sum of the infinite geometry Green's function and a correction term G_c that arises from the presence of the boundary:

$$G_S^{pf} = G_I([\rho, z], [\rho_s = 0, z_s = \ell_{tr}]) + G_c([\rho, z], [\rho_s = 0, z_s = \ell_{tr}]). \tag{2.95}$$

The partial-flux boundary condition (Equation 2.80) for Equation 2.95 is

$$(G_I + G_c)_{z=0} = z_b \left[\frac{\partial G_I}{\partial z} + \frac{\partial G_c}{\partial z} \right]_{z=0}. \tag{2.96}$$

Substituting Equation 2.94 into Equation 2.96, we obtain

$$\begin{aligned}
\left(\frac{\partial G_c}{\partial z} - \frac{1}{z_b} G_c \right)_{z=0} &= - \left(\frac{\partial G_I}{\partial z} - \frac{1}{z_b} G_I \right)_{z=0} \\
&= \left(\frac{v}{4\pi D r_1^2} \mathrm{e}^{-kr_1} \left[k(z - \ell_{tr}) + \frac{z - \ell_{tr}}{r_1} \right] + \frac{v}{4\pi D z_b r_1} \mathrm{e}^{-kr_1} \right)_{z=0} \\
&= \frac{v \exp\left[-k\sqrt{\ell_{tr}^2 + \rho^2} \right]}{4\pi D(\ell_{tr}^2 + \rho^2)} \left(-k\ell_{tr} - \frac{\ell_{tr}}{\sqrt{\ell_{tr}^2 + \rho^2}} + \frac{1}{z_b} \right),
\end{aligned} \tag{2.97}$$

where z_b is given by Equation 2.81.

The next step is to consider the infinite Green's function for an image point source (Figure 2.10) at ($\rho_s = 0$, $z_s = -\ell_{tr}$), i.e.,

$$G_I^{\text{image}} = \frac{v}{4\pi D r_2} \exp[-kr_2], \tag{2.98}$$

where $r_2 \equiv \sqrt{(z + \ell_{tr})^2 + \rho^2}$.

Notice at the interface, $z = 0$, that

$$\begin{aligned}
\left[\left(\frac{\partial}{\partial z} + \frac{1}{z_b} \right) G_I^{\text{image}} \right]_{z=0} &= \left(-\frac{v}{4\pi D r_2^2} \mathrm{e}^{-kr_2} \left[k(z + \ell_{tr}) + \frac{z + \ell_{tr}}{r_2} \right] + \frac{v}{4\pi D z_b r_2} \mathrm{e}^{-kr_2} \right)_{z=0} \\
&= \frac{v \exp\left[-k\sqrt{\ell_{tr}^2 + \rho^2} \right]}{4\pi D(\ell_{tr}^2 + \rho^2)} \left(-k\ell_{tr} - \frac{\ell_{tr}}{\sqrt{\ell_{tr}^2 + \rho^2}} + \frac{1}{z_b} \right).
\end{aligned} \tag{2.99}$$

The right hand sides of Equations 2.97 and 2.99 are identical, which means that a solution for G_c that satisfies

$$\frac{\partial G_c}{\partial z} - \frac{1}{z_b} G_c = \left(\frac{\partial}{\partial z} + \frac{1}{z_b} \right) G_I^{\text{image}} \tag{2.100}$$

will also satisfy the partial-flux boundary condition.

To solve Equation 2.100, multiply both sides by $\exp[-z/z_b]$ and then integrate the resulting

equation, i.e.,

$$\begin{aligned}
\int_z^\infty \frac{\partial}{\partial z'}\left(\mathrm{e}^{-z'/L_s}G_c\right)\mathrm{d}z' &= \int_z^\infty \frac{\partial}{\partial z'}\left(\frac{v}{4\pi D r_2}\mathrm{e}^{-(kr_2+z'/z_b)}\right)\mathrm{d}z' + \\
&\quad \frac{2}{z_b}\int_z^\infty \frac{v}{4\pi D r_2}\mathrm{e}^{-(kr_2+z'/z_b)}\mathrm{d}z', \\
\Rightarrow -G_c &= -\frac{v}{4\pi D r_2}\mathrm{e}^{-kr_2} - \frac{2}{z_b}\int_z^\infty \frac{v}{4\pi D r_2}\mathrm{e}^{-(k_0 r_2+[z'-z]/L_s)}\mathrm{d}z', \\
\Rightarrow G_c &= \frac{v}{4\pi D r_2} - \frac{2}{z_b}\int_0^\infty \frac{v}{4\pi D r_2(u)}\mathrm{e}^{-(k_0 r_2(u)+u/z_b)}\mathrm{d}u, \qquad (2.101)
\end{aligned}$$

where a change of variables $u = z' - z$ was made between lines 2 and 3.

Substituting Equation 2.101 into Equation 2.95 results in the Green's function that satisfies the diffusion equation inside the semi-infinite medium ($z > 0$) as well as the partial-flux boundary condition:

$$\begin{aligned}
G_S^{pf} = \frac{v}{4\pi D}\Bigg[&\frac{\mathrm{e}^{-kr_1}}{r_1} + \frac{\mathrm{e}^{-kr_2}}{r_2} - \\
&\frac{2}{z_b}\int_0^\infty \mathrm{e}^{-u/z_b}\frac{\exp\left[-k\sqrt{(z+\ell_{tr}+u)^2+\rho^2}\right]}{\sqrt{(z+\ell_{tr}+u)^2+\rho^2}}\mathrm{d}u\Bigg]. \qquad (2.102)
\end{aligned}$$

We know that Equation 2.102 satisfies the photon diffusion equation (Equation 2.54) in addition to the partial-flux boundary condition because it is a linear sum of infinite media Green's functions (Equation 2.94). Each infinite Green's function satisfies the photon diffusion equation, and therefore their sum will also satisfy the photon diffusion equation.

As illustrated in the left panel of Figure 2.10, the first two terms in Equation 2.102 are the infinite medium Green's functions from a point source at ($\rho_s = 0$, $z_s = \ell_{tr}$) and an image source at ($\rho_s = 0$, $z_s = -\ell_{tr}$). The integral in Equation 2.102 represents a continuous line of infinite Green's functions from image sinks (i.e., image sinks contribute negatively to G_S) that starts at ($\rho_s = 0$, $z = -\ell_{tr}$) and extends to ($\rho_s = 0$,$z = -\infty$). The magnitudes of the sinks are exponentially damped as $z \to -\infty$ with a characteristic decay length of z_b (Figure 2.10).

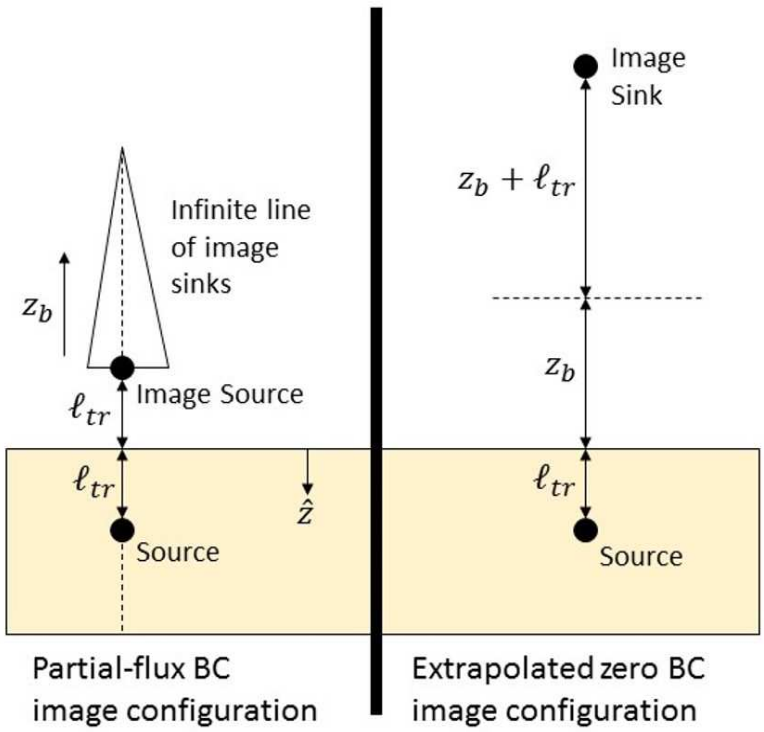

Figure 2.10: Analytical Green's functions in homogeneous semi-infinite media for both the partial-flux (Equation 2.80) and extrapolated-zero (Equation 2.83) boundary conditions can be derived using the method of images. The method of images finds the superposition of infinite media Green's functions (Equation 2.94) that satisfies the appropriate boundary condition. One term in the superposition is the infinite Green's function from the "real light source". The other terms arise from image sources (e.g., positive terms) and image sinks (e.g., negative terms). The image source and sink distributions for the partial-flux (left panel) and extrapolated-zero (right panel) boundary conditions are shown. For the partial-flux case, the infinite line of sinks is exponentially damped as $z \to -\infty$ with a characteristic decay length of z_b. This figure is adapted from Haskell [123, Fig. 4].

2.9 Semi-infinite Frequency-Domain Green's Function for Extrapolated-Zero Boundary Condition

In the semi-infinite geometry, the extrapolated-zero boundary condition (Equation 2.83) is satisfied by a superposition of only two infinite medium Green's functions (Equation 2.94), i.e.,

$$G_S([\rho, z], [\rho_s = 0, z_s = \ell_{tr}]) = \frac{v}{4\pi D}\left[\frac{\exp(-kr_1)}{r_1} - \frac{\exp(-kr_b)}{r_b}\right], \tag{2.103}$$

where

$$r_1 = \sqrt{(z - \ell_{tr})^2 + \rho^2} \tag{2.104}$$

$$r_b = \sqrt{(z + 2z_b + \ell_{tr})^2 + \rho^2}.. \tag{2.105}$$

The first term is from the source at ($\rho_s = 0$, $z_s = \ell_{tr}$) and the second term is from an image sink at ($\rho_s = 0$, $z_s = -(\ell_{tr} + 2z_b)$) (Figure 2.10). Obviously, the extrapolated-zero solution (Equation 2.103) is more tractable than the partial-flux solution (Equation 2.102) because there is no integral to evaluate.

2.9.1 Extrapolated-zero and partial-flux multipole expansion

The extrapolated-zero image configuration (Figure 2.10) is the best single-point image representation of the partial-flux configuration, differing only in octupole and higher multipole moments [123]. Thus, far away from the image configurations, the partial-flux and extrapolated-zero solutions are virtually the same. The semi-infinite Green's functions Equation 2.102 and Equation 2.103 have the same $1/|\mathbf{r}-\mathbf{r}_s|$ dependence as the electrostatics Coulomb potential [116, Section 3.4].

Therefore, a multipole expansion on the semi-infinite photon fluence rate solutions can be done, and it's useful to compare the "image configuration dipole moments" for the partial-flux and extrapolated-zero fluence rates. Recall from electrostatics that two charge distributions with the same dipole moment have virtually the same electrostatic potential at distances far from the the distribution [116]. Similarly, two image configurations with the same dipole moment have virtually the same fluence rate at distances far from the image distribution.

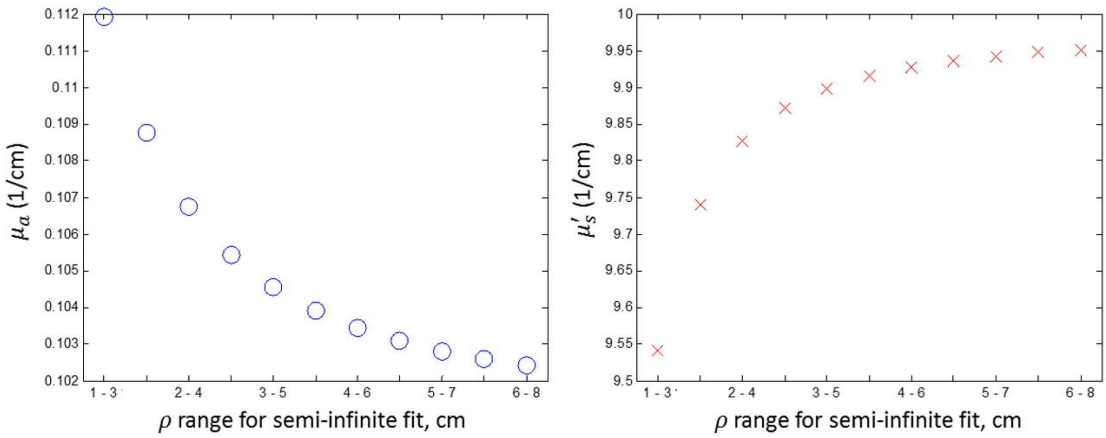

Figure 2.11: Simulated amplitude and phase data as a function of source-detector separation, ρ, was generated using the exact semi-infinite Green's function (Equation 2.103) with $\mu_a = 0.1$ cm^{-1}, $\mu_s' = 10$ cm^{-1}, $n = 1.4$, $n_{out} = 1$, and $f = \omega/2\pi = 70$ MHz. Equations 2.110 and 2.111 were employed to calculate μ_a (left) and μ_s' (right) from linear fits to five equally spaced source-detector separations spaced over the ranges specified on the horizontal axis, i.e., [1, 1.5, 2, 2.5, 3] cm, [1.5, 2, 2.5, 3, 3.5] cm, . . ., [6, 6.5, 7, 7.5, 8] cm.

I will first compute the dipole moment of the partial-flux image configuration in Figure 2.10:

$$\mathbf{p} \approx \left(2\ell_{tr} + \frac{2}{z_b}\int_0^\infty z\mathrm{e}^{-z/z_b}\right)\mathrm{e}^{-k\rho}\hat{z} = 2(z_b + \ell_{tr})\mathrm{e}^{-k\rho}\hat{z}. \tag{2.106}$$

Here, I made the approximation that $\exp[-k|\mathbf{r} - \mathbf{r}_s|] \approx \exp[-k\rho]$, which is the case on the planar interface for large ρ. Also, I used the image source position as the origin for the dipole calculation.

The dipole moment of the extrapolated-zero image configuration in Figure 2.10 is

$$\mathbf{p} \approx 2(\ell_{tr} + z_b)\mathrm{e}^{-k\rho}\hat{z}, \tag{2.107}$$

which is the same as Equation 2.106. It also turns out that the two image configurations have the same quadrupole moments for the origin on the planar interface [123].

The main point to remember is that for measurements with long source-detector separations compared to ℓ_{tr}, the extrapolated-zero fluence rate is an excellent approximation of the partial-flux fluence rate [123].

2.9.2 Extrapolated-zero Green's function at the boundary (large ρ limit)

In diffuse optical measurements, the fluence rate is typically detected at the tissue-air interface, i.e., $z = 0$. Equation 2.83 can be fit exactly, but in the limit $\rho \gg (\ell_{tr}+2z_b)$, the extrapolated-zero Green's function simplifies considerably. Following Li's discussion [170, Sec. 1.6], at $z = 0$ and $\rho \gg (\ell_{tr} + 2z_b)$ (see Equations 2.104 and 2.105),

$$
\begin{aligned}
r_1 &\approx \rho \left[1 + \frac{1}{2}\left(\frac{\ell_{tr}}{\rho}\right)^2\right], \\
r_b &\approx \rho \left[1 + \frac{1}{2}\left(\frac{\ell_{tr} + 2z_b}{\rho}\right)^2\right], \\
\frac{1}{r_1} &\approx \frac{1}{\rho}\left[1 - \frac{1}{2}\left(\frac{\ell_{tr}}{\rho}\right)^2\right], \\
\frac{1}{r_b} &\approx \frac{1}{\rho}\left[1 - \frac{1}{2}\left(\frac{\ell_{tr} + 2z_b}{\rho}\right)^2\right].
\end{aligned}
$$

Applying these approximations to Equation 2.83 and dropping all terms of order higher than $1/\rho^2$, we obtain

$$
\begin{aligned}
G([\rho, z = 0], [\rho_s = 0, z_s = \ell_{tr}]) &\approx \frac{v}{4\pi D}\frac{\mathrm{e}^{-k\rho}}{\rho}\left[\exp\left(-k\frac{\ell_{tr}^2}{2\rho}\right)\left(1 - \frac{1}{2}\left[\frac{\ell_{tr}}{\rho}\right]^2\right) - \right. \\
&\qquad \left. \exp\left(-k\frac{(\ell_{tr} + 2z_b)^2}{2\rho}\right)\left(1 - \frac{1}{2}\left[\frac{\ell_{tr} + 2z_b}{\rho}\right]^2\right)\right], \\
&\approx \frac{v}{4\pi D}\frac{\mathrm{e}^{-k\rho}}{\rho}\left[\left(1 - \frac{k\ell_{tr}^2}{2\rho}\right)\left(1 - \frac{1}{2}\left[\frac{\ell_{tr}}{\rho}\right]^2\right) - \right. \\
&\qquad \left. \left(1 - \frac{k_0(\ell_{tr} + 2z_b)^2}{2\rho}\right)\left(1 - \frac{1}{2}\left[\frac{\ell_{tr} + 2z_b}{\rho}\right]^2\right)\right], \\
&\approx \frac{v}{4\pi D}\frac{\mathrm{e}^{-k\rho}}{\rho}\left[1 - \frac{k\ell_{tr}^2}{2\rho} - 1 + \frac{k(\ell_{tr} + 2z_b)^2}{2\rho}\right], \\
&= \frac{v}{4\pi D}\frac{\mathrm{e}^{-k\rho}}{\rho^2}[2k(z_b\ell_{tr} + z_b^2)]. \qquad (2.108)
\end{aligned}
$$

For an oscillating point source $S(\mathbf{r}) = MS_0\mathrm{e}^{i\omega t}\delta(z-\ell_{tr})\delta(\rho)$, the frequency-domain photon fluence rate is obtained from substituting Equation 2.108 into 2.88, i.e.,

$$
U(\rho, z = 0) \approx \frac{MS_0 v}{4\pi D}\frac{\mathrm{e}^{-k\rho}}{\rho^2}\left[2k(z_b\ell_{tr} + z_b^2\right]. \qquad (2.109)
$$

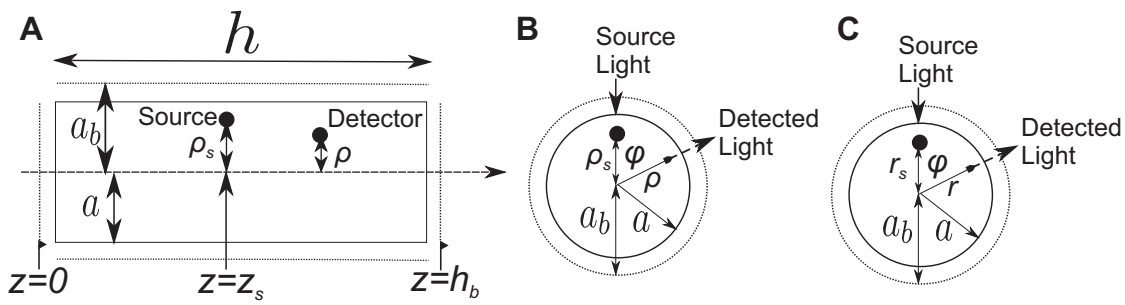

Figure 2.12: Two orthogonal cross-sections of the cylindrical geometry (**A**, **B**) and one cross section of the spherical geometry (**C**). For the infinite cylindrical geometry, $h \to \infty$.

The amplitude and phase of this diffuse photon density wave (i.e., $U(\rho, z = 0) = A(\rho)\mathrm{e}^{-i\theta(\rho)}$; see Equation 2.61) satisfy

$$\log(\rho^2 A(\rho)) = -k_r \rho + \log(A_0), \tag{2.110}$$

$$\theta = \theta_0 - k_i \rho, \tag{2.111}$$

where k_r and k_i are given by Equations 2.59 and 2.60, respectively. Therefore, in the large ρ limit of the semi-infinite geometry, k_r and k_i are determined from linear fits to measurements of $\log(\rho^2 A(\rho)$ and $\theta(\rho)$ at multiple source-detector separations. Then, μ_a and μ_s' are determined from k_r and k_i via Equations 2.66 and 2.67.

Equations 2.110 and 2.111 are an approximation of the semi-infinite fluence rate, which can lead to a systematic error of up to 10% in the calculated absorption coefficient (Figure 2.11). This systematic effect approximately divides out when computing fractional changes in hemoglobin concentration or the tissue oxygen saturation with multispectral measurements.

2.10 Extrapolated-zero Green's Functions in Spherical, Cylindrical, Slab, and Two-layer Geometries

Tables 2.5 and 2.6 show the frequency-domain and time-domain Green's functions subject to the extrapolated-zero boundary condition for cylindrical (Figure 2.12), spherical (Figure 2.12), and slab (Figure 2.8 homogeneous geometries [10]. Again, the photon fluence rates are calculated from the Green's functions using Equations 2.88 and 2.86.

Case	Green's function (frequency-domain)
Infinite	$G(\mathbf{r},\mathbf{r}_s) = \frac{v}{4\pi D\lvert\mathbf{r}-\mathbf{r}_s\rvert}\exp(-k\lvert\mathbf{r}-\mathbf{r}_s\rvert)$
Semi-infinite	$G([\rho,z],[\rho_s=0,z_s=\ell_{tr}]) = \frac{v}{4\pi D}\left[\frac{\exp(-kr_1)}{r_1} - \frac{\exp(-kr_b)}{r_b}\right]$
Infinite Slab	$G([\rho,z],[\rho_s=0,z_s=\ell_{tr}]) = \frac{v}{4\pi D}\sum_{m=-\infty}^{\infty}\left(\frac{\exp[-kr_{+,m}]}{r_{+.m}} - \frac{\exp[-kr_{-.m}]}{r_{-,m}}\right)$
Infinite Cylindrical	$G([\rho,\phi,z],[\rho_s,z_s]) = \frac{v}{2\pi D a_b^2}\sum_{m=-\infty}^{\infty}\cos m\phi\sum_{\beta_m}\frac{\mathrm{e}^{-\lvert z-z_s\rvert/\sqrt{k^2+\beta_m^2}}}{\sqrt{k^2+\beta_m^2}}\frac{J_m(\beta_m\rho)J_m(\beta_m\rho_s)}{[J'_m(\beta_m a_b)]^2}$
Finite Cylindrical	$G([\rho,\phi,z],[\rho_s,z_s]) = \frac{v}{\pi D(h+2z_b)}\sum_{m=1}^{\infty}\sin\frac{m\pi z}{h+2z_b}\sin\frac{m\pi z_s}{h+2z_b}\times$ $\sum_{n=-\infty}^{\infty}\frac{I_n(\rho k_m)[I_n(a_b k_m)K_n(\rho_s k_m)-I_n(\rho_s k_m)K_n(a_b k_m)]}{I_n(a_b k_m)}\cos n\phi$
Spherical ($r_s < r < a$)	$G([r,\phi],r_s) = \frac{v}{4\pi D\sqrt{rr_s}}\sum_{n=0}^{\infty}\frac{K_{n+1/2}(kr)I_{n+1/2}(ka_b)-I_{n+1/2}(kr)K_{n+1/2}(ka_b)}{I_{n+1/2}(ka_b)}\times$ $(2n+1)I_{n+1/2}(kr_s)P_n(\cos\phi)$

$k \equiv \sqrt{(\mu_a v + i\omega)/D}$	$J_m(z)$ m^{th} order Bessel function, 1st kind
$r_1 \equiv \sqrt{(z-\ell_{tr})^2+\rho^2}$	$I_m(z)$ m^{th} order modified Bessel function, 1st kind
$r_b \equiv \sqrt{(z+2z_b+\ell_{tr})^2+\rho^2}$	$K_m(z)$ m^{th} order modified Bessel function, 2nd kind
$z_b = 2\ell_{tr}\frac{1+R_{eff}}{3(1-R_{eff})}$	$R_{eff} \approx -1.440\left(\frac{n}{n_{out}}\right)^{-2} + 0.701\left(\frac{n}{n_{out}}\right)^{-1} + 0.668 + 0.0636\left(\frac{n}{n_{out}}\right)$
m, an integer	$P_m(z)$ m^{th} order Legendre polynomial
$r_{\pm,m} \equiv \sqrt{\rho^2+(z-z_{\pm,m})^2}$	a, cylinder/sphere radius (Fig. 2.12)
$z_{+,m} \equiv 2m(d+2z_b)+\ell_{tr}$	$a_b = a + z_b$, i.e., extrapolated-zero boundary (cylinder/sphere)
$z_{-,m} \equiv 2m(d+2z_b)-2z_b-\ell_{tr}$	β_m, a positive root of $J_m(\beta_m a_b)=0$
d, slab thickness (Fig. 2.8)	ϕ, angle between input/output light beams (cylinder/sphere, Fig. 2.12)
$k_m \equiv \sqrt{k^2+m^2\pi^2/(h+2z_b)^2}$	ρ, radial cylindrical coordinate
r, radial spherical coordinate	h, finite cylinder axial length (Fig. 2.12)

Table 2.5: Frequency-domain Green's functions (Equation 2.87) in several homogeneous geometries subject to the extrapolated-zero boundary condition (Equation 2.83). Notation is defined in the lower part of the Table, and for more details about the geometries, refer to Figures 2.8 and 2.12. The sum over β_m for the infinite cylindrical Green's function explicitly means to sum over all positive roots of the mth order Bessel function, $J_m(z)$, and $J'_m(z)$ is the derivative of $J_m(z)$. In practice, the infinite sums are truncated after a desired accuracy has been reached. Further, note that the special case $\omega = 0$ corresponds to the continuous-wave Green's functions (Equation 2.93).

Case	Green's function (time-domain)
Infinite	$g(\mathbf{r},\mathbf{r}_s,t,t_s) = \frac{v}{(4\pi D(t-t_s))^{3/2}} \exp\left[-\frac{\lvert\mathbf{r}-\mathbf{r}_s\rvert^2}{4D(t-t_s)} - \mu_a v(t-t_s)\right]$
Semi-infinite	$g([\rho,z],[\rho_s=0,z_s=\ell_{tr}],t,t_s) = \frac{v\exp[-\mu_a v(t-t_s)]}{(4\pi D(t-t_s))^{3/2}}\left(\exp\left[-\frac{r_1^2}{4D(t-t_s)}\right] - \exp\left[-\frac{r_b^2}{4D(t-t_s)}\right]\right)$
Infinite Slab	$g([\rho,z],[\rho_s=0,z_s=\ell_{tr}],t,t_s) = \frac{v\exp[-\mu_a v(t-t_s)]}{(4\pi D(t-t_s))^{3/2}}\sum_{m=-\infty}^{\infty}\left(\exp\left[-\frac{r_{+,m}^2}{4D(t-t_s)}\right] - \exp\left[-\frac{r_{-,m}^2}{4D(t-t_s)}\right]\right)$
Infinite Cylindrical	$g([\rho,\phi,z],[\rho_s,z_s],t,t_s) = \frac{v\exp\left[-\left(\mu_a v(t-t_s)+\frac{(z-z_s)^2}{4D(t-t_s)}\right)\right]}{2\pi a_b^2\sqrt{\pi D(t-t_s)}}\times \sum_{m=-\infty}^{\infty}\cos m\phi\sum_{\beta_m}\exp[-D\beta_m^2(t-t_s)]\frac{J_m(\beta_m\rho)J_m(\beta_m\rho_s)}{[J_m'(\beta_m a_b)]^2}$
Finite Cylindrical	$g([\rho,\phi,z],[\rho_s,z_s],t,t_s) = \frac{2v\mathrm{e}^{-\mu_a v(t-t_s)}}{\pi a_b^2(h+2z_b)}\sum_{m=1}^{\infty}\exp\left[\frac{-Dm^2\pi^2(t-t_s)}{(h+2z_b)^2}\right]\sin\frac{m\pi z}{h+2z_b}\sin\frac{m\pi z_s}{h+2z_b}\times \sum_{n=-\infty}^{\infty}\cos n\phi\times\sum_{\beta_n}\mathrm{e}^{-D\beta_n^2(t-t_s)}\frac{J_n(\beta_n\rho)J_n(\beta_n\rho_s)}{[J_n'(\beta_n a_b)]^2}$
Spherical ($r_s < r < a$)	$g([r,\phi],r_s,t,t_s) = \frac{-v\exp[-\mu_a v(t-t_s)]}{2\pi a_b^2\sqrt{rr_s}}\sum_{m=0}^{\infty}\sum_{\beta_{m+1/2}}\frac{J_{m+1/2}(\beta_{m+1/2}r)J_{m+1/2}(\beta_{m+1/2}r_s)}{\left[J_{m+3/2}(\beta_{m+1/2}a_b)\right]^2}\times (2m+1)P_m(\cos\phi)\mathrm{e}^{-D\beta m+1/2^2(t-t_s)}$

Table 2.6: Time-domain Green's functions (Equation 2.85) in several homogeneous geometries subject to the extrapolated-zero boundary condition (Equation 2.83). Notation is defined in Table 2.5. As with the frequency-domain Green's functions, in practice, the infinite sums are truncated after a desired accuracy has been reached.

Analytical Green's functions also exist for heterogeneities such as spherical [22] and cylindrical inclusions [252] in homogeneous media as well as for multi-layer media [129, 157, 212].

I have used the Green's function for the two-layer geometry extensively to distinguish between cerebral and superficial tissue layers (Figure 2.13). The two-layer geometry is comprised of a semi-infinite bottom layer (e.g., corresponding to the cortical regions of the brain) with a distinct absorption coefficient and scattering coefficient of $\mu_{a,c}$ and $\mu'_{s,c}$, respectively, and a superficial top layer (e.g., corresponding to extra-cerebral scalp and skull tissue) with thickness ℓ, and distinct tissue properties denoted by $\mu_{a,ec}$, and $\mu'_{s,ec}$. The frequency-domain Green's function for this geometry at the $z = 0$ plane is [157]

$$G([\rho, z = 0], [\rho_s = 0, z_s = z_0]) = \frac{1}{2\pi} \int_0^\infty \tilde{G}(s) s J_0(s\rho) \mathrm{d}s, \tag{2.112}$$

$$\tilde{G}(s) = \frac{v \sinh[k_{ec}(z_b + z_0)]}{D_{ec} k_{ec}} \frac{D_{ec} k_{ec} \cosh[k_{ec}\ell] + D_c k_c \sinh[k_{ec}\ell]}{D_{ec} k_{ec} \cosh[k_{ec}(\ell + z_b)] + D_c k_c \sinh[k_{ec}(\ell + z_b)]} - \frac{v \sinh[k_{ec} z_0]}{D_{ec} k_{ec}},$$

where $D_j = v/[3(\mu'_{s,j} + \mu_{a,j})]$, $k_j^2 = (D_j s^2 + v\mu_{a,j} + i\omega)/D_j$ (with subscript j denoting c (cerebral) or ec (extra-cerebral)), $z_b = 2(D_{ec}/v)(1 + R_{eff})/(1 - R_{eff})$, $z_0 = 3D_{ec}/v$, and R_{eff} is defined by Equation 2.79 (this solution assumes the top and bottom layers have the same optical index of refraction).

Although an analytical solution for the time-domain two-layer Green's function does not exist, it can be determined numerically from substituting Equation 2.112 into Equation 2.91 and evaluating the resulting expression with a fast Fourier transform technique [108, 157].

2.11 Relationship Between the Fluence Rate and the Detected Signal

From the previous sections, I presented the photon diffusion model and its solutions in several geometries for the photon fluence rate. I will now discuss the relationship between the photon fluence rate and the detected light intensity [52, 123]. Two common methods for light detection are depicted in 2.14.

Let's first consider the case of optical fiber based detection at position $\mathbf{r}$ on the boundary. The

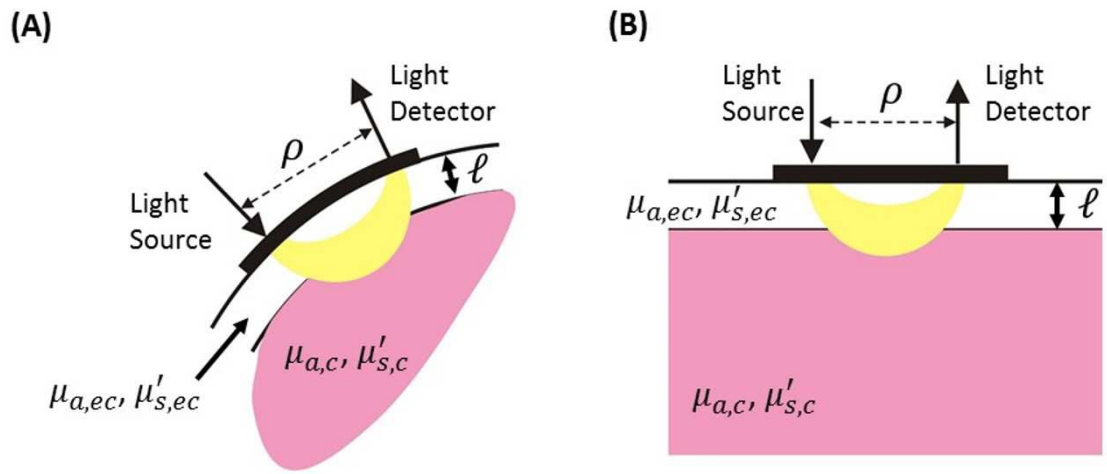

Figure 2.13: **(A)** Two-layer tissue model of the head and **(B)** parallel plane two-layer tissue geometry.

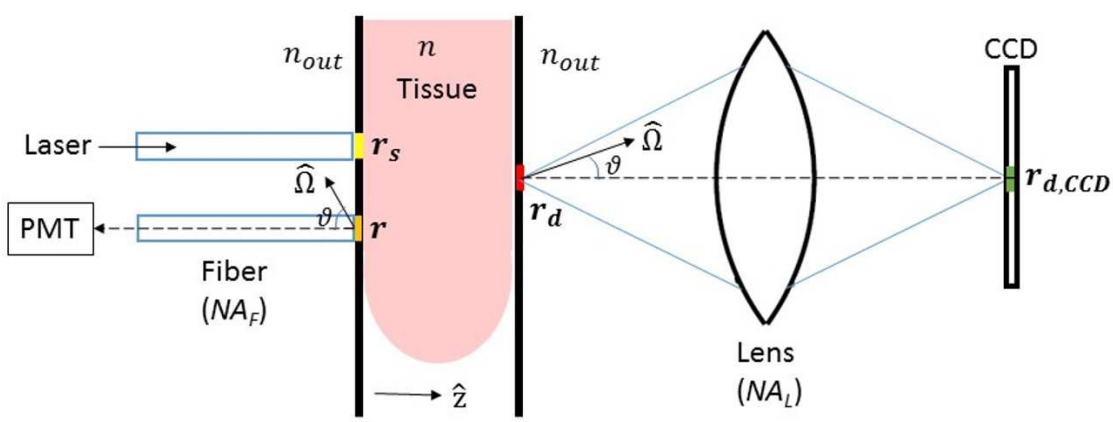

Figure 2.14: Diffusing light can be detected with both contact and non-contact probes. Contact probes typically use an optical fiber (with numerical aperture NA_F) to transport light emerging from a point $\mathbf{r}$ to a light detector (e.g., photomultiplier tube). Non-contact probes typically utilize a lens (with numerical aperture NA_L) to image the light emerging from a point $\mathbf{r}_d$ onto its corresponding point on the detector plane, i.e., $\mathbf{r}_{d,CCD}$. As in Figure 2.8, n is the tissue index of refraction and n_{out} is the refractive index of the non-scattering medium bounding the tissue.

detected light intensity, $I(\mathbf{r},t)$, is the light radiance integrated over the collection solid angle and detection area (σ_{fiber}) of the fiber, i.e.,

$$I(\mathbf{r},t) = \int\limits_{\sigma_{\text{fiber}}} \mathrm{d}^2 r \int\limits_{NA_F} \mathrm{d}\Omega T(\mathbf{r},\hat{\Omega},t) L(\mathbf{r},\hat{\Omega},t). \tag{2.113}$$

Here, $T(\mathbf{r},\hat{\Omega},t)\mathrm{d}\Omega$ is the probability that a photon at position $\mathbf{r}$ and time t traveling in the $\hat{\Omega}$ direction is detected. To relate the detected signal to the fluence rate, the P_1 approximation of the light radiance (Equation 2.27) is employed in Equation 2.113, i.e.,

$$I(\mathbf{r},t) = \int\limits_{\sigma_{\text{fiber}}} \mathrm{d}^2 r \int_0^{\vartheta_c} \mathrm{d}\vartheta \sin\vartheta \int_0^{2\pi} \mathrm{d}\phi T(\mathbf{r},\hat{\Omega},t) \frac{1}{4\pi} \left[\Phi(\mathbf{r},t) + 3\mathbf{J}(\mathbf{r}) \cdot \hat{\Omega}\right], \tag{2.114}$$

where the half-angle of the maximum cone of light that can propagate through the fiber, ϑ_c, is determined from the fiber's numerical aperture via $\vartheta_c = \arcsin(NA_F/n)$. With the additional assumptions that T is spatially homogeneous across the fiber detection area and is symmetric about the central optical axis of the fiber, i.e., $T = T(\vartheta,t)$ (see Figure 2.14), Equation 2.114 simplifies to

$$\begin{aligned} I(\mathbf{r},t) &= \int\limits_{\sigma_{\text{fiber}}} \mathrm{d}^2 r \int_0^{\vartheta_c} \mathrm{d}\vartheta \sin\vartheta T(\vartheta,t) \int_0^{2\pi} \mathrm{d}\phi \frac{1}{4\pi} [\Phi(\mathbf{r},t) + \\ &\quad 3\mathbf{J}(\mathbf{r},t) \cdot (\sin(\vartheta)\cos(\phi)\hat{x} + \sin(\vartheta)\sin(\phi)\hat{y} - \cos(\vartheta)\hat{z}]] \\ &= \int\limits_{\sigma_{\text{fiber}}} \mathrm{d}^2 r \int_0^{\vartheta_c} \mathrm{d}\vartheta T(\vartheta,t) \frac{1}{2} [\Phi(\mathbf{r},t) - 3J_z(\mathbf{r},t)\cos(\vartheta)] \sin(\vartheta). \end{aligned} \tag{2.115}$$

Since the fluence rate is proportional to the flux at the boundary, i.e., the partial-flux boundary condition (Equation 2.78), Equation 2.115 is equivalent to

$$I(\mathbf{r},t) = \left[\int_0^{\vartheta_c} T(\vartheta,t) \frac{1}{2} \left(1 + \frac{3}{2}\frac{1-R_{eff}}{1+R_{eff}}\right) \mathrm{d}\vartheta\right] \int\limits_{\sigma_{\text{fiber}}} \Phi(\mathbf{r},t) \mathrm{d}^2 r. \tag{2.116}$$

If the fluence rate is approximately constant over the area σ_{fiber}, then the detected signal is directly proportional to $\Phi(\mathbf{r},t)$, i.e.,

$$I(\mathbf{r},t) = \left[\sigma_{\text{fiber}} \int_0^{\vartheta_c} T(\vartheta,t) \frac{1}{2} \left(1 + \frac{3}{2}\frac{1-R_{eff}}{1+R_{eff}}\right] \mathrm{d}\vartheta\right] \Phi(\mathbf{r},t) = C(t)\Phi(\mathbf{r},t). \tag{2.117}$$

Here, the multiplicative factor in brackets is the so-called light coupling coefficient, C, which is the proportionality constant between the detected signal intensity and the photon fluence rate.

It depends on many factors, such as the Fresnel transmission coefficient from the tissue to the fiber, the light sensitivity of the detector, "fiber-detector coupling", and physical properties of the tissue surface (e.g., hair follicles, melanin content in the skin, thin layers of dust and/or water droplets, etc.). If any of these aspects of the measurement changes with time, then C will also change with time. It is very difficult to predict C theoretically, so in practical measurements, C is regarded as an unknown.

Equation 2.117 applies to the non-contact detection arrangement in Figure 2.14 as well, i.e., $I(\mathbf{r}_{d,CCD}, t) = C_L \Phi(\mathbf{r}_d, t)$. Non-contact detection has a different light coupling coefficient wherein the critical angle ϑ_c in Equation 2.117 is given by the numerical aperture of the lens, i.e., $\vartheta_c = \arcsin(NA_L/n_{out})$, and the fiber detection area σ_{fiber} is replaced by σ_{L}, which is the area of the "resolution cell" just resolved by the lens imaging the surface. Further, the probability density function for light detection, i.e., $T(\vartheta)$, for the lens/CCD scheme is different from the fiber/PMT scheme. Note that the lens detection scheme works best if the detection point of interest, $\mathbf{r}_d$, is not too far from the central optical axis of the lens. At points far from the axis, larger aberrations could induce significant contamination at $\mathbf{r}_{d,CCD}$ from light emerging at neighboring positions to $\mathbf{r}_d$ on the tissue surface. Effectively, aberrations increase the resolution cell area and affect ϑ_c, thus altering the light coupling coefficient C_L. Finally, beam vignetting decreases the light coupling coefficient, C_L, at detection points on the tissue surface far from the lens axis [52].

2.11.1 Strategies for Estimating Light Coupling Coefficients

For a frequency-domain measurement with a single source-detector optical fiber pair (e.g., Figure 2.8), there are two equations, i.e., one for the measured amplitude (Equation 2.110) and one for the measured phase (Equation 2.111), but four unknowns. In addition to tissue absorption and scattering, there are also two light coupling coefficient unknowns for amplitude and phase, i.e., C_a and C_p, where $C = C_a \exp(-iC_p)$ (see Equation 2.117). Thus, for accurate estimates of μ_a and μ_s', frequency-domain measurements at multiple source-detector separations is preferred. If the source fiber is physically translated across the medium using a translation stage [121], then to a decent approximation, C_a and C_p will be the same at every separation. In this case, Equations 2.110 and 2.111 can be directly applied to linearly fit the measured amplitude and phase

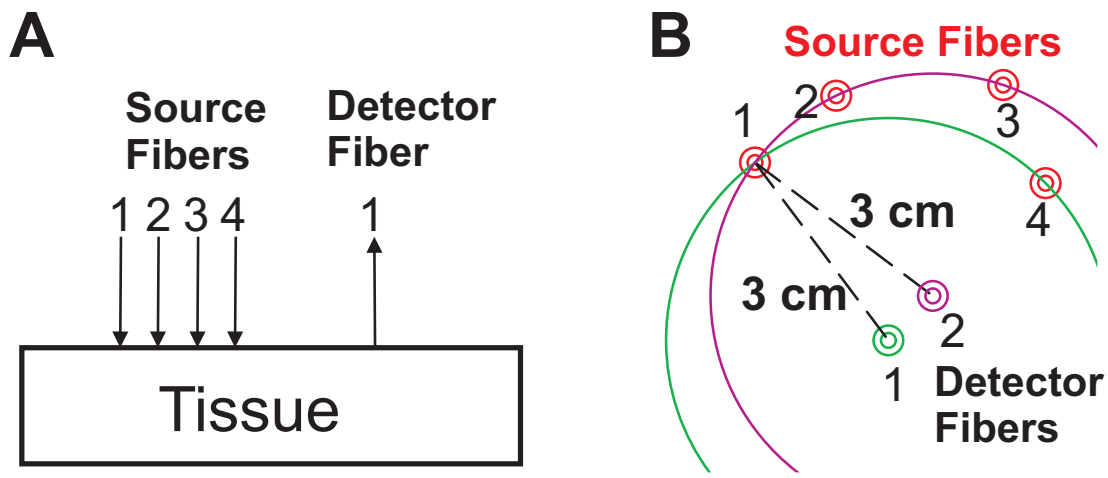

Figure 2.15: **(**A) Multiple source-detector separations are highly preferred for accurate measurements of tissue absorption and scattering with intensity modulated light sources. **(**B) Top view of an exemplar self-calibrating probe. Both the self-calibrating probe and the linear probe in panel (A) have four source-detector separations. A self-calibrating probe requires at least two sources and two detectors (see text).

data for $-k_r$ and k_i, which are then used to calculate μ_a and μ_s' via Equations 2.66 and 2.67.

However, physically translating a single fiber places a severe limit on time resolution, and the measurement is also prone to motion artifacts and light leakage since the moving fiber is not fixed to the tissue. Another, more practical approach utilizes multiple fibers secured to the tissue of interest (Figure 2.15A). The drawback here, though, is that since each fiber has its own light coupling coefficient, there will be two additional unknowns for each additional fiber used. Two methods are commonly employed to address this problem. One approach uses calibration phantoms with known optical properties to determine the coupling coefficients before and after each experiment [36, 133, 253]. A second approach employs self-calibrating probes [268]. The first method assumes the coupling coefficients will be the same for tissue and phantom; the second method assumes axially symmetric tissue. The subsequent discussions of these approaches are for optical fibers, but the results are also applicable for non-contact detection.

2.11.1.1 Phantom Calibration

The phantom calibration technique estimates the fiber light coupling coefficients from measurements on a homogeneous semi-infinite phantom with known optical properties (μ_a^P, $\mu_s'^P$). For

an arbitrary source-detector pair (i.e., source fiber i, coupling coefficient $C_{s,i}$; detector fiber j, coupling coefficient $C_{d,j}$) with source-detector separation ρ_{ij}, the measured signal intensity is given by (Equation 2.117)

$$I_{ij}^P = |I_{ij}^P| \exp[-ip_{ij}^P] = C_{s,ai}C_{d,aj} \exp\left[-i(C_{s,pi} + C_{d,pj})\right] A^P(\rho_{ij}) \exp[-i\theta^P(\rho_{ij}]. \quad (2.118)$$

Here, $A^P(\rho_{ij})$ and the $\theta^P(\rho_{ij}$ are the calculated amplitude and phase obtained from substituting the known phantom optical properties into the frequency-domain semi-infinite diffusion Green's function (e.g., Equation 2.103); p_{ij}^P is the measured phase difference between the intensities detected by fiber j and delivered by fiber i on the phantom, and the measured amplitude is $|I_{ij}^P| \equiv \sqrt{I_{ij}^{P*} I_{ij}^P}$. Equation 2.118 is a system of two equations, i.e.,

$$C_{s,ai}C_{d,aj} = |I_{ij}^P|/A^P(\rho_{ij}), \quad (2.119)$$

$$C_{s,pi} + C_{d,pj} = p_{ij}^P - \theta^P(\rho_{ij}). \quad (2.120)$$

After the phantom calibration, the probe is attached to the tissue of interest, and the measured amplitude and phase on the tissue are

$$|I_{ij}| = C_{s,ai}C_{d,aj}A(\rho_{ij}), \quad (2.121)$$

$$p_{ij} = C_{s,pi} + C_{d,pj} + \theta(\rho_{ij}), \quad (2.122)$$

where $A(\rho_{ij})$ and $\theta(\rho_{ij})$ are the amplitude and phase predicted by the photon diffusion model (Equation 2.52). To correct the measured amplitude and phase for the light coupling coefficients, substitute Equations 2.119 and 2.120 into Equations 2.121 and 2.122, i.e.,

$$A(\rho_{ij}) = \frac{A^P(\rho_{ij})}{|I_{ij}^P|}|I_{ij}|, \quad (2.123)$$

$$\theta(\rho_{ij}) = p_{ij} - \left(p_{ij}^P - \theta^P(\rho_{ij})\right). \quad (2.124)$$

The tissue optical properties can then be extracted from fitting these corrected amplitude and phase measurements at all source-detector separations to the photon diffusion model.

A big advantage of the phantom calibration technique is its flexibility. It can be utilized for any arrangement of source and detector fibers. With phantom calibration, it is even possible to estimate absolute absorption and scattering with only a single source-detector separation.

Equations 2.123 and 2.124 form a system of two equations, wherein the two unknowns are μ_a and μ_s'. However, the single separation frequency-domain measurement is not recommended because it is highly prone to cross talk induced by measurement noise.

The phantom calibration technique also has drawbacks. Its underlying assumption is that the fiber coupling coefficients calculated on the phantom remain the same when the probe is moved to tissue. This assumption is not always valid. Hair follicles strongly effect the coupling coefficients, and can easily have a heterogeneous effect across different fibers. If this is the case, the phantom calibration technique will not work. Another extreme case is if there is any liquid underneath the fibers. The light coupling coefficients on a solid phantom are different than they are on a liquid (e.g., intralipid), which is why the phantom calibration approach usually fails when using a probe calibrated on a solid phantom to measure optical properties of a liquid. Finally, the phantom calibration technique assumes temporally constant light coupling coefficients. In principle, the coupling coefficients will change with time if any of the factors they depend on changes with time (see Equation 2.117). Although it is feasible to reset the calibration with additional phantom measurements, it is not possible to monitor the coupling coefficients continuously.

2.11.1.2 Self Calibrating Probes

Self-calibrating probes rely on tissue symmetry to estimate the light coupling coefficients without phantom calibration. Specifically, the underlying assumption is that the tissue is appropriately symmetric such that the fluence rate predicted by the photon diffusion model (i.e., $A\exp(-i\theta)$) is the same for equidistant source-detector pairs. Semi-infinite/slab (Figure 2.8), spherical (Figure 2.12, and two-layer geometries (Figure 2.13) have this symmetry on the tissue-air boundaries. This assumption also applies in the cylindrical geometry (Figure 2.12) if the equidistant source-detector pairs on the boundary also have the same z-component separations. More generally, the self-calibrating technique is appropriate for N-layered planar, spherical, and cylindrical geometries (N is an integer). They are best understood by example (Figure 2.15B).

Light coupling coefficients are estimated from ratios of the signals from equidistant source-detector pairs. Using the same notation defined in Equation 2.118 for the probe in Figure 2.15B,

these ratios are

$$
\begin{aligned}
r_1 &\equiv \frac{I_{11}}{I_{12}} = \frac{C_{s,a1}C_{d,a1}}{C_{s,a1}C_{d,a2}} \frac{\exp[-i(C_{s,p1}+C_{d,p1}]}{\exp[-i(C_{s,p1}+C_{d,p2}]} \frac{A(\rho)\mathrm{e}^{-i\theta(\rho)}}{A(\rho)\mathrm{e}^{-i\theta(\rho)}}, \\
r_2 &\equiv \frac{I_{11}}{I_{41}} = \frac{C_{s,a1}C_{d,a1}}{C_{s,a4}C_{d,a1}} \frac{\exp[-i(C_{s,p1}+C_{d,p1}]}{\exp[-i(C_{s,p4}+C_{d,p1}]} \frac{A(\rho)\mathrm{e}^{-i\theta(\rho)}}{A(\rho)\mathrm{e}^{-i\theta(\rho)}}, \\
r_3 &\equiv \frac{I_{12}}{I_{22}} = \frac{C_{s,a1}C_{d,a2}}{C_{s,a2}C_{d,a2}} \frac{\exp[-i(C_{s,p1}+C_{d,p2}]}{\exp[-i(C_{s,p2}+C_{d,p2}]} \frac{A(\rho)\mathrm{e}^{-i\theta(\rho)}}{A(\rho)\mathrm{e}^{-i\theta(\rho)}}, \\
r_4 &\equiv \frac{I_{12}}{I_{32}} = \frac{C_{s,a1}C_{d,a2}}{C_{s,a3}C_{d,a2}} \frac{\exp[-i(C_{s,p1}+C_{d,p2}]}{\exp[-i(C_{s,p3}+C_{d,p2}]} \frac{A(\rho)\mathrm{e}^{-i\theta(\rho)}}{A(\rho)\mathrm{e}^{-i\theta(\rho)}},
\end{aligned} \tag{2.125}
$$

where $\rho = 3cm$. Separating these ratios into their amplitude and phase components (e.g., $r_1 = r_{1,a}\exp(-ir_{1,p})$), we obtain

$$
\begin{aligned}
r_{1,a} &= C_{d,a1}/C_{d,a2}, & r_{1,p} &= C_{d,p1} - C_{d,p2}, \\
r_{2,a} &= C_{s,a1}/C_{s,a4}, & r_{2,p} &= C_{s,p1} - C_{s,p4}, \\
r_{3,a} &= C_{s,a1}/C_{s,a2}, & r_{3,p} &= C_{s,p1} - C_{s,p2}, \\
r_{4,a} &= C_{s,a1}/C_{s,a3}, & r_{4,p} &= C_{s,p1} - C_{s,p3}.
\end{aligned} \tag{2.126}
$$

The self-calibrating probe in Figure 2.15B has four distinct separations. The measured signals at these separations are

$$
\begin{aligned}
|I_{42}| &= C_{s,a4}C_{d,a2}A(\rho_{42}), & p_{42} &= C_{s,p4} + C_{d,p2} + \theta(\rho_{42}), \\
|I_{11}| &= C_{s,a1}C_{d,a1}A(\rho_{11}), & p_{11} &= C_{s,p1} + C_{d,p1} + \theta(\rho_{11}), \\
|I_{21}| &= C_{s,a2}C_{d,a1}A(\rho_{21}), & p_{21} &= C_{s,p2} + C_{d,p1} + \theta(\rho_{21}), \\
|I_{31}| &= C_{s,a3}C_{d,a1}A(\rho_{31}), & p_{31} &= C_{s,p3} + C_{d,p1} + \theta(\rho_{31}).
\end{aligned} \tag{2.127}
$$

The signal measurements given by Equation 2.127 are corrected for light coupling using Equation 2.126, i.e.,

$$
\begin{aligned}
A(\rho_{42}) &= \frac{r_{2,a}r_{1,a}}{C_{s,a1}C_{d,a1}}|I_{42}|, & \theta(\rho_{42}) &= p_{42} - (C_{s,p1} + C_{d,p1}) + r_{2,p} + r_{1,p}, \\
A(\rho_{11}) &= \frac{1}{C_{s,a1}C_{d,a1}}|I_{11}|, & \theta(\rho_{11}) &= p_{11} - (C_{s,p1} + C_{d,p1}), \\
A(\rho_{21}) &= \frac{r_{3,a}}{C_{s,a1}C_{d,a1}}|I_{21}|, & \theta(\rho_{21}) &= p_{21} - (C_{s,p1} + C_{d,p1}) + r_{3,p}, \\
A(\rho_{31}) &= \frac{r_{4,a}}{C_{s,a1}C_{d,a1}}|I_{31}|, & \theta(\rho_{31}) &= p_{31} - (C_{s,p1} + C_{d,p1}) + r_{4,p}.
\end{aligned} \tag{2.128}
$$

Notice that there are only two unknowns from light coupling in the system of equations given by Equation 2.127, which are $C_{s,a1}C_{d,a1}$ and $C_{s,p1} + C_{d,p1}$. Thus, Equation 2.128 is readily solved for the tissue optical properties.

In addition to the self-calibration technique not requiring phantom calibration, its other big advantage is that it can be applied for every measurement time point. Thus, unlike the phantom calibration technique, the self-calibration technique accurately handles time-varying light coupling coefficients. However, self-calibrating probes are larger in size than corresponding probes using phantom calibration (compare Figure 2.15A with Figure 2.15B). Self-calibrating probes also require very accurate source-detector separations to ensure equidistant source-detector pairs. A difference in separation of ~ 1 mm between two pairs that are supposed to be equidistant is enough to induce significant errors. For this reason, self-calibrating probes work best for rigid probes.

2.11.2 Validity of P_1 Approximation at Tissue Boundary

The key step in relating the detected signal to the photon fluence rate is using the P_1 approximation for the light radiance (i.e., Equation 2.114). The P_1 approximation is accurate for nearly isotropic light wherein $\Phi \gg |\mathbf{J}|$ (Equation 2.28). On examination of Table 2.4, though, the fluence rate is not a lot greater than the photon flux at the boundary, especially for the index-matched case wherein $n = n_{out}$. This consequentially raises questions about the accuracy of the P_1 approximation at the boundary. Specifically, does the boundary perturb incident diffusive light enough to induce light anisotropy beyond the P_1 approximation?

To answer this, I used the MCML Monte Carlo software package [255] to solve the linear transport equation (Equation 2.9) directly at a semi-infinite index-matched tissue boundary. This Monte Carlo solution is compared to the continuous-wave semi-infinite photon diffusion fluence rate solution (i.e., Equation 2.103 with $\omega = 0$) in Figure 2.16A. Recall that the photon diffusion equation is the P_1 approximation to the linear transport equation. Therefore, since there is excellent agreement between the Monte Carlo and photon diffusion solutions, the P_1 approximation is accurate at the boundary. Intuitively, this result makes sense because the detected signal is sensitive only to light propagating in directions within the fiber's numerical aperture. The light radiance in these "incident directions" is much less affected by the boundary than the

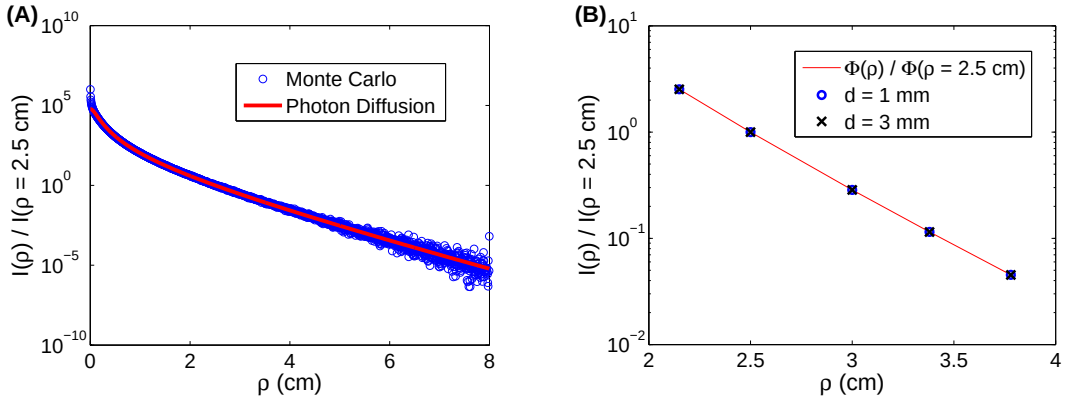

Figure 2.16: **(A)** Comparison of Monte Carlo and continuous-wave photon diffusion solutions as a function of source-detector separation, ρ, for the detected light signal at the boundary of an index-matched semi-infinite medium ($\mu_a = 0.1$, $\mu_s' = 10$ cm^{-1}, $n = n_{out} = 1.4$; see Figure 2.8). The Monte Carlo simulation utilized 10 million photons to numerically solve the linear transport equation (Equation 2.9), while the photon diffusion model is the P_1 approximation of the linear transport equation. In the photon diffusion model, $I(\rho)/I(\rho = 2.5\text{ cm}) = \Phi(\rho)/\Phi(\rho = 2.5\text{ cm})$ (Equation 2.117), where the fluence rate $\Phi(\rho)$ is given by the continuous-wave semi-infinite Green's function (i.e., Equation 2.103 with $\omega = 0$). **(B)** Simulated "normalized" detected signals, $I(\rho)/I(\rho = 2.5\text{ cm})$, for detection fiber core diameters of $d = 1$ mm and $d = 3$ mm, plotted against ρ. The simulated detected signals were computed by spatially integrating $\Phi(\rho)$ (i.e., continuous-wave semi-infinite Green's function) over the detection fiber areas (see Equation 2.116). The normalization by $I(\rho = 2.5\text{ cm})$ was done to divide out the light coupling coefficient in Equation 2.116.

light radiance traveling in opposite directions back into the tissue. Therefore, even though the light radiance at the boundary is not nearly isotropic over all directions, it is nearly isotropic over the incident directions that are detected, provided that the incident light is diffusive. Thus, the photon diffusion model is valid at the boundary for the detected signal if the incident light on the boundary is diffusive. At short separations, the incident light is not diffusive, and there is deviation between the Monte Carlo and photon diffusion models (Figure 2.16A).

2.11.3 Signal Detection with "Large-diameter" Optical Fibers

In the derivation of Equation 2.117, I assumed that the fluence rate is approximately constant over the detection area of the fiber. In practical measurements, though, large-diameter optical fibers with diameters of 1 mm or 3 mm are often used. These fibers are big enough for the fluence rate to change significantly over their area. However, the spatial integral of the fluence rate across the

fiber detection area for these two diameters is still proportional to $\Phi(\rho)$ (Figure 2.16B). Thus, Equation 2.117 is still valid for large-diameter optical fiber detection. The spatial integration over the fiber area is another factor perturbing the light coupling coefficient ($C(t)$) from its theoretical value, which is corrected for by the calibration schemes discussed above.

2.12 Penetration Depth of Diffusing Light

As illustrated in Figure 2.6, for a basic DOS measurement comprised of a point source and a point detector, the detected light interacts with a "banana shaped" volume of tissue. In this section, I quantitatively characterize this "banana shaped" volume of tissue sampled by a single source-detector pair in homogeneous media. The key to understanding the sampled tissue volume is knowledge of the probability that a detected photon visits (i.e., passes through) a point $\mathbf{r}$ inside the tissue [200]. I will first focus on the simpler case of continuous-wave light.

Let's consider a point source at position $\mathbf{r}_s$ with source power S_0, i.e., $S(\mathbf{r}) = S_0\delta(\mathbf{r} - \mathbf{r}_s)$. The fluence rate at point $\mathbf{r}$ inside the tissue is given by (Equation 2.93)

$$\Phi_{cw}(\mathbf{r}) = S_0 G_{cw}(\mathbf{r}, \mathbf{r}_s), \tag{2.129}$$

where $G_{cw}(\mathbf{r}, \mathbf{r}_s)$ is the continuous-wave Green's function for the geometry of interest. Since diffusive light is nearly isotropic, $\Phi_{cw}(\mathbf{r})$ can be regarded as another point source with a light power of $S_0 G_{cw}(\mathbf{r}, \mathbf{r}_s)$ [146]. The photon fluence rate at the detector position, $\mathbf{r}_d$, from this "point source" at $\mathbf{r}$ is then given by $S_0 G_{cw}(\mathbf{r}, \mathbf{r}_s) G_{cw}(\mathbf{r}_d, \mathbf{r})$, which is the contribution to the total fluence rate at the detector from photons that have visited the tissue point $\mathbf{r}$.

Consequentially, the probability that a detected photon at position $\mathbf{r}_d$ has visited the infinitesimal tissue volume $\mathrm{d}^3 r$ centered at $\mathbf{r}$ is

$$P(\mathbf{r}_d, \mathbf{r}, \mathbf{r}_s)\mathrm{d}^3 r = \frac{G_{cw}(\mathbf{r}, \mathbf{r}_s) G_{cw}(\mathbf{r}_d, \mathbf{r})\mathrm{d}^3 r}{\int\limits_V G_{cw}(\mathbf{r}, \mathbf{r}_s) G_{cw}(\mathbf{r}_d, \mathbf{r})\mathrm{d}^3 r}, \tag{2.130}$$

where the spatial integration is over the entire tissue volume, V. Note that because $P(\mathbf{r}_d, \mathbf{r}, \mathbf{r}_s)$ is a "photon visitation" probability density function, the probability that a detected photon has visited a volume of tissue $\tilde{V}$ within the total volume of tissue is

$$Prob(\mathbf{r}_s \rightarrow \tilde{V} \rightarrow \mathbf{r}_d) = \int\limits_{\tilde{V}} P(\mathbf{r}_d, \mathbf{r}, \mathbf{r}_s)\mathrm{d}^3 r. \tag{2.131}$$

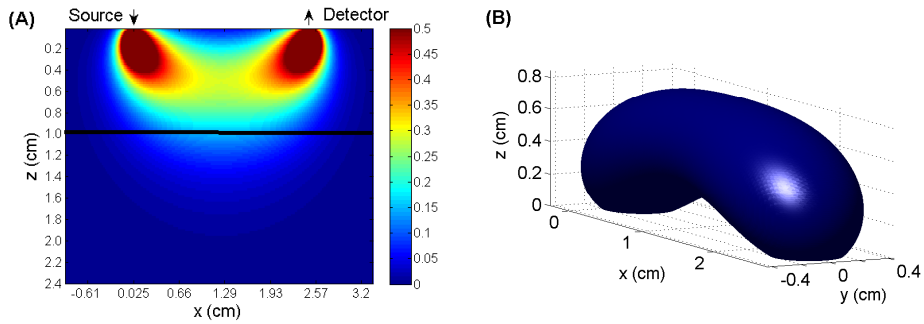

Figure 2.17: **(A)** Cross-section of the photon visitation probability density function (Equation 2.130) for a semi-infinite medium ($\mu_a = 0.1$, $\mu_s' = 10$ cm^{-1}, $n = 1.4$, $n_{out} = 1.0$) probed with a source-detector separation of $\rho = 2.5$ cm. Only 15% of the detected light has visited tissue depths greater than $z = 1$ cm (black horizontal line). **(B)** Photon probability density function isosurface at the $P = 0.2$ level for the same semi-infinite geometry.

In the semi-infinite geometry, $P(\mathbf{r}_d, \mathbf{r}, \mathbf{r}_s)$ has a "banana shaped profile" (Figure 2.17) [15] that is weighted towards superficial tissue depths. The mean depth of photon visitation (or penetration depth), $\langle z \rangle$, given by

$$\langle z \rangle = \int_V z P(\mathbf{r}_d, \mathbf{r}, \mathbf{r}_s) \mathrm{d}^3 r, \tag{2.132}$$

is substantially less than the source-detector separation (Figure 2.18A). However, the width of the banana shaped profile (e.g., $\sigma_z = (\langle z^2 \rangle - \langle z \rangle^2)^{1/2}$) encompasses greater tissue depths. Since a typical scalp/skull thickness in adult humans is ~ 1 cm, the fraction of detected photons that have visited tissue deeper than a depth of $z = 1$ cm, i.e.,

$$Prob(z > 1 \text{ cm}) = \int_{-\infty}^{\infty} \mathrm{d}x' \int_{-\infty}^{\infty} \mathrm{d}y' \int_{z}^{\infty} \mathrm{d}z' P(\mathbf{r}_d, \mathbf{r}, \mathbf{r}_s), \tag{2.133}$$

is informative. Although this fraction is significant, the majority of the detected light has only visited tissue at depths shallower than 1 cm (Figure 2.18B). For example, at $\rho = 2.5$ cm, only 15% of the detected light samples tissue below depths of 1 cm. The influence of optical properties on the fraction of detected light sampling depths greater than 1 cm is investigated in Figure 2.18C. Both μ_a and μ_s' influence this fraction, though the absorption influence is stronger. Since the detected light is heavily weighted towards superficial tissue, cerebral monitoring in

[15] To compute the photon visit probability density function numerically in the semi-infinite geometry, it is helpful to use the relation $G(\mathbf{r}, \mathbf{r}_d) = G(\mathbf{r}_d, \mathbf{r})$. Explicitly, evaluate the semi-infinite Green's functions in Cartesian coordinates, e.g., $G(\mathbf{r}_d, \mathbf{r}) = G([\rho, 0, 0], [x, y, z])$

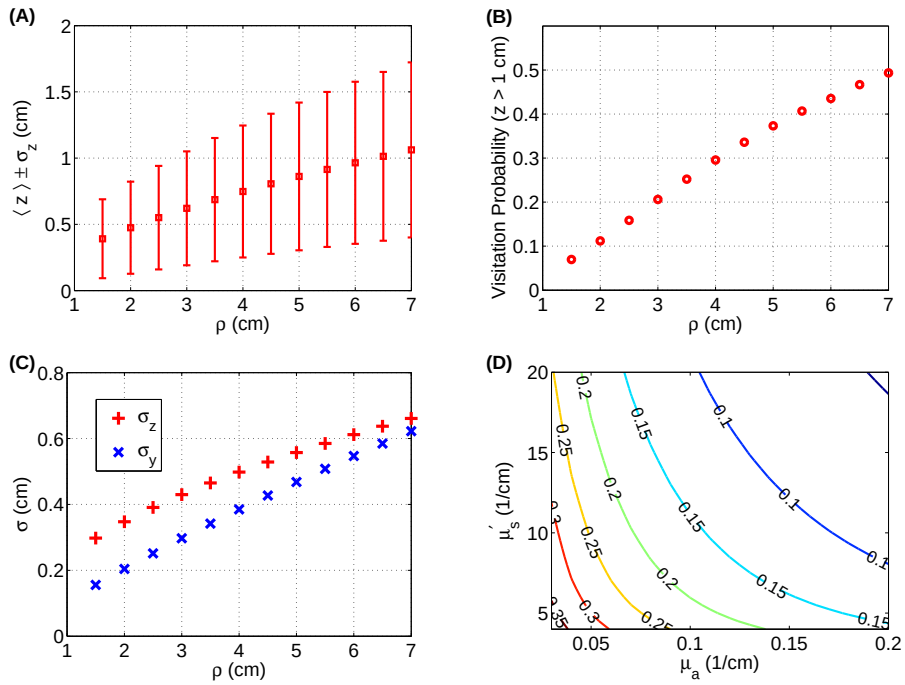

Figure 2.18: For a typical semi-infinite medium ($\mu_a = 0.1$, $\mu_s' = 10\,\text{cm}^{-1}$, $n = 1.4$, $n_{out} = 1.0$), the mean depth of detected photon visitation (**(A)**), the fraction of detected photons visiting tissue depths greater than 1 cm (**(B)**), and the standard deviations of detected photon visitation for the two orthogonal directions to the "source-detector line" (**(C)**), are plotted against the source-detector separation, ρ. **(**D) Contour plot of the fraction of detected photons visiting tissue depths greater than 1 cm as a function of tissue scattering (vertical axis) and tissue absorption (horizontal axis).

adults is prone to superficial tissue contamination. I discuss strategies for filtering this superficial tissue contamination in Chapter 6.

Finally, notice that the banana shaped profile has a narrower width than depth, i.e., $\sigma_y < \sigma_z$ (Figure 2.18D).

2.12.1 Photon Visitation Probability Density Function for Frequency-Domain Light

The frequency-domain analogue of Equation 2.130 for intensity modulated light is

$$P(\mathbf{r}_d, \mathbf{r}, \mathbf{r}_s)\mathrm{d}^3 r = \frac{|G(\mathbf{r}, \mathbf{r}_s)G(\mathbf{r}_d, \mathbf{r})|\,\mathrm{d}^3 r}{\left|\int_V G_{cw}(\mathbf{r}, \mathbf{r}_s)G_{cw}(\mathbf{r}_d, \mathbf{r})\mathrm{d}^3 r\right|}, \tag{2.134}$$

where $G(\mathbf{r}, \mathbf{r}_s)$ is the frequency-domain Green's function for the geometry of interest (Equation 2.87). Equation 2.134 can in turn be used to compute the frequency-domain analogues

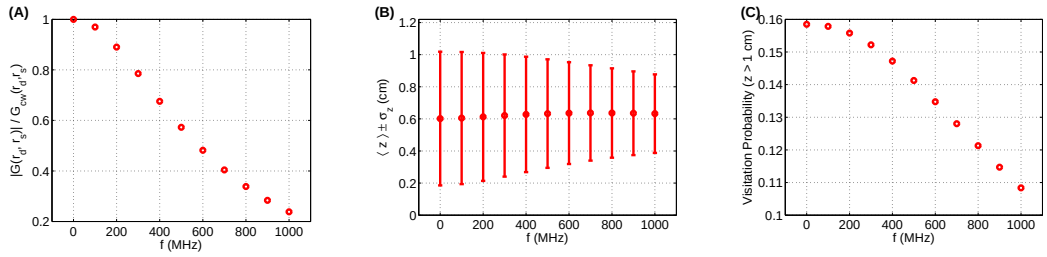

Figure 2.19: For a typical semi-infinite medium ($\mu_a = 0.1$, $\mu_s' = 10$ cm^{-1}, $n = 1.4$, $n_{out} = 1.0$) probed with a source-detector separation of $\rho = 2.5$ cm, the signal modulation depth (i.e., the ratio of the detected signal amplitude divided by the CW amplitude) (**(A)**), the mean depth of detected photon visitation (**(B)**), and the fraction of detected photons visiting tissue depths greater than 1 cm (**(C)**), are plotted against intensity modulation frequency, $f = \omega/(2\pi)$.

of Equations 2.132 and 2.133. Interestingly, although the signal amplitude (i.e., $|G(\mathbf{r}_d, \mathbf{r}_s)|$) is strongly attenuated with increasing modulation frequency (Figure 2.19A), the mean photon penetration depth remains the same (Figure 2.19B). However, the standard deviation of the photon visitation depth in the frequency-domain decreases with increasing frequency (Figure 2.19B), and thus the fraction of detected photons visiting tissue depths greater than 1 cm also decreases with increasing frequency (Figure 2.19C).

2.12.2 Photon Visitation Probability Density Function for Time-resolved Light

I will now briefly present the photon visitation probability density function from an infinitesimally narrow light pulse emitted at position $\mathbf{r}_s = 0$ and time $t = 0$, i.e., $S(\mathbf{r}, t) = S_0\delta(\mathbf{r})\delta(t)$. From applying the argument presented in the previous section to time-resolved data, the probability that a detected photon at position $\mathbf{r}_d$ and time t has visited the infinitesimal tissue volume d^3r centered at $\mathbf{r}$ is

$$P_{tr}(\mathbf{r}_d, \mathbf{r}, \mathbf{r}_s, t)\mathrm{d}^3r = \frac{\left(\int_{|\mathbf{r}|/v}^{t-|\mathbf{r}_d-\mathbf{r}|/v} g(\mathbf{r}, 0, t', 0)g(\mathbf{r}_d, \mathbf{r}, t, t')\mathrm{d}t'\mathrm{d}^3r\right)}{\int V\mathrm{d}^3r \int_{|\mathbf{r}|/v}^{t-|\mathbf{r}_d-\mathbf{r}|/v} g(\mathbf{r}, 0, t', 0)g(\mathbf{r}_d, \mathbf{r}, t, t')\mathrm{d}t'}. \tag{2.135}$$

The temporal integration limits in Equation 2.135 correspond to the shortest and longest possible times for a detected photon at time t to reach the position $\mathbf{r}$ in the tissue. The shortest time is the time it takes a photon to travel in a straight line from source to $\mathbf{r}$, i.e., $\mathbf{r}/v$. The longest time is the detection time t subtracted by the time it takes a photon to travel in a straight line from $\mathbf{r}$ to the detector, i.e., $t - |\mathbf{r}_d - \mathbf{r}|/v$. One intuitive result arising from Equation 2.135 is that P_{tr} at

longer detection times, t, is more sensitive to deeper tissue depths [200].

2.13 Spectroscopy for Determination of Tissue Chromophore Concentrations

The tissue absorption depends linearly on the concentrations of tissue chromophores. In particular, the wavelength-dependent absorption coefficient is given by

$$\mu_a(\lambda) = \log(10) \sum_i \varepsilon_i(\lambda)\ c_i. \tag{2.136}$$

Here $\varepsilon_i(\lambda)$ [$M^{-1}cm^{-1}$] is the wavelength-dependent extinction coefficient (usually known for typical tissue chromophores, see Figure 2.20), c_i [M] represents the concentration of the ith chromophore, and $\log(10)$ is the natural logarithm of ten.[16] We have seen above that the diffusion approximation enables us to separate the scattering and absorption contributions in the detected light signals. Thus, by measuring μ_a at multiple optical wavelengths, we generate a system of coupled equations (Equation 2.136) that can be solved to yield the unknown chromophore concentrations. Generally, to estimate the concentrations of N chromophores, one must determine μ_a at N or more wavelengths.

DOS is most typically employed to measure oxygenated and de-oxygenated hemoglobin; thus a bare minimum of phase and amplitude measurements at two wavelengths are required. Use of more wavelengths permits inclusion of other tissue chromophores such as water and lipid, and also improves the accuracy of the hemoglobin measurements because measurement redundancy reduces systematic errors. Of course, more wavelengths increase the cost and complexity of the instrument and require longer data acquisition times.

For tissue spectroscopy, if the water concentration is not measured, then it should be assumed (e.g., a 75% water volume fraction corresponds to a water concentration of 0.75×55 M) and incorporated in Equation 2.136. In some tissues such as breast, fat contributes significantly to the absorption coefficient, especially at longer wavelengths in the near-infrared around 900

[16] The absorption coefficient is defined such that the transmittance through a non-scattering homogeneous medium is $T \equiv I/I_s = \exp[-\mu_a \rho]$, where ρ is the distance between source and detector. Thus, $-\log(T) = \mu_a \rho$. Tabulated extinction coefficients, though, are determined from the base 10 logarithm of the transmittance [207], i.e., $-\log_{10}(T) = \mu_a \rho / \log(10)$. This explains the presence of the factor $\log(10)$ in Equation 2.136.

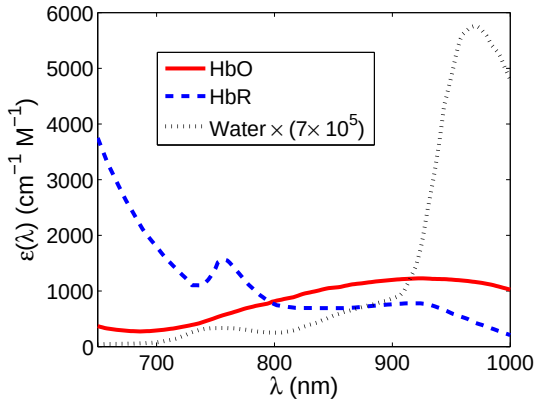

Figure 2.20: Extinction coefficient spectra in the near-infrared spectral window for oxy-hemoglobin (HbO), deoxy-hemoglobin (HbR), and water, plotted as a function of wavelength, λ [207]. The values plotted for water are the actual extinction coefficients multiplied by 700 thousand. I chose this scaling factor because the concentration of water in tissue is typically 700 thousand times higher than the oxy-hemoglobin concentration.

nm [52,144]. As with water, lipid content should be assumed in applications where its absorption coefficient contribution is significant [52]. Equation 2.136 is equivalent to [144]

$$\mu_a(\lambda) = \sum_i f_{v,i}\mu_{a,i}^{\text{pure}}(\lambda), \tag{2.137}$$

where $f_{v,i}$ is the tissue volume fraction of the ith chromophore, and $\mu_{a,i}^{\text{pure}}$ is the absorption coefficient of that pure chromophore. For some chromophores, $\mu_{a,i}^{\text{pure}}$ is tabulated as a function of wavelength rather than the extinction coefficient [207].

Finally, melanin content in the skin affects the detected signal (e.g., a higher melanin content corresponds to a lower signal). Assuming that melanin is only in the skin, its effect is similar to hair follicles in that it influences the light coupling coefficient for the detected signal (2.117). As with hair, the phantom calibration technique for estimating light coupling coefficients (Section 2.11.1.1) does not take into account melanin content. However, it is typically reasonable to assume uniform melanin content in the skin across the area of the optical probe. For this case, the component in the coupling coefficient from melanin is the same for every source-detector separation, and melanin will not affect the slopes in amplitude and phase given by Equations 2.110 and 2.111.

DOS provides quick estimates of bulk chromophore concentrations in large tissue volumes.

These estimates are often accurate enough to be useful in many monitoring applications. Imaging schemes employ Equation 2.136 on a volume-element-by-volume-element basis to assign chromophore concentrations to particular voxels in the tissue sample. The oxy- and deoxy-hemoglobin concentrations measured by DOS (i.e., HbO and HbR) are per volume of tissue, not per volume of blood. Normal hemoglobin concentration in blood is around 2300 μM. However, blood typically occupies only a 5% volume fraction of tissue, meaning that the hemoglobin concentration in tissue is around 100 μM. Typically, the total hemoglobin concentration in blood remains constant, i.e., the hematocrit remains constant. Consequentially, changes in the measured total hemoglobin concentration with DOS, i.e., $HbT = HbO + HbR$, correspond to changes in tissue blood volume. If the hematocrit is constant, the tissue total hemoglobin concentration is proportional to tissue blood volume, i.e.,

$$HbT \equiv HbO + HbT \propto \text{Tissue Blood Volume [mL Blood / mL Tissue]}. \tag{2.138}$$

Further, the tissue oxygen saturation,

$$StO_2 = \frac{HbO}{HbT}, \tag{2.139}$$

is equivalent to the blood oxygen saturation.

The DOS measurements of tissue blood volume and tissue oxygen saturation are bulk averages weighted towards the microvasculature (e.g., capillaries, small venules, arterioles). The reason DOS is most sensitive to the microvasculature is that photon absorption in larger vessels is much higher than it is in smaller vessels. Since the total hemoglobin in blood is $\sim 2300\ \mu M$, the photon absorption length when it is actually traveling inside a blood vessel is about 2.5 mm. For small vessels, the photon exits the vessel well before this length scale. In large vessels, though, it is more likely for photons to travel this length scale before exiting. Thus, photons passing through large vessels are preferentially absorbed, which means that detected photons have preferentially visited smaller vessels, making the DOS measurement predominantly sensitive to the tissue microvasculature.

2.13.1 Optimal Wavelengths for Diffuse Optical Spectroscopy

Determination of tissue chromophore concentrations requires the separation of tissue absorption from tissue scattering at more than one optical wavelength. The optimal choice of wavelengths for chromophore concentration determination is an important topic in its own right, with an interesting history that involved careful consideration of measurement type, i.e. frequency-domain, time-domain, CW, and measurement signal-to-noise. For simple, two-wavelength time- and frequency-domain instruments, early experimenters wondered about which wavelengths to choose to minimize cross-talk between chromophores when inverting Equation 2.136. Superficially, one might expect that at least one wavelength within the NIR window should be below the isosbestic point of hemoglobin and one should be above this isosbestic point. The isosbestic point is the wavelength wherein the extinction coefficients of oxygenated and de-oxygenated hemoglobin are the same ($\sim$800 nm, see Figure 2.20); wavelengths below the isosbestic point are thus more sensitive to deoxy-hemoglobin, while wavelengths above are more sensitive to oxy-hemoglobin. However, such wavelength selection processes are limited. Yamashita *et al* [263], Strangman *et al* [235], and Boas *et al* [26] have shown theoretically and experimentally that when using only two wavelengths, a pair at $660 - 760$ nm and 830 nm provides superior oxy- and deoxy- hemoglobin separation by comparison to what was the more commonly used choice of 780 nm and 830 nm.

A formal evaluation of the optimum wavelength selection for an arbitrary number of wavelengths was carried out by Corlu *et al* [58, 60]; they introduced a general procedure for finding those wavelengths which best differentiate tissue chromophores using CW and frequency-domain light. These results built on a theoretical approach developed in a classic paper by Lionheart and Arridge [8]. That paper [8] theoretically proved that it is impossible to uniquely separate scattering from absorption in a diffuse optical imaging experiment employing CW light. In an attempt to circumvent this uniqueness problem for CW imaging, Corlu *et al* demonstrated that a multi-spectral approach can be employed to uniquely reconstruct the chromophore concentrations, c_i. In a key advance, Corlu *et al* [58, 60] abandoned the two-step approach of determining μ_a at each wavelength first and then inverting Equation 2.136. Instead, they introduced

a multi-spectral approach that exploits known spectral properties of the medium *a priori* to directly reconstruct chromophore concentrations with better fidelity than the traditional two-step method. Specifically, *a priori* assumptions about the form of the scattering (e.g., $\mu_s'(\lambda) = a\lambda^{-b}$) and wavelength-dependent absorption extinction factors (i.e., Equation 2.136) are used, and the wavelength independent variables c_i, a, and b are reconstructed directly from all of the data simultaneously. Because the data from all wavelengths are simulataneously used, the inverse problem is better-constrained than the traditional approach (see [58] for details). The multi-spectral technique is now commonly used, and has been extended for frequency domain sources [232], for including uncertainties in the hemoglobin extinction coefficients [34], and for spectral window optimization when using broadband sources [87].

Chapter 3

Diffuse Optical Spectroscopy (DOS): Modified Beer-Lambert Law Approach

3.1 Introduction

In Chapter 2, I presented the photon diffusion approach for analysis of DOS signals to separate tissue absorption from tissue scattering. Multi-spectral measurements of tissue absorption then enable estimation of blood volume and blood oxygen saturation in the tissue microvasculature. In this chapter, I discuss an alternative approach for DOS analysis, which is the Modified Beer-Lambert law [10, 67, 130]. The Modified Beer-Lambert law is arguably the most widely used approach for analysis of DOS signals [99,122,166,175,219,248], in large part because of its simplicity. With this approach, researchers have monitored temporal changes in blood oxygenation and blood volume with CW light, using only one source-detector separation.

The Modified Beer-Lambert law scheme relates differential light transmission changes (in any geometry) to differential changes in tissue absorption[1]. In essence, this scheme accounts for tissue scattering by using the mean pathlength traveled by photons through the highly scattering sample as a best estimate for the actual photon pathlengths. The mean pathlength provides a natural constant of proportionality between the measured differential intensity and the sample's differential absorption.

[1]The term differential refers to a comparison between a baseline state and a perturbed state.

The Modified Beer-Lambert law is well suited for monitoring temporal variations in blood oxygenation and blood volume with respect to some perturbation, as in brain mapping. Importantly, it is also valid in tissues/geometries wherein light transport is not diffusive, which facilitates accurate absorption monitoring for small source-detector separations typical of endoscopic probes, for visible light wherein tissue absorption is very high, and for tissue that contain very high concentrations of blood, as in the liver. A drawback of this approach, though, is that it cannot determine absolute tissue hemoglobin concentrations. Most of this chapter (Sections 3.3 - 3.3.7) focuses on utilizing the Modified Beer-Lambert law in homogeneous media for both diffusive and non-diffusive light transport. The heterogeneous media Modified Beer-Lambert law is discussed briefly in Section 3.4.

3.2 Beer-Lambert Law for Optically Thin Homogeneous Media

In optically thin (i.e., non-scattering) homogeneous media, light travels in a straight line between source and detector, and is exponentially attenuated by absorption, i.e.,

$$I = I_s \exp[-\mu_a \rho], \tag{3.1}$$

where I_s is the source intensity delivered to the sample, I is the detected intensity emerging from the sample, and ρ is the straight line distance between source and detector (Figure 3.1). Thus, the sample optical density (OD), which is defined as the negative logarithm of the ratio of transmitted to incident light intensity, is proportional to the absorption coefficient:

$$OD \equiv -\log[I/I_s] = \mu_a \rho. \tag{3.2}$$

Equation 3.2 is the Beer-Lambert law, which utilizes multi-spectral measurements of the optical density to measure absolute chromophore concentrations (c_i) in optically thin homogeneous media via the system of equations

$$OD(\lambda) = \rho \log(10) \sum_i \varepsilon_i(\lambda) c_i, \tag{3.3}$$

where $\varepsilon_i(\lambda)$ is the wavelength-dependent extinction coefficient for chromophore i. Chromophore extinction coefficients can be calculated from multi-spectral light transmission measurements

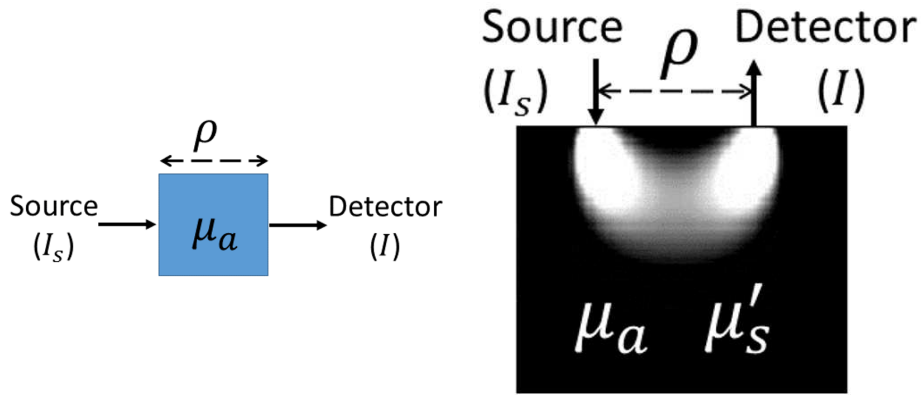

Figure 3.1: Schematics of an optically thin homogeneous medium (left) and an optically thick turbid homogeneous medium (right).

through pure solutions with a known chromophore concentration, c_i, i.e.,

$$\varepsilon_i(\lambda) = \frac{-1}{c_i \rho} \log_{10}\left(\frac{I(\lambda)}{I_s(\lambda)}\right) = \frac{OD(\lambda)}{c_i \rho \log(10)}. \tag{3.4}$$

3.3 Modified Beer-Lambert Law for Turbid Homogeneous Media

When light scattering within the sample is significant, then light attenuation is affected by both absorption and scattering, and the Beer-Lambert law (Equation 3.2) is no longer applicable. As discussed in Chapter 2, photon trajectories through turbid tissues are well approximated as random walks, and photons therefore travel over a distribution of pathlengths from source to detector (Figure 3.1), wherein the average length of a photon path is much greater than the straight-line distance between source and detector, ρ.

In turbid media, the effects of scattering are tangled with those of absorption. Although the photon diffusion model can be employed to separate scattering from absorption (Chapter 2), an alternative paradigm is the Modified Beer-Lambert law [10, 67], which is readily derived from the first order Taylor expansion of the optical density:

$$OD \approx OD^0 + \frac{\partial OD^0}{\partial \mu_a}\Delta\mu_a + \frac{\partial OD^0}{\partial \mu_s'}\Delta\mu_s', \tag{3.5}$$

where the optical densities $OD \equiv -\log(I/I_s)$ and $OD^0 \equiv -\log(I^0/I_s)$ correspond to a "perturbed" tissue state (e.g., at time t) with optical properties of (μ_a, μ_s') and a "baseline" tissue state (e.g., at time t^0) with optical properties of $(\mu_a^0, \mu_s'^0)$, respectively. Further, $\Delta\mu_a \equiv$

$\mu_a - \mu_a^0$ and $\Delta\mu_s' \equiv \mu_s' - \mu_s'^0$ are the differential changes in absorption and scattering between the perturbed and baseline tissue states. The Modified Beer-Lambert law is a rearrangement of Equation 3.5 wherein the source intensity I_s is assumed to remain constant, i.e.,

$$\Delta OD = -\log\left(\frac{I(\rho)}{I^0(\rho)}\right) \approx L(\rho)\Delta\mu_a + \left(\frac{\mu_a^0}{\mu_s'^0}\right) L(\rho)\Delta\mu_s' \approx L(\rho)\Delta\mu_a. \tag{3.6}$$

Here, $L(\rho) \equiv \partial OD^0/\partial\mu_a$ [cm] is the so-called differential pathlength, which is approximately the mean pathlength that diffusing photons travel through the medium from a point source to a point detector with separation ρ [10], and $\partial OD^0/\partial\mu_s' \approx (\mu_a^0/\mu_s'^0)L(\rho)$ (Section 3.3.1). It is often reasonable to neglect the scattering term in Equation 3.6 because (1), the multiplicative factor $\mu_a^0/\mu_s'^0$ for many tissues is much less than one, and (2), tissue scattering changes that accompany hemodynamic variations are often negligible [12].

Notice that whereas the Beer-Lambert law (Equation 3.2) relates *absolute* optical densities to *absolute* absorption coefficients, the Modified Beer-Lambert law (Equation 3.6) relates *differential changes* in the optical density to *differential changes* in the absorption coefficient. Implementation of Equation 3.6 requires knowledge of the differential pathlength, $L(\rho)$, which not only depends on the source-detector separation, ρ, but also the tissue geometry and the wavelength-dependent baseline tissue absorption and scattering properties, μ_a^0 and $\mu_s'^0$. The differential pathlength can be measured with time-resolved [67] or frequency-domain techniques [10, 75]; or computed with a diffusion model [94] or radiative transport models [162, 255]. Direct measurements of $L(\rho)$ do not require *a priori* knowledge of the baseline optical properties or tissue geometry, but light transport must be diffusive, and the instrumentation is considerably more complex and expensive than CW measurements. Conversely, the computation of $L(\rho)$ from light transport models permits accurate tissue absorption monitoring with the Modified Beer-Lambert law for non-diffusive light transport and for spatially extended light sources (e.g., plane waves), but utilization of the light transport models requires *a priori* knowledge of the baseline optical properties and tissue geometry.

3.3.1 Time-resolved Measurement of Differential Pathlength

For continuous-wave, diffusive light traveling through the medium from a point source to a point detector, the differential pathlength is the speed of light through tissue multiplied by the

mean time of flight of photons in tissue, i.e., $L(\rho) = v\langle t - t_s\rangle$. Here, t_s is the time that an infinitesimally narrow source pulse of light is emitted at position $\mathbf{r}_s$, t is the photon detection time at position $\mathbf{r}_d$, and v is the speed of light through tissue. Thus, the differential pathlength can be measured via direct measurement of the mean time of flight with a time-resolved instrument [67].

I will now explicitly derive this relationship between $L(\rho)$ and $\langle t - t_s\rangle$. The probability that a photon emitted at ($\mathbf{r}_s$, t_s) reaches the detector at $\mathbf{r}_d$ in a time interval dt around the detection time t is proportional to the time-domain photon diffusion Green's function (see Section 2.12 and Equation 2.85), i.e.,

$$P([t, \mathbf{r}_d], [t_s, \mathbf{r}_s]) = \frac{g(\mathbf{r}_d, \mathbf{r}_s, t, t_s)\mathrm{d}t}{\int_{-\infty}^{\infty} g(\mathbf{r}_d, \mathbf{r}_s, t, t_s)\mathrm{d}t}. \tag{3.7}$$

Therefore, the mean time of flight is

$$\langle t - t_s\rangle = \int_{-\infty}^{\infty} (t - t_s)P([t, \mathbf{r}_d], [t_s, \mathbf{r}_s])\mathrm{d}t = \frac{\int_{-\infty}^{\infty}(t - t_s)g(\mathbf{r}_d, \mathbf{r}_s, t, t_s)\mathrm{d}t}{\int_{-\infty}^{\infty} g(\mathbf{r}_d, \mathbf{r}_s, t, t_s)\mathrm{d}t}. \tag{3.8}$$

From Equation 2.91, the mean time of flight is alternatively given by

$$\langle t - t_s\rangle = \frac{i\frac{\partial}{\partial\omega}\int_{-\infty}^{\infty} g(\mathbf{r}_d, \mathbf{r}_s, t, t_s)\mathrm{e}^{-i\omega(t-t_s)}\mathrm{d}t}{G_{cw}(\mathbf{r}_d, \mathbf{r}_s)} = \frac{i\ \partial G(\mathbf{r}_d, \mathbf{r}_s)/\partial\omega|_{\omega=0}}{G_{cw}(\mathbf{r}_d, \mathbf{r}_s)}. \tag{3.9}$$

Here, $G_{cw}(\mathbf{r}_d, \mathbf{r}_s)$ and $G(\mathbf{r}_d, \mathbf{r}_s)$ are the continuous-wave (Equation 2.93) and frequency-domain (Equation 2.87) photon diffusion Green's functions, respectively, evaluated at the baseline tissue optical properties μ_a^0 and $\mu_s'^0$. The frequency derivative, $\partial G/\partial\omega$, is additionally evaluated at the modulation frequency $\omega = 0$.

For continuous-wave diffusive light transport, the detected light intensity is proportional to $G_{cw}(\mathbf{r}_d, \mathbf{r}_s)$ (Section 2.11). Consequentially, the differential pathlength is

$$L(\rho) \equiv \frac{\partial OD^0}{\partial\mu_a} = -\frac{\partial}{\partial\mu_a}\log[G_{cw}(\mathbf{r}_d, \mathbf{r}_s)] = \frac{-1}{G_{cw}(\mathbf{r}_d, \mathbf{r}_s)}\frac{\partial G_{cw}(\mathbf{r}_d, \mathbf{r}_s)}{\partial\mu_a}, \tag{3.10}$$

where again, $G_{cw}(\mathbf{r}_d, \mathbf{r}_s)$ is evaluated at the baseline tissue optical properties. Combining Equations 3.9 and 3.10, we obtain

$$\langle t - t_s\rangle = \frac{-iL(\rho)\ \frac{\partial}{\partial\omega}G(\mathbf{r}_d, \mathbf{r}_s)\big|_{\omega=0}}{\frac{\partial}{\partial\mu_a}G_{cw}(\mathbf{r}_d, \mathbf{r}_s)}. \tag{3.11}$$

From examining the homogeneous frequency-domain photon diffusion equation (Equation 2.54), the modulation frequency dependence of $G(\mathbf{r}_d, \mathbf{r}_s)$ is contained in the variable $k^2 \equiv (v\mu_a +$

$i\omega)/D$, while the absorption dependence of $G_{cw}(\mathbf{r}_d, \mathbf{r}_s)$ is contained in the variable $k_0^2 \equiv v\mu_a/D$. Thus[2],

$$\frac{\partial}{\partial\omega}G(\mathbf{r}_d, \mathbf{r}_s)\bigg|_{\omega=0} = \frac{\partial G_{cw}(\mathbf{r}_d, \mathbf{r}_s)}{\partial k_0^2} \times \frac{\partial k^2}{\partial\omega}, \tag{3.12}$$

$$\frac{\partial}{\partial\mu_a}G_{cw}(\mathbf{r}_d, \mathbf{r}_s) = \frac{\partial G_{cw}(\mathbf{r}_d, \mathbf{r}_s)}{\partial k_0^2} \times \frac{\partial k_0^2}{\partial\mu_a}. \tag{3.13}$$

Substituting Equations 3.12 and 3.13 into 3.11 reveals that the differential pathlength is approximately the mean photon pathlength traveled from source to detector, i.e.,

$$L(\rho) = \frac{\langle t - t_s\rangle \partial k_0^2/\partial\mu_a}{-i\partial k^2/\partial\omega} = \left[1 + \frac{\mu_a^0}{\mu_a^0 + \mu_s'^0}\right] v\langle t - t_s\rangle \approx v\langle t - t_s\rangle. \tag{3.14}$$

The latter approximation in Equation 3.14 is equivalent to the approximation $D \approx v/(3\mu_s')$.

An advantage of measuring $L(\rho)$ directly with a time-resolved technique is that no *a priori* knowledge of baseline optical properties for the homogeneous medium is required. Compared to continuous-wave measurements, though, time-resolved instrumentation is complex and expensive.

3.3.2 Frequency-Domain Measurement of Differential Pathlength

If the time-domain Green's function for homogeneous media, i.e., $g(\mathbf{r}_d, \mathbf{r}_s, t-t_s)$, is symmetrical about the mean time of flight, $\langle t - t_s\rangle$, then the phase of the corresponding frequency-domain Green's function is $\theta = \omega\langle t - t_s\rangle$ [10]. To derive this, consider an infinitesimal pulse of light emitted at $t_s = 0$. If g is symmetrical about the mean time of flight, i.e., $g(\mathbf{r}_d, \mathbf{r}_s, t + \langle t\rangle) = g(\mathbf{r}_d, \mathbf{r}_s, \langle t\rangle - t)$, then the frequency-domain Green's function is determined from substituting $g(\mathbf{r}_d, \mathbf{r}_s, t + \langle t\rangle)$ into Equation 2.91:

$$\begin{aligned}
G(\mathbf{r}_d, \mathbf{r}_s) &= \int_{-\infty}^{\infty} g(\mathbf{r}_d, \mathbf{r}_s, t + \langle t\rangle)\mathrm{e}^{-i\omega(t+\langle t\rangle)}\mathrm{d}t \\
&= \mathrm{e}^{-i\omega\langle t\rangle}\left(\int_{-\infty}^{\infty} g(\mathbf{r}_d, \mathbf{r}_s, t + \langle t\rangle)\cos(\omega t)\mathrm{d}t - i\int_{-\infty}^{\infty} g(\mathbf{r}_d, \mathbf{r}_s, t + \langle t\rangle)\sin(\omega t)\mathrm{d}t\right) \\
&= \mathrm{e}^{-i\omega\langle t\rangle}\int_{-\infty}^{\infty} g(\mathbf{r}_d, \mathbf{r}_s, t + \langle t\rangle)\cos(\omega t)\mathrm{d}t, \\
&= A(\mathbf{r}_d, \mathbf{r}_s)\mathrm{e}^{-i\omega\langle t\rangle}.
\end{aligned} \tag{3.15}$$

[2]Note that $\partial G(\mathbf{r}_d, \mathbf{r}_s)/\partial k^2|_{\omega=0} = \partial G_{cw}(\mathbf{r}_d, \mathbf{r}_s)/\partial k_0^2$.

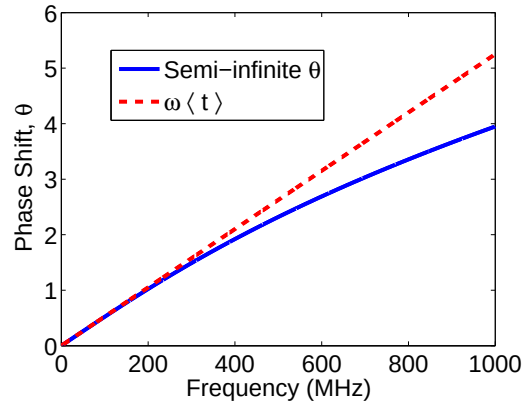

Figure 3.2: For a semi-infinite medium with $\mu_a = 0.1$, $\mu_s' = 10$ cm^{-1}, $R_{eff} = 0.493$, $n = 1.4$, and $\rho = 2.5$ cm, the mean photon time of flight (see Equation 3.23) and the frequency-domain phase shift, θ (as a function of ω), were calculated using the semi-infinite frequency-domain Green's function (Equation 2.103). Both θ and $\omega\langle t\rangle$ are plotted against the oscillation frequency.

Thus, from Equation 3.15, the phase shift acquired by intensity modulated light propagating from a point source to a point detector is $\theta = \omega\langle t\rangle$, provided that $g(\mathbf{r}_d, \mathbf{r}_s, t)$ is symmetrical about the mean time of flight, $\langle t\rangle$. The second term in line two of Equation 3.15 is zero because the integral is over the product of an even function (i.e., $g(\mathbf{r}_d, \mathbf{r}_s, t + \langle t\rangle)$) and an odd function (i.e., $\sin(\omega t)$). Further, since g is real, the integral in the third line is the frequency-domain amplitude, $A(\mathbf{r}_d, \mathbf{r}_s)$. Although g is not truly symmetrical, it is nearly symmetrical, and $\theta = \omega\langle t\rangle$ is a good approximation for modulation frequencies less than 200 MHz (Figure 3.2). The differential pathlength is then (Equation 3.14)

$$L(\rho) \approx v\theta(\rho)/\omega. \tag{3.16}$$

The drawback of using Equation 3.16 to measure the differential pathlength is its sensitivity to the assumption that the phase light coupling coefficient obtained from phantom calibration (Section 2.11.1.1) remains the same on tissue. Nonetheless, reasonable measurements of $L(\rho)$ have been made using this approach in a variety of tissues [75]. If multi-separation frequency-domain measurements are not practical, the phase information from a single separation can be used to measure the differential pathlength, enabling tissue absorption monitoring with the Modified Beer-Lambert law (Equation 3.6).

3.3.3 Scattering Weighting Factor in Modified Beer-Lambert Law

For diffusive light, the scattering factor weighting factor in the Modified Beer-Lambert Law, i.e., $L_s(\rho) \equiv \partial OD^0/\partial\mu_s'$, is determined from evaluating

$$L_s(\rho) = -\frac{1}{G_{cw}(\mathbf{r}_d, \mathbf{r}_s)} \frac{\partial G_{cw}(\mathbf{r}_d, \mathbf{r}_s)}{\partial \mu_s'}, \tag{3.17}$$

at the baseline tissue optical properties. Combining Equation 3.17 with Equation 3.9, we obtain

$$L_s(\rho) = \frac{\langle t - t_s \rangle (\partial k_0^2/\partial \mu_s')}{-i\partial k^2/\partial\omega} = \frac{\mu_a^0}{\mu_a^0 + \mu_s'^0} v \langle t - t_s \rangle, \tag{3.18}$$

which in the limit $\mu_s' \gg \mu_a$ is

$$L_s(\rho) \approx \frac{\mu_a^0}{\mu_s'^0} L(\rho). \tag{3.19}$$

In tissue, the ratio $\mu_a^0/\mu_s'^0$ is typically small, and consequentially, $L(\rho) \gg L_s(\rho)$.

3.3.4 Computing Differential Pathlength from Tissue Optical Properties

The differential pathlength can also be computed for any homogeneous geometry through evaluating the absorption derivative of the optical density at the baseline tissue optical properties, i.e.,

$$L(\rho) \equiv -\frac{\partial}{\partial \mu_a} \log[I(\rho, \mu_a^0, \mu_s'^0)] \approx \frac{1}{\Delta\mu_a} \log\left[\frac{I(\rho, \mu_a^0 - \Delta\mu_a/2, \mu_s'^0)}{I(\rho, \mu_a^0 + \Delta\mu_a/2, \mu_s'^0)}\right], \tag{3.20}$$

where $\Delta\mu_a/\mu_a^0 = 10^{-5}$. For continuous-wave (CW) diffusive light, I is proportional to the continuous-wave photon diffusion Green's function, $G_{cw}(\rho, \mu_a, \mu_s')$, for the appropriate geometry, i.e.,

$$L(\rho) = -\frac{\partial}{\partial \mu_a} \log[G_{cw}(\rho, \mu_a^0, \mu_s'^0)] \approx \frac{1}{\Delta\mu_a} \log\left[\frac{G_{cw}(\rho, \mu_a^0 - \Delta\mu_a/2, \mu_s'^0)}{G_{cw}(\rho, \mu_a^0 + \Delta\mu_a/2, \mu_s'^0)}\right]. \tag{3.21}$$

Substitution of the semi-infinite continuous-wave Green's function (Equation 2.103 at $\omega = 0$) into Equation 3.21 and taking the analytical absorption derivative results in a simple expression for the differential pathlength in terms of the baseline optical properties:

$$L(\rho) = \frac{3 r_1 r_b \mu_s'^0}{2k_0} \left[\frac{\mathrm{e}^{k_0 r_1} - \mathrm{e}^{k_0 r_b}}{r_1 \mathrm{e}^{k_0 r_1} - r_b \mathrm{e}^{k_0 r_b}}\right], \tag{3.22}$$

where $k_0 = \sqrt{3\mu_a^0(\mu_a^0 + \mu_s'^0)}$, $r_1 = \sqrt{(\mu_s'^0 + \mu_a^0)^{-2} + \rho^2}$, $r_b = \sqrt{((\mu_s'^0 + \mu_a^0)^{-1} + 2z_b)^2 + \rho^2}$, $z_b = 2(1+R_{eff})/[3(\mu_s'^0 + \mu_a^0)(1-R_{eff})]$, and R_{eff} is an effective Fresnel reflection coefficient

defined by Equation 2.79. The corresponding mean time of photon flight in the semi-infinite geometry is given by (Equation 3.9)

$$\langle t \rangle = \frac{3(\mu_a^0 + \mu_s'^0)\left(\mathrm{e}^{-k_0 r_1} - \mathrm{e}^{-k_0 r_b}\right)}{2vk_0\left[\frac{\mathrm{e}^{-k_0 r_1}}{r_1} - \frac{\mathrm{e}^{-k_0 r_b}}{r_b}\right]} \tag{3.23}$$

For more complex geometries, it is usually easier to compute $L(\rho)$ by evaluating the derivative in Equation 3.21 numerically.

Importantly, the Modified Beer-Lambert law is applicable for non-diffusive light transport. In this regime, the differential pathlength is determined from evaluating Equation 3.20, where I is modeled with solutions of the radiative transport equation (Equation 2.9) for the tissue optical properties and tissue geometry of interest. The radiative transport equation can be solved with a Monte Carlo method [25, 145, 255] or with finite difference or finite volume methods [162].

Additionally, the Modified Beer-Lambert law can be utilized for applications with spatially extended light sources. For example, the so-called optical imaging of intrinsic signals (OIS) technique uses the Modified Beer-Lambert law to obtain 2-dimensional maps of hemoglobin concentration changes from intensity images of a surface illuminated with planar light [77, 78, 163]. Although the source-detector separation no longer has meaning in this context, the differential pathlength is still evaluated via

$$L \approx \frac{1}{\Delta\mu_a} \log\left[\frac{I(\mu_a^0 - \Delta\mu_a/2, \mu_s'^0)}{I(\mu_a^0 + \Delta\mu_a/2, \mu_s'^0)}\right], \tag{3.24}$$

where $I(\mu_a, \mu_s')$ is the detected signal from the spatially extended source when the tissue optical properties are (μ_a, μ_s'). $I(\mu_a, \mu_s')$ is obtained from solving the photon diffusion equation for the appropriate source and geometry (e.g., Equation 2.93), or solving the radiative transport equation. I discuss OIS further in Chapter 7.

3.3.5 Differential Pathlength Factor

In the large source-detector limit (i.e., $\rho \gg 2z_b + (\mu_a^0 + \mu_s'^0)^{-1}$), the semi-infinite differential pathlength (Equation 3.22) simplifies to [94]

$$L(\rho) \approx \frac{3\mu_s'^0 \rho^2}{2\left(\rho\sqrt{3\mu_a^0\mu_s'^0} + 1\right)}. \tag{3.25}$$

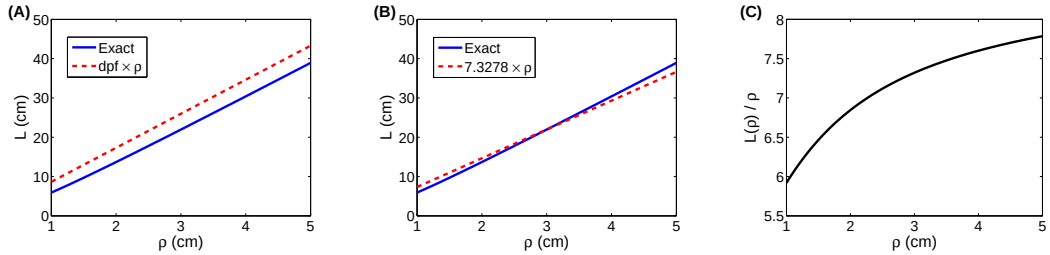

Figure 3.3: Comparison of the exact semi-infinite differential pathlength (Equation 3.22) plotted against source-detector separation, ρ, with **(A)**, the "large ρ dpf" approximation (Equation 3.26), and with **(B)**, the "empirical dpf" approximation, $L(\rho) \approx 7.3278\rho$, i.e., $dpf = L(\rho = 3\text{ cm})/(3\text{ cm}) = 7.3278$. **(C)** Ratio of the exact semi-infinite differential pathlength divided by the source-detector separation, plotted against ρ. In all three panels, the semi-infinite medium properties are $\mu_a = 0.1$, $\mu_s' = 10\text{ cm}^{-1}$, $n = 1.4$, and $R_{eff} = 0.493$. The empirical dpf approximation is in good agreement with the exact differential pathlength for separations close to the "calibration separation", i.e., 3 cm. Further, the ratio $L(\rho)/\rho$ slowly approaches a constant value (i.e., $dpf = 8.66$ from Equation 3.26) as ρ increases.

A more severe approximation than Equation 3.25 is

$$L(\rho) \approx \frac{3\mu_s'^0}{2\sqrt{3\mu_a^0\mu_s'^0}}\rho = dpf \times \rho. \tag{3.26}$$

Here, the differential pathlength is proportional to the source-detector separation, and the proportionality coefficient is the so-called differential pathlength factor, i.e., dpf. The $\rho-$independence of dpf makes it more convenient to tabulate in the literature as a function of wavelength for a given tissue type, and it is in large part for this reason that the dpf is commonly used. Typically, the differential pathlength is measured using a time-resolved technique (Equation 3.14) at multiple wavelengths and then divided by the source-detector separation, ρ, to empirically compute the differential pathlength factor. In addition to depending on wavelength, the dpf depends on age and tissue type, since the tissue optical properties vary with age and tissue type. Scholkmann and Wolf have recently reviewed the wavelength and age dependence of the dpf for the frontal human head [220]. Differential pathlength values have also been published for other regions of the adult human head [272], and in muscle [243].

However, even when accounting for age and tissue type, there is still considerable variability across human subjects in the dpf, because the tissue optical properties are heterogeneous across different subjects [144]. Further, Equation 3.26 only roughly approximates the true differential pathlength (Figure 3.3), which could be a source of systematic error. When employing the dpf

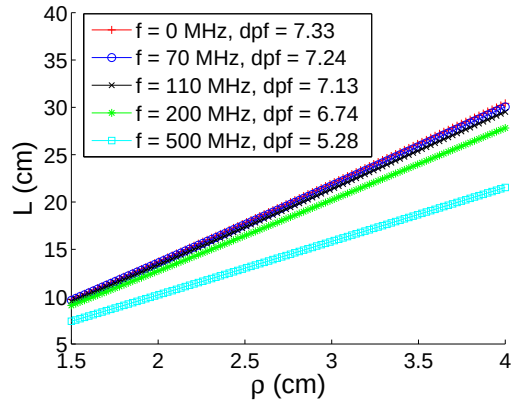

Figure 3.4: For a semi-infinite medium with $\mu_a = 0.1$, $\mu_s' = 10$ cm^{-1}, $R_{eff} = 0.493$, and $n = 1.4$, the differential pathlength for intensity modulated light ($L(\rho)$, Equation 3.27) is plotted against the source-detector separation ρ for several different intensity modulation frequencies f. The dpf values in the legend are $L(2.5$ cm$)/(2.5$ cm).

approach for analysis, it is of course best to use published values of the dpf that were measured in a sample of statistically similar tissue types with a similar source-detector separation and similar wavelengths. It is even more preferable to use time-resolved or frequency-domain instrumentation to measure subject-specific differential pathlengths for the Modified Beer-Lambert law.

3.3.6 Differential Pathlength with Intensity Modulated Light

The Modified Beer-Lambert law (Equation 3.6) can also be employed for intensity modulated light. For this case, the optical density is the negative logarithm of the detected intensity modulated amplitude, and the differential pathlength is

$$L(\rho) = -\frac{\partial}{\partial \mu_a} \log[|G(\rho, \mu_a^0, \mu_s'^0)|], \tag{3.27}$$

where $|G(\rho, \mu_a^0, \mu_s'^0)|$ is the amplitude of the frequency-domain Green's function. For lower modulation frequencies (< 100 MHz), the differential pathlength is roughly equivalent to the CW differential pathlength (Figure 3.4). Thus, for lower modulation frequencies, it is a decent approximation to utilize the measured CW differential pathlength given by Equation 3.14 or Equation 3.16 in the frequency-domain Modified Beer-Lambert law.

3.3.7 Spectroscopy for Determination of Tissue Chromophore Concentration Changes

Recall that the absorption coefficient depends on the tissue chromophore concentrations (Equation 2.136), and therefore multi-spectral measurements of the tissue optical density enables monitoring of differential changes in chromophore concentrations (Δc_i) with the Modified Beer-Lambert law, i.e.,

$$\Delta OD(\lambda) = -\log\left(\frac{I(\rho,\lambda)}{I^0(\rho,\lambda)}\right) \approx L(\rho,\lambda)\log(10)\sum_i \varepsilon_i(\lambda)\Delta c_i. \tag{3.28}$$

The Modified Beer-Lambert law is most typically employed to measure changes in oxy-hemoglobin concentration (ΔHbO) and deoxy-hemoglobin concentration (ΔHbR).

Since the Modified Beer-Lambert law is the first order Taylor series expansion of the optical density, it is expected to be accurate in the limit $\Delta\mu_a/\mu_a^0 \ll 1$. However, simulations show that Equation 3.28 remains accurate for substantial changes in HbO and HbR (Figure 3.5). Even for $\pm 50\%$ changes, the Modified Beer-Lambert law still recovers the true hemoglobin changes within $\sim 5\%$ (Figure 3.5). Notice also that the Modified Beer-Lambert is more erroneous for decreases in HbO and HbR than increases.

As I mentioned previously, the main drawback of Equation 3.28 is its inability to estimate absolute "basline" hemoglobin concentrations. Further, if it's not feasible to measure the differential pathlengths directly, then the baseline hemoglobin concentrations along with the baseline tissue scattering ($\mu_s'^0(\lambda)$) are needed for calculating the differential pathelengths $L(\rho,\lambda)$ (e.g., Equation 3.22, where $\mu_a^0(\lambda)$ is obtained from the baseline chromophore concentrations (Equation 2.136). Often, the baseline hemoglobin concentrations and tissue scattering must be assumed, which leads to errors in the differential pathlengths used for hemoglobin monitoring.

Simulations, however, show the computed hemoglobin concentration changes with the Modified Beer-Lambert law to be fairly robust to differential pathlength errors (Figure 3.6). Recall that wavelengths above the hemoglobin spectral isobestic point of $\lambda = 800$ nm are more sensitive to HbO, while wavelengths below 800 nm are more sensitive to HbR. Thus, computation of ΔHbO is more sensitive to errors in $L(830\text{ nm})$ than in $L(690\text{ nm})$, and vice versa for computation of ΔHbR (Figure 3.6). Further, the simulations show that underestimating the differential pathlengths induce larger errors in the computed hemoglobin concentrations than overestimating the differential pathlengths does. For example, underestimation of the differential pathlengths by

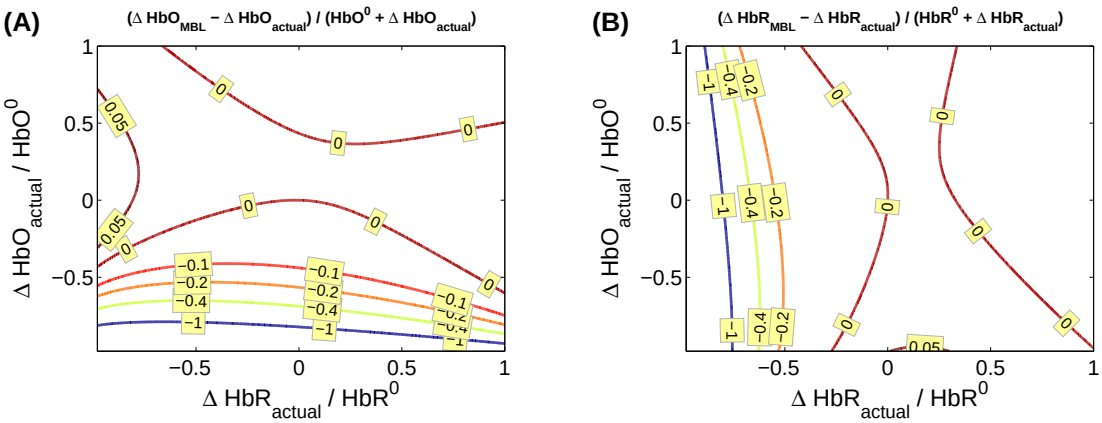

Figure 3.5: Contour plots of **(A)**, the fractional error between the oxy-hemoglobin computed with the Modified Beer-Lambert law ($HbO_{MBL} \equiv HbO^0 + \Delta HbO_{MBL}$; ΔHbO_{MBL} determined from Equation 3.28) and the actual oxy-hemoglobin ($HbO_{actual} \equiv HbO^0 + \Delta HbO_{actual}$), i.e., $HbO_{MBL}/HbO_{actual} - 1$, and **(B)**, the fractional error between the deoxy-hemoglobin computed with the Modified Beer-Lambert law ($HbR_{MBL} \equiv HbR^0 + \Delta HbR_{MBL}$; ΔHbR_{MBL} determined from Equation 3.28) and the actual deoxy-hemoglobin ($HbR_{actual} \equiv HbR^0 + \Delta HbR_{actual}$), i.e., $HbR_{MBL}/HbR_{actual} - 1$. For both panels, the contour levels are plotted as a function of the actual fractional oxy-hemoglobin change (vertical axis) and the actual fractional deoxy-hemoglobin change (horizontal axis). These plots were generated from applying the Modified Beer-Lambert law to simulated multi-spectral data (λ = 690, 786, 830 nm) at a source-detector separation of $\rho = 2.5$ cm. The simulated data was generated from varying HbO and HbR from baseline hemoglobin concentrations representative of the brain (i.e., $HbO^0 = 58\ \mu M$, $HbR^0 = 27\ \mu M$) while tissue scattering remained constant ($\mu_s'(\lambda) = 10$ cm^{-1}) [86]. Equation 2.136, with an assumed water volume fraction of 80%, was employed to convert each oxy-hemoglobin and deoxy-hemoglobin concentration pair to multi-spectral absorption coefficients ($\mu_a(\lambda)$). Then, the semi-infinite continuous-wave diffusion Green's function (Equation 2.103 with $\omega = 0$) was utilized to compute simulated detected intensities ($I(\lambda)$) from $\mu_a(\lambda)$ and a constant tissue scattering coefficient of $\mu_s' = 10$ cm^{-1}. The multi-spectral differential pathlengths were computed with Equation 3.25.

$\sim 25\%$ induces underestimations in the computed hemoglobin concentrations of $\sim 10\%$, while overestimation of the differential pathlengths by $\sim 25\%$ induces $< 5\%$ errors in the computed hemoglobin concentrations (Figure 3.6).

3.4 Modified Beer-Lambert Law for Turbid Heterogeneous Media

The homogeneous Modified Beer-Lambert law discussed above assumes that the absorption change, $\Delta\mu_a$, is homogeneously distributed across the sampled light volume. This has the advantage of simplicity, but realistically, tissue is heterogeneous; it contains multiple compartments with different optical properties due to vasculature, fat, and bone. Often these regions arise as "layers" below the tissue surface such as scalp, skull, and cortex. Under these conditions, a Taylor series expansion of the optical density can also be used to derive the Modified Beer-Lambert law for heterogeneous media [130]. Assuming that the heterogeneous tissue can be divided into N piecewise homogeneous regions, then the first-order Taylor series expansion of the optical density is

$$OD \approx OD^0 + \sum_{k=1}^{N} \left[\frac{\partial OD^0}{\partial \mu_{a,k}} \Delta\mu_{a,k} + \frac{\partial OD^0}{\partial \mu'_{s,k}} \Delta\mu'_{s,k} \right]. \tag{3.29}$$

Here, $\mu_{a,k}$ and $\mu'_{s,k}$ are the tissue absorption and scattering for the kth homogeneous region in the tissue, and $\Delta\mu_{a,k} \equiv \mu_{a,k} - \mu^0_{a,k}$ and $\Delta\mu'_{s,k} \equiv \mu'_{s,k} - \mu'^0_{s,k}$ denote the differential changes in absorption and scattering from baseline. Rearranging Equation 3.29, the Modified Beer-Lambert law for heterogeneous media is:

$$\Delta OD \approx \sum_{k=1}^{N} \left[L_k(\rho)\Delta\mu_{a,k} + \frac{\mu^0_{a,k}}{\mu'^0_{s,k}} L_k(\rho)\Delta\mu'_{s,k} \right] \approx \sum_{k=1}^{N} L_k(\rho)\Delta\mu_{a,k}, \tag{3.30}$$

where the partial pathlengths, $\{L_k(\rho) \equiv \partial OD^0/\partial\mu_{a,k}\}$, are the mean pathlengths that detected photons travel in the kth region [130, 235]. In other words, the kth partial pathlength is the photon mean time of flight in the kth region multiplied by the speed of light in the kth region, i.e., $L_k(\rho) = v_k\langle t_k\rangle$. As in Equation 3.6, the scattering term $\partial OD^0/\partial\mu'_{s,k}\Delta\mu'_{s,k} \approx L_k(\mu^0_{a,k}/\mu'^0_{s,k})\Delta\mu'_{s,k}$ is often negligible compared to the absorption term.

In addition to the partial pathlengths depending on source-detector separation, ρ, they also

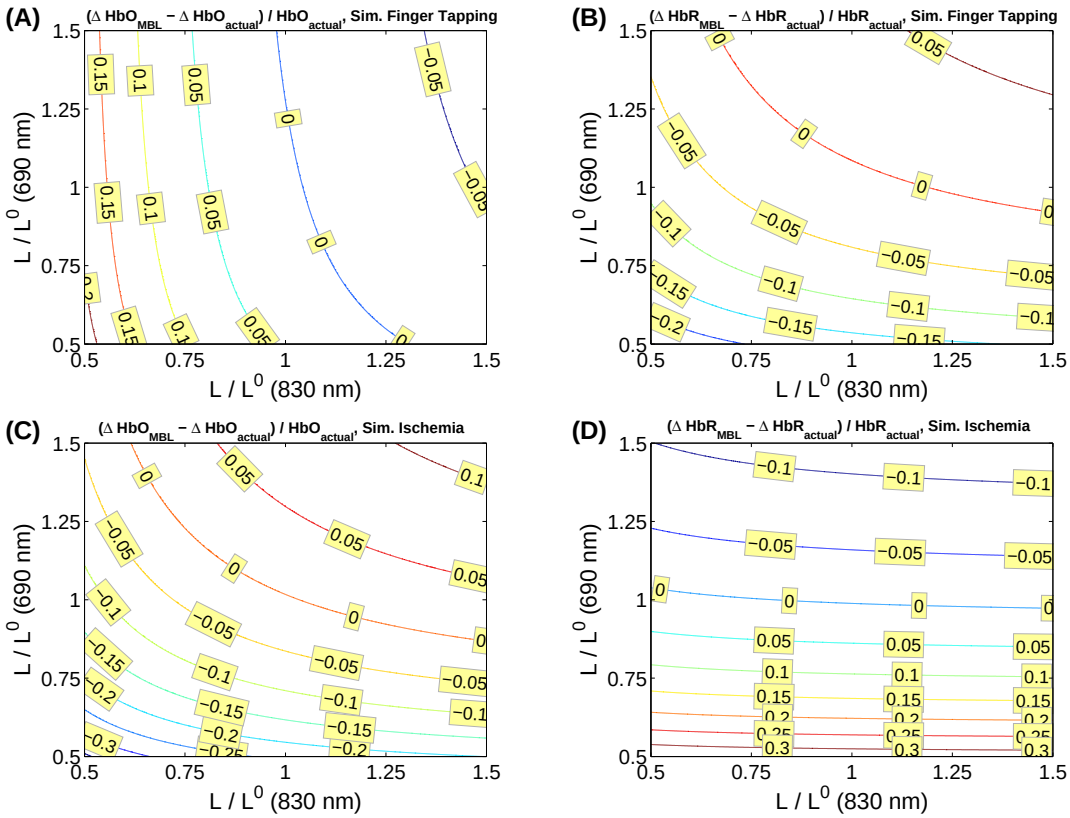

Figure 3.6: Semi-infinite simulated data sets imitating cerebral signal changes induced by finger tapping (panels A, B) and induced by ischemic stroke (panels C, D), were utilized to make contour plots showing the sensitivity of the computed hemoglobin concentration changes from Equation 3.28 ($\lambda = 690,\ 830$ nm; $\rho = 2.5$ cm) to errors in the differential pathlength at $\lambda = 830$ nm (horizontal axis) and at $\lambda = 690$ nm (vertical axis). The contour levels are the fractional errors in the Modified Beer-Lambert law calculations (using the erroneous differential pathlengths specified on the horizontal and vertical axes) of **(A)** oxy-hemoglobin ($HbO_{MBL}/HbO_{actual} - 1$; HbO_{MBL} defined in Figure 3.5) and **(B)** deoxy-hemoglobin ($HbR_{MBL}/HbR_{actual} - 1$; HbR_{MBL} defined in Figure 3.5). Here, the actual oxy- and deoxy-hemoglobin concentration changes are representative of the finger tapping task-induced changes in the motor cortex, i.e., $\Delta HbO_{actual} = 15\ \mu M$, $\Delta HbR_{actual} = -5\ \mu M$ [85]. Contour plots are also generated for the fractional errors in the Modified Beer-Lambert law calculations of **(C)** oxy-hemoglobin and **(D)** deoxy-hemoglobin for a different set of actual concentration changes that mimic the changes induced by an ischemic stroke in the core of the lesion, i.e., $\Delta HbO_{actual} = -15\ \mu M$, $\Delta HbR_{actual} = 15\ \mu M$ [62]. The baseline tissue state is the same for all contour plots (i.e., $HbO_0 = 58\ \mu M$, $HbR_0 = 27\ \mu M$, $\mu_s'^0 = 10$ cm^{-1}), and the actual differential pathlengths, $L^0(830\text{ nm}) = 13.2$ cm and $L^0(690\text{ nm} = 14.1$ cm, were computed with Equation 3.25. Tissue scattering was not varied. Additional details on generating the simulated data are provided in the caption for Figure 3.5. The reason that the zero-level contours do not intersect the point (1,1) is because of errors in the Modified Beer-Lambert law itself (3.5). The Modified Beer-Lambert law is a first-order Taylor series approximation, so it will not calculate the true hemoglobin changes with perfect accuracy.

depends on tissue geometry and the baseline tissue properties, $\{\mu_{a,k}^0, \mu_{s,k}'^0\}$. The partial pathlengths cannot be directly measured, but they can be numerically computed with the heterogeneous analogue of Equation 3.20, which requires *a priori* knowledge of the baseline tissue optical properties and tissue geometry.

The heterogeneous analogue of Equation 3.28 for spectroscopy with Equation 3.30 is

$$\Delta OD(\lambda) = -\log\left(\frac{I(\rho,\lambda)}{I^0(\rho,\lambda)}\right) \approx \log(10)\sum_{k=1}^{N}\left[L_k(\rho,\lambda)\sum_i \varepsilon_i(\lambda)\Delta c_{i,k}\right], \tag{3.31}$$

where $\Delta c_{i,k}$ is the differential concentration change for the ith chromophore in the kth region.

3.4.1 Two-layer Modified Beer-Lambert Law

The simplest heterogeneous model for tissue is the two-layer geometry (Figure 3.7), which many researchers use to model the brain as a compromise between simplicity and accuracy [55, 91, 108, 120, 172, 208, 215]. The two-layer Modified Beer-Lambert law is the special case of Equation 3.30 for $N = 2$ homogeneous layered regions, i.e.,

$$\Delta OD = -\log\left(\frac{I(\rho)}{I^0(\rho)}\right) \approx L_c(\rho)\Delta\mu_{a,c} + L_{ec}(\rho)\Delta\mu_{a,ec}. \tag{3.32}$$

Here, $\Delta\mu_{a,c}$ and $\Delta\mu_{a,ec}$ are the differential absorption changes in the cerebral and extra-cerebral layers, respectively, and $L_c(\rho)$ and $L_{ec}(\rho)$ are the cerebral and extra-cerebral partial pathlengths, which depend on ρ, baseline optical properties, and the extra-cerebral layer thickness, ℓ.

I presented the two-layer photon diffusion Green's function for the planar two-layer geometry in Section 2.10 (Equation 2.112), which can be utilized to compute the two-layer partial pathlengths:

$$L_c(\rho) \equiv \frac{\partial OD^0}{\partial \mu_{a,c}} \approx \frac{1}{\Delta\mu_{a,c}}\log\left[\frac{G(\rho,\mu_{a,c}^0 - \Delta\mu_{a,c}/2, \mu_{a,ec}^0, \mu_{s,c}'^0, \mu_{s,ec}'^0, \ell)}{G(\rho,\mu_{a,c}^0 + \Delta\mu_{a,c}/2, \mu_{a,ec}^0, \mu_{s,c}'^0, \mu_{s,ec}'0, \ell)}\right], \tag{3.33}$$

$$L_{ec}(\rho) \equiv \frac{\partial OD^0}{\partial \mu_{a,ec}} \approx \frac{1}{\Delta\mu_{a,ec}}\log\left[\frac{G(\rho,\mu_{a,c}^0, \mu_{a,ec}^0 - \Delta\mu_{a,ec}/2, \mu_{s,c}'^0, \mu_{s,ec}'^0, \ell)}{G(\rho,\mu_{a,c}^0, \mu_{a,ec}^0 + \Delta\mu_{a,ec}/2, \mu_{s,c}'^0, \mu_{s,ec}'0, \ell)}\right], \tag{3.34}$$

where $\Delta\mu_{a,c}/\mu_{a,c}^0 = \Delta\mu_{a,ec}/\mu_{a,ec}^0 = 10^{-5}$. Alternatively, a Monte Carlo technique [255] can be utilized to evaluate Equations 3.33 and 3.34 for $L_c(\rho)$ and $L_{ec}(\rho)$.

The two-layer partial pathlengths for representative baseline tissue optical properties of the head are plotted as a function of source-detector separation in Figure 3.8. The extra-cerebral

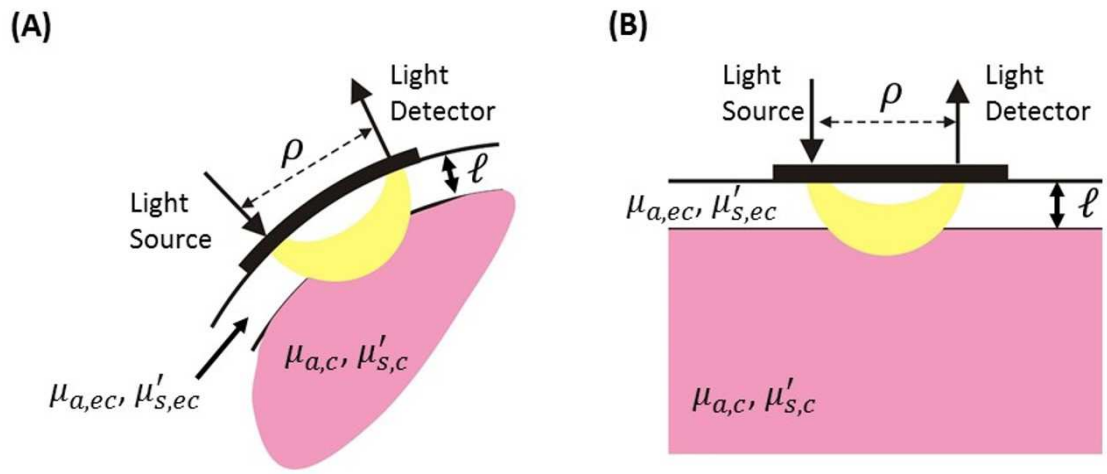

Figure 3.7: **(A)** Two-layer tissue model of the head and **(B)** parallel plane two-layer tissue geometry.

partial pathlength is substantially greater than the cerebral partial pathlength, which confirms that the detected light is weighted towards superficial tissue. Further, the partial pathlengths are significanlty influenced by even small changes in the layer thickness, e.g., $\Delta\ell = 2$ mm (Figure 3.8B).

The two-layer model is useful in many tissues for distinguishing between superficial tissue (e.g., scalp/skull) and the tissue of interest (e.g., brain). However, the problem in general with heterogeneous tissue models is that there are too many unknowns. Even with the two-layer model, the partial pathlength computation requires 5 input parameters (i.e., $\mu^0_{a,c}$, $\mu^0_{a,ec}$, $\mu'^0_{s,c}$, $\mu'^0_{s,ec}$, ℓ) that are potentially unknowns. Heterogeneous models also rely on the "finer features" of the detected signal to distinguish between the different tissue regions, and are consequentially less robust to measurement noise than the homogeneous model is.

In chapter 6, I will discuss how probe pressure modulation and multiple source-detector separations can be utilized to add constraints to the two-layer model, making cerebral absorption monitoring with the two-layer model more tractable.

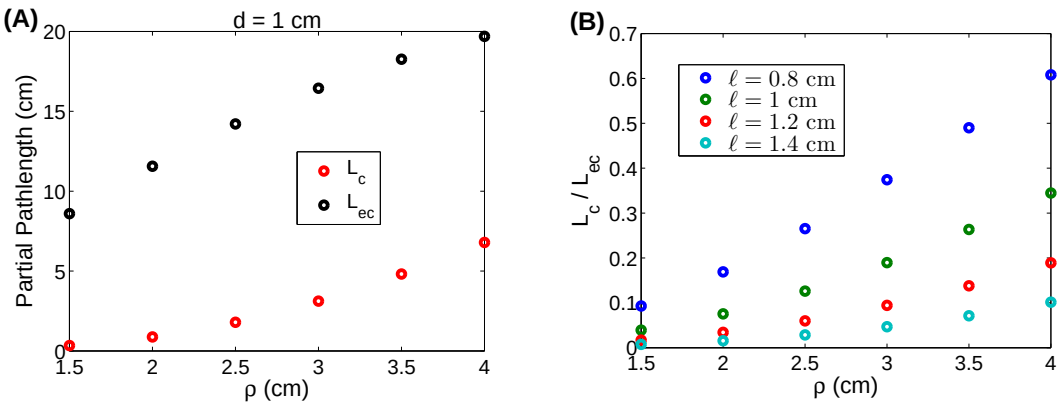

Figure 3.8: **(A)** Computed cerebral (L_c; Equation 3.33) and extra-cerebral (L_{ec}; Equation 3.34) partial pathlengths, plotted as function of source-detector separation, ρ, for a two-layer medium representative of the head [55], i.e., $\mu^0_{a,c} = 0.16$, $\mu^0_{a,ec} = 0.12$, $\mu'^0_{s,c} = 6$, $\mu'^0_{s,ec} = 10$ cm^{-1}, $\ell = 1$ cm, $n = 1.4$, and $R_{eff} = 0.493$. **(B)** The ratio $L_c(\rho)/L_{ec}(\rho)$ is plotted as a function of ρ for different extra-cerebral layer thicknesses, ℓ.

Chapter 4

Diffuse Correlation Spectroscopy (DCS): Correlation Diffusion Approach

4.1 Introduction

Diffuse optical spectroscopy (DOS) (Chapters 2, 3) is a static technique that measures slow (0.1 - 1 s) variations in the detected light intensity (I) induced by changes in tissue absorption (μ_a) and tissue scattering (μ_s'). Diffuse correlation spectroscopy (DCS) is a qualitatively different dynamic light scattering technique that measures the rapid (*e.g.*, microsecond scale fluctuations) speckle light intensity fluctuations induced by red blood cell motion (Figure 4.1) [24, 37, 84]. DCS is a variant of the diffusing wave spectroscopy technique used in condensed matter physics to study particle dynamics [179, 204, 257].

To probe blood flow, DCS uses the same measurement geometry as DOS, wherein NIR light travels diffusively through tissue over a distribution of pathlengths from source to detector. At the detector, the light electric fields from the different pathlengths interfere constructively or destructively to produce a bright or dark spot, or speckle. The motion of red blood cells within the tissue slightly alters these light pathlengths, inducing speckle intensity fluctuations between constructive and destructive interference. Higher blood flows correspond to faster speckle fluctuations.

Quantitatively, these speckle intensity fluctuations are characterized by computing the normalized intensity autocorrelation function, i.e.,

$$g_2(\tau) \equiv \frac{\langle I(t)I(t+\tau)\rangle}{\langle I(t)\rangle^2}, \tag{4.1}$$

at multiple delay-times, τ, where $I(t)$ is the detected light intensity at time t, and the brackets $\langle\rangle$ represent time-averages (for experiments) or ensemble averages (for calculations) [18]. It is straight forward to show that [18]

$$g_2(\tau) = \frac{\langle \delta I(t)\delta I(t+\tau)}{\langle I(t)\rangle^2} + 1, \tag{4.2}$$

where the fluctuation, $\delta I(t) \equiv I(t) - \langle I(t)\rangle$, represents the deviation of the intensity from its average value. At "long delay-times" wherein the intensity fluctuation at time t is not predictive of the fluctuation at time $t+\tau$, $\langle \delta I(t)\delta I(t+\tau)\rangle = \langle \delta I(t)\rangle^2 = 0$, and $g_2(\tau) = 1$. At $\tau = 0$,

$$g_2(0) = \frac{\langle [I(t)]^2\rangle - \langle I(t)\rangle^2}{\langle I(t)\rangle^2} + 1 = 1 + \Lambda^2 = 1 + \beta, \tag{4.3}$$

where $\Lambda \equiv \sigma_I/\langle I\rangle$ is the speckle contrast of the speckle fluctuations, and $\beta \equiv \Lambda^2$. Thus, $g_2(\tau)$ decays from $1+\beta$ to 1 as τ increases. Faster intensity fluctuations, which are associated with higher blood flow, correspond to steeper decays in $g_2(\tau)$ (Figure 4.1C).

For "fully developed" speckle, the speckle contrast is unity, i.e., $g_2(0) = 2$, which indicates that the speckle intensity fluctuations are of the same order as the average intensity (Section 4.2) [112]. However, in practice there are a number of measurement-related factors that can reduce speckle contrast, such as source coherence and experimental collection optics. If the width of the pathlength distribution (i.e., the spread of different pathlengths) is comparable to or exceeds the coherence length of the source, then the speckle contrast is substantially reduced. The phase of the source light needs to remain constant on a length scale comparable to the spread of light pathlengths between source and detector for the detectable interference that underlies a high speckle contrast to exist [100, Section 32-4]. On the detection side of the measurement, the detected signal is typically a sum over independent speckle intensities with the same statistics [168]. For example, these independent speckle intensities can arise from orthogonal polarization states and optical fiber modes. The effect of summing over independent speckle intensities is a reduction in speckle contrast [112, 168] (Section 4.2).

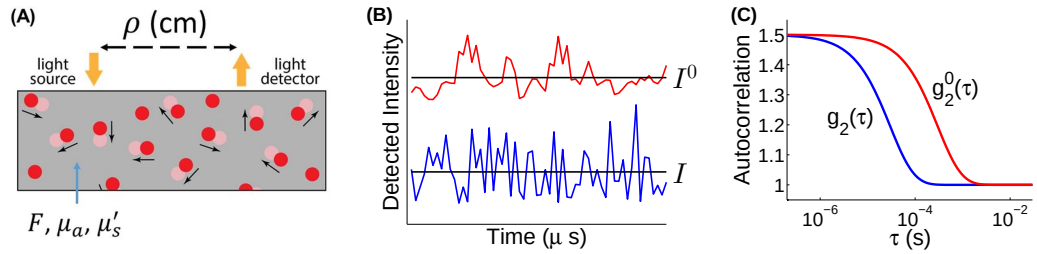

Figure 4.1: **(A)** Schematic for a homogeneous, semi-infinite model of the head with a blood flow index, absorption coefficient, and reduced scattering coefficient of F, μ_a, and μ_s', respectively. The incident continuous wave source intensity, I_s, is assumed to remain constant over time. Blood cell motion (e.g., red disks at time t and light-red disks at time $t+\tau$) induces fast temporal fluctuations (i.e., speckle intensity fluctuations) in the detected light intensity on the time scale of μs, while absorption changes modify mean light intensities (e.g., averaged on time scales of ms or greater). **(B)** Schematic of detected intensity fluctuations for a baseline tissue state (red curve) and a perturbed state from baseline with higher blood flow and absorption (blue curve). The horizontal black lines are the mean intensities for the two states, denoted as I^0 and I. **(C)** The fast speckle intensity fluctuations in the two states are characterized by normalized intensity autocorrelation functions (i.e., $g_2^0(\tau)$, $g_2(\tau)$). The decay of the intensity autocorrelation function curves is related to tissue blood flow.

For DCS, low speckle contrast is bad. The closer β is to zero, the more difficult it is to ascertain blood flow from the decay in $g_2(\tau)$. With no speckle contrast (i.e., $\beta = 0$), there is no decay in the autocorrelation function at all, making it impossible to estimate blood flow. To maximize speckle contrast in the DCS measurement, a high-coherence light source (e.g., coherence length > 5 m) and single-mode fiber detection should be used (Section 4.10). However, since single mode fibers have low numerical apertures and small core diameters, the detected light intensities are quite low at longer source-detector separations (e.g., 3 cm), and the DCS signal suffers from low SNR. Several strategies for improving SNR in the DCS measurement are discussed in Section 4.10.

To quantitatively relate the measurements of $g_2(\tau)$ to blood flow, a correlation diffusion approach (Section 4.5) is employed to calculate the electric field autocorrelation function, i.e., $g_1(\tau) \equiv \langle E^*(t)E(t+\tau)\rangle / \langle I(t)\rangle$ ($I(t) = |E(t)|^2$), as a function of a blood flow index describing the dynamics of red blood cells (F [cm^2/s]) [23, 24, 79]. The blood flow index is ascertained by fitting the calculated $g_1(\tau)$ to the experimentally measured $g_2(\tau)$ using the Siegert relation [168]:

$$g_2(\tau) = 1 + \beta |g_1(\tau)|^2, \tag{4.4}$$

with β defined in Equation 4.3. The Siegert relation is valid if $E(t)$ is a Gaussian variable with zero mean. This is the case for any linear combination of "fully developed" speckle electric fields (Section 4.2) [112]. For DCS measurements of tissue, the Siegert relation is generally a good approximation (Section 4.10).

Although the blood flow index does not have absolute blood flow units, it is directly proportional to tissue blood flow (Section 4.9), and has been successfully validated against a plethora of gold-standard techniques [149, 182]. Further, it is feasible to calibrate DCS for absolute blood flow monitoring with an "initial" measurement of absolute blood flow from another technique such as time-domain measurements of the contrast agent ICG [70].

Two key approximations of light transport make the calculation of $g_1(\tau)$ tractable. The first approximation is the photon diffusion model of light transport (Chapter 2), wherein each path from source to detector involves many scattering events, and the photon directions of light transport are completely randomized. The second approximation uses the phase change from an average scattering event as the phase change for each individual photon scattering event.

4.2 Speckle Statistics

Speckle fluctuations, which appear in a signal that is composed of a large number of independent phasors [112], are fundamental to the DCS measurement of blood flow. For many scattering media, including tissue in the NIR spectral regime, the polarized light electric field at a point in space and time, i.e., $E(\mathbf{r}_d, t)$, is described by a random phasor sum:

$$E(\mathbf{r}_d, t) = \sum_{n=1}^{N} a_n \mathrm{e}^{i\phi_n}. \tag{4.5}$$

Here, $N \gg 1$ is the number of phasor components, and (a_n, ϕ_n) denote the amplitude and phase of the nth phasor in the sum. For "fully developed" speckle fields, the statistics of the phasor components satisfy the following three fundamental assumptions:

- The amplitudes and phases a_n and ϕ_n are statistically independent of a_m and ϕ_m provided $n \neq m$.
- For any n, a_n and ϕ_n are statistically independent of each other.

- The phases ϕ_n are uniformly distributed on the interval $(-\pi, \pi)$, i.e., all values of phase are equally likely.

Recall that two parameters are statistically independent if knowledge of one parameter conveys no knowledge of the other parameter. Equation 4.5 constitutes a random walk in the complex plane, and it is straight forward to show that $E(\mathbf{r}, t)$ is a Gaussian-distributed variable with zero mean [112]. The probability density function for the amplitude of the electric field is therefore given by the Rayleigh distribution [112], i.e.,

$$P_E(|E|) = \frac{|E|}{2\pi\sigma^2} \exp\left[-\frac{|E|^2}{2\sigma^2}\right], \tag{4.6}$$

where $\sigma^2 = \langle a^2 \rangle / 2$.

Dynamic light scattering techniques generally measure the intensity, $I(\mathbf{r}_d, t) = |E(\mathbf{r}_d, t)|^2$, instead of the electric field. The probability density function for the intensity of a fully developed speckle field is the negative exponential distribution [112], i.e.,

$$P_I(I) = \left|\frac{d|E|}{dI}\right| P_E(\sqrt{I}) = \frac{1}{\langle I \rangle} \exp\left(-\frac{I}{\langle I \rangle}\right). \tag{4.7}$$

Thus, a histogram of intensities measured over many time points at the spatial location $\mathbf{r}_d$ is characterized by an exponential distribution[1]. One characteristic of the exponential distribution is that there are many more intensities below the mean ("dark spots") than above the mean ("bright spots"). Another property is that the standard deviation of intensities is equal to the mean, and the speckle contrast is therefore unity. Recall that unity speckle contrast is expected for polarized light detected at one spatial point. In practice, the detected light intensity is typically a sum over multiple independent fully developed speckle intensities, each governed by the same statistics (Equation 4.7).

For example, consider the case of partially polarized light. Here, the detected light intensity is the sum of two independent speckle intensities corresponding to the two orthogonal polarization states, i.e., $I = I_1 + I_2$, which reduces the speckle contrast to [112, 168]

$$\Lambda = \frac{\sqrt{\langle I_1 \rangle^2 + \langle I_2 \rangle^2}}{\langle I_1 \rangle + \langle I_2 \rangle} = \frac{\sqrt{1 + r^2}}{1 + r}, \tag{4.8}$$

[1]The exponential distribution also applies for intensities sampled over many spatial locations at one time point, i.e., an image.

where $r = \langle I_2 \rangle / \langle I_1 \rangle$. For completely unpolarized light, i.e., $r = 1$, $\Lambda = 1/\sqrt{2}$, and the intensity autocorrelation intercept is $\beta = g_2(0) - 1 = 0.5$ (see Equation 4.3).

More generally, if there are N fully developed speckles present in the detected signal, the speckle contrast is [112, 168]

$$\Lambda = \sqrt{\beta} = \frac{\sqrt{\sum_{n=1}^{N} \langle I_n \rangle^2}}{\sum_{n=1}^{N} \langle I_n \rangle}, \tag{4.9}$$

where $\langle I_n \rangle$ is the mean intensity of the nth speckle. For light detection with a multimode fiber that supports M independent modes of light propagation, the number of speckles is $N = M$ for polarized light, and $N = 2M$ for unpolarized light (discussed further in Section 4.10). In the special case wherein the mean speckle light intensities are equal (i.e., $\langle I_n \rangle = I_0$ for all n), then Equation 4.9 simplifies to

$$\Lambda = \sqrt{\beta} = \frac{1}{\sqrt{N}}. \tag{4.10}$$

As a brief digression, for an imaging detection scheme with a lens and CCD camera (Figure 2.14), the spatial size of a speckle, b, is roughly the diffraction-limited spot size on the CCD from the lens, i.e., $b \approx 2.44\lambda/NA$, where λ is the wavelength of light, and NA is the numerical aperture of the lens [112]. The number of speckles detected by a pixel on the CCD is then $N \approx A_{pixel}/[(\pi/4)b^2]$ for polarized light, and $N \approx 2A_{pixel}/[(\pi/4)b^2]$ for unpolarized light. In this detection scheme, Equation 4.9 is still valid.

4.3 Dynamic Light Scattering in the Single-scattering Limit

Before developing the theory of DCS in the high multiple-scattering limit, it is useful to review a simple traditional dynamic light scattering (DLS) (sometimes called quasi-elastic light scattering (QELS)) experiment in the single-scattering limit (Figure 4.2). In the experiment, coherent, polarized light illuminates a dilute sample of scatterers; dilute in the sense that an incident photon is scattered once or not at all as it traverses the sample (see Figure 2.1B for the definition of a scattering event). From the classical electromagnetic wave point of view, each scatterer develops an induced dipole moment in the presence of the incident light given by

$$\mathbf{p} = (\tilde{\chi} \cdot \mathbf{m}_i) E_i(t), \tag{4.11}$$

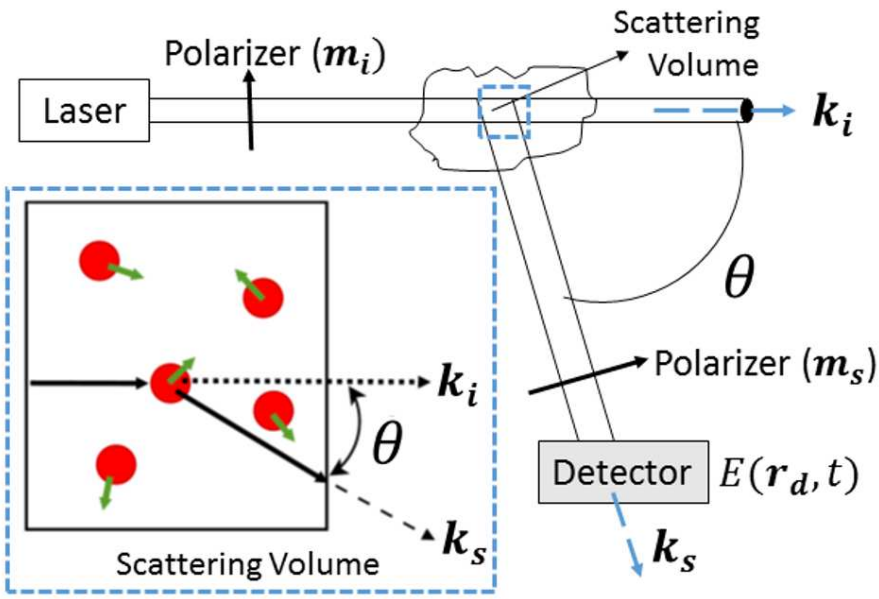

Figure 4.2: Illustration of a single scattering experiment for a dilute solution of N independent scatterers. Light with polarization $\mathbf{m}_i$ and wavevector $\mathbf{k}_i$ is scattered in all directions. The component of the scattered light with polarization $\mathbf{m}_s$ and wavevector $\mathbf{k}_s$, i.e., $E(\mathbf{r}_d, t)$, is detected in the far field. The scattering wavevector, $\mathbf{q} \equiv \mathbf{k}_s - \mathbf{k}_i$, is proportional to the momentum transferred from the incident light to the detected light. For elastic scattering, $|\mathbf{q}| = 2|\mathbf{k}_i| \sin(\theta/2)$.

where $\tilde{\chi}$ is the polarizability tensor of the scatterer [116]. The oscillating dipole moment in the scatterer, in turn, emits scattered light in all directions, which at the detector is given by [206, Chapter 15]

$$E_s(\mathbf{r}_d, t) = \frac{\mu_0 |E_i|}{4\pi |\mathbf{r}_d - \mathbf{r}_j(t)|} \omega^2 \chi_{is}(t) \mathrm{e}^{-i\mathbf{q}\cdot\mathbf{r}_j(t)} \mathrm{e}^{i(\mathbf{k}_s \cdot \mathbf{r}_d - \omega t)}. \tag{4.12}$$

Here, $\mathbf{r}_d$ is the detector position, $\mathbf{r}_j$ is the position of the jth scatterer, $\chi_{is} \equiv \mathbf{m}_s \cdot \tilde{\chi} \cdot \mathbf{m}_i$, and $\mathbf{q} \equiv \mathbf{k}_s - \mathbf{k}_i$ (Figure 4.2). The term $\mathrm{e}^{-i\mathbf{q}\cdot\mathbf{r}_j(t)}$ varies in time because of translation, while the term $\chi_{is}(t)$ varies in time because of rotation or vibration.

In the single-scattering limit, only the incident light interacts with the scatterers, and therefore, the total light electric field at the detector is the superposition of the dipole contribution from each scatterer (i.e., Equation 4.12). Therefore, in the far field limit,

$$E(\mathbf{r}_d, t) \propto \sum_{j=1}^{N(t)} \chi_{is}(t) \exp[-i\mathbf{q} \cdot \mathbf{r}_j(t)], \tag{4.13}$$

where $N(t)$ is the number of scatterers within the scattering volume at time t. Notice that if $N \gg 1$ and the scatterer positions are independent, Equation 4.13 is a random phasor sum

that describes speckle fluctuations (Section 4.2). The electric field autocorrelation function of Equation 4.13 is related to the scatterer displacements, $\Delta\mathbf{r}(\tau) = \mathbf{r}_j(t+\tau) - \mathbf{r}_j(t)$, via [18, Chapter 5]

$$g_1(\tau) \equiv \frac{\langle E^*(t)E(t+\tau)\rangle}{\langle I\rangle} = \langle \exp[i\mathbf{q}\cdot\Delta\mathbf{r}(\tau)]\rangle, \tag{4.14}$$

provided the scatterers satisfy the following two assumptions:

1. The scatterer size is small compared to the light wavelength, λ,

2. The scatterer positions, $\{\mathbf{r}_j\}$, are statistically independent.

Assumption two is usually valid in dilute liquid solutions wherein scatterers rarely encounter each other, but violated in solids wherein the scatterers are fixed in placed. Assumption one ensures that the decay of $g_1(\tau)$ is only due to translational motion (i.e., χ_{is} does not depend on time). This assumption is discussed further in Section 4.3.4.

Again, recall that the $\langle\rangle$ brackets in Equation 4.14 indicate an ensemble average for the calculation of $g_1(\tau)$, i.e.,

$$g_1(\tau) = \int P(\Delta\mathbf{r}(\tau))\exp[i\mathbf{q}\cdot\Delta\mathbf{r}(\tau)]\mathrm{d}^3(\Delta r), \tag{4.15}$$

where the integration limits are from $-\infty$ to ∞ in all dimensions, and $P(\Delta\mathbf{r}(\tau))$ is the probability density function for a particle to travel a distance of $\Delta\mathbf{r}$ in time τ. Calculation of $g_1(\tau)$ thus requires knowledge of $P(\Delta\mathbf{r}(\tau))$.

4.3.1 Brownian Motion

A very important and common type of particle motion is Brownian motion. The underlying equation describing Brownian motion is the Langevin equation [49, 50], i.e.,

$$\frac{\mathrm{d}\mathbf{u}}{\mathrm{d}t} = -\gamma\mathbf{u} + \mathbf{F}(t). \tag{4.16}$$

Here, $\mathbf{u}$ is the velocity of the particle, γ [s^{-1}] is the frictional drag coefficient of the particle moving through the medium divided by the particle's mass [17], and $\mathbf{F}(t)$ is a stochastic term accounting for collisions between the Brownian particle and molecules in the surrounding fluid (e.g., water molecules). The key assumptions of Brownian motion are (1), $\mathbf{F}(t)$ is independent

of $\mathbf{u}$, and (2), $\mathbf{F}(t)$ varies extremely rapidly compared with $\mathbf{u}$ [49, 50]. Physically, the second assumption means that there exist time intervals, Δt, during which the Brownian particle velocity changes inifinitesimally while the particle experiences a very large number of collisions with molecules of the surrounding fluid.

On time scales $t \gg \gamma^{-1}$, the probability distribution for the Brownian particle's displacement, which can be derived from Equation 4.16, is Gaussian [49, 50], i.e.,

$$P(\Delta\mathbf{r}(t)) = \frac{1}{(4\pi D_b t)^{3/2}} \exp\left[-\frac{|\Delta\mathbf{r}(t)|^2}{4D_b t}\right]. \tag{4.17}$$

Here, the Brownian particle's diffusion coefficient, D_b, is [17, 49, 50] (see Equation 2.45)

$$D_b = \frac{v_b \ell_p}{3(1 - \langle\cos\vartheta\rangle)}, \tag{4.18}$$

where v_b is the constant speed of the Brownian particle along a straight-line trajectory (or run), ℓ_p is the mean run length (i.e., mean distance traveled between direction changes), and $\langle\cos\vartheta\rangle$ is the average of the cosine of the angle between successive runs.

Substituting Equation 4.17 into Equation 4.15, we obtain

$$g_1(\tau) = \exp\left[-\frac{1}{6}q^2\langle|\Delta\mathbf{r}(\tau)|^2\rangle\right]. \tag{4.19}$$

The particle mean-squared displacement is also determined from Equation 4.17:

$$\langle|\Delta\mathbf{r}(\tau)|^2\rangle = \int |\Delta\mathbf{r}(\tau)|^2 P(\Delta\mathbf{r})\mathrm{d}^3\Delta r = 6D_b\tau. \tag{4.20}$$

Thus, in the single-scattering limit for Brownian motion, the electric-field autocorrelation function is

$$g_1(\tau) = \exp[-q^2 D_b \tau]. \tag{4.21}$$

Since the particle positions are independent, and the number of particles in the scattering volume is assumed to be much greater than one, the detected electric field (Equation 4.13) is a fully developed speckle field, and the Siegert relation (Equation 4.4) is valid. Thus, the measured intensity auto-correlation function for Brownian motion is

$$g_2(\tau) = 1 + \beta\exp[-2q^2 D_b \tau]. \tag{4.22}$$

4.3.2 Brownian Motion with Drift

If Brownian particles are exposed to a constant external force (e.g., gravity, pressure gradiant, centrifugal), the particles still diffuse similarly to how they would in the absence of the external force, but with a small persistent directional bias [17]. This motion is Brownian motion with drift (or diffusion with drift). The extension of the Langevin equation (Equation 4.16) to include an external force, $\mathbf{F}_{ext}$, is

$$\frac{\mathrm{d}\mathbf{u}}{\mathrm{d}t} = -\gamma\mathbf{u} + \mathbf{F}(t) + \frac{\mathbf{F}_{ext}}{m}, \tag{4.23}$$

where m is the particle's mass. On the same time scale $t \gg \gamma^{-1}$, the probability distribution for Brownian particle displacement derived from Equation 4.23 is [49]

$$P(\Delta\mathbf{r}(t)) = \frac{1}{(4\pi D_b t)^{3/2}} \exp\left[-\frac{|\Delta\mathbf{r}(t) - \mathbf{v}_d t|^2}{4D_b t}\right]. \tag{4.24}$$

Here, $\mathbf{v}_d$ is the terminal drift velocity obtained from the external force, i.e., $\mathbf{v}_d = \mathbf{F}_{ext}/(m\gamma)$.

Substituting Equation 4.24 into Equation 4.15, the electric field autocorrelation function for diffusion with drift is

$$g_1(\tau) = \exp(i\mathbf{q}\cdot\mathbf{v}_d\tau)\exp(-q^2 D_b\tau), \tag{4.25}$$

and the corresponding intensity autocorrelation function is (Equation 4.4)

$$g_2(\tau) = 1 + \beta\exp[-2q^2 D_b\tau] \tag{4.26}$$

Equations 4.26 and 4.22 are identical, indicating that the measured intensity autocorrelation function cannot distinguish between isotropic Brownian motion and Brownian motion with drift. This is also true for the high multiple-scattering limit. Importantly, the measured DCS/DLS signal is only sensitive to the relative motions between scattering particles. Uniform motion that is present in all of the scattering particles is not detected.

4.3.3 Random Flow

Random flow is the opposite of Brownian motion in the sense that it applies to very dilute solutions (e.g., ideal gas) with scattering particles that seldom experience collisions. In this case, the scattering particles move ballistically with velocity $\mathbf{u}$ between collisions. For a ballistic process,

$\Delta r_j(t) = \mathbf{u}_j t$. Ideal gases are accurately modeled with the Maxwell-Boltzmann distribution, such that the distribution function for random flow displacement is

$$P(\Delta\mathbf{r}) = t\left[\frac{m}{2\pi k_B T}\right]^{3/2} \exp\left(-\frac{m|\Delta\mathbf{r}(t)|^2}{2k_B T t^2}\right), \tag{4.27}$$

where T is the temperature, m is the particle mass, and k_B is Boltzmann's constant. Substitution of Equation 4.27 into Equation 4.15, we obtain

$$g_1(\tau) = \exp\left[-\frac{1}{6}q^2\langle|\Delta\mathbf{r}(\tau)|^2\rangle\right] = \exp\left[-\frac{1}{6}q^2\langle u^2\rangle\tau^2\right]. \tag{4.28}$$

Here, $\langle u^2\rangle = 3k_B T/m$ is the mean square velocity of the moving particles.

Of course, on small enough time scales, all motion is ballistic. DLS probes particle motion, though, on the length scale of q^{-1}. Looking at Equations 4.28 and 4.19, it is evident that significant decays in $g_1(\tau)$ occur on a particle displacement ($\Delta\mathbf{r}$) length scale of q^{-1}. Thus, if the mean free path between collisions is long compared to q^{-1}, then the measured particle dynamics are ballistic. Conversely, if the mean free path between collisions is short compared to q^{-1}, then the measured particle dynamics are Brownian.

4.3.4 Large Particle Scattering

Equation 4.14 assumes that the scatterer size is small compared to the wavelength. However, red blood cells, with a typical size of roughly 10 um, are substantially bigger than the wavelength. For this regime, Equation 4.13 is [18, Chapter 8]

$$E(\mathbf{r}_d, t) \propto \sum_{j=1}^{N} \Psi_j(\mathbf{q}, t)\exp[-i\mathbf{q}\cdot\mathbf{R}_j(t)], \tag{4.29}$$

where $\mathbf{R}_j(t)$ is the particle center of mass, and $\Psi_j(\mathbf{q}, t)$ is a particle form factor, i.e.,

$$\Psi_j(\mathbf{q}, t) = \int \chi_{is}(\mathbf{r}_{rel}, t)\mathrm{e}^{i\mathbf{q}\cdot\mathbf{r}_{rel}}\mathrm{d}^3 r_{rel}. \tag{4.30}$$

Here, the integral is over the particle volume, and $\mathbf{r}_{rel} \equiv \mathbf{r} - \mathbf{R}_k$ is a position in the particle relative to the center of mass. The origin of the time-dependence in χ_{is} is particle rotation and particle morphology changes. For rigid spheres, the rotational symmetry ensures that the form

factor is time-independent, and the electric field autocorrelation function is determined from the translational motion of the spheres:

$$g_1(\tau) = \langle \exp[i\mathbf{q} \cdot \Delta\mathbf{R}(t)\rangle. \tag{4.31}$$

However, many particles, including red blood cells, are not rigid spheres. If significant rotational and morphologial motion occurs over the length scale of q^{-1}, then the changes in atomic form factor from these motions will significantly affect $g_1(\tau)$. For elastic scattering, $q = 2k_i \sin(\theta/2)$ (see Figure 4.2) and the length scale q^{-1} is approximately the light wavelength λ. Therefore, for $\lambda = 785$ nm, $q^{-1} \approx 0.1$ micron. If rotational and/or morphological changes are minimal over this length scale, then Equation 4.31 is a good approximation for large particle motions, and the results derived above for small scatterer size remain applicable.

4.4 Static and Dynamic Light Scattering in Tissue

In tissues, some scatterers are static (or very slowly moving) and some scatterers move (e.g., red blood cells). Photon scattering from static tissue elements (Figure 4.3A) does not contribute to the decay of $g_1(\tau)$, but photon scattering from dynamically moving tissue elements (Figure 4.3B, C) does. In tissue, red blood cells are usually the predominant dynamic light scatterers[2] [30, 79, 190].

The tissue blood volume is typically a small fraction ($< 4\%$) of the tissue volume, and red blood cells account for only a small fraction of tissue scattering [30]. Thus, the scattering cross section for static elements in the tissue is much greater than that for moving red blood cells, which in turn means that the vast majority of scattering in tissue is static (type A; corresponds to Figure 4.3A). However, on their journey from source to detector, photons will encounter red blood cells, and these encounters are dynamic scatttering events (type B; corresponds to Figure 4.3B).

A typical photon path through tissue consists of many static scattering steps prior to encountering a red blood cell (e.g., in a capillary), and then many more static scattering steps prior to encountering another red blood cell (e.g., in another capillary), and so on. Mathematically,

[2] A notable exception is in exercising muscle, wherein the motion of muscle fibers has a big effect on the $g_1(\tau)$ decay [226].

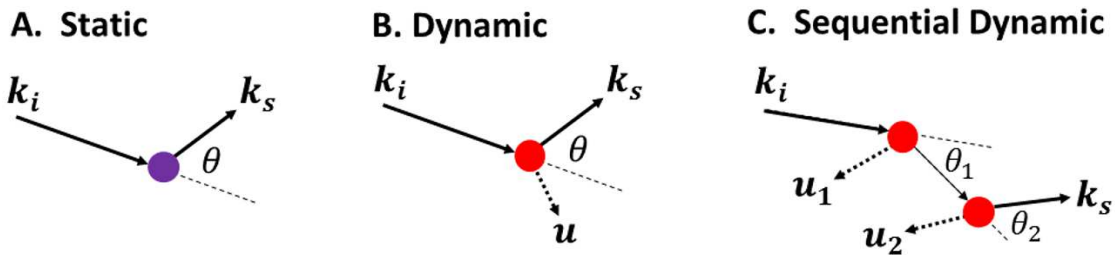

Figure 4.3: Photon scattering within tissue can be represented as a series of scattering steps of types A, B, or C. $\mathbf{k}_i$ and $\mathbf{k}_s$ are the incident and scattered light wavevectors, and $\mathbf{u}$ denotes the velocity of moving scatterers (red circles), which are assumed to be red blood cells.

this path is written as $(A, A, \ldots, A, B, A, \ldots, A, B, A, \ldots)$, which means that there are many static scattering steps between each dynamic scattering event. Here, the red blood cells (RBC) contributing to the decay of $g_1(\tau)$ are independent particles.

It is also possible for photons to sequentially scatter off moving red blood cells (Figure 4.3C), which mainly occurs within larger vessels (> 50 microns) [30]. Mathematically, this type of scattering is $(A, A, \ldots, A, B, B, A, \ldots)$ or $(A, A, \ldots, A, B, B, B, A, \ldots)$, etc. A key assumption for deriving the multiply scattered light electric field autocorrelation function is scatterer independence (Section 4.5). Moving red blood cells within the same vessel, though, may not be independent.

Carp *et. al.* argued that the majority of photon-RBC interactions occur in larger vessels wherein sequential RBC scattering is likely, because the majority of the tissue blood volume ($\sim 70\%$) is contained in these larger vessels [44]. However, as I discussed in Section 2.13, light that propagates inside large vessels is preferentially absorbed because of the high light absorption in blood. Then, the photons that are actually detected preferentially only encounter small vessels. The contributions to the decay of $g_1(\tau)$ as a function of vessel size is not well understood, and is an interesting problem for future work.

4.5 Dynamic Light Scattering in the High Multiple-scattering Limit (Diffuse Correlation Spectroscopy)

I will now derive the electric field autocorrelation function in the high multiple-scattering limit (i.e., correlation diffusion limit) [23, 24, 179, 204, 257]. The starting point is to consider a single photon passing through tissue from source to detector that scatters N times along an arbitrary light path p (Figure 4.4). The total pathlength of this photon is

$$s_p = \sum_{j=0}^{N} |\mathbf{r}_{j=1} - \mathbf{r}_j| = \sum_{j=0}^{N} \left(\frac{\mathbf{k}_j}{|\mathbf{k}_j|} \right) \cdot (\mathbf{r}_{j+1} - \mathbf{r}_j), \tag{4.32}$$

where $\mathbf{k}_j$ is the wavevector of the light after j scattering events, $\mathbf{r}_j$ is the position of scatterer j at time t for $j \leq 1 \leq N$, $\mathbf{r}_0 = \mathbf{r}_s$ is the light source position, and $\mathbf{r}_{N+1} = \mathbf{r}_d$ is the detector position. The light scattering is assumed to be quasi-elastic, which means that all wavevectors have the same magnitude ($|\mathbf{k}_j| = \kappa_\circ = 2\pi n/\lambda$, for all j). Therefore, the total phase shift, $\phi_p(t)$, acquired by the photon after traveling from the source to the detector along path p is

$$\phi_p(t) = \kappa_\circ s_p(t) = \sum_{j=0}^{N} \mathbf{k}_j(t) \cdot [\mathbf{r}_{j+1}(t) - \mathbf{r}_j(t)]. \tag{4.33}$$

Further, the contribution to the polarized detected electric field from this light path is $E_p \mathrm{e}^{i\phi(t)}$, where E_p is the amplitude of the field from path p at the detector. The field amplitude depends primarily on the optical absorption and scattering coefficients of the medium. In tissue, these optical properties change on a much slower time scale than the phase fluctuations. Thus, E_p is temporally constant, and it is the phase fluctuations that induce the speckle fluctuations.

The total polarized detected electric field is the sum of $E_p \mathrm{e}^{i\phi(t)}$ over all light paths from source to detector, i.e.,

$$E(t) = \sum_p E_p \mathrm{e}^{i\phi_p(t)}. \tag{4.34}$$

Equation 4.34 represents a fully developed speckle field if the following assumptions are satisfied (see Section 4.2):

- E_p and ϕ_p are statistically independent of $E_{p'}$ and $\phi_{p'}$ for $p \neq p'$,
- For any light path p, E_p and ϕ_p are statistically independent of each other,

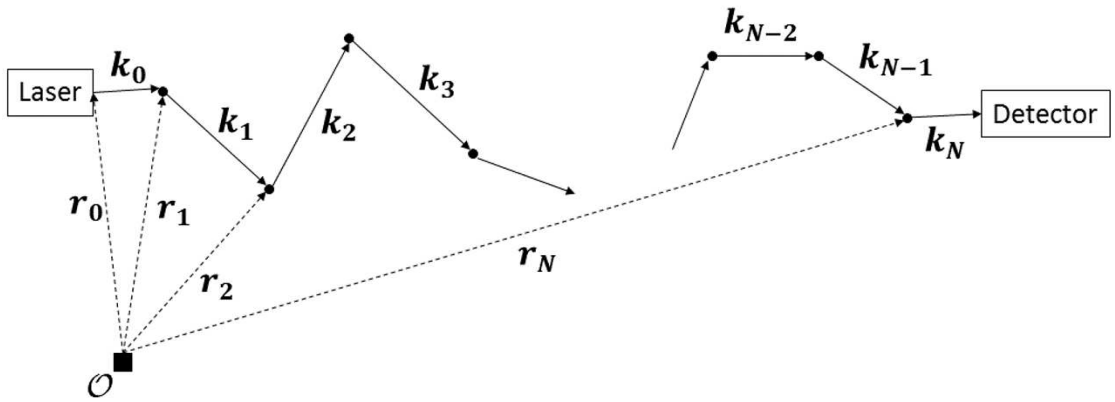

Figure 4.4: A single light path p from source to detector in a turbid medium. The scattering is quasi-elastic, such that the magnitudes of the wavevectors $\{\mathbf{k}_j\}$ are the same. Further, $\mathbf{k}_j$ points in the propagation direction for light scattered from the jth particle, and $\mathbf{r}_j$ is the position of the jth particle.

- The phases ϕ_p are uniformly distributed on the interval $(-\pi, \pi)$.

All three of these assumptions are valid if (1), the dynamic scatterers are independent, and (2), the contribution to $E(t)$ from photons that have only experienced static scattering on their path from source to detector is negligible [14, 168]. Since $g_1(\tau)$ does not decay from static scattering, the physical meaning of point two is that the field autocorrelation function $g_1(\tau)$ fully decays to zero over a time scale much shorter than the duration of the measurement [14]. From scatterer independence, Equation 4.34 can be interpreted as a random walk in the complex plane. If $g_1(\tau)$ fully decays to zero over a shorter time scale than the measurement duration, then many random walks will be sampled, and the distribution of $E(t)$ over the time course of the measurement is Gaussian with zero mean. For tissue, this means that the red blood cells contributing to the decay of $g_1(\tau)$ are independent, and that all photons in the detected signal have interacted at least once with a red blood cell.

The electric field autocorrelation function of Equation 4.34 is

$$g_1(\tau) \equiv \frac{\langle E^*(t)E(t+\tau)\rangle}{\langle I\rangle} = \frac{1}{\langle I\rangle}\left\langle \left(\sum_p E_p \mathrm{e}^{-i\phi_p(t)}\right)\left(\sum_{p'} E^*_{p'} \mathrm{e}^{i\phi_{p'}(t+\tau)}\right)\right\rangle, \tag{4.35}$$

where $\langle I\rangle$ is the average detected intensity. From the speckle field assumptions, terms with $p \neq p'$ do not contribute, i.e.,

$$\langle E^*_p E_{p'} \mathrm{e}^{-i\phi_p(t)} \mathrm{e}^{i\phi_{p'}(t+\tau)}\rangle = \langle E^*_p\rangle\langle E_{p'}\rangle\langle e^{-i\phi_p(t)}\rangle\langle e^{i\phi_{p'}(t+\tau)}\rangle = 0. \tag{4.36}$$

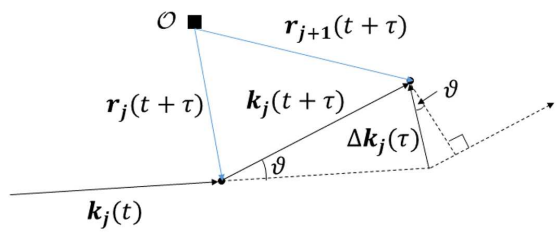

Figure 4.5: Since $\mathbf{k}_j(t+\tau)$ is in the same direction as $[\mathbf{r}_{j+1}(t+\tau)-\mathbf{r}_j(t)]$, $\Delta\mathbf{k}_j(\tau)\cdot[\mathbf{r}_{j+1}(t+\tau)-\mathbf{r}_j(t)] \propto \sin\vartheta$. To leading order, $\sin\vartheta \approx 0$, and the second term in Equation 4.38 is negligible compared to the first term.

Thus, Equation 4.35 simplifies to

$$\begin{aligned} g_1(\tau) &= \left\langle \sum_p \frac{|E_p|^2}{\langle I\rangle} \mathrm{e}^{-i[\phi_p(t)-\phi_p(t+\tau)]} \right\rangle \\ &= \sum_p \frac{\langle I_p\rangle}{\langle I\rangle} \langle \mathrm{e}^{i\Delta\phi_p(\tau)}\rangle, \end{aligned} \tag{4.37}$$

where $\langle I_p\rangle \equiv \langle |E_p|^2\rangle$ is the average intensity from path p, and $\Delta\phi_p(\tau) \equiv \phi_p(t+\tau)-\phi_p(t)$. Defining $\mathbf{q}_j \equiv \mathbf{k}_j(t)-\mathbf{k}_{j-1}(t)$ and $\Delta\mathbf{k}_j(\tau) \equiv \mathbf{k}_j(t+\tau)-\mathbf{k}_j(t)$, we obtain from Equation 4.33 that

$$\Delta\phi_p(\tau) = \sum_{j=1}^{N} \mathbf{q}_j \cdot \Delta\mathbf{r}_j(\tau) + \sum_{j=0}^{N} \Delta\mathbf{k}_j(\tau)\cdot[\mathbf{r}_{j+1}(t+\tau)-\mathbf{r}_j(t+\tau)], \tag{4.38}$$

where $\Delta\mathbf{r}_j(\tau) \equiv \mathbf{r}_j(t+\tau)-\mathbf{r}_j(t)$ is the scatterer displacement in time τ.

Notice that since $[\mathbf{r}_{j+1}(t+\tau)-\mathbf{r}_j(t+\tau)]$ is in the same direction as $\mathbf{k}_j(t+\tau)$ (Figure 4.4),

$$\Delta\mathbf{k}_j(\tau)\cdot[\mathbf{r}_{j+1}(t+\tau)-\mathbf{r}_j(t+\tau)] \propto \sin\vartheta, \tag{4.39}$$

where ϑ is the angle between $\mathbf{k}_i(t+\tau)$ and $\mathbf{k}_i(t)$ (Figure 4.5). For the time scales associated with the decay of $g_1(\tau)$, the angle ϑ is small, and to leading order, $\sin\vartheta \approx 0$. Thus, neglecting the second sum in Equation 4.38, we obtain

$$\Delta\phi_p(\tau) = \sum_{j=1}^{N} \mathbf{q}_j \cdot \Delta\mathbf{r}_j(\tau). \tag{4.40}$$

Along a given light path in tissue, both static scattering and dynamic scattering occurs (Section 4.4). Let N_s and $N_d = N - N_s$ denote the number of static scattering events and number of dynamic scattering events, respectively. Since $\Delta\mathbf{r}_j(\tau) = 0$ for static scattering events, they

will not contribute to the sum in Equation 4.41, i.e.,

$$\Delta\phi_p(\tau) = \sum_{j=1}^{N_d} \mathbf{q}_j \cdot \Delta\mathbf{r}_j(\tau). \tag{4.41}$$

From the central limit theorem, $\Delta\phi_p(\tau)$ is a random Gaussian variable because it is a sum of N_d independent random variables wherein N_d is assumed to be large (Equation 4.41). For the special case of isotropic particle dynamics[3], $\langle\Delta\phi_p(\tau)\rangle = 0$, and

$$\langle \mathrm{e}^{i\Delta\phi_p(\tau)}\rangle = \frac{1}{\sqrt{2\pi\langle\Delta\phi_p^2(\tau)\rangle}} \int_{-\infty}^{\infty} \mathrm{e}^{i\Delta\phi_p(\tau)} \exp\left[-\frac{\Delta\phi_p^2(\tau)}{2\langle\Delta\phi_p^2(\tau)\rangle}\right] \mathrm{d}(\Delta\phi_p) = \mathrm{e}^{-\langle\Delta\phi_p^2(\tau)\rangle/2}. \tag{4.42}$$

Taking the ensemble average of the square of Equation 4.41, we obtain

$$\langle\Delta\phi_p^2(\tau)\rangle = \sum_{i=1}^{N_d}\sum_{j=1}^{N_d}\langle[\mathbf{q}_i \cdot \Delta\mathbf{r}_i(\tau)][\mathbf{q}_j \cdot \Delta\mathbf{r}_j(\tau)]\rangle = \sum_{j=1}^{N_d}\langle[\mathbf{q}_j \cdot \Delta\mathbf{r}_j(\tau)]^2\rangle, \tag{4.43}$$

where again, the latter equality is true because of scatterer independence. Additionally, the scattering vector $\mathbf{q}_j$ and displacement vector $\Delta\mathbf{r}_j(\tau)$ are assumed to be independent, and for isotropic dynamics, $\langle\Delta x^2\rangle = \langle\Delta y^2\rangle = \langle\Delta z^2\rangle = \langle\Delta r^2\rangle/3$, where $\langle\Delta r^2\rangle$ is the magnitude of the mean-square dynamic scatterer (e.g., red blood cell) displacement. Therefore,

$$\begin{aligned}\langle\Delta\phi_p^2(\tau)\rangle &= \sum_{j=1}^{N_d}\langle[\mathbf{q}_j \cdot \Delta\mathbf{r}_j(\tau)]^2\rangle \\ &= N_d\langle[\mathbf{q}_j \cdot \Delta\mathbf{r}_j(\tau)]^2\rangle \\ &= \frac{\alpha N}{3}\langle q^2\rangle\langle\Delta r^2(\tau)\rangle,\end{aligned} \tag{4.44}$$

where $\alpha \equiv N_d/N$ is the fraction of photon scattering events that occur from moving particles in the medium (e.g., red blood cells).

For quasi-elastic light scattering,

$$\langle q^2\rangle = \langle[2\kappa_\circ \sin(\vartheta/2)]^2\rangle = 2\kappa_\circ^2(1 - \langle\cos\vartheta\rangle) = 2\kappa_\circ^2\ell_s\mu_s', \tag{4.45}$$

where ϑ is the scattering angle (Figure 4.5), μ_s' is the reduced scattering coefficient (Equation 2.44), ℓ_s is the scattering length (i.e., mean photon distance traveled between scattering

[3]Deterministic motion is briefly discussed in Section 4.7

events), and $\kappa_\circ = 2\pi n/\lambda$ is the magnitude of the light wavevectors propagating through the medium. Substituting Equation 4.45 into Equation 4.44 and noting that $N = s/\ell_s$ for large N, we obtain

$$\langle \Delta\phi_p^2(\tau)\rangle = \frac{\alpha}{3}\frac{s}{\ell_s}2\kappa_\circ^2\ell_s\mu_s'\langle\Delta r^2(\tau)\rangle = \frac{2\alpha}{3}\kappa_\circ^2\langle\Delta r^2(\tau)\rangle\mu_s' s. \tag{4.46}$$

Importantly, $\langle \Delta\phi_p^2(\tau)\rangle$ does not depend on any other path-dependent property besides the path-length s. Consequentially, the sum over paths in Equation 4.37 can be recast as a sum over pathlengths. In the sum over pathlengths, $\langle I_p\rangle/\langle I\rangle$ is replaced by the pathlength distribution function $P(s)$, which is the fraction of the detected scattered light intensity in paths of length s. Recasting Equation 4.37 this way and combining it with Equations 4.46 and 4.42, we find that the electric field autocorrelation function in the high multiple-scattering limit is

$$g_1(\tau) = \sum_s P(s)\exp\left(-\frac{\alpha}{3}\kappa_\circ^2\langle\Delta r^2(\tau)\rangle\mu_s' s\right). \tag{4.47}$$

In the continuum limit, Equation 4.47 becomes

$$g_1(\tau) = \int_0^\infty P(s)\exp\left(-\frac{\alpha}{3}\kappa_\circ^2\langle\Delta r^2(\tau)\rangle\mu_s' s\right)\mathrm{d}s, \tag{4.48}$$

where $P(s)$ can be calculated from the photon diffusion model of light transport (Section 4.5.1). Equation 4.48 assumes that the decay of $g_1(\tau)$ is dominated by translational motion from red blood cells. Rotational and morphological internal motion in red blood cells can contribute to the decay of $g_1(\tau)$ (Section 4.3.4), but this type of motion is not accounted for in Equation 4.48.

The DCS autocorrelation function measured in tissue decays on the order of 100 μs (e.g., Figure 4.6). Therefore, in addition to assuming scatterer independence, isotropic dynamics, and that $N_d \gg 1$ for all photon paths from source to detector, Equation 4.48 assumes that blood cell morphology remains constant and that rotation is negligible on time scales of ~ 100 μs. Finally, the blood cell dynamics are assumed to remain in equilibrium over the time scale of the measurement (ms to seconds).

Importantly, the autocorrelation function decay times associated with long light paths are relatively short, while the decay times associated with short light paths are relatively long [186, 221, 257]. This is due to the factor $\mu_s' s$ in the exponent in Equation 4.48. At short delay-times, the small particle displacement $\langle\Delta r^2(\tau)\rangle$ is obviously amplified more by $\mu_s' s$ at long light paths than short light paths, and thus the long light paths contribute more to the exponential decay at

short τ. Consequentially, the DCS autocorrelation measurement at shorter τ in the remission geometry (Figure 4.1A) is inherently more sensitive to deeper tissue depths [12, 221].

Since Equation 4.34 is a fully developed speckle field (i.e., a Gaussian variable with zero mean), the Siegert relation (Equation 4.4) can be employed to convert $g_1(\tau)$ (Equation 4.48) to the intensity autocorrelation function, $g_2(\tau)$ (Equation 4.1).

4.5.1 Calculation of $g_1(\tau)$

The calculation of $g_1(\tau)$ given by Equation 4.48 is greatly facilitated through utilizing the photon diffusion model. Recall that the photon diffusion equation for a point source is (Equation 2.46)

$$D\nabla^2\Phi(\mathbf{r},t) - v\mu_a\Phi(\mathbf{r},t) - \frac{\partial}{\partial t}\Phi(\mathbf{r},t) = -vS_0'\delta(\mathbf{r})\delta(t), \tag{4.49}$$

and that the photon fluence rate, $\Phi(\mathbf{r},t)$, is proportional to the "time of flight" distribution function $\xi(t)$, i.e., $\xi(t)\mathrm{d}t$ is the probability for a photon to reach position $\mathbf{r}$ at time t (see Section 2.12.2). Analogously, the pathlength distribution function $P(s)$ is directly proportional to the photon fluence rate as a function of light pathlength, i.e., $\tilde{\Phi}(\mathbf{r},s) = \Phi(\mathbf{r},s/v)$. Explicitly,

$$P(s) = \tilde{\Phi}(\mathbf{r},s)/\int_0^\infty \tilde{\Phi}(\mathbf{r},s)\mathrm{d}s, \tag{4.50}$$

and the field autocorrelation function (Equation 4.48) is in turn

$$g_1(\mathbf{r},\tau) = \frac{\int_0^\infty \tilde{\Phi}(\mathbf{r},s)\mathrm{e}^{-\nu s}\mathrm{d}s}{\int_0^\infty \tilde{\Phi}(\mathbf{r},s)\mathrm{d}s}, \tag{4.51}$$

where $\nu \equiv \alpha\mu_s'\kappa_\circ^2\langle\Delta r^2(\tau)\rangle/3$.

Note that the diffusion equation describing $\tilde{\Phi}(\mathbf{r},s)$ is easily obtained from introducing the change of variables $t = s/v$ into Equation 4.49:

$$D\nabla^2\tilde{\Phi}(\mathbf{r},s) - v\mu_a\tilde{\Phi}(\mathbf{r},s) - v\frac{\partial}{\partial s}\tilde{\Phi}(\mathbf{r},s) = -vS_0'\delta(\mathbf{r})\delta(s/v). \tag{4.52}$$

Therefore, one approach for determining $g_1(\mathbf{r},\tau)$ is to substitute the solution of Equation 4.52 (for the appropriate geometry) into Equation 4.51. Another, more versatile approach is the correlation diffusion approach described in the next section.

4.6 Homogeneous Correlation Diffusion Equation

The correlation diffusion equation formally models $G_1(\mathbf{r},\tau) \equiv \langle E^*(\mathbf{r},t)E(\mathbf{r},t+\tau)\rangle$ [W cm^{-2}], which is the so-called unnormalized electric field autocorrelation function. By definition, the normalized field autocorrelation function is

$$g_1(\mathbf{r},\tau) \equiv G_1(\mathbf{r},\tau)/G_1(\mathbf{r},\tau=0). \tag{4.53}$$

Comparing Equation 4.53 with Equation 4.51, it is evident that

$$G_1(\mathbf{r},\tau) = \frac{1}{h}\int_0^\infty \tilde{\phi}(\mathbf{r},s)\mathrm{e}^{-\nu s}\mathrm{d}s, \tag{4.54}$$

where h [cm] is a proportionality constant.

The homogeneous correlation diffusion equation is the Laplace transform of Equation 4.52, i.e.,

$$\begin{aligned}\int_0^\infty (D\nabla^2 - v\mu_a)\tilde{\Phi}(\mathbf{r},s)\mathrm{e}^{-\nu s}\mathrm{d}s - v\int_0^\infty \left(\frac{\partial}{\partial s}\tilde{\Phi}(\mathbf{r},s)\right)\mathrm{e}^{-\nu s}\mathrm{d}s = \\ - v\int_0^\infty S_0'\delta(\mathbf{r})\delta(s/v)\mathrm{e}^{-\nu s}\mathrm{d}s,\end{aligned} \tag{4.55}$$

which is (Equation 4.54)

$$\nabla^2 G_1(\mathbf{r},\tau) - \frac{v}{D}\left[\mu_a + \frac{\alpha}{3}\mu_s'\kappa_\circ^2\langle\Delta r^2(\tau)\rangle\right]G_1(\mathbf{r},\tau) = -\frac{v}{D}S_0\delta(\mathbf{r}). \tag{4.56}$$

Here, I substituted in $\alpha\mu_s'\kappa_\circ^2\langle\Delta r^2(\tau)\rangle/3$ for ν, and $S_0 \equiv S_0'v/h$ [W]. Recall that S_0' from Equation 4.49 has units of energy, and therefore S_0 has units of power. S_0 can be regarded as the power of the continuous-wave light source, which divides out in the normalization of G_1 (i.e., Equation 4.53). Further, as the correlation diffusion equation is the Laplace transform of the photon diffusion equation, the correlation diffusion boundary conditions are the Laplace transform of the photon diffusion boundary conditions (Equations 2.80, 2.83):

$$G_1(\mathbf{r},\tau) = z_b\hat{z}\nabla G_1(\mathbf{r},\tau) \qquad \text{Partial-flux.} \tag{4.57}$$

$$G_1(z=-z_b,\tau) = 0. \qquad \text{Extrapolated zero.} \tag{4.58}$$

Since Equation 4.56 with its boundary conditions has the same form as the homogeneous photon diffusion equation (Equation 4.49) for CW sources, the Green's function solutions of the

correlation diffusion equation will also have the same form. For example, the continuous-wave photon diffusion Green's functions listed in Table 2.5 are converted to the correlation diffusion Green's functions by replacing $k = (\mu_a v/D)^{1/2}$ with

$$K(\tau) = \sqrt{\left(\mu_a + \frac{\alpha}{3}\mu_s' \kappa_\circ^2 \langle \Delta r^2(\tau)\rangle\right)\frac{v}{D}}. \tag{4.59}$$

For the important special case of the homogeneous semi-infinite geometry, the explicit solution to Equation 4.56 subject to the extrapolated-zero boundary condition (Equation 4.58) is (see Equation 2.103)

$$G_1(\mathbf{r},\tau) = \frac{vS_0}{4\pi D}\left[\frac{\exp(-K(\tau)r_1)}{r_1} - \frac{\exp(-K(\tau)r_b)}{r_b}\right]. \tag{4.60}$$

4.6.1 Heterogeneous Correlation Diffusion Equation

Equation 4.56 is only applicable for homogeneous media. For heterogeneous media, the correlation diffusion equation is derived from the steady-state correlation transport equation for continuous-wave sources and systems in equilibrium [3, 73]:

$$\nabla \cdot G_1^T(\mathbf{r},\hat{\Omega},\tau)\hat{\Omega} + \mu_t G_1^T(\mathbf{r},\hat{\Omega},\tau) = Q(\mathbf{r},\hat{\Omega}) + \mu_s \int G_1^T(\mathbf{r},\hat{\Omega}',\tau) g_1^s(\mathbf{r},\hat{\Omega},\hat{\Omega}',\tau) f(\mathbf{r},\hat{\Omega},\hat{\Omega}')\mathrm{d}\Omega'. \tag{4.61}$$

Here, $G_1^T(\mathbf{r},\hat{\Omega},\tau) = \langle E^*(\mathbf{r},\hat{\Omega},t)E(\mathbf{r},\hat{\Omega},t+\tau)\rangle$ is the autocorrelation function of the polarized electric field (with arbitrary polarization state) at position $\mathbf{r}$ and time t propagating in the $\hat{\Omega}$ direction (see Equation 2.4), $g_1^s(\mathbf{r},\hat{\Omega},\hat{\Omega}',\tau)$ is the normalized temporal field autocorrelation function for single scattering (Equation 4.14), $f(\mathbf{r},\hat{\Omega},\hat{\Omega}')$ is the normalized differential single scattering cross-section (see Table 2.1), $Q(\mathbf{r},\hat{\Omega})$ is the light source distribution (see Table 2.1), and $\mu_t = \mu_a + \mu_s$.

Given Equation 4.61, one can implement a set of steps formally identical to the steps used to derive the photon diffusion equation from the radiative transport equation (Section 2.3). That is, using a P_1 approximation for G_1^T, the correlation transport equation reduces to the correlation diffusion equation [23, 24]:

$$\nabla \cdot (D(\mathbf{r})\nabla G_1(\mathbf{r},\tau) - v\left(\mu_a(\mathbf{r}) + \frac{\alpha}{3}\mu_s'(\mathbf{r})\kappa_\circ^2\langle\Delta r^2(\mathbf{r},\tau)\rangle\right)G_1(\mathbf{r},\tau) = -vS(\mathbf{r}). \tag{4.62}$$

Here, $G_1(\mathbf{r},\tau)$ is the "total" electric field autocorrelation function modeled in Equation 4.56, i.e.,

$$G_1(\mathbf{r},\tau) = \int_{4\pi} G_1^T(\mathbf{r},\hat{\Omega},\tau)\mathrm{d}\Omega = \langle E^*(\mathbf{r},t)E(\mathbf{r},t+\tau)\rangle, \tag{4.63}$$

where $E(\mathbf{r},t)$ is the total light electric field with arbitrary polarization at $(\mathbf{r},t)$, and $S(\mathbf{r})$ is an isotropic CW source term (Equation 2.18). Further, $D(\mathbf{r})$, $\mu_a(\mathbf{r})$, $\mu_s'(\mathbf{r})$, and $v = c/n$ are the photon diffusion coefficient, absorption coefficient, reduced scattering coefficient, and speed of light in tissue, respectively (see Table 2.2), $\kappa_\circ = (2\pi n/\lambda)$ is the light wavevector in tissue, α represents the fraction of photon scattering events that occur from moving particles, and $\langle \Delta r^2(\mathbf{r},\tau)\rangle$ is the mean-square displacement in time τ of the moving scattering particles at position $\mathbf{r}$. Of course, for the special case of homogeneous media, Equation 4.62 becomes Equation 4.56. Finally, the correlation diffusion boundary conditions given by Equations 4.57 and 4.58 remain valid for heterogeneous media.

As with the radiative transport equation, in geometries/conditions where light transport is non-diffusive, it is necessary to solve the correlation transport equation directly with Monte Carlo techniques [24, 25, 186].

4.7 Diffuse Correlation Spectroscopy for Shear Laminar Flow

Brownian motion (Section 4.3.1) and random flow (Section 4.3.3) are examples of stochastic dynamics. Here, I will very briefly discuss the DCS field autocorrelation function obtained for deterministic laminar shear flow in the high multiple-scattering limit [260]. A special case of laminar shear flow is planar couette flow, where the velocity of scatterers is described by

$$\mathbf{u} = \Gamma z \hat{x}, \tag{4.64}$$

and the DCS field autocorrelation function is [260]

$$g_1(\tau) = \int_0^\infty P(s)\exp\left(-\frac{\kappa_\circ^2 s}{15\mu_s'}\Gamma^2\tau^2\right)\mathrm{d}s. \tag{4.65}$$

Note that the decay of $g_1(\tau)$ for laminar shear flow depends on the *gradient* of the flow velocity, i.e., $\partial u/\partial z = \Gamma$, not the absolute flow velocity. For uniform flow velocity ($\mathbf{u} = u_0\hat{x}$), there would be no decay in $g_1(\tau)$. Thus, as in the single-scattering limit (4.3.2), the DCS autocorrelation signal is only sensitive to the relative motions between scatterers [19, 260].

4.8 α is proportional to tissue blood volume fraction

To derive α (Equation 4.44), let N_0 be the number of incident photons on an infinitesimal volume of tissue. The total number of these incident photons scattered within the infinitesimal volume is $N_0\mu_s \mathrm{d}^3 r$, where μ_s (not μ_s') is the tissue scattering coefficient (see Section 2.2). Of these scattered photons, the number that have been scattered by moving red blood cells is $N_0\mu_s^{RBC}\mathrm{d}^3 r$, where the scattering coefficient μ_s^{RBC} is the blood cell contribution to μ_s. Therefore, the fraction of photon scattering events that occur on red blood cells is

$$\alpha = \frac{\mu_s^{RBC}}{\mu_s} = \frac{\sigma_{RBC}\varrho_{RBC}}{\mu_s}, \tag{4.66}$$

where σ_{RBC} [cm^2] is the scattering cross-section of a red blood cell (RBC), and ϱ_{RBC} is the number density of red blood cells in the tissue sample. Note that

$$\varrho_{RBC} = \frac{(Hct)(BV)}{V_{RBC}V_{\text{tissue}}}, \tag{4.67}$$

where Hct is the hematocrit (i.e., volume fraction of red blood cells in blood), BV [mL] is the blood volume, V_{RBC} [mL] is the volume of a red blood cell, and V_{tissue} [mL] is the total tissue volume. Substituting Equation 4.67 into Equation 4.66, we obtain

$$\alpha = \left(\frac{\sigma_{RBC}}{\mu_s}\right)\left(\frac{Hct}{V_{RBC}}\right)\left(\frac{BV}{V_{\text{tissue}}}\right). \tag{4.68}$$

Thus, unsurprisingly, α is proportional to the tissue blood volume fraction BV/V_{tissue}. If there is more blood, then there are more scattering interactions with blood, and α increases.

4.9 Tissue Blood Flow Index

DCS is most sensitive to the motion of blood cells in the microvasculature (i.e., capillaries, arterioles, venules), since the diffusing light is mostly absorbed when traversing large arteries and veins (Section 2.13). Since the microvasculature is convoluted, the correlation diffusion model (Equation 4.56) assumption of isotropic RBC directions is reasonable. The red blood cell dynamics are incorporated into the correlation diffusion equation via their mean-square displacement, $\langle \Delta r^2(\tau)\rangle$. For the case of Brownian motion (Section 4.3.1), $\langle \Delta r^2(\tau)\rangle = 6D_b\tau$, where D_b is the particle diffusion coefficient. For the case of random ballistic flow (Section 4.3.3),

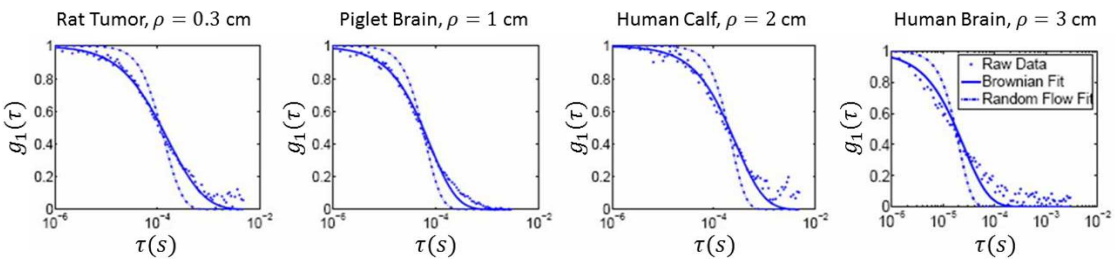

Figure 4.6: Exemplar autocorrelation measurements from a mouse tumor, a piglet brain, an adult human calf muscle, and an adult human brain. The dashed lines denote the fits to the semi-infinite correlation diffusion solution (Equation 4.60) with $\langle \Delta r^2 \rangle \sim \tau^2$ (random flow), and the solid lines denote the fits with $\langle \Delta r^2 \rangle \sim \tau$ (Brownian). This figure is reprinted from [79].

$\langle \Delta r^2(\tau) \rangle = \langle u^2 \rangle \tau^2$, where $\langle u^2 \rangle$ is the second moment of the particle speed distribution. Extensive DCS autocorrelation measurements collected over a wide range of tissue types and length scales all fit the correlation diffusion solution with Brownian dynamics better than the correlation diffusion solution with ballistic dynamics (Figure 4.6). Equation 4.59 for the Brownian model is

$$K(\tau) = \sqrt{(\mu_a + 2\mu_s' \kappa_\circ^2 F)\,\frac{v}{D}}, \tag{4.69}$$

where

$$F \equiv \alpha D_b \tag{4.70}$$

is the tissue blood flow index [cm^2/s].

A standard approach for blood flow monitoring with DCS is to derive $g_1(\tau)$ (Equation 4.53) from measurements of $g_2(\tau)$ (Equation 4.1) via the Siegert relation (Equation 4.4). Then, the correlation diffusion solution for the geometry of interest (e.g., Equation 4.60 for semi-infinite geometry) is fit to $g_1(\tau)$ using a nonlinear minimization algorithm, and an estimate of the blood flow index (F) is obtained from the fit. We (and others) have found that the blood flow index correlates well with other blood flow measurement modalities [149, 182]. Additionally, Durduran *et al* [79] and Ninck *et al* [190] directly demonstrated that the observed decay in $g_1(\tau)$ measurements on tissue arise from red blood cell motion. As a result, it is natural to identify F as a flow index that is directly proportional to blood flow.

4.9.1 Brownian Motion of Red Blood Cells

Recall from Section 4.3.2 that particles with velocities well-modeled by Equation 4.23 exhibit Brownian motion on time scales of $t \gg \gamma^{-1}$, where γ is the linear drag coefficient of the particle divided by the particle's mass, m. Equation 4.23 assumes that the drag force on the particle depends linearly on particle velocity, which is valid for fluids at low Reynolds number [240, Chapter 2]. The Reynolds number of a fluid is [17, Chapter 6]

$$\mathsf{R} = \frac{ub\varsigma}{\eta}, \tag{4.71}$$

where u is the particle's speed moving through the fluid, b is the size of the particle, ς is the mass density of the fluid, and η is the viscosity of the fluid. For blood in the microvasculature, $\eta \approx 2 \times 10^{-2}$ g/(cm s) [32], $u \approx 0.05$ cm/s (in capillaries) [249], $b \approx 10$ microns, and $\varsigma \approx 1$ g/mL, which results in a Reynolds number of $\mathsf{R} = 0.003$. In arterioles, the blood cell speed is considerably faster than capillaries, but even for a blood cell speed of $u = 1$ cm/s, the Reynolds number is still only $\mathsf{R} = 0.05$. Since $\mathsf{R} \ll 1$ for blood in the microvasculature, the drag force on red blood cells is linear, i.e., $\mathsf{f} = \gamma m u$.

An important time scale for assessing blood cell dynamics is γ^{-1} for blood cells. If we approximate the blood cell as a sphere of radius a, then from Stoke's law, the linear drag on the blood cell is

$$\mathsf{f} = 6\pi\eta a,$$

and

$$\gamma^{-1} = \frac{m}{\mathsf{f}} = \frac{2\varsigma_{RBC}a^2}{9\eta} \approx 3\ \mu\text{s}. \tag{4.72}$$

The estimate of 3 μs was obtained from using $a = 5\ \mu$m, a blood cell mass density of $\varsigma_{RBC} = 1$ g/cm^3, and a blood viscosity of $\eta = 2 \times 10^{-2}$ g/(cm s). The time scale on which the autocorrelation function decays is on the order of 50-100 μs, so the red blood cells in the microvasculature plausibly undergo a biased random walk, wherein the diffusion coefficient is (Equation 4.18)

$$D_b = \frac{v_b \ell_{RBC}}{3(1 - \langle \cos\vartheta \rangle)} = \frac{1}{3} v_b \ell^*_{RBC}. \tag{4.73}$$

Here, v_b is the average speed of the red blood cells, ℓ_{RBC} is the mean run length of red blood cells (i.e., mean straight-line distance traveled between direction changes), $\langle \cos\vartheta \rangle$ is the average of the cosine of the angle between successive runs, and $\ell^*_{RBC} \equiv \ell_{RBC}/(1 - \langle \cos\vartheta \rangle)$.

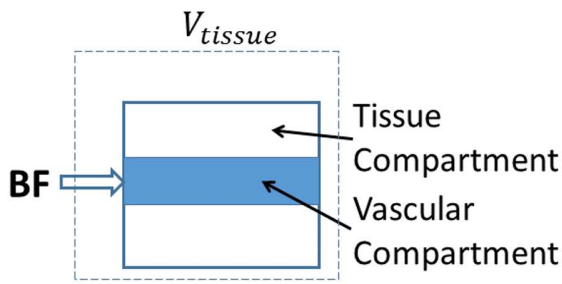

Figure 4.7: An arbitrary tissue volume V_{tissue} is comprised of a vascular compartment (with blood volume BV) and a tissue compartment. The blood flow (BF) in the vascular compartment is the total blood flow supplying V_{tissue}.

Note that the motion of blood cells is highly biased in the forward direction, i.e., ϑ is very small. Further, tissue blood flow is not in thermal equilibrium, and the diffusion coefficient given by Equation 4.73 is a few orders of magnitude higher than the diffusion coefficient given by the Einstein-Smoluchowski relation, i.e., $D_b = k_b T/\mathsf{f}$ [79]. This is analogous to bacteria swimming in water (via flagellar propulsion), which have a diffusion coefficient three orders of magnitude higher than dead bacteria in water [17, 209].

4.9.2 Relation Between Blood Flow Index and Blood Flow

A compartment model of tissue (Figure 4.7) is commonly employed to obtain bulk estimates of average tissue blood flow and oxygen consumption [42, 62, 132, 242, 246, 273]. In this model, the tissue is comprised of a vascular compartment and a tissue compartment, and red blood cells with number density ψ_{RBC} (i.e., # RBC per blood volume (BV)) move with speed v_b through the vascular compartment. The compartment model is obviously an unrealistic geometry for the actual vasculature, but it still provides a reasonable estimate of bulk blood flow in the tissue volume V_{tissue} (discussed further in Section 7.6).

From Equations 4.73 and 4.66, the blood flow index (Equation 4.70) is

$$F \equiv \alpha D_b = \left(\frac{\sigma_{RBC}\ell^*_{RBC}}{3\mu_s}\right)(\varrho_{RBC} v_b). \tag{4.74}$$

Note that the RBC number density per volume of tissue, ϱ_{RBC}, is related to the RBC number density per volume of blood, ψ_{RBC}, via

$$\psi_{RBC} = \frac{V_{\text{tissue}}}{BV}\varrho_{RBC}. \tag{4.75}$$

Multiplying both sides of Equation 4.74 by V_{tissue}/BV and utilizing Equation 4.75, we find that

$$F = \left(\frac{BV}{V_{\text{tissue}}}\right)\left(\frac{\sigma_{RBC}\ell^*_{RBC}}{3\mu_s}\right)(\psi_{RBC}v_b). \tag{4.76}$$

Here, $\psi_{RBC}v_b$ [# RBC / (s cm^2)] is the flow of red blood cells per vascular cross-sectional area per time. The blood volume (BV) is related to the number of red blood cells (# RBC) via

$$BV = \frac{V_{RBC}(\#RBC)}{Hct}, \tag{4.77}$$

where V_{RBC} is the volume of a red blood cell, and Hct is the hematocrit. From multiplying both sides of Equation 4.76 by V_{RBC}/Hct, we see that F is proportional to tissue blood flow, i.e.,

$$F = \left(\frac{BV}{V_{\text{tissue}}}\right)\left(\frac{Hct}{V_{RBC}}\right)\left(\frac{\sigma_{RBC}\ell^*_{RBC}}{3\mu_s}\right)BF. \tag{4.78}$$

Here, $BF = (\psi_{RBC}V_{RBC}/Hct)v_b$ [(mL blood) / (s (cm^2 tissue)] is the tissue blood flow in units of blood volume per time per cross-sectional area of the vascular compartment. Thus, the blood flow index, F, is proportional to tissue blood flow. The proportionality coefficient depends directly on the tissue blood volume fraction (BV/V_{tissue}), hematocrit (Hct), RBC scattering cross-section (σ_{RBC}), and RBC transport mean free path (ℓ^*_{RBC}), and inversely on the RBC volume (V_{RBC}) and the tissue scattering coefficient (μ_s, not μ'_s).

Clinically, absolute blood flow is reported in confusing units of blood volume per time per tissue volume, e.g., [(mL blood) / (min (100 mL tissue))]. These units are understood through the compartment model of tissue (Figure 4.7). The "clinical blood flow", BF_c, is the total volume of blood flowing into V_{tissue} per time, divided by V_{tissue}. BF_c and BF (Equation 4.78) are related by the expression

$$BF_c = BF\left(\frac{A_{\text{tissue}}}{V_{\text{tissue}}}\right), \tag{4.79}$$

where A_{tissue} is the total cross-sectional area of the tissue volume of the vascular compartment supplying V_{tissue}.

4.10 DCS Signal Measurement

4.10.1 Validity of the Siegert Relation

DCS estimates the tissue blood flow index F from a nonlinear fit of the measured intensity autocorrelation function signal, $g_2(\tau)$, to the electric field autocorrelation function correlation

diffusion solution, $g_1(\tau)$. A key step in this fit is using the Siegert relation (Equation 4.4) to derive $g_1(\tau)$ from the $g_2(\tau)$ measurement. The Siegert relation is valid if the detected electric field is a Gaussian distributed variable with zero mean. This is the case if the detected electric field is a sum of fully developed speckle fields (see Section 4.2).

For tissue measurements, it is feasible for a component of the detected signal to arise from light paths that have only experienced static scattering (Section 4.4). In this scenario, the detected electric field can be written as

$$E(\mathbf{r}, t) = E_c(\mathbf{r}) + E_f(\mathbf{r}, t), \tag{4.80}$$

where $E_f(\mathbf{r}, t)$ is the fully developed speckle electric field arising from light paths that have encountered at least one moving scatterer, and $E_c(\mathbf{r})$ is a constant term arising from light paths that have encountered no moving scatterers. $E_c(\mathbf{r})$ is cleary not a speckle field, and therefore the Siegert relation is not valid for Equation 4.80. The relation between $g_2(\tau)$ and $g_1(\tau)$ for Equation 4.80 is [168]

$$g_2(\tau) = 1 + \frac{\beta_f}{(I_f + I_s)^2} \left[I_f^2 |g_1(\tau)|^2 + 2 I_f I_s |g_1(\tau)| \right]. \tag{4.81}$$

Here, $I_f \equiv \langle E_f^* E_f \rangle$, $I_s \equiv E_s^* E_s$, and β_f is the speckle contrast arising from the fluctating component of the electric field (i.e., Equation 4.9). The intercept of Equation 4.81 is

$$g_2(0) = 1 + \beta_f \frac{I_f^2 + I_f I_s}{(I_f + I_s)^2}, \tag{4.82}$$

so the effect of the static scattering field component is to reduce the speckle contrast. For single mode fiber detection of unpolarized light, if $\beta = 0.5$, then the static scattering component is negligible. However, if the speckle contrast is lower than expected, one potential explanation for it is that E_c in the detected signal is significant. The expectation is that this problem is more of a risk for short separations than long separations. In most practical tissue measurements with single mode detection, we have found that the β coefficient is about 0.5, even at short separations around 0.7 cm. This suggests that E_c is typically small in practice.

However, recall from Section 4.5 that one of the assumptions used in the derivation of the correlation diffusion equation is that the detected light paths from source to detector encounter a large number of red blood cells. Therefore, even if the Siegert relation is valid, the correlation

diffusion model may still break down if a significant fraction of the photon paths involve only a few RBC scattering interactions. This will not be an issue for long separations, but it could be a problem for short separations.

4.10.2 Fiber Detection with DCS

I mentioned in Section 4.2 that for detection with optical fibers, each mode propagating through the fiber is a fully developed speckle field. The electric fields from all of the modes have identical statistics (i.e., Gaussian-distributed with zero mean), but they are independent fields that add incoherently. The incoherent sum of independent speckle fields results in reduced speckle contrast (i.e., Equation 4.9). From a geometrical optics point of view, various rays propagate down a multimode fiber at different angles to the axis of the fiber (Figure 4.8). Each angle of propagation is a fiber optic mode, and the fiber optic modes are independent because the quasi plane wave electric fields incident on the fiber from different angles are independent (see Equation 2.4). The numerical aperture (NA) of the fiber specifies the acceptance cone of incident light angles allowed into the fiber, i.e., $\theta < \vartheta_c = \arcsin(NA/n)$ (n is the refractive index of the medium in contact with the fiber). However, not every ray that enters an optical fiber within its acceptance cone can propagate successfully through the fiber. Only certain ray directions (modes) are allowed that satisfy a "resonance condition" (see [202, Section 10-5]). The number of modes supported by a multimode step-index fiber is $M \approx (2\pi n/\lambda)(NA)a$, where λ is the light wavelength in air and a is the radius of the fiber core [112]. For a 62.5 micron fiber with a $NA = 0.22$, $n = 1.4$, and $\lambda = 785$ nm, $M \approx 80$ modes. . Further, for unpolarized light, there are two independent speckle fields for each mode that correspond to the two orthogonal polarization states. Thus, the detected intensity from the 62.5 micron fiber for unpolarized light is a sum of $2M = 160$ speckle fields. This corresponds to a β coefficient of 0.006, i.e., essentially no speckle contrast.

Single mode fibers have very low numerical apertures such that only the $\theta = 0$ mode can propagate through the fiber (Figure 4.8). With only one mode (2 speckle fields for unpolarized light), single mode fibers maximize the contrast of the detected signal, but they also have drawbacks. Because of their very small size and numerical aperture (5 micron core diameter, 0.13 NA), single mode fibers do not collect much light, and low signal-to-noise is a commonly

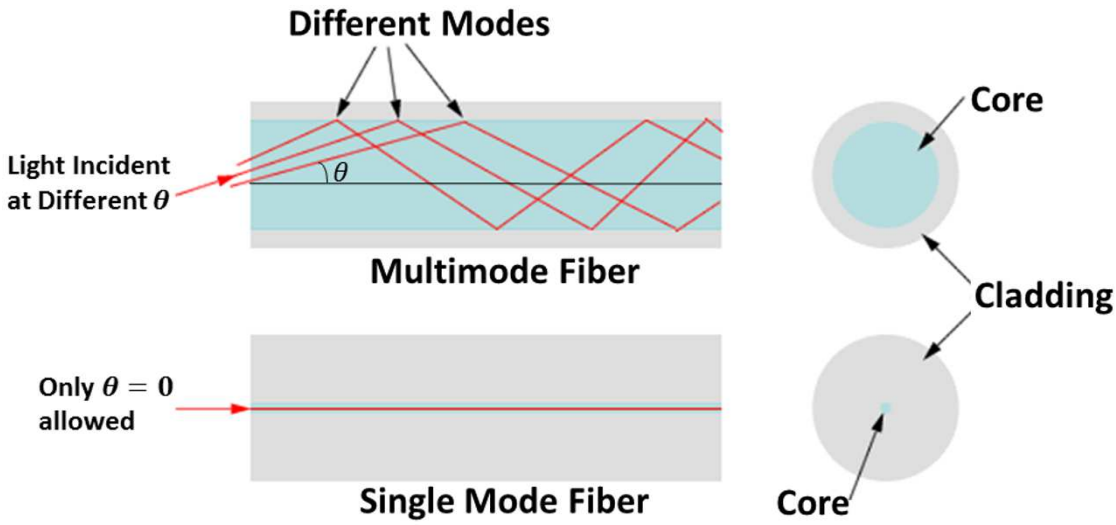

Figure 4.8: Schematics of a multimode and single mode fiber. Multimode fibers have high numerical apertures, enabling light propagation at multiple angles (i.e., modes) to the axis of the fiber. Single mode fibers have very low numerical apertures, and therefore light only propagates in the $\theta = 0$ mode. This figure is adapted from [1].

encountered problem in the DCS measurement at longer source-detector separations (e.g., 3 cm) [37]. The "hair problem" is also a bigger issue for DCS than it is for DOS, because it is easier for single mode fibers to be completely blocked by a light absorbing hair follicle than the multimode fibers used for DOS detection [37, 84].

There are several strategies for ameliorating the DCS signal-to-noise problem. First is to use high quantum efficiency single-photon detectors, such as the SPCM-AQ4C (Excelitas, Canada) APD detector array. Second is to incorporate multiple detection channels in the DCS instrument. For example, with 8 detection channels, DCS signals can be collected in parallel from 8 single mode fibers bundled together at nearly the same position on tissue. Averaging across these 8 channels to derive a single autocorrelation curve will improve SNR by $\sim \sqrt{8}$. For N detection channels, the improvement in SNR is $\sim \sqrt{N}$. However, the single photon detectors used for DCS detection are currently expensive, placing a practical limit on the total number of detection channels. In the future, DCS would benefit greatly from the lower costs permitted by economies of scale in the production of single-photon counting detectors [84].

A third strategy is to increase the light source power delivered to tissue, but the maximum power is limited by ANSI standards for maximum permissible skin exposure. For continuous

exposure (i.e., laser is always on), the maximum permissible power delivered to a point on the skin for $\lambda = 785$ nm is $P = 28$ mW, though higher powers are permissible if the laser is pulsed (Section 4.10.4).

A fourth strategy some researchers have pursued is the use of few-mode fibers for DCS detection [69, 125, 169]. The light intensity itself is of course greater with few-mode detection. If N modes can propagate through the fiber, then the detected intensity is

$$\langle I_d \rangle = \langle \sum_{j=1}^{N} I_j \rangle = N \langle I_j \rangle, \tag{4.83}$$

which is a factor of N higher than the single mode intensity. However, as discussed above, the summation over N independent modes reduces the β coefficient by a factor of N (4.10). If the DCS signal decays exponentially (i.e., $g_2(\tau) - 1 = \beta \exp[-2\Gamma\tau]$), then the SNR of the signal measurement is [274, 276]

$$SNR = \frac{g_2(\tau) - 1}{\sigma_{g_2 - 1}(\tau)} \approx \langle I_d \rangle \beta \sqrt{T t_{avg}} \frac{\exp[-2\Gamma\tau]}{\sqrt{1 + \beta \exp[-\Gamma\tau]}}, \tag{4.84}$$

where t_{avg} is the DCS signal averaging time, and T is the correlator delay-time bin width. The DCS signal typically is well approximated by an exponential decay, and therefore 4.84 is a reasonable model for the SNR [274, 276]. For few-mode fiber detection then, the gain from increased signal intensity is canceled by the reduction in β, and the SNR is about the same as single-mode fiber detection. However, few-mode fibers are also prone to modal noise (e.g., from fiber bending) [112], which is an additional source of noise not accounted for in Equation 4.84. For these reasons, single-mode fibers are usually optimal for DCS detection, though perhaps few-mode fibers can obtain better SNR through hair. Finally, the SNR will increase with the square root of the averaging time (t_{avg} in Equation 4.84) at the cost of a lower time resolution.

4.10.3 Source Coherence

As I already discussed, the coherence length of the source should be substantially greater than the spread of light pathlengths through tissue to ensure detected speckle fluctuations with high speckle contrast. The width of the pathlength distribution depends on the separation and optical properties, but for practical measurements, it is less than 1 meter [201]. The source itself, though, has to have a greater coherence length than this (roughly > 5 m) if a mulitmode fiber is utilized

for light delivery. This is because light propagation through a multimode source fiber effectively reduces the coherence length of the light source. The time delays introduced by the differences in pathlength between the different light modes propagating in the fiber induce speckle fluctuations at the end of the fiber that interrupt the constant phase of a monochromatic source.

An alternative way to understand coherence effects is in terms of the power spectrum of the light, $\mathsf{I}(\omega)$. The power spectrum is defined as the Fourier transform of the electric field autocorrelation function [18]:

$$\mathsf{I}(\omega) \equiv \frac{1}{2\pi} \int_{-\infty}^{\infty} \mathrm{d}\tau \mathrm{e}^{-i\omega\tau} \langle E^*(t)E(t+\tau)\rangle. \tag{4.85}$$

Consequentially, the field autocorrelation function is the inverse Fourier transform of $\mathsf{I}(\omega)$:

$$\langle E^*(t)E(t+\tau)\rangle = \int_{-\infty}^{\infty} \mathrm{d}\omega \mathrm{e}^{i\omega\tau} \mathsf{I}(\omega). \tag{4.86}$$

Note that

$$\langle |E|^2\rangle = \langle I\rangle = \int_{-\infty}^{\infty} \mathrm{d}\omega \mathsf{I}(\omega), \tag{4.87}$$

so $\mathsf{I}(\omega)\mathrm{d}\omega$ is the "amount" of the light intensity in the frequency interval $(\omega, \omega + \mathrm{d}\omega)$. The decay of the field autocorrelation function ($G_1(\tau)$) is related to the width of the power spectrum. If $G_1(\tau)$ decays exponentially with decay time τ_c, the half-width at half maximum of $\mathsf{I}(\omega)$ is $\Delta\omega_c = \tau_c^{-1}$. In fact, blood cell motions could be estimated from the measurements of the power spectrum as an alternative to measurements of the intensity autocorrelation function. However, the autocorrelation function measurement is preferable to its Fourier counterpart in the low signal limit, because the photon correlation instrumentation is a single photon counting device [81].

The power spectrum of the light source is close to monochromatic, and thus very sharply peaked at $\omega = 2\pi c/\lambda$. As light travels through tissue from source to detector, the time delays from the different light paths increases the spectral linewidth of the power spectrum, $\Delta\omega_c$. The longer the source-detector separation, the greater the time delays between the different path-lengths become. These greater time delays in turn increase the width of the power spectrum and decrease the decay time of the autocorrelation function. This is why the DCS autocorrelation signals decay substantially faster at longer source-detector separations than they do at shorter separations.

Analogously, the time delays from the different light paths in a multimode fiber broaden the power spectrum. The longer the optical fiber is, the greater these time delays are, and correspondingly, the broader the power spectrum is. Thus, the coherence of the source light delivered to the tissue will depend on the fiber length. For optimal sensitivity to blood flow, the broadening of the light power spectrum from this loss of coherence needs to be much less than the broadening of the light power spectrum from the blood cell motion. If the broadening from coherence loss is comparable to the broadening from blood cell motion, then coherence effects "wash out" the speckle fluctuation effects from blood cell motion, and the signal is not sensitive to blood cell motion.

The speckle contrast is clearly sensitive to the coherence of the source. Thus, if the speckle contrast is fluctuating (i.e., the $g_2(\tau)$ intercept is unstable during the measurement integration time), this could indicate that the coherence of the source is unstable. This source instability could arise from Fresnel reflections back into the laser from improper probe contact with the tissue (e.g., air gaps often lead to big Fresnel reflections). An unstable contrast could also arise from light leakage into the probe from room light, since multispectral light affects the power spectrum of the detected signal. Finally, if the probe is not well-secured to tissue, any sort of movement could lead to sampling of different tissue locations (i.e., different speckle fields) during the integration time of the measurement, which is another source of instability.

4.10.4 ANSI standards for Maximum Permissible Light Powers

For the DCS measurement, the total light power delivered to the tissue must be below the ANSI standards for maximum permissible skin exposure to light [5]. According to Table 7 of the ANSI regulation [5], the long term maximum permissible skin exposure is

$$E_{lt} = 0.2C_A \text{ [W / cm}^2\text{]}, \tag{4.88}$$

where the constant $C_A = 1$ W / cm^2 for $\lambda < 700$ nm and $10^{2(\lambda/1000-0.7)}$ W / cm^2 for $\lambda > 700$ nm. The ANSI standard clearly states the limiting aperture diameter for skin exposure to account for scattering once it penetrates the skin. This value can be found in Table 8a of the ANSI standard [5], and it is 3.5 mm for exposures ranging from 1 ms to 30,000 s and for wavelengths lying between 400 nm and 1400 nm. For a fiber-coupled laser that delivers a light power P [W]

continuously to a point on the skin, the experimental skin exposure is

$$E_{lt,exp} = P/(\pi(0.35/2)^2 \text{ [W / cm}^2\text{]}. \tag{4.89}$$

Comparing Equations 4.89 to 4.88, the maximum permissible power that can be delivered continuously (i.e., laser is always on) to a point on the skin at $\lambda = 785$ nm is $P = 28.4$ mW.

However, the permissible power can be higher for non-continuous light power delivery, e.g., the laser is on for time t_{on}, off for time t_{off}, on for time t_{on}, off for time t_{off}, and so on. From Table 7 of the ANSI regulation [5], for exposures t_{on} between 10^{-7} and 10 seconds, the maximum permissible skin exposure is given by

$$E = 1.1 C_A t_{on}^{0.25} \text{ [J / cm}^2\text{]}, \tag{4.90}$$

where C_A is defined below Equation 4.88. The experimental skin exposure from a single laser pulse with power P and duration t_{on} is

$$E_{exp} = P t_{on}/(\pi(0.35/2)^2 \text{ [J / cm}^2\text{]}, \tag{4.91}$$

and the average long-term experimental skin exposure from a train of these laser pulses is

$$E_{lt,avg} = E_{exp}/(t_{on} + t_{off}) \text{ [W / cm}^2\text{]}, \tag{4.92}$$

where again, t_{off} is the time interval between laser pulses. The ANSI regulations are satisfied when E_{exp} (Equation 4.91) is less than E (Equation 4.90) and $E_{lt,avg}$ (Equation 4.92) is less than E_{lt} (Equation 4.88). Thus, the duty cycle of the laser needs to be chosen appropriately to ensure these two conditions are not violated.

As a concrete example, let's suppose that $t_{on} = 2.5$ s. Setting Equation 4.91 equal to Equation 4.90, the maximum permissible power for a pulse with duration 2.5 s is $P = 79$ mW. For $E_{lt,avg}$ to be less than E_{lt} for a train of pulses with $t_{on} = 2.5$ s and $P = 79$ mW, t_{off} has to be greater than 4.5 s.

Chapter 5

Diffuse Correlation Spectroscopy (DCS): Modified Beer-Lambert Law Approach

5.1 Introduction

Here, I present an alternative approach to the correlation diffusion approach for analysis of DCS signals, which is a Modified Beer-Lambert law for flow. This method linearly relates measured changes of a newly-defined "DCS optical density" to the variation of tissue blood flow, tissue scattering, and tissue absorption. The novel algorithm parallels the DOS/NIRS Modified Beer-Lambert law, but it has interesting differences that should be useful for applications that require continuous monitoring of blood flow. It also has similar advantages to the DOS Modified Beer-Lambert law. The rest of this chapter is essentially a verbatim reprint of my biomedical optics express paper on the Modified Beer-Lambert law for flow [12]. Although some of the introduction material here has been covered in previous chapters, I kept the introduction material in to keep this chapter self-contained.

Traditional optical spectroscopy measures the attenuation of light traveling through a sample as a function of wavelength. In cases where scattering is negligible, i.e., in which the reduced scattering coefficient (μ_s') is zero, light attenuation is dominated by absorption, and the

transmitted intensity ($I(t)$) at time t is related to the sample absorption coefficient (μ_a) via the Beer-Lambert law: $I(t) = I_s \exp[-\mu_a \rho]$. Here, I_s is the incident light intensity, and ρ is the sample length. The sample optical density (OD) is defined as the negative logarithm of the ratio of transmitted to incident light intensity; it is proportional to the absorption coefficient, i.e., $OD \equiv -\log[I(t)/I_s] = \mu_a \rho$. When scattering within the sample is significant, however, then light attenuation is affected by both absorption and scattering. In these situations, the effects of scattering become tangled with those of absorption [79]. Typically, the photon trajectories through tissue samples with significant scattering are well approximated as random walks, and the average length of a photon path through tissue is much greater than the straight-line distance between source and detector.

Among the most widely used approaches for analysis of such DOS/NIRS reflectance signals is the so-called Modified Beer-Lambert law [10, 67, 130]. The Modified Beer-Lambert paradigm is an algorithm that derives changes in tissue optical properties based on continuous-wave (CW) diffuse optical intensity measurements. In its simplest form, the scheme relates differential light transmission changes (in any geometry) to differential changes in tissue absorption. Here the term differential refers to a comparison between a baseline state and a perturbed state. In essence, the Modified Beer-Lambert law accounts for tissue scattering by using the mean pathlength traveled by photons through the highly scattering sample as a best estimate for the actual photon pathlengths. The mean pathlength provides a natural constant of proportionality between the measured differential intensity and the sample's differential absorption.

The Modified Beer-Lambert law is readily derived from the first order Taylor expansion of the optical density: $OD \approx OD^0 + (\partial OD^0/\partial \mu_a)\Delta\mu_a + (\partial OD^0/\partial \mu_s')\Delta\mu_s'$, wherein the partial derivatives are evaluated in the "baseline" state ($\mu_a = \mu_a^0$, $\mu_s' = \mu_s'^0$), $OD^0 \equiv -\log[I^0/I_s]$ is the baseline optical density, and the differential changes in absorption and scattering are denoted by $\Delta\mu_a \equiv \mu_a(t) - \mu_a^0$ and $\Delta\mu_s' \equiv \mu_s'(t) - \mu_s'^0$, respectively. Note that the superscript "0" indicates baseline. Within this approximation, the change in optical density from baseline is

$$\Delta OD = -\log\left(\frac{I(t)}{I^0}\right) \approx \langle L\rangle \Delta\mu_a(t) + \left(\frac{\mu_a^0}{\mu_s'^0}\right)\langle L\rangle \Delta\mu_s'(t) \approx \langle L\rangle \Delta\mu_a(t). \tag{5.1}$$

Here, $\langle L\rangle \equiv \partial OD^0/\partial\mu_a$ is the so-called differential pathlength, which is approximately the mean pathlength that diffusing photons travel through the medium from source to detector [10].

Notice that whereas the traditional Beer-Lambert law relates *absolute* optical densities to *absolute* absorption coefficients, the Modified Beer-Lambert law (Equation 5.1) relates *differential changes* in the optical density to *differential changes* in the absorption coefficient. This algorithm has proved useful for many reasons; it is simple, fast, and fairly accurate. To date the Modified Beer-Lambert algorithms have been applied predominantly to monitor hemoglobin concentration changes in the brain; within this context, it has been extended from semi-infinite geometries to two-layer geometries [91, 130, 215, 234, 235] characteristic of many tissues, especially the human head.

Herein, we derive a Modified Beer-Lambert law for measurement of blood flow based on the DCS technique in turbid tissues, and we validate the approach. The Modified Beer-Lambert law for blood flow linearly relates changes in tissue blood flow, tissue scattering, and tissue absorption to variation of a newly-defined "DCS optical density" (OD_{DCS}). The new algorithm parallels the DOS/NIRS Modified Beer-Lambert law, since the transport of both the light fluence rate and the electric field autocorrelation function through highly scattering tissues is well approximated as a diffusive process [79]. Importantly, however, the diffusion equation for the DCS signal is sensitive to the movement of red blood cells in tissue microvasculature, and therefore the precise form of the Modified Beer-Lambert law for blood flow is different from the traditional (DOS/NIRS) form. The weighting factors in the new law, for example, are not as easily interpreted in terms of a mean pathlength. We derive general theoretical results for measurement of flow changes in any geometry, and then we obtain specific expressions for two common tissue models: homogeneous semi-infinite turbid media and two-layer turbid media. We demonstrate the new approach with simulations and with an *in-vivo* pig-brain experiment. In the future, we expect the Modified Beer-Lambert law for flow to offer increased DCS measurement speed, simpler DCS instrumentation, and, importantly, access to novel measurement paradigms based on differential blood flow signals. Ultimately, these developments should lead to improvements in characterization of cerebral flow and metabolism, with concomitant clinical impact.

5.2 Diffuse Correlation Spectroscopy

Diffuse correlation spectroscopy (DCS) employs NIR light to non-invasively measure tissue blood flow. Since early work with *in-vitro* phantoms and *in-vivo* tissues [23, 24, 179, 204], it has been used in a variety of clinical applications such as stroke [62, 86, 97, 224], brain injury [159, 160], muscle disease [183,185,225], cancer [54,83,236,270], and in functional activation studies [85,147,169,213]. In addition, the DCS blood flow index has been successfully validated against a plethora of gold-standard techniques [149, 182]. Several recent reviews highlight the theory, implementation and applications of DCS [37, 79, 84, 182, 269], and therefore our background discussion will be brief.

DCS detects tissue blood flow using speckle correlation techniques. It measures the temporal intensity fluctuations of coherent NIR light that has scattered from moving particles (red blood cells) in tissue (Figure 5.1(A)). These temporal fluctuations (Figure 5.1(B)) are quantified by computing the normalized intensity temporal autocorrelation function at multiple delay-times, τ, i.e., we compute $g_2(\tau) \equiv \langle I(t)I(t+\tau)\rangle / \langle I(t)\rangle^2$, where $I(t)$ is the intensity of the detected light at time t, and the angular brackets, $\langle\rangle$, represent time-averages. An index of tissue blood flow is then provided by the temporal decay of the detected intensity autocorrelation function (Figure 5.1(C)).

Formally, the transport of the electric field ($\mathbf{E}(t)$) autocorrelation function, $G_1(\tau) \equiv \langle \mathbf{E}^*(t) \cdot \mathbf{E}(t+\tau)\rangle$, is well modeled by the so-called correlation diffusion equation [23, 24], which can be solved analytically or numerically for tissue geometries of interest [24, 79]. Tissue blood flow can be ascertained by fitting the solution for the normalized electric field autocorrelation function, $g_1(\tau) = G_1(\tau)/G_1(\tau = 0)$, to the measured (normalized) intensity autocorrelation function via the Siegert relation [168]: $g_2(\tau) = 1 + \beta |g_1(\tau)|^2$, where β is a constant determined primarily by the experimental collection optics.

As an example, for the simple case of point illumination and point detection on the surface of semi-infinite homogeneous tissue (Figure 5.1(A)) with absorption coefficient μ_a, reduced scattering coefficient μ_s', and tissue blood flow index F, the solution to the correlation diffusion equation is [24, 79]:

$$G_1(\tau) = \frac{3}{4\pi\ell_{tr}} \left[\frac{\exp\left(-K(\tau)r_1\right)}{r_1} - \frac{\exp\left(-K(\tau)r_b\right)}{r_b} \right]. \tag{5.2}$$

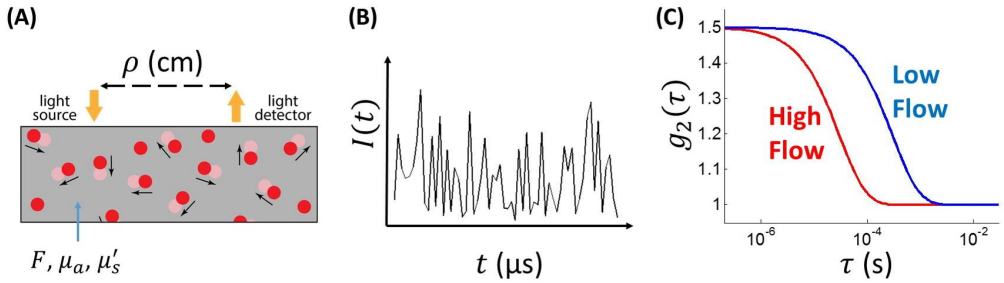

Figure 5.1: **(A)** Schematic for blood flow monitoring in a homogeneous, semi-infinite turbid tissue (see text for details). Blood cell (e.g., red disks at time t and light-red disks at time $t+\tau$) motion induces temporal fluctuations in the scattered light intensity, $I(t)$, at the light detector (panel **B**). These intensity fluctuations are characterized by the normalized intensity autocorrelation function ($g_2(\tau)$). **(C)** The decay of the intensity autocorrelation function curves is related to tissue blood flow.

Here, $K(\tau) = [3\mu_a(\mu_a + \mu_s')(1 + 2\mu_s' k_0^2 F\tau/\mu_a)]^{1/2}$, $r_1 = (\ell_{tr}^2 + \rho^2)^{1/2}$, $r_b = [(2z_b + \ell_{tr})^2 + \rho^2]^{1/2}$, ρ is the source-detector separation, and $\ell_{tr} = 1/(\mu_a + \mu_s')$. Further, $k_0 = 2\pi n/\lambda$ is the magnitude of the light wave vector in the medium, and $z_b = 2\ell_{tr}(1+R_{eff})/(3(1-R_{eff}))$, where R_{eff} is the effective reflection coefficient that accounts for the mismatch between the index of refraction of tissue (n) and the index of refraction of the non-scattering medium bounding the tissue (n_{out}), such as air [123].

A standard approach for blood flow monitoring with DCS in this geometry is to derive $g_1(\tau)$ from measurements of $g_2(\tau)$ via the Siegert relation. Then, the semi-infinite correlation diffusion solution (Equation 5.2) is fit to $g_1(\tau)$ using a nonlinear minimization algorithm, and an estimate of the blood flow index (F) is obtained from the fit.

5.3 Modified Beer-Lambert Law for Flow

We now develop a "Modified Beer-Lambert law" for tissue blood flow based on the DCS measurement. The first step in this process is to define a "DCS optical density" (OD_{DCS}), in analogy with the OD for DOS/NIRS. For source-detector separation ρ and delay-time τ, we define the DCS optical density as: $OD_{DCS}(\tau, \rho) \equiv -\log(g_2(\tau, \rho) - 1)$. Notice that in addition to delay time and source-detector separation, the DCS optical density also implicitly depends on tissue absorption, scattering, and blood flow (e.g, Equation 5.2).

5.3.1 DCS Modified Beer-Lambert law for homogeneous tissue

We first derive a general expression for homogeneous tissue characterized by a blood flow index, F, an absorption coefficient, μ_a, and a reduced scattering coefficient, μ_s'. The DCS Modified Beer-Lambert law is obtained by truncating the Taylor series expansion of the DCS optical density to first order in F, μ_a, and μ_s', i.e.,

$$OD_{DCS}(\tau,\rho) \approx OD^0_{DCS}(\tau,\rho) + \frac{\partial OD^0_{DCS}}{\partial F}\Delta F + \frac{\partial OD^0_{DCS}}{\partial \mu_a}\Delta\mu_a + \frac{\partial OD^0_{DCS}}{\partial \mu_s'}\Delta\mu_s'. \quad (5.3)$$

Here, $OD^0_{DCS}(\tau,\rho) \equiv -\log(g^0_2(\tau,\rho)-1)$ is the "baseline" DCS optical density with a baseline blood flow index, F^0, and with baseline optical properties μ_a^0 and $\mu_s'^0$. Correspondingly, $OD_{DCS}(\tau,\rho) \equiv -\log(g_2(\tau,\rho)-1)$ is the DCS optical density for the intensity autocorrelation function in the "perturbed" state with blood flow index F, and with optical properties μ_a and μ_s'. The differential changes from baseline of tissue blood flow, absorption, and scattering are $\Delta F \equiv F - F^0$, $\Delta\mu_a \equiv \mu_a - \mu_a^0$, and $\Delta\mu_s' \equiv \mu_s' - \mu_s'^0$, respectively.

Comparing Equation 5.3 with Equation 5.1, the DCS analogues of the differential pathlength are $d_F(\tau,\rho) \equiv \partial OD^0_{DCS}/\partial F$, $d_a(\tau,\rho) \equiv \partial OD^0_{DCS}/\partial \mu_a$, and $d_s(\tau,\rho) \equiv \partial OD^0_{DCS}/\partial \mu_s'$, which can be estimated analytically or numerically using the correlation diffusion model applied to the appropriate geometry (Section 5.7). All three of these weighting factors depend on τ and ρ, on tissue geometry, and on the baseline parameters F^0, μ_a^0, and $\mu_s'^0$. Rearranging Equation 5.3, we arrive at the "DCS" Modified Beer-Lambert law for homogeneous tissue:

$$\Delta OD_{DCS}(\tau,\rho) = -\log\left(\frac{g_2(\tau,\rho)-1}{g^0_2(\tau,\rho)-1}\right) \approx d_F(\tau,\rho)\Delta F + d_a(\tau,\rho)\Delta\mu_a + d_s(\tau,\rho)\Delta\mu_s'. \quad (5.4)$$

If the blood flow and optical properties change only slightly, then the perturbation in the DCS optical density is small, and the first order expansion (Equation 5.3) is a good approximation. Notice, however, that even for large tissue hemodynamic changes, ΔOD_{DCS} can still be small at *short delay-times*, because in this limit, d_F, d_a, and d_s are close to zero (Figure 5.2). Analytical and numerical computation of these weighting factors (d_F, d_a, d_s) are described and given in Section 5.7.

Equation 5.4 is a general result that describes the change in DCS optical density for homogeneous tissue. For a given tissue/measurement geometry, the change in blood flow can be

computed by evaluating the weighting factors for the geometry in question, and then inserting these resultant weighting factors into Equation 5.4.

5.3.2 DCS Modified Beer-Lambert law for homogeneous semi-infinite geometries

It is straightforward to evaluate the weighting factors in Equation 5.4 for the special case of the homogeneous semi-infinite geometry (Figure 5.1(A)). Recall from Equation 5.2 that the normalized electric field autocorrelation function is

$$g_1(\tau) = \frac{\exp(-K(\tau)r_1)/r_1 - \exp(-K(\tau)r_b)/r_b}{\exp(-K_0 r_1)/r_1 - \exp(-K_0 r_b)/r_b}, \tag{5.5}$$

where $K(\tau)$, r_1, and r_b are as defined in *Section 5.2*, and $K_0 = K(\tau = 0) = [3\mu_a(\mu_a + \mu_s')]^{1/2}$. The multiplicative weighting factors in the semi-infinite geometry can be computed from substitution of Equation 5.5 into Equations (5.11) and (5.12), e.g.,

$$d_F(\tau,\rho) = \frac{6\mu_s'^0\left(\mu_s'^0 + \mu_a^0\right)k_0^2\tau}{K^0(\tau)}\left[\frac{\exp\left(-K^0(\tau)r_1^0\right) - \exp\left(-K^0(\tau)r_b^0\right)}{\exp\left(-K^0(\tau)r_1^0\right)/r_1^0 - \exp\left(-K^0(\tau)r_b^0\right)/r_b^0}\right]. \tag{5.6}$$

In Figure 5.2, d_F, d_a, and d_s in the semi-infinite geometry are plotted as a function of τ using typical tissue properties. Note that all three weighting factors are small in magnitude for short delay-times. Further, the weighting factor for absorption is negative, i.e., an increase in absorption is accompanied by a decrease in the DCS flow optical density (compared to baseline), and the weighting factors for flow and scattering are positive.

Because the weighting factors are small at shorter delay-times (Figure 5.2), the DCS optical density perturbation will also be small, which in turn implies higher accuracy for the DCS Modified Beer-Lambert law (Equation 5.4). Ideally, in the semi-infinite geometry, the delay-times used for Equation 5.4 should satisfy the limits $2\mu_s' k_0^2 F\tau/\mu_a \ll 1$ and $2\mu_s'^0 k_0^2 F^0\tau/\mu_a^0 \ll 1$ to obtain the most quantitatively accurate results (see Section 5.8). From our experience with simulations and real data, we have found that a good "rule of thumb" for accurately using Equation 5.4 is to utilize data wherein $g_1^0(\tau) > 0.5$, which corresponds to $g_2^0(\tau) > 1.1$ for $\beta = 0.5$.

Figure 5.2(B) shows that for the same *fractional* changes (10%) in blood flow, tissue scattering, and tissue absorption, the change in DCS optical density is greatest due to scattering, followed by flow; changes in absorption have the least influence on the DCS signal. In practice,

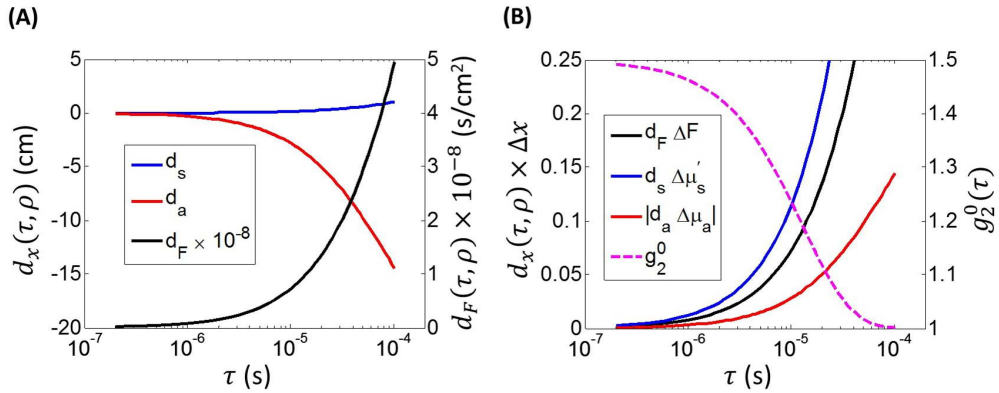

Figure 5.2: **(A)** The semi-infinite multiplicative weighting factors (see Equation 5.4) for tissue scattering (d_s), for tissue absorption (d_a), and for tissue blood flow (d_F, right vertical-axis). They are plotted as a function of the correlation time, τ, for source-detector separation, $\rho = 3$ cm, and optical wavelength, $\lambda = 785$ nm, given a typical set of cerebral tissue properties, i.e., $\mu_a^0 = 0.1$ cm^{-1}, $\mu_s'^0 = 8$ cm^{-1}, $F^0 = 10^{-8}$ cm^2/s, $n = 1.4$, $n_{out} = 1$. **(B)** The semi-infinite DCS Modified Beer-Lambert components $d_F(\tau,\rho)\Delta F$, $d_s(\tau,\rho)\Delta\mu_s'$, and $|d_a(\tau,\rho)\Delta\mu_a|$, plotted as a function of τ for a 10% increase in blood flow, tissue scattering, and tissue absorption, respectively. On the right vertical-axis is the intensity autocorrelation function, $g_2^0(\tau)$, for $\beta = 0.5$. Given the same fractional change in tissue properties, the DCS signal is most sensitive to scattering changes, followed by flow changes, and finally absorption changes. In many applications, however, the scattering changes associated with hemodynamic perturbations are negligible, e.g., such as an increase in blood flow and blood volume; in these situations the scattering component can be neglected (see text).

concurrent frequency-domain or time-domain DOS/NIRS can (and should) be employed to directly measure tissue absorption and scattering [79, 101, 201] and account for their effects. This mode of operation, i.e., with concurrent optical measurements, is always desirable. Importantly, however, the tissue scattering changes that typically accompany hemodynamic concentration variations are often negligible; the origin of hemodynamic variation is blood, but the origin of tissue scattering is predominantly from interfaces between cells and the extracellular space, or between cellular cytoplasm and cellular organelles [57]. The tissue blood volume (BV) is typically a small fraction ($< 4\%$) of the tissue volume (V_{tissue}), and red blood cells account for only a small fraction of the tissue scattering [30]. Scattering from blood ($\mu'_{s,\text{blood}}$) is proportional to the blood volume, i.e., $\mu'_{s,\text{blood}} = \sigma_{\text{blood}}(1-g)(Hct/V_{RBC})(BV/V_{\text{tissue}})$, where σ_{blood}, g, and V_{RBC} are the scattering cross-section, scattering anisotropy factor, and volume of a red blood cell, and Hct is the hematocrit. Consequentially, while tissue scattering can change with variation in blood volume, the magnitude of this change is often quite small, because the overall volume fraction of blood in tissue is quite small.

As an example, the finger tapping functional task induces a localized increase in cerebral blood volume of roughly 10% [85], which corresponds approximately to a 10% increase in scattering from blood. However, the fractional increase in total scattering is much less than 10% because blood only accounts for a small fraction of tissue scattering. If we assume that blood accounts for less than 5% of total tissue scattering [57], then the tissue scattering change due to increased blood volume from finger tapping is less than 0.5%.

5.3.3 DCS Modified Beer-Lambert law for heterogeneous tissue

Tissue is perhaps too often approximated to be optically homogeneous for hemodynamic monitoring, an approach which has the advantage of simplicity. Realistically, however, tissue is heterogeneous; it contains multiple compartments with different optical properties due to vasculature, fat, and bone. Often these regions arise as "layers" below the tissue surface such as scalp, skull, and cortex. Under these conditions, a Taylor series expansion of the DCS optical density can also be used to derive the DCS Modified Beer-Lambert law for heterogeneous media. Assuming that the heterogeneous tissue can be divided into N piecewise homogeneous regions,

then the first-order Taylor series expansion of the DCS optical density is

$$OD_{DCS}(\tau,\rho) \approx OD^0_{DCS}(\tau,\rho) + \sum_{k=1}^{N} \left[\frac{\partial OD^0_{DCS}}{\partial F_k}\Delta F_k + \frac{\partial OD^0_{DCS}}{\partial \mu_{a,k}}\Delta\mu_{a,k} + \frac{\partial OD^0_{DCS}}{\partial \mu'_{s,k}}\Delta\mu'_{s,k} \right]. \tag{5.7}$$

Here, F_k, $\mu_{a,k}$, and $\mu'_{s,k}$ denote the blood flow index, tissue absorption, and tissue scattering for the kth homogeneous region in the tissue, respectively, and $\Delta F_k \equiv F_k - F^0_k$, $\Delta\mu_{a,k} \equiv \mu_{a,k} - \mu^0_{a,k}$, and $\Delta\mu'_{s,k} \equiv \mu'_{s,k} - \mu'^0_{s,k}$ denote the changes in these parameters from baseline. Rearranging Equation 5.7, the DCS Modified Beer-Lambert law for heterogeneous media is:

$$-\log\left(\frac{g_2(\tau,\rho)-1}{g^0_2(\tau,\rho)-1}\right) \approx \sum_{k=1}^{N} \left[d_{F,k}(\tau,\rho)\Delta F_k + d_{a,k}(\tau,\rho)\Delta\mu_{a,k} + d_{s,k}(\tau,\rho)\Delta\mu'_{s,k} \right], \tag{5.8}$$

where $\{d_{F,k} \equiv \partial OD^0_{DCS}/\partial F_k,\ d_{a,k} \equiv \partial OD^0_{DCS}/\partial\mu_{a,k},\ d_{s,k} \equiv \partial OD^0_{DCS}/\partial\mu'_{s,k}\}$ are DCS analogues of the partial pathlengths from DOS/NIRS [130]. These multiplicative weighting factors depend on tissue geometry, on the baseline tissue properties, i.e., $\{F^0_k,\ \mu^0_{a,k},\ \mu'^0_{s,k}\}$, and on τ and ρ. They account for the relative importance of the various regional hemodynamic changes in the DCS optical density perturbation, and they can be estimated in the same manner as described in 5.7.

5.3.4 DCS Modified Beer-Lambert law for two-layer media

The simplest heterogeneous model for tissue is the two-layer geometry, an important special case (Figure 5.3). Researchers have used this geometry in order to distinguish cerebral tissue from extra-cerebral tissue in optical measurements of the head [55, 85, 106, 120, 172, 208, 215], to model tissue burns [24], to distinguish skin from fat/muscle [95, 156], to distinguish fetal from maternal tissues [53], and in other applications. For cerebral applications, the two-layer geometry is comprised of a semi-infinite bottom layer (i.e., corresponding to the cortical regions of the brain) with a distinct blood flow index, absorption coefficient, and scattering coefficient of F_c, $\mu_{a,c}$, and $\mu'_{s,c}$, respectively, and a superficial top layer (i.e., corresponding to extra-cerebral scalp and skull tissue) with thickness ℓ, and distinct tissue properties denoted by F_{ec}, $\mu_{a,ec}$, and $\mu'_{s,ec}$.

The two-layer DCS Modified Beer-Lambert law is the special case of Equation 5.8 for $N = 2$

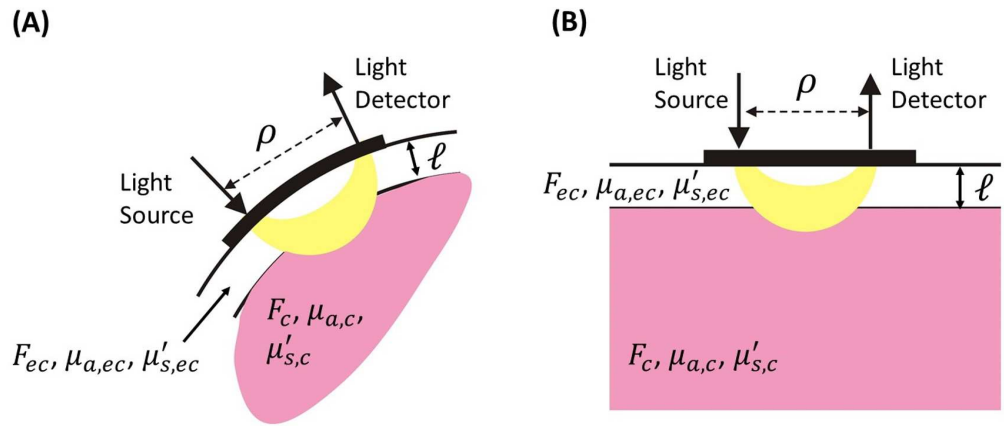

Figure 5.3: **(A)** Two-layer tissue model of the head and **(B)** parallel plane two-layer tissue geometry.

piecewise homogeneous (layered) regions, i.e.,

$$\Delta OD_{DCS}(\tau,\rho) = -\log\left(\frac{g_2(\tau,\rho)-1}{g_2^0(\tau,\rho)-1}\right) \approx d_{F,c}(\tau,\rho)\Delta F_c + d_{F,ec}(\tau,\rho)\Delta F_{ec} + d_{a,c}(\tau,\rho)\Delta\mu_{a,c} + d_{a,ec}(\tau,\rho)\Delta\mu_{a,ec} + d_{s,c}(\tau,\rho)\Delta\mu'_{s,c} + d_{s,ec}(\tau,\rho)\Delta\mu'_{s,ec}. \tag{5.9}$$

Again, the multiplicative weighting factors, $d_{F,i} \equiv \partial OD^0_{DCS}/\partial F_i$, $d_{a,i} \equiv \partial OD^0_{DCS}/\partial \mu_{a,i}$, and $d_{s,i} \equiv \partial OD^0_{DCS}/\partial \mu'_{s,i}$ (with subscript i denoting c (*cerebral*) or ec (*extra-cerebral*)), indicate the relative sensitivity of the DCS optical density variation to cerebral versus extra-cerebral hemodynamic changes. All six parameters depend on delay-time τ, source-detector separation ρ, top layer thickness ℓ, and baseline tissue properties F^0_c, F^0_{ec}, $\mu^0_{a,c}$, $\mu^0_{a,ec}$, $\mu'^0_{s,c}$, and $\mu'^0_{s,ec}$. They can be computed by numerically taking the appropriate derivatives of the two-layer solution to the correlation diffusion equation. For the parallel plane two-layer geometry (Figure 5.3(B)), the solution is [24, 106]:

$$g_1(\tau) = G_1(\tau)/G_1(0),$$
$$G_1(\tau) = \frac{1}{2\pi}\int_0^\infty \tilde{G}_1(\tau) s J_0(s\rho)\mathrm{d}s,$$
$$\tilde{G}_1(\tau) = \frac{\sinh[\kappa_{ec}(z_b+z_0)]}{D_{ec}\kappa_{ec}} \frac{D_{ec}\kappa_{ec}\cosh[\kappa_{ec}\ell] + D_c\kappa_c\sinh[\kappa_{ec}\ell]}{D_{ec}\kappa_{ec}\cosh[\kappa_{ec}(\ell+z_b)] + D_c\kappa_c\sinh[\kappa_{ec}(\ell+z_b)]} - \frac{\sinh[\kappa_{ec}z_0]}{D_{ec}\kappa_{ec}},$$

where $D_i = 1/[3(\mu'_{s,i}+\mu_{a,i})]$, $\kappa_i^2 = (D_i s^2 + \mu_{a,i} + 2\mu'_{s,i}k_0^2 F_i\tau)/D_i$, $z_b = 2D_{ec}(1+R_{eff})/(1-R_{eff})$, $z_0 = 3D_{ec}$, and R_{eff} and k_0 are defined in *Section 5.2* (this solution assumes the top and

bottom layers have the same optical index of refraction).

The two-layer weighting factors for a typical set of extra-cerebral/cerebral tissue properties are plotted in Figure 5.4. Importantly, for a source-detector separation $\rho = 3$ cm, the change in the DCS optical density is more sensitive to changes in flow and absorption in the cerebral layer than in the extra-cerebral layer (except for at very long delay-times). This sensitivity is especially prominent at the shorter delay-times (Figs. 5.4(B), 5.4(C)). In practice the situation is helped by differences in magnitude of cerebral versus extra-cerebral flow (e.g., cerebral flow is quite often 10 times larger than extra-cerebral flow) [250]. We note here that the sensitivity to cerebral flow changes (Figure 5.4(C)) depends on the specific ratio of cerebral to extra-cerebral flow [221]. For example, if $F_c^0 = 6F_{ec}^0$, the ratio of the cerebral flow component ($d_{F,c}\Delta F_c$) to extra-cerebral flow component ($d_{F,ec}\Delta F_{ec}$) is 0.7 at short delay-times for $\rho = 3$ cm (compared to 1.15 for $F_c^0 = 10F_{ec}^0$ in Figure 5.4(C)). Further, this ratio depends on the extra-cerebral layer thickness, because the NIR light intensity is exponentially attenuated with increasing tissue depth. For example, if the extra-cerebral layer thickness is increased to $\ell = 1.1$ cm, then the ratio of the flow components in Figure 5.4(C) at short delay-times is 0.8 for $\rho = 3$ cm.

The increase in the influence of the extra-cerebral layer at longer delay times (Figure 5.4(C)) can be explained from consideration of the pathlengths of light, specifically their association with short versus long correlation decay times τ. Briefly, in the temporal autocorrelation function, long light paths contribute to rapid decays of the signal (short τ) and short light paths contribute to slow decays of the signal (large τ) [186, 257]. Short source-detector separations, e.g., $\rho = 0.5$ cm, mostly sample the superficial layer, and the DCS optical density perturbation is predominantly sensitive to the superficial layer in this case (Figure 5.4(C)). Interestingly, a comparison of Figs. 5.4(C) and 5.4(D) reveals that the DCS optical density is more sensitive to cerebral changes than the DOS/NIRS optical density (consistent with findings of Selb *et al* [221]). Again, this effect arises in part because cerebral blood flow is much greater than extra-cerebral blood flow, and in part because DCS is effectively a time-resolved technique that permits separation of long light paths (shorter delay-times) from short light paths (longer delay-times) [221].

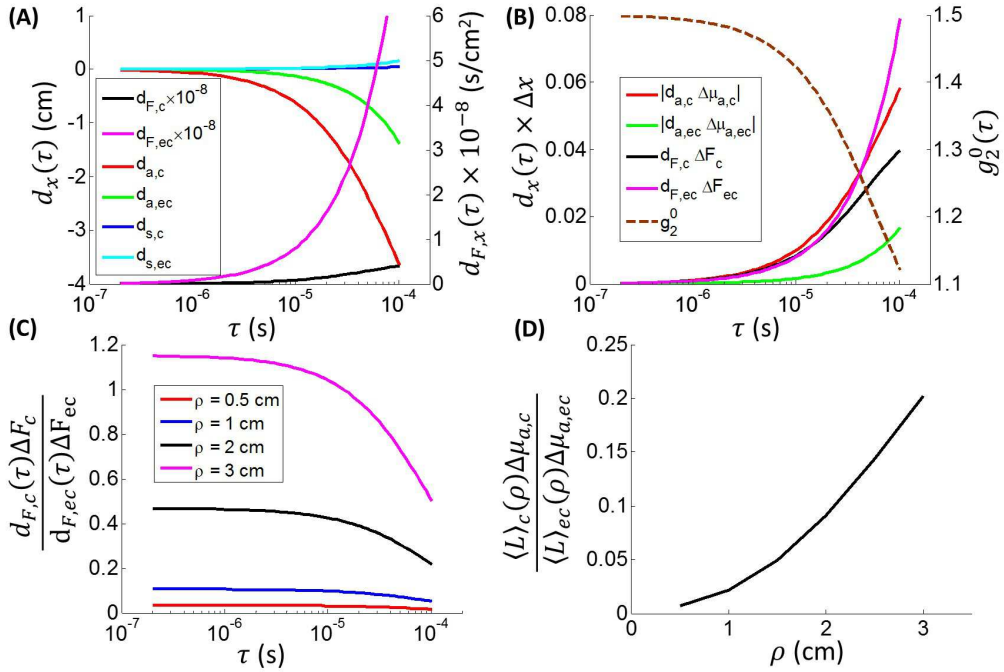

Figure 5.4: **(A)** The two-layer multiplicative weighting factors (see Equation 5.9) for $d_{F,c}$ and $d_{F,ec}$ (right vertical-axis); and for $d_{a,c}$, $d_{a,ec}$, $d_{s,c}$, and $d_{s,ec}$. They are plotted as a function of the correlation time, τ, for source-detector separation, $\rho = 3$ cm, and optical wavelength, $\lambda = 785$ nm, given a set of typical extra-cerebral and cerebral tissue properties [55], i.e., $\mu^0_{a,c} = 0.16$, $\mu^0_{a,ec} = 0.12$, $\mu'^0_{s,c} = 6$, $\mu'^0_{s,ec} = 10$ cm^{-1}; $F^0_c = 10^{-8}$, $F^0_{ec} = 10^{-9}$ cm^2/s; $\ell = 1$ cm, $n = 1.4$, and $n_{out} = 1$. **(B)** The two-layer DCS Modified Beer-Lambert components $d_{F,c}\Delta F_c$, $d_{F,ec}\Delta F_{ec}$, $|d_{a,c}\Delta\mu_{a,c}|$, and $|d_{a,ec}\Delta\mu_{a,ec}|$, plotted as a function of τ for a 10% increase in each parameter. On the right vertical-axis is the intensity autocorrelation function, $g^0_2(\tau)$, for $\beta = 0.5$. Notice that at shorter delay-times for $\rho = 3$ cm, the change in DCS optical density is equally sensitive to changes in cerebral blood flow, extra-cerebral blood flow, and cerebral absorption. The change in DCS optical density (OD_{DCS}) is less sensitive, however, to changes in extra-cerebral absorption. **(C)** The ratio of the cerebral (c) and extra-cerebral (ec) flow components in the DCS optical density perturbation, $\Delta OD_{DCS}(\tau)$ (Equation 5.9), for 4 separations, $\rho = 0.5$, 1, 2, and 3 cm. These data are plotted as a function of τ assuming a 10% increase in cerebral and extra-cerebral blood flow. For the shorter separations of 0.5 and 1 cm, the ratio is substantially less than one; in this case, the DCS optical density is predominantly sensitive to the extra-cerebral layer. At the 3 cm separation, the DCS optical density is more sensitive to cerebral blood flow than extra-cerebral blood flow at the short delay-times, i.e., the ratio is greater than one. However, at longer delay-times, the ratio decreases. **(D)** The ratio of the cerebral and extra-cerebral absorption components in the two-layer Modified Beer-Lambert law for DOS/NIRS, plotted as a function of ρ for a 10% increase in cerebral and extra-cerebral absorption. $\langle L\rangle_c$ and $\langle L\rangle_{ec}$ are the cerebral and extra-cerebral partial pathlengths [91, 130]. Notice from panels (C) and (D) that the DCS optical density is more sensitive to the cerebral layer than the NIRS optical density is, consistent with findings in work of reference [221].

5.4 Results

5.4.1 Validation with simulated data

We tested the semi-infinite DCS Modified Beer-Lambert law (Equation 5.4) using simulated data (Figure 5.5), as well as real data collected from a juvenile pig (Figs. 5.7, 5.8). The simulated DCS data was generated from semi-infinite analytical solutions of the correlation diffusion equation (Equation 5.5) with added noise [276]. Baseline tissue blood flow and optical properties in the simulated data were chosen to be representative of the head [121], and perturbations from baseline were induced by varying blood flow (F) from $+50\%$ to -50%, with constant tissue optical properties. Figure 5.5(A) shows the simulated intensity autocorrelation functions for these baseline and perturbed conditions, plotted as a function of delay-time. The DCS Modified Beer-Lambert law (Equation 5.4) was then applied to this simulated data set to calculate the flow change as a function of delay-time (Figure 5.5(B)). Good agreement between the calculated and actual flow changes is found for a wide range of delay-times.

We next quantified the range of delay-times for which the DCS Modified Beer-Lambert law can be accurately employed. First, recall that the semi-infinite DCS Modified Beer-Lambert law is expected to be accurate in the limit $2\mu_s' k_0^2 F\tau/\mu_a \ll 1$ (5.8). The simulations show that it will remain fairly accurate even when $2\mu_s' k_0^2 F\tau/\mu_a \sim 1$. In order to appreciate the simulation results more generally, we introduce the dimensionless delay-time, $\tau\gamma^0 F^0$, which depends on baseline blood flow (F^0), correlation time-delay (τ), and $\gamma^0 \equiv K_0^0(\mu_s'^0/\mu_a^0)k_0^2 r_1^0$ (see Equation 5.17). When this dimensionless delay-time is ~ 1, then the baseline electric field autocorrelation function has decayed by $\sim 1/\mathrm{e}$. In terms of this dimensionless delay-time, the limit $2\mu_s' k_0^2 F\tau/\mu_a \ll 1$ corresponds to the baseline condition $\tau\gamma^0 F^0 \ll \alpha$, where $\alpha \equiv \gamma^0 \mu_a^0/(2\mu_s'^0 k_0^2)$. For the "typical" conditions chosen for Figure 5.5, $\alpha = 2.3$.

Figure 5.5(B) plots the calculated DCS Modified Beer-Lambert flow change for each dimensionless delay-time. The difference (error) between the calculated flow change and the true flow change (simulated value) is relatively small, even for dimensionless delay-times approaching $\alpha = 2.3$. We also see that for a 50% *increase* in flow, the DCS Modified Beer-Lambert law is accurate over a narrower range of dimensionless delay-time than for a 50% *decrease* (Figure 5.5(B)). The latter behavior is a consequence of the fact that when flow is increased,

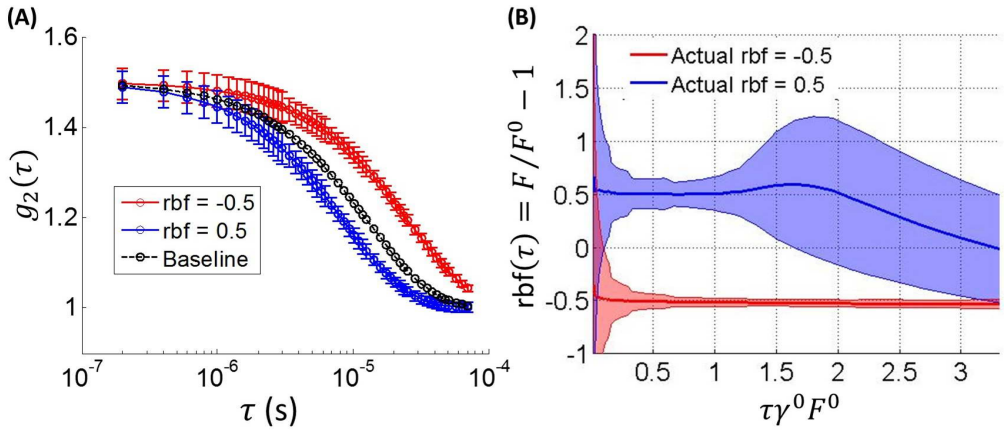

Figure 5.5: **(A)** Simulated semi-infinite intensity autocorrelation curves (mean $\pm$ SD across $N = 10k$ curves) plotted as a function of the delay-time τ for a -50% and $+50\%$ change in flow while tissue optical properties were held constant. The source-detector separation, light wavelength, and baseline tissue properties are $\rho = 3$ cm, $\lambda = 785$ nm, and $\mu_a^0 = 0.1$ cm^{-1}, $\mu_s'^0 = 8$ cm^{-1}, $F^0 = 10^{-8}$ cm^2/s, $n = 1.4$, $n_{out} = 1$, respectively. The simulated DCS data were generated from the semi-infinite solution of the correlation diffusion equation (Equation 5.5) with added noise derived from a correlation noise model [276]. The correlation noise model was evaluated at a baseline DCS intensity of $50k$ photons a second and an averaging time of 2.5 seconds. **(B)** Fractional blood flow changes (mean $\pm$ SD) estimated by applying the semi-infinite DCS Modified Beer-Lambert law, i.e., $rbf(\tau) = \Delta OD_{DCS}(\tau)/(d_F(\tau)F^0)$ (Equation 5.4), to the simulated data. To appreciate the simulated results more generally, these fractional blood flow changes are plotted against the dimensionless delay-time $\tau\gamma^0 F^0$. Here, $(\gamma^0 F^0)^{-1}$, where $\gamma^0 \equiv K_0^0(\mu_s'^0/\mu_a^0)k_0^2 r_1^0$ (see Equation 5.17), is approximately the characteristic decay time of the baseline electric field autocorrelation function (see Section 5.8).

the intensity autocorrelation function decays more rapidly. When the autocorrelation curves are close to fully decayed, then the DCS Modified Beer-Lambert law is predominantly sensitive to correlation noise instead of flow. For a perturbed state from baseline (e.g., $rbf = 50\%$), the limit $2\mu_s' k_0^2 F\tau/\mu_a \ll 1$ corresponds to $\tau\gamma^0 F^0 \ll \alpha(F^0/F)$ (assuming constant optical properties). Thus, a larger value of F reduces the value of the dimensionless delay-time upper limit.

5.4.2 Noise consideration

At very short delay-times, there is little difference between the intensity autocorrelation curves corresponding to different blood flows (Figure 5.5(A)). In this limit, the changes to the DCS optical density are heavily influenced by correlation noise, and flow calculations at the very short delay-times in Figure 5.5(B) are noisy. In general, from applying error propagation rules to Equation 5.4, the noise in the calculated flow change ($\delta(rbf(\tau))$) as a function of τ for constant tissue optical properties is

$$\delta(rbf(\tau)) = \frac{1}{d_F(\tau)F^0}\delta(\Delta OD_{DCS}(\tau)) = \frac{1}{d_F(\tau)F^0}\frac{\delta(g_2(\tau)-1)}{|g_2(\tau)-1|}. \tag{5.10}$$

A correlation noise model can be used to accurately estimate $\delta(g_2(\tau)-1)$ [276]. As τ increases, the correlation noise decreases, and $d_F(\tau)F_0$ increases (Figure 5.2(A)). Both trends reduce the noise in rbf. However, when $|g_2(\tau)-1|$ goes to zero as τ increases, an accompanying increase in noise is expected. From Figure 5.5(B), the noise in rbf falls with increasing delay-time and then levels off around $\tau\gamma^0 F^0 \approx 0.3$; the noise then remains constant for a large range of delay-times.

As one would expect, the flow change computed with a single τ in the DCS Modified Beer-Lambert law is more sensitive to noise than the flow change extracted from nonlinear fits to the semi-infinite correlation diffusion solution across many delay-times. To ameliorate sensitivity to noise, multiple delay-times can also be used for the DCS Modified Beer-Lambert law. Then Equation 5.4 becomes a system of linear equations, i.e., one equation for each delay-time, which can very rapidly be solved to derive flow changes.

5.4.3 In-vivo validation

Finally, we validated the semi-infinite DCS Modified Beer-Lambert law *in-vivo*. In this case, the scalp of a juvenile pig was reflected and 2.5-mm burr holes were drilled through the skull down

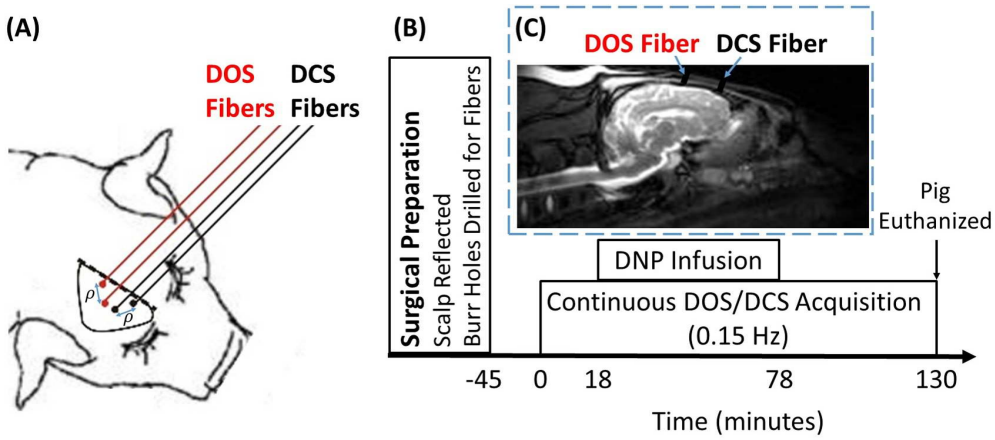

Figure 5.6: **(A)** To monitor hemodynamics in the semi-infinite geometry, a juvenile pig's scalp was reflected, and 2.5 mm burr holes were drilled through the skull for placement of 90-degree optical fibers. A DOS/NIRS source-detector pair (red circles) measured cerebral tissue absorption, and a DCS source-detector pair (black circles) measured cerebral blood flow. The source-detector separation of both pairs is $\rho \approx 1.5$ cm. **(B)** Schematic showing the timeline of the experiment in minutes. Venous infusion of dinitrophenol (DNP, 9 mg/kg) dramatically stimulated cerebral oxygen metabolism and induced a 200% increase in cerebral blood flow. The DCS and DOS techniques were interleaved to measure blood flow and tissue absorption every 7 seconds. **(C)** Anterior-posterior slice of an anatomical MRI scan of a pig with similar weight to the juvenile pig used in this measurement. The burr holes for the two optical fibers closest to the midline in panel (A) have been artificially overlayed on this scan.

to the dura (Figure 5.6). Optical fibers were inserted into the holes to comprise a single DCS source-detector pair for measurement of cerebral blood flow, and a single DOS/NIRS source-detector pair for measurement of cerebral tissue absorption (Figure 5.6(A)). The source-detector separations of both pairs were approximately 1.5 cm, and the baseline cerebral optical properties of the pig were assumed to be $\mu_a^0(785\text{ nm}) = 0.2$ and $\mu_s'^0(785\text{ nm}) = 8\text{ cm}^{-1}$ [140]. Importantly, in this measurement the semi-infinite geometry is a good approximation for the true tissue geometry, because the optical fibers are very close to the brain.

Figure 5.6(B) is a schematic showing the timeline of the experiment. While monitoring with DOS and DCS, a 200% increase in cerebral blood flow was induced in the pig via venous infusion of 9 mg/kg of the drug dinitrophenol (DNP). DNP is a proton transporter across cell membranes which disrupts the mitochondrial proton gradient [181]. In an effort to restore the proton gradient, cells stimulate cerebral oxygen metabolism [181], which in turn leads to a large increase in cerebral blood flow. Additional details about the animal preparation and measurement are in Section 5.9.

The calculated temporal cerebral blood flow changes in the pig (due to DNP) using the DCS Modified Beer-Lambert law are in good agreement with the calculated changes from nonlinear fits to the semi-infinite solution of the correlation diffusion equation (Figure 5.7). Measured cerebral absorption changes (Figure 5.8(B)) were incorporated in the blood flow calculations. Note, when using multiple delay-times in the DCS Modified Beer-Lambert law, the noise in temporal blood flow estimates is comparable to the nonlinear diffusion fit (Figure 5.7(A)). For single τ blood flow monitoring, the temporal blood flow noise is larger, but the average blood flow changes are the same (Figure 5.7(B)); this behavior demonstrates the feasibility of accurate single τ blood flow monitoring with DCS. In Figure 5.7(B), the dimensionless delay-time $\tau\gamma^0 F^0 = 0.33$ (corresponding to $g_2^0(\tau) = 1.3$) was used for single delay-time monitoring.

The estimated cerebral blood flow changes from the DCS Modified Beer-Lambert law are also plotted as a function of dimensionless delay-time in Figure 5.8(A) for two quasi steady-state temporal intervals. During these temporal flow intervals, the blood flow changes were also determined from nonlinear fits to the semi-infinite correlation diffusion solution. The average blood flow changes from the nonlinear fit estimates are 185% and 64% (solid black lines). The horizontal dashed lines in Figure 5.8(A) indicate the noise in the nonlinear fit estimates of blood

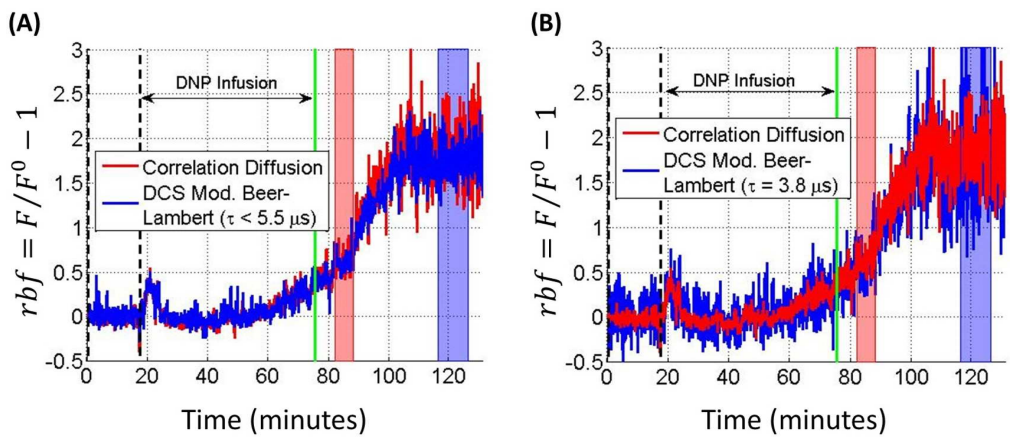

Figure 5.7: Temporal fractional cerebral blood flow changes induced by injection of the drug dinitrophenol (DNP) in a juvenile pig. The baseline flow is $F^0 = 5.34 \times 10^{-8}$ cm^2/s, which is the average blood flow index over the 18 minute time interval between the vertical dashed lines. Cerebral blood flow changes were calculated from nonlinear fits to the semi-infinite correlation diffusion solution (Equation 5.5) and from the semi-infinite DCS Modified Beer-Lambert law (Equation 5.4) using **(A)** multiple delay-times, i.e., $\tau < 5.5$ μs, which corresponds to $g_2^0(\tau) > 1.25$, and **(B)** a single delay-time, i.e., $\tau = 3.8$ μs, which corresponds to $g_2^0(\tau) = 1.3$. Measured tissue absorption changes (Figure 5.8(B)) were incorporated in both the correlation diffusion fit and the DCS Modified Beer-Lambert law. Tissue scattering was assumed to remain constant at $\mu_s' = 8$ cm^{-1}, and the red and blue shaded regions indicate quasi steady-state temporal intervals that are analyzed further in Figure 5.8.

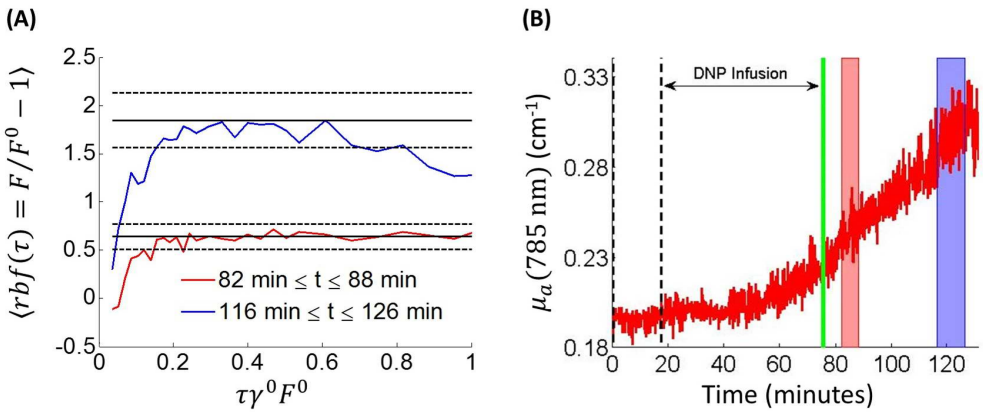

Figure 5.8: **(A)** Mean fractional cerebral blood flow changes (averaged across indicated time intervals in the legend) as a function of the dimensionless delay-time $\tau\gamma^0 F^0$ (see Figure 5.5 caption) in a juvenile pig. **(B)** The pig's cerebral absorption over time, which was calculated from applying the semi-infinite Modified Beer-Lambert law (Equation 5.1) to the measured DOS/NIRS intensity changes from baseline. Note that the shaded regions in panel (B) indicate the temporal intervals averaged over in panel (A). The cerebral blood flow changes in panel (A) were obtained from applying the semi-infinite DCS Modified Beer-Lambert law (Equation 5.4) to the measured intensity autocorrelation curves and the measured cerebral absorption changes. The horizontal solid and dashed black lines in panel (A) indicate the fractional blood flow changes (Mean $\pm$ SD) obtained from fitting the intensity autocorrelation curves to the non-linear semi-infinite correlation diffusion solution (Equation 5.5).

flow (constant because the nonlinear correlation diffusion fit uses all delay-times). Note that the average value of the DCS Modified Beer-Lambert law estimate of the larger flow increase is within the noise of the nonlinear correlation diffusion fit estimate for the delay-time interval $0.16 < \tau\gamma^0 F^0 < 0.82$, which corresponds to the baseline intensity autocorrelation function range $1.15 < g_2^0(\tau) < 1.40$. The smaller flow increase in Figure 5.8(A) is accurate for an even wider range of delay-times, because the intensity autocorrelation function associated with this increase requires a longer delay-time to completely decay (see *Section 5.4.1*).

5.5 Discussion

The Modified Beer-Lambert approach has been employed extensively in the biomedical optics community [99, 122, 166, 175, 219, 248], in large part because of its simplicity. With this approach, researchers have monitored temporal changes in blood oxygenation and blood volume with CW light, using only one source-detector separation. In the present paper, we have extended the Modified Beer-Lambert approach to the DCS measurement, and we have demonstrated the accuracy of this extension in both simulations (Figure 5.5) and *in-vivo* data (Figs. 5.7, 5.8). The DCS Modified Beer-Lambert approach offers some advantages compared to the traditional analysis scheme of fitting intensity autocorrelation data to nonlinear solutions of the correlation diffusion equation.

5.5.1 Real-time estimates of blood flow changes

The DCS Modified Beer-Lambert law is a linear equation relating changes in blood flow to changes in signal for *any* tissue geometry. Although the correlation diffusion solution in the semi-infinite geometry is closed form, the correlation diffusion solutions in more intricate geometries (e.g., curved, layered) are vastly more complex, and consequentially quite time-consuming when fitting data. With the DCS Modified Beer-Lambert approach, the correlation diffusion solutions are needed only once to evaluate the multiplicative weighting factors at the "baseline" tissue state, e.g., Equation 5.13. We emphasize that even for geometries where closed form solutions are not available, these multiplicative weighting factors can still be evaluated numerically. Then, blood flow changes from baseline are rapidly determined by solving a linear equation (Eq.

(5.4) or (5.8)). Consequentially, the DCS Modified Beer-Lambert law is well suited for real-time blood flow monitoring, especially in tissue geometries that are not semi-infinite.

5.5.2 Blood flow monitoring in tissues wherein light propagation is non-diffusive

Diffusive light transport is not required for using the DCS Modified Beer-Lambert approach. In blood flow monitoring applications wherein the photon diffusion model is not valid, the multiplicative weighting factors can be evaluated using solutions of the correlation transport equation [3,73] instead of the correlation diffusion equation (see Section 5.7). For the tissue geometry of interest, the correlation transport equation can be solved numerically with Monte Carlo techniques [24, 186]. Thus, the DCS Modified Beer-Lambert approach facilitates accurate blood flow monitoring for the small source-detector separations typical of endoscopic probes, for complex tissues that contain "non-diffusing" domains such as (arguably) cerebral spinal fluid inside the head [63, 148, 196], and for tissues that contain very high concentrations of blood, as in the liver [144]. In all three of these examples, the assumptions underlying the photon diffusion model are violated, and therefore the photon diffusion model is not expected to be accurate. Another potential application of the non-diffusive DCS Modified Beer-Lambert approach is blood flow monitoring with visible light.

5.5.3 Improved depth sensitivity

The DCS Modified Beer-Lambert law permits blood flow monitoring with intensity autocorrelation measurements at a single delay-time, in contrast to the traditional correlation diffusion approach wherein blood flow estimates are obtained by acquiring and fitting a full, nearly continuous, intensity autocorrelation curve. It is now well established that the autocorrelation function decay times associated with long light paths are relatively short, while the decay times associated with short light paths are relatively long [186, 221, 257]. Thus, the autocorrelation function at shorter delay-times will be inherently more sensitive to deeper tissues in remission geometries (Figure 5.4), which in turn means that the sensitivity of the DCS measurement to blood flow at deeper tissue depths is improved by using short delay-times in the DCS Modified Beer-Lambert

law. Conversely, using long delay-times improves the sensitivity of the DCS measurement to tissue blood flow at shallow depths. This same effect can be achieved by fitting different parts of the intensity autocorrelation curve to the correlation diffusion model. In practice, these correlation diffusion fits still require several delay-times spanning a significant portion of the autocorrelation curve. By using a single delay-time, the experimenter has finer control of the measurement depth sensitivity for DCS measurements. Note that for DCS measurements in transmission geometries [40], the autocorrelation function at longer delay-times (short light paths) will be more sensitive to tissue adjacent to the straight line between source and detector.

5.5.4 Increased temporal resolution of DCS measurements

The DCS Modified Beer-Lambert law offers new routes for increased DCS measurement speed and for simpler instrumentation. Underlying these advantages is again blood flow monitoring with a single delay-time. We and others have used multiple-τ hardware correlators to measure the intensity autocorrelation function [72, 218] at delay-times spanning several orders of magnitude from ~ 100 ns to ~ 10 ms. Achieving sufficient SNR for deep tissue DCS measurements (e.g., as in the brain) typically requires averaging many ($N > 100$) of these 10-ms autocorrelation curves. The single delay-time cerebral blood flow monitoring in the pig shown in Figure 5.7(B) was done at $\tau = 3.8$ μs. Thus, in this example, $\sim$250 blood flow measurements can be acquired in 1 ms, which can then be temporally averaged to reduce noise. In 10 ms, which is roughly the time required to measure a single autocorrelation curve with a multiple-τ correlator, ~ 2500 blood flow measurements can be acquired and averaged. Therefore, even though single-τ blood flow monitoring with the DCS Modified Beer-Lambert law is more sensitive to correlation noise than multiple-τ monitoring (Figure 5.7), the substantial improvement in the blood flow sampling rate with single-τ monitoring means that enough averaging can be employed to compensate for this additional noise while still maintaining high DCS measurement speeds. Blood flow measurements at high acquisition rates are advantageous in several applications, including schemes to filter out motion artifacts in exercising muscle [226]. Single-τ monitoring also makes it possible to use single-τ hardware correlators, which are cheaper than multiple-τ hardware correlators. Alternatively, software correlators [72] for a single delay-time could be implemented.

5.5.5 Filtering contamination from superficial tissues in deep tissue flow monitoring

The same paradigms that have been developed with the Modified Beer-Lambert law to filter contamination from superficial tissues in blood oxygenation measurements of the tissue of interest (e.g., the brain) [91, 197, 215, 217, 235] can also be used in the DCS Modified Beer-Lambert formulation for blood flow monitoring. In fact, these paradigms are likely to work even better with DCS, because DCS is more sensitive to deep brain hemodynamics than continuous-wave DOS/NIRS (Figs. 5.4C, 5.4D) [221].

Building on work done with the DOS/NIRS Modified Beer-Lambert law [91, 215], a useful scheme for filtering superficial tissue contamination in the DCS signal is to employ two source-detector separations. One source-detector separation should be long and the other short. Detected light from the long separation travels through both superficial and deep layers of tissue, but detected light at the short separation is predominantly confined to the superficial layer. Two two-layer DCS Modified Beer-Lambert law equations (corresponding to the two source-detector separations) can then be employed to better isolate the deep tissue blood flow component from the superficial blood flow component. Ideally the experimenter would acquire "initial/baseline" measurements wherein only superficial blood flow is changing.

In cerebral monitoring, one way to change superficial blood flow without affecting cerebral blood flow is to vary the pressure of the optical probe against the head [184]. Initial measurements acquired during probe pressure modulation can then be used to derive the patient-specific weighting factors in the DCS Modified Beer-Lambert law. These weighting factors would subsequently be used to filter superficial contamination in cerebral blood flow monitoring. We will develop this idea further in a future paper.

5.6 Conclusion

The Modified Beer-Lambert extension to the DCS measurement is accurate enough to be useful for blood flow monitoring. It facilitates real-time flow monitoring in complex tissue geometries, provides a novel route for increasing DCS measurement speed, and can be used to probe tissues wherein light transport is non-diffusive. It also can be used to filter signals from superficial

tissues.

5.7 Appendix 1

The multiplicative weighting factors d_F, d_a, and d_s in Equation 5.4 can be estimated by taking the appropriate derivative of the solutions to the correlation diffusion equation applied to the appropriate geometry (e.g., semi-infinite homogeneous, etc.). First, using the Siegert relation, we have:

$$\begin{aligned} d_F(\tau,\rho) &\equiv \frac{\partial OD^0_{DCS}}{\partial F} = \frac{\partial}{\partial F}\left[-\log(g^0_2(\tau,\rho)-1)\right] = \frac{\partial}{\partial F}\left[-\log(\beta[g^0_1(\tau,\rho)]^2)\right] \\ &= \frac{\partial}{\partial F}\left[-\log(\beta) - 2\log(g^0_1(\tau,\rho))\right] = 2\frac{\partial}{\partial F}\left[-\log(g^0_1(\tau,\rho))\right]. \end{aligned} \tag{5.11}$$

Similarly,

$$\begin{aligned} d_a(\tau,\rho) &= 2\frac{\partial}{\partial \mu_a}\left[-\log(g^0_1(\tau,\rho))\right], \\ d_s(\tau,\rho) &= 2\frac{\partial}{\partial \mu'_s}\left[-\log(g^0_1(\tau,\rho))\right]. \end{aligned} \tag{5.12}$$

Here, $g_1(\tau,\rho)$ is the solution to the correlation diffusion equation for the geometry of interest [24, 79], and the derivatives of the solution are evaluated at baseline conditions. In conditions where an analytical solution for the correlation diffusion equation does not exist, the multiplicative weighting factors can be computed numerically:

$$\begin{aligned} d_F(\tau,\rho) &= \frac{2}{\Delta F}\log\left(\frac{g_1(\tau,\rho,F^0-\Delta F/2,\mu^0_a,\mu'^0_s)}{g_1(\tau,\rho,F^0+\Delta F/2,\mu^0_a,\mu'^0_s)}\right), \\ d_a(\tau,\rho) &= \frac{2}{\Delta \mu_a}\log\left(\frac{g_1(\tau,\rho,F^0,\mu^0_a-\Delta\mu_a/2,\mu'^0_s)}{g_1(\tau,\rho,F^0,\mu^0_a+\Delta\mu_a/2,\mu'^0_s)}\right), \\ d_s(\tau,\rho) &= \frac{2}{\Delta \mu'_s}\log\left(\frac{g_1(\tau,\rho,F^0,\mu^0_a,\mu'^0_s-\Delta\mu'_s/2)}{g_1(\tau,\rho,F^0,\mu^0_a,\mu'^0_s+\Delta\mu'_s/2)}\right), \end{aligned} \tag{5.13}$$

where $\Delta F/F^0 = \Delta\mu_a/\mu^0_a = \Delta\mu'_s/\mu'^0_s = 10^{-5}$. Equations (5.11), (5.12), and (5.13) are important intermediate results, which provide generalized expressions for the analytical and numerical computation of the multiplicative weighting factors in the DCS Modified Beer-Lambert law for any homogeneous geometry.

Evaluating these equations requires knowledge of the baseline tissue optical properties and the baseline flow index. The baseline flow index can be obtained from a nonlinear fit of the

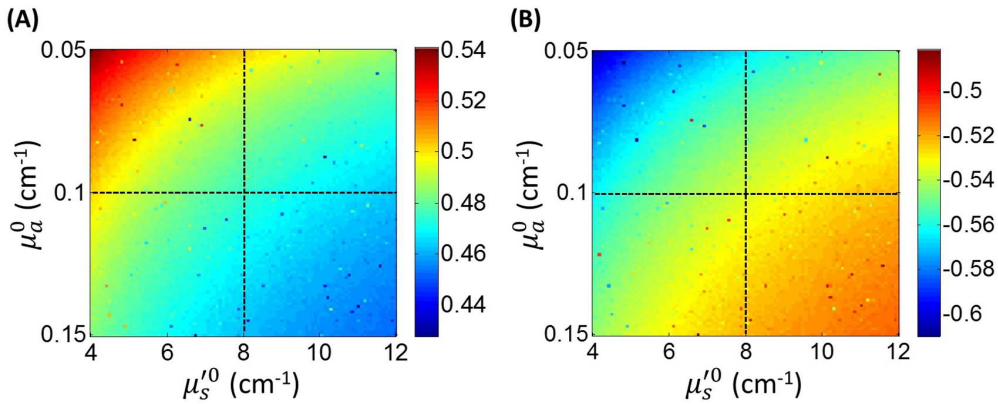

Figure 5.9: Fractional blood flow changes (i.e., $F/F^0 - 1$) computed from applying the semi-infinite DCS Modified Beer-Lambert law (Equation 5.4) with assumed baseline optical properties of μ_a^0 (vertical axis) and $\mu_s'^0$ (horizontal axis) to semi-infinite simulated data with noise ($N = 1k$ curves). The actual blood flow and absorption changes are **(A)** 50% and 15%, and **(B)** -50% and -15%, respectively. Tissue scattering was constant, and the actual baseline properties (including simulated noise parameters) are identical to those in Figure 5.5, e.g., $\mu_a^0 = 0.1$, $\mu_s'^0 = 8$ cm^{-1} (denoted by dashed lines). To compute the absorption changes from the simulated data, the Modified Beer-Lambert law (Equation 5.1) was employed. The differential pathlength ($\langle L \rangle$) in Equation 5.1 was calculated from the assumed baseline optical properties [94]. Finally, the baseline flow index, F^0, was extracted from a nonlinear fit of the simulated baseline data to the semi-infinite correlation diffusion solution (Equation 5.5) evaluated at the assumed baseline optical properties. Errors in the assumed baseline optical properties only have small effects on the computed fractional flow change. Note that the computed fractional blood flow changes are not exactly 50% and -50% when the exact optical properties are assumed because of small errors arising from truncating the tissue absorption terms in the Taylor Series expansion of the DCS optical density (Equation 5.3) to first order.

baseline intensity autocorrelation curve to the correlation diffusion solution (see *Section 5.2*). The baseline tissue optical properties can either be assumed from the literature (e.g., [144]) or measured with time-domain or frequency-domain DOS/NIRS [101, 201]. For typical tissue measurements wherein scattering does not change, the sensitivity in the computed fractional blood flow change to assumed baseline optical properties is small (Figure 5.9). For the example of flow changes shown in Figure 5.9, $\pm 50\%$ errors in the assumed baseline optical properties affected the estimated fractional flow change by only ± 5 percentage points (e.g., from 0.50 to 0.45). Thus, for many applications, errors in the assumed baseline optical properties have little effect on calculated changes in blood flow. Computed fractional flow changes are a little more sensitive to errors in baseline flow than to errors in baseline optical properties. Specifically, for the example of flow changes in Figure 5.9, $\pm 10\%$ errors in baseline flow affected the estimated fractional flow change by ± 5 percentage points, and $\pm 25\%$ errors in baseline flow affected the estimated fractional flow change by ± 10 percentage points (results not shown).

An important assumption in this approach is that the correlation diffusion equation accurately models the electric field autocorrelation function in tissue. This assumption is valid when using large source-detector separations, $\rho \gg 1/(\mu_a + \mu_s')$, to measure highly scattering media with isotropic dynamics [24]. The DCS Modified Beer-Lambert law, Equation 5.4, however, can also be used for correlation transport conditions wherein the correlation diffusion equation breaks down. In this case, the derivatives in Equations (5.11) and (5.12) will have to be applied to the solutions of the so-called correlation transport equation [3, 73], which can be solved numerically with Monte Carlo techniques [24, 186].

5.8 Appendix 2

The semi-infinite solution to the correlation diffusion equation (Equation 5.5) is approximately exponential in the small delay-time limit, i.e., $g_1(\tau) \approx \exp(-\gamma F \tau)$, with $\gamma \equiv K_0(\mu_s'/\mu_a) k_0^2 r_1$. Normalizing the delay-time by the characteristic decay-time, i.e., $\tau_c = (\gamma F)^{-1}$, is a meaningful dimensionless way to express delay-times (Figs. 5.5, 5.8), e.g., $g_1 \approx 0.4$ for $\tau \gamma F = 1$. Further, the DCS Modified Beer-Lambert law (Equation 5.4) is a good approximation in the small delay-time limit because $-\log(g_2(\tau) - 1) = -\log(\beta g_1^2) = 2\gamma\tau F - \log(\beta)$ is linear with respect to

F. To derive the small delay-time limit of the semi-infinite correlation diffusion solution, first note that if the source-detector separation, ρ, is much greater than the photon transport mean-free path through tissue, ℓ_{tr}, then (see Equation 5.2)

$$\begin{aligned} r_b &\approx r_1(1 + x/r_1^2), \\ \frac{1}{r_b} &\approx \frac{1}{r_1}\left(1 - \frac{x}{r_1^2}\right), \end{aligned} \tag{5.14}$$

where $x \equiv 2z_b(z_b + \ell_{tr})$. Substituting Equation 5.14 into Equation 5.2, we see that

$$G_1(\tau) = \frac{3}{4\pi\ell_{tr}} \frac{\exp(-K(\tau)r_1)}{r_1} \left[1 - \exp\left(\frac{-K(\tau)x}{r_1}\right)\left(1 - \frac{x}{r_1^2}\right)\right]. \tag{5.15}$$

In the limit $K(\tau)x/r_1 \ll 1$, which is satisfied at small delay-times, Equation 5.15 simplifies further to

$$G_1(\tau) \approx \frac{3}{4\pi\ell_{tr}} \frac{x\exp(-K(\tau)r_1)}{r_1^2}\left(K(\tau) + \frac{1}{r_1}\right). \tag{5.16}$$

In the more stringent limit $2(\mu_s'/\mu_a)k_0^2 F\tau \ll 1$, the electric field autocorrelation function in Equation 5.16 is approximately exponential:

$$g_1(\tau) = \frac{G_1(\tau)}{G_1(0)} \approx \exp(-\gamma F\tau)\left(1 + \frac{\gamma F\tau}{r_1 K_0 + 1}\right) \approx \exp(-\gamma F\tau), \tag{5.17}$$

where $\gamma = K_0(\mu_s'/\mu_a)k_0^2 r_1$ and $K_0 \equiv K(0) = [3\mu_a(\mu_a + \mu_s')]^{1/2}$.

5.9 Appendix 3

All animal procedures were in accordance with guidelines established by the National Institutes of Health and approved by the Institutional Animal Care and Use Committee of the University of Pennsylvania. Diffuse optical measurements were performed on a male Yorkshire juvenile pig (28 kg). The animal was anesthetized with an initial intramuscular injection of ketamine (25 mg/kg), dexmedetomidine (0.025 mg/kg), and glycopyrolate (0.02 mg/kg), intubated, and then mechanically ventilated with a mixture of $\sim 3\%$ isoflurane in pure oxygen gas. To prepare for hemodynamic monitoring in the semi-infinite geometry, the pig's scalp was reflected over the left hemisphere of the brain, and a dental drill was used to form 2.5 mm burr holes through the skull down to the dura for the placement of optical fibers (see Figure 5.6). One DCS source-detector pair and one DOS/NIRS source-detector pair were used for hemodynamic monitoring. The

positions of these fibers, denoted as (lateral distance from the center of the eye, lateral distance from midline), are (10 mm, 5 mm), (21 mm, 15 mm), (26 mm, 15 mm), and (37 mm, 5 mm) for the DCS source, DCS detector, DOS/NIRS source, and DOS/NIRS detector, respectively. Thus, the source-detector separations for both the DOS/NIRS and DCS pairs are approximately 15 mm.

Upon completion of the surgical preparation, the ventilation of the pig was switched to a mixture of oxygen and nitrogen (3:7) with no isoflurane. Anesthesia was maintained instead with intravenous administration of ketamine (20-60 mg/kg/h). Throughout the rest of the study, arterial oxygen saturation and end-tidal CO2 were continually monitored with blood gas samples from the femoral artery and with a capnograph, respectively. The ventilation rate was initially adjusted to maintain an end-tidal CO2 between 40 and 50 mm Hg.

After inserting ninety-degree bend terminated optical fibers (Fiberoptic Systems, Simi Valley, CA) in the burr holes, a 5-pound sandbag weight was carefully placed on top of the fibers to secure them in place. Two 1-mm diameter multi-mode borosilicate fibers (Fiberoptic Systems) delivered source light to the cerebral tissue, and a third 1-mm diameter multi-mode fiber received diffusing light from the tissue for DOS/NIRS detection. For DCS detection, a 4×1 bundle of 780HP single-mode fibers (Fiberoptic Systems) was used. These fibers interfaced to a portable custom-built instrument designed for hemodynamic monitoring, which is described in detail elsewhere [36, 158]. In the DCS measurement, a continuous wave, long coherence length 785 nm laser (CrystaLaser Inc., Reno, NV) was employed to deliver source light, and the outputs from an array of 4 high sensitivity avalanche photodiodes (SPCM-AQ4C, Excelitas, Canada) operating in photon counting mode were connected to a multiple-τ hardware correlator (Correlator.com, Bridgewater, NJ). In the DOS/NIRS measurement, three lasers (690 nm, 785 nm, 830 nm; OZ Optics, Canada) intensity modulated at 70 MHz were coupled to an optical switch (Di-Con Fiberoptics, Richmond, CA), which sequentially cycled the source light between the three wavelengths. A heterodyne detection scheme using a photomultiplier tube (R928, Hamamatsu, Bridgewater, NJ) was employed for DOS/NIRS detection. The data acquisition was interleaved between DOS/NIRS and DCS to measure blood flow and blood oxygenation with a sampling rate of 0.15 Hz.

After ten minutes of baseline cerebral hemodynamic monitoring in the pig, the drug dinitrophenol (DNP, 9mg/kg) was injected intravenously over an hour to dramatically increase cerebral oxygen metabolism and blood flow [181] (see Figure 5.6(B)). The oxygen content in the ventilated gas was increased as needed to maintain the arterial oxygen saturation in the pig above 95%. Ketamine was also supplemented as needed with boluses of diazapam (0.1-0.2 mg/kg) to ensure adequate sedation as the oxygen metabolism increased. After two hours of hemodynamic monitoring, the pig was euthanized with pentobarbital.

Chapter 6

Pressure Modulation Algorithm to Separate Cerebral Hemodynamic Signals from Extra-cerebral Artifacts

6.1 Introduction

Diffuse correlation spectroscopy [37, 79, 84, 182, 269] (DCS) and near-infrared or diffuse optical spectroscopy [99, 115, 166, 175, 193, 219, 231, 248] (DOS/NIRS) are important optical techniques that employ near-infrared light (NIR) to measure cerebral blood flow, oxygen saturation, and total hemoglobin concentration continuously, non-invasively, and at the bedside. Further, in combination these measurements of blood flow and blood oxygenation provide access to the oxygen metabolic status of the brain [28, 62, 233].

As might be anticipated, this information about cerebral blood flow, blood oxygenation and oxygen metabolism has clinical value. All three parameters, for example, are important biomarkers for brain diseases such as ischemic stroke [127, 229]. Treatments for ischemic stroke (and other diseases) aim to minimize neurological damage by maximizing perfusion to the brain lesion [86, 97, 259]. Numerous treatment interventions for stroke are available, but variability in response-to-treatment has been observed [86, 97, 155], and an effective treatment for one patient may be ineffective, or even harmful, for another patient. Thus, a promising clinical application

for DCS and DOS/NIRS is rapid patient-specific assessment of treatment efficacy. Indeed, DCS and DOS/NIRS enable detection of hemodynamic changes before new neurological symptoms emerge [84, 192, 277].

Unfortunately, the optical techniques have limitations. A well-known drawback for optical monitoring of cerebral tissue is its significant sensitivity to blood flow and oxygenation in the *extra-cerebral* tissues (scalp and skull) [26, 184, 221, 237, 238]. Traditional diffuse optics analyses approximate the head as a homogeneous medium, *e.g.*, no *a priori* anatomical knowledge is used. The homogenous models ignore differences between extra-cerebral hemodynamics and cerebral hemodynamics in the brain, and because extra-cerebral blood flow and blood oxygenation are non-negligible, their responses contaminate the DCS and DOS/NIRS signals. Specifically, extra-cerebral contributions can lead experimenters to incorrectly assign cerebral physiological responses [64, 237, 239].

The DOS/NIRS community has, of course, developed/adapted a number of approaches to ameliorate the extra-cerebral tissue problem. Time series analysis techniques, for example, use filtering schemes to minimize superficial tissue contamination in functional brain mapping measurements [26, 90, 109, 137, 161, 216, 237, 238, 262, 271]. An assumption that underlies these techniques is that superficial tissue contamination arises from systemic effects (*e.g.*, heart rate) that do not correlate with cerebral response because systemic variations are typically damped by cerebral autoregulation. However, for numerous brain diseases, including ischemic stroke, cerebral autoregulation is impaired [65, 111]. In fact, many stroke treatment interventions are based on the notion of impaired cerebral autoregulation and are designed to increase cerebral blood flow through systemic mechanisms (*e.g.*, increased blood pressure). Thus, it is preferable not to filter systemic components from the measured signals. In a different vein, more complex, computationally intensive models have been proposed to handle extra-cerebral heterogeneities directly, including layered models [148, 171, 173, 174, 212, 223, 234, 255, 261], Monte Carlo techniques in realistic geometries of the head [25, 92, 145, 235], and imaging [26, 89, 114, 258]. The complexity of these models, however, can make them impractical to implement for real-time monitoring. Further, these models often require *a priori* anatomical information about the patient's head, as well as knowledge of the optical properties of different tissue types.

In this contribution, we report on a novel implementation scheme for real-time cerebral monitoring with the two-layer model. The two-layer model in cerebral monitoring offers a compromise between simplicity and accuracy [55, 85, 91, 106, 108, 120, 172, 208, 215]. The two-layer model consists of a homogeneous superficial (extra-cerebral) layer above a homogeneous cerebral layer. The key to our new approach is to acquire DCS and DOS/NIRS measurements at multiple optical probe pressures and at multiple source-detector separations. Variations in probe pressure against the head induce variations in extra-cerebral hemodynamics, while cerebral hemodynamics remain constant [184]. We will show how this information can be utilized to derive patient-specific analysis parameters that help to separate cerebral hemodynamics from extra-cerebral blood flow and oxygenation signals. For DCS measurements of blood flow, we employ the pressure modulation scheme and a two-layer Modified Beer-Lambert framework for analysis [12]. For DOS/NIRS measurements, we extend Fabbri *et. al.*'s two-layer Modified Beer-Lambert formulation [91] to include a pressure calibration stage prior to monitoring.

After describing the theory, we demonstrate the ability of this new measurement paradigm/algorithm to filter extra-cerebral contamination in simulations and in functional activation experiments in healthy adult humans. Ultimately, these developments should lead to improved accuracy in real-time monitoring of cerebral flow and oxygen metabolism.

6.2 DCS and DOS/NIRS Monitoring (Homogeneous Tissue Model)

Traditionally, diffuse optical monitoring utilizes homogeneous tissue models of the head, which we review first. The basic measurement geometry for diffuse optical monitoring consists of point illumination and point detection on the tissue surface; the distance between source and detector is ρ (Figure 6.1A). DOS/NIRS is a static technique that measures slow ($0.1 - 1$ s) variations in the detected light intensity induced by changes in tissue absorption (μ_a) and tissue scattering (μ_s'). DCS is a qualitatively different dynamic light scattering technique that measures the rapid (*e.g.*, microsecond scale fluctuations) speckle light intensity fluctuations induced by red blood cell motion. DOS/NIRS measurements are most commonly analyzed with photon diffusion models [96,266] and the Modified Beer-Lambert law [10,67]. Analogously, correlation diffusion models [23, 24] and the so-called DCS Modified Beer-Lambert law [12] can be employed for

analysis of DCS measurements.

The Modified Beer-Lambert law is arguably the most widely used homogeneous tissue model for analysis of DOS/NIRS measurements [10, 67]. The Modified Beer-Lambert law relates changes in tissue optical properties to changes in continuous-wave diffuse optical intensity measurements for light that has been multiply scattered in its trajectory through tissue (Figure 6.1). Specifically, the measured difference in optical density between a "perturbed" state and a "baseline" state is related to tissue scattering and tissue absorption differences of the corresponding perturbed and baseline states, *i.e.*,

$$\Delta OD = -\log\left(\frac{I}{I^0}\right) \approx L\Delta\mu_a + \frac{\mu_a^0}{\mu_s'^0} L\Delta\mu_s' \approx L\Delta\mu_a. \tag{6.1}$$

Here, the tissue optical density is defined as the negative logarithm of the ratio of the detected and incident light intensities (time-averaged), *i.e.*, $OD \equiv -\log(I/I_s)$ for the perturbed state, and $OD^0 \equiv -\log(I^0/I_s)$ (Figure 6.1B) for the baseline state; the incident light intensity, I_s, is assumed to remain constant. $\Delta OD \equiv OD - OD^0$, $\Delta\mu_a \equiv \mu_a - \mu_a^0$, and $\Delta\mu_s' \equiv \mu_s' - \mu_s'^0$ are the differential changes in tissue optical density, tissue absorption, and tissue reduced scattering, respectively, between a perturbed state (OD, μ_a, μ_s') and the baseline state (OD^0, μ_a^0, $\mu_s'^0$). The multiplicative factor, $L \equiv \partial OD^0/\partial\mu_a$, is the so-called differential pathlength, which is approximately the mean pathlength that diffusing photons travel through the medium from source to detector [10]. The Modified Beer-Lambert law (Equation 6.1) is a first order Taylor series expansion of the tissue optical density about tissue absorption and tissue scattering. It is often reasonable to make the additional approximation that the scattering term in Equation 6.1 is negligible compared to the absorption term, because (1), tissue scattering changes that accompany hemodynamic variations are often negligible [12], and (2), the multiplicative factor $\mu_a^0/\mu_s'^0$ for many tissues is much less than one. Multispectral tissue absorption changes determined from Equation 6.1 are then readily converted to estimates of tissue oxy-hemoglobin (HbO) and deoxy-hemoglobin (HbR) concentration changes using the well-known spectra of these molecules [79, 207]. The total hemoglobin concentration (HbT) is the sum of these two chromophore concentrations, and the tissue oxygen saturation (StO_2) is the ratio of oxy-hemoglobin to total hemoglobin: $HbT = HbO + HbR$, $StO_2 = HbO/HbT$.

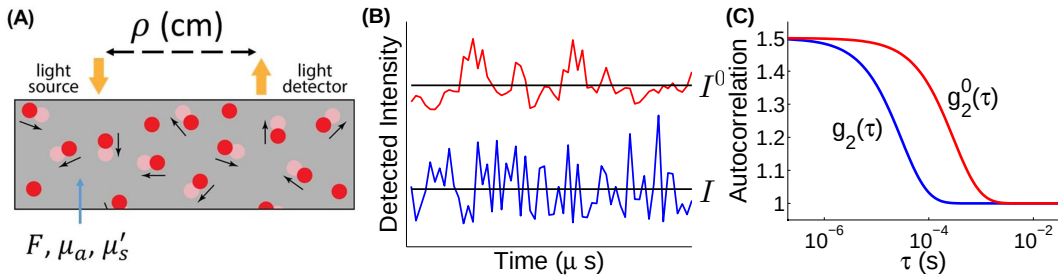

Figure 6.1: **(A)** Schematic for a homogeneous, semi-infinite model of the head with a blood flow index, absorption coefficient, and reduced scattering coefficient of F, μ_a, and μ_s', respectively. The incident source intensity, I_s, is assumed to remain constant over time. Blood cell motion (e.g., red disks at time t and light-red disks at time $t+\tau$) induces fast temporal fluctuations (i.e., speckle intensity fluctuations) in the detected light intensity on the time scale of μs, while absorption changes modify mean light intensities (e.g., averaged on time scales of ms or greater). **(B)** Schematic of detected intensity fluctuations for a baseline tissue state (red curve) and a perturbed state from baseline with higher blood flow and absorption (blue curve). The horizontal black lines are the mean intensities for the two states, denoted as I^0 and I. The fast speckle intensity fluctuations in the two states are characterized by normalized intensity autocorrelation functions (i.e., $g_2^0(\tau)$, $g_2(\tau)$). **(C)** The decay of the intensity autocorrelation function curves is related to tissue blood flow.

Equation 6.1 is valid for any homogeneous geometry, provided the correct differential pathlength is used. The differential pathlength depends on the source-detector separation (ρ), the tissue geometry, and the baseline tissue optical properties (μ_a^0, $\mu_s'^0$) [10, 79]. For the important special case of the semi-infinite homogeneous geometry (Figure 6.1A), the differential pathlength is given by [94]

$$L \approx \frac{3\mu_s'^0\rho^2}{2\left(\rho\sqrt{3\mu_a^0\mu_s'^0}+1\right)}. \tag{6.2}$$

A drawback of the Modified Beer-Lambert law is that it only determines changes in hemoglobin concentrations. For measurement of absolute oxy- and deoxy-hemoglobin concentrations, a photon diffusion model is commonly used. Formally, the detected light intensity is directly proportional to the photon diffusion equation Green's function for the appropriate tissue geometry [79], *i.e.*, $\Phi(\rho)$, which depends on the tissue optical properties (μ_a, μ_s'). Note that the proportionality constant between the measured light intensity , $I(\rho)$, and the photon diffusion Green's function, $\Phi(\rho)$, is the so-called light coupling coefficient to tissue for the source-detector pair. For semi-infinite homogeneous tissue, the continuous-wave photon diffusion equation Green's function

is [79, 123]

$$\Phi(\rho) = \frac{1}{4\pi}\left[\frac{\exp\left(-r_1\sqrt{3\mu_a/\ell_{tr}}\right)}{r_1} - \frac{\exp\left(-r_b\sqrt{3\mu_a/\ell_{tr}}\right)}{r_b}\right]. \tag{6.3}$$

Here, $\ell_{tr} = 1/(\mu_a + \mu_s')$, $r_1 = (\ell_{tr}^2 + \rho^2)^{1/2}$, $r_b = [(2z_b + \ell_{tr})^2 + \rho^2]^{1/2}$, and $z_b = 2\ell_{tr}(1 + R_{eff})/(3(1 - R_{eff}))$, where R_{eff} is the effective reflection coefficient that accounts for the mismatch between the index of refraction of tissue (n) and the index of refraction of the non-scattering medium bounding the tissue (n_{out}), such as air [123]. A standard approach for absolute tissue absorption monitoring in this geometry is to measure $I(\rho)$ at multiple source-detector separations, and then obtain an estimate of μ_a from fitting these measured intensities to the semi-infinite Green's function solution (Equation 6.3). Required inputs for this fit are the light coupling coefficients for each source-detector pair and the tissue scattering coefficient, μ_s'. Knowledge of the light coupling coefficients is typically obtained from phantom calibration [133, 253], and μ_s' is assumed. The assumption of μ_s' is an obvious source of error for continuous-wave DOS/NIRS. In more complex frequency-domain [101] and time-domain [201] DOS/NIRS measurements, both μ_a and μ_s' can be uniquely determined from fitting these measurements to their respective frequency-domain and time-domain Green's functions [79].

To estimate blood flow, DCS quantifies the fast speckle intensity fluctuations of multiply scattered coherent NIR light (coherence length > 5 m) induced by red blood cell motion (Figure 6.1). Specifically, the normalized intensity temporal autocorrelation function, $g_2(\tau) \equiv \langle I(t)I(t+\tau)\rangle/\langle I(t)\rangle^2$, is computed at multiple delay-times, τ, where $I(t)$ is the detected light intensity at time t, and the angular brackets, $\langle\rangle$, represent time-averages. A DCS blood flow index, F, is ascertained from the decay of $g_2(\tau)$ (Figure 6.1C, discussed in more detail below). The DCS blood flow index is directly proportional to tissue blood flow, and has been successfully validated against a plethora of gold-standard techniques [149, 182].

In analogy to DOS/NIRS, a DCS Modified Beer-Lambert law [12] relates differential changes in a "DCS optical density," *i.e.*, $OD_{DCS} \equiv -\log(g_2(\tau) - 1)$, to differential changes in tissue blood flow index (F), tissue absorption (μ_a), and tissue scattering (μ_s'):

$$\Delta OD_{DCS} = -\log\left(\frac{g_2(\tau,\rho) - 1}{g_2^0(\tau,\rho) - 1}\right) \approx d_F(\tau)\Delta F + d_a(\tau)\Delta\mu_a + d_s(\tau)\Delta\mu_s'. \tag{6.4}$$

The multiplicative weighting factors $d_F(\tau) \equiv \partial OD_{DCS}^0/\partial F$, $d_a(\tau) \equiv \partial OD_{DCS}^0/\partial\mu_a$, and

$d_s(\tau) \equiv \partial OD^0_{DCS}/\partial \mu'_s$, can be estimated analytically or numerically using the correlation diffusion model applied to the appropriate geometry [12]. They are analogues of the differential pathlength in the Modified Beer-Lambert law, but note their dependence on delay-time, τ. The DCS optical density is about equally sensitive to blood flow and tissue scattering changes, but less sensitive to tissue absorption changes [12]. If tissue scattering remains constant, and the fractional absorption change is small compared to the blood flow change, then $\Delta OD_{DCS} \approx d_F(\tau)\Delta F$. This is a system of equations, *i.e.*, one equation for each τ, that can be solved for ΔF in a least squares sense. For the special case of the semi-infinite homogeneous geometry, the multiplicative weighting factor is given by [12]

$$d_F(\tau,\rho) = \frac{6\mu_s'^0\left(\mu_s'^0+\mu_a^0\right)k_0^2\tau}{K^0(\tau)}\left[\frac{\exp\left(-K^0(\tau)r_1^0\right)-\exp\left(-K^0(\tau)r_b^0\right)}{\exp\left(-K^0(\tau)r_1^0\right)/r_1^0-\exp\left(-K^0(\tau)r_b^0\right)/r_b^0}\right], \tag{6.5}$$

where $K^0(\tau) = [3\mu_a^0(\mu_a^0+\mu_s'^0)(1+2\mu_s'^0k_0^2F^0\tau/\mu_a^0)]^{1/2}$, $r_1 = (\ell_{tr}^2+\rho^2)^{1/2}$, $k_0 = 2\pi n/\lambda$ is the magnitude of the light wave vector in the medium, and r_1 and r_b are defined in Equation 6.3.

The DCS Modified Beer-Lambert law has a similar drawback to DOS/NIRS in that it only determines blood flow changes. To estimate the absolute blood flow index, F, a correlation diffusion approach is used. Formally, the electric field ($\mathbf{E}(t)$) autocorrelation function, $G_1(\tau) \equiv \langle \mathbf{E}^*(t)\cdot\mathbf{E}(t+\tau)\rangle$, is well modeled by the so-called correlation diffusion equation [23,24], which can be solved analytically or numerically for tissue geometries of interest [24,79]. Tissue blood flow is ascertained by fitting the solution for the normalized electric field autocorrelation function, $g_1(\tau) = G_1(\tau)/G_1(\tau=0)$, to the measured normalized intensity autocorrelation function using the Siegert relation [168]: $g_2(\tau) = 1+\beta|g_1(\tau)|^2$, where β is a constant determined primarily by experimental collection optics and source coherence.

For semi-infinite homogeneous tissue, the solution to the correlation diffusion equation is [24,79]:

$$G_1(\tau) = \frac{3}{4\pi\ell_{tr}}\left[\frac{\exp\left(-K(\tau)r_1\right)}{r_1}-\frac{\exp\left(-K(\tau)r_b\right)}{r_b}\right], \tag{6.6}$$

where $K(\tau)$ is defined in Equation 6.5, and r_1, r_b, and ℓ_{tr} are defined in Equation 6.3.

A standard approach for blood flow monitoring with DCS in this geometry is to derive $g_1(\tau)$ from measurements of $g_2(\tau)$ via the Siegert relation. Then, the semi-infinite correlation diffusion solution (Equation 6.6) is fit to $g_1(\tau)$ using a nonlinear minimization algorithm, and an estimate of the blood flow index (F) is obtained from the fit. As discussed above, these homogeneous

head models do not distinguish cerebral hemodynamics from extra-cerebral hemodynamics, and are thus prone to extra-cerebral contamination.

6.3 Probe Pressure Modulation Algorithm for Cerebral Blood Flow Monitoring with DCS

Here we introduce our pressure modulation algorithm. The scheme employs DCS measurements of the brain tissues at two probe pressures and two source-detector separations to reduce extra-cerebral contamination in cerebral blood flow monitoring. To distinguish extra-cerebral flow from cerebral flow, the head is modeled as a two-layer medium [24, 91, 106, 215], and the source-detector separations are chosen such that detected light at the long separation (*e.g.*, $\rho_l = 3$ cm) travels through both layers, but detected light at the short separation (*e.g.*, $\rho_s = 1$ cm) is predominantly confined to the extra-cerebral layer (Figure 6.2A). Underlying this approach is our previous work which showed that an increased probe pressure on the head is accompanied by a decrease in extra-cerebral flow; cerebral blood flow is unchanged by probe pressure variation [184]. Thus, the pressure-induced variation in the long-separation DCS signal (*e.g.*, Figure 6.2B) is due only to changes in extra-cerebral flow. This extra-cerebral flow change, in turn, is readily determined by the pressure-induced change measured in the short DCS separation signal (*e.g.*, Figure 6.2C) which can be analyzed using the semi-infinite medium approximation (Equation 6.6).

We will show that the subject-specific relative contributions of extra-cerebral and cerebral tissues to the long separation DCS signal can be determined from the measured pressure-induced changes in the DCS signal at the long and short separations. Importantly, this patient specific calibration with pressure modulation permits separation of the cerebral and extra-cerebral blood flow components in all subsequent measurements.

The results derived in Sections 6.3.1 and 6.3.2 are for the special case of constant tissue absorption and tissue scattering. In practice tissue scattering often remains roughly constant during hemodynamic changes. Further, for many cerebral processes, blood flow changes by a substantially larger fraction than absorption. For example, for the finger tapping functional response [85], $F_c/F_c^0 \sim 1.5$, $\mu_{a,c}/\mu_{a,c}^0 \sim 1.1$ (at $\lambda = 785$ nm); in this case the flow contribution

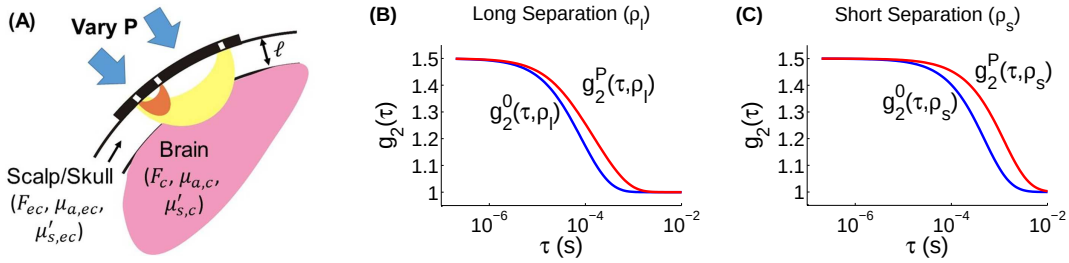

Figure 6.2: **(A)** Two-layer tissue model of the head, which is comprised of a semi-infinite bottom layer (i.e., corresponding to the cortical regions of the brain) with a distinct blood flow index, absorption coefficient, and scattering coefficient of F_c, $\mu_{a,c}$, and $\mu'_{s,c}$, respectively, and a superficial top layer (i.e., corresponding to extra-cerebral scalp and skull tissue) with thickness ℓ, and distinct tissue properties denoted by F_{ec}, $\mu_{a,ec}$, and $\mu'_{s,ec}$. The head is probed with a long source-detector separation, ρ_l (yellow shading), and a short source-detector separation, ρ_s (red shading), and the probe pressure against the head is varied. Increasing the probe pressure from P^0 (blue curves) to P (red curves) induces a change in the DCS signal ($g_2(\tau)$) at both the long separation (panel **(B)**) and the short separation (panel **(C)**). These signal changes arise entirely from pressure-induced changes in extra-cerebral flow [184].

dominates the DCS signal change [12]. We derive the general case wherein tissue absorption and scattering vary in Appendix 6.10.

6.3.1 Two-layer Modified Beer-Lambert Laws for Flow at Long and Short Separations

To filter contamination from extra-cerebral tissues in blood flow measurements of cerebral tissue, we use a two-layer Modified Beer-Lambert formulation for blood flow based on the DCS measurement [12]. In analogy with the DOS/NIRS Modified Beer-Lambert law [10, 67, 130], a "DCS optical density" for the long and short source-detector separations at delay-time τ is defined as $OD_{DCS}^{\text{long}} \equiv -\log(g_2(\tau,\rho_l)-1)$ and $OD_{DCS}^{\text{short}} \equiv -\log(g_2(\tau,\rho_s)-1)$, respectively. Here, $g_2(\tau,\rho_l)$ and $g_2(\tau,\rho_s)$ are the measured long and short separation intensity autocorrelation functions with cerebral and extra-cerebral DCS blood flow indices F_c and F_{ec}. Assuming constant tissue absorption and scattering, the two-layer Modified Beer-Lambert laws for the long

and short separations are [12]:

$$\Delta OD_{DCS}^{\text{long}} \equiv -\log\left[\frac{g_2(\tau,\rho_l)-1}{g_2^0(\tau,\rho_l)-1}\right] = d_{F,c}(\tau,\rho_l)\Delta F_c + d_{F,ec}(\tau,\rho_l)\Delta F_{ec}, \tag{6.7}$$

$$\Delta OD_{DCS}^{\text{short}} \equiv -\log\left[\frac{g_2(\tau,\rho_s)-1}{g_2^0(\tau,\rho_s)-1}\right] = d_{F,ec}(\tau,\rho_s)\Delta F_{ec}, \tag{6.8}$$

where $g_2^0(\tau,\rho_l)$ and $g_2^0(\tau,\rho_s)$ are the "baseline" intensity autocorrelation functions at the long and short separations with cerebral and extra-cerebral DCS blood flow indices F_c^0 and F_{ec}^0 (note that the superscript "0" indicates baseline). The differential changes from baseline of cerebral and extra-cerebral blood flow are $\Delta F_c \equiv F_c - F_c^0$ and $\Delta F_{ec} \equiv F_{ec} - F_{ec}^0$, and the multiplicative weighting factors $d_{F,c}(\tau,\rho_l) \equiv \partial OD_{DCS}^{\text{long},0}/\partial F_c$ and $d_{F,ec}(\tau,\rho_l) \equiv \partial OD_{DCS}^{\text{long},0}/\partial F_{ec}$ indicate the relative sensitivity of the long separation DCS optical density variation to cerebral versus extra-cerebral blood flow changes. For the short separation, the sensitivity of DCS optical density variation to extra-cerebral blood flow changes is $d_{F,ec}(\tau,\rho_l) \equiv \partial OD_{DCS}^{\text{short},0}/\partial F_{ec}$, and we assume that because the short separation predominantly samples the extra-cerebral layer, the short separation signal is not sensitive to cerebral blood flow changes.

Solving the system of Eqs. (6.7) and (6.8) for ΔF_c, we obtain

$$\Delta F_c = \frac{1}{d_{F,c}(\tau,\rho_l)}\left[\Delta OD_{DCS}^{\text{long}} - \frac{d_{F,ec}(\tau,\rho_l)}{d_{F,ec}(\tau,\rho_s)}\Delta OD_{DCS}^{\text{short}}\right]. \tag{6.9}$$

Notice that Equation 6.9 is a linearized implementation of the two-layer head model (Figure 6.2) that enables rapid monitoring of cerebral blood flow changes in real time. This implementation requires only one DCS delay-time τ for cerebral monitoring, but to ameliorate sensitivity to noise, multiple delay-times can also be used. Then, Equation 6.9 becomes a system of linear equations, i.e., one equation for each delay-time, which can be rapidly solved for ΔF_c. Utilizing Equation 6.9 in both the single and multiple delay-time implementations requires knowledge of $d_{F,c}(\tau,\rho_l)$ and $d_{F,ec}(\tau,\rho_l)/d_{F,ec}(\tau,\rho_s)$. A key result of this paper is that these weighting factors can be estimated from "initial/baseline" DCS measurements acquired during probe pressure modulation against the head.

6.3.2 Probe Pressure Modulation Calibration of DCS

A simple way to calibrate DCS for cerebral flow monitoring is to acquire long and short separation DCS measurements of the brain tissues at two probe pressures (i.e., P, P^0). It is not

necessary to know the exact magnitudes of the probe pressures against the head, and neither probe pressure has to be high enough for there to be risk of patient discomfort. The key is that changing the probe pressure from P^0 to P induces a large enough change in extra-cerebral blood flow such that both the long and short separation DCS signals change measurably (e.g., as in Figure 6.2B,C).

6.3.2.1 Determination of $d_{F,ec}(\tau,\rho_l)/d_{F,ec}(\tau,\rho_s)$

Recall that probe pressure modulation against the head affects extra-cerebral blood flow, but not cerebral blood flow [184], i.e., $\Delta F_c = 0$ from probe pressure changes. Thus, for relating DCS measurements acquired at two different probe pressures, Eqs. (6.7) and (6.8) simplify to

$$\Delta OD_{DCS}^{\text{long},P} \equiv -\log\left[\frac{g_2^P(\tau,\rho_l)-1}{g_2^0(\tau,\rho_l)-1}\right] = d_{F,ec}(\tau,\rho_l)\Delta F_{ec}^P, \tag{6.10}$$

$$\Delta OD_{DCS}^{\text{short},P} \equiv -\log\left[\frac{g_2^P(\tau,\rho_s)-1}{g_2^0(\tau,\rho_s)-1}\right] = d_{F,ec}(\tau,\rho_s)\Delta F_{ec}^P, \tag{6.11}$$

where $g_2^P(\tau,\rho_l)$ and $g_2^P(\tau,\rho_s)$ are the long and short separation intensity autocorrelation functions acquired at pressure P wherein the cerebral and extra-cerebral flow indices are F_c^0 and F_{ec}^P, and $\Delta F_{ec}^P \equiv F_{ec}^P - F_{ec}^0$ is the pressure induced extra-cerebral flow change. Dividing Equation 6.10 by Equation 6.11 enables direct measurement of the ratio $d_{F,ec}(\tau,\rho_l)/d_{F,ec}(\tau,\rho_s)$, i.e.,

$$\frac{d_{F,ec}(\tau,\rho_l)}{d_{F,ec}(\tau,\rho_s)} = \frac{\Delta OD_{DCS}^{\text{long},P}}{\Delta OD_{DCS}^{\text{short},P}}. \tag{6.12}$$

Substituting Equation 6.12 into Equation 6.9, we obtain

$$\Delta F_c = \frac{1}{d_{F,c}(\tau,\rho_l)}\left[\Delta OD_{DCS}^{\text{long}} - \frac{\Delta OD_{DCS}^{\text{long},P}}{\Delta OD_{DCS}^{\text{short},P}}\Delta OD_{DCS}^{\text{short}}\right]. \tag{6.13}$$

To the extent that the two-layer model (Figure 6.2) accurately models the head, cerebral blood flow monitoring obtained from Equation 6.13 will not be affected by extra-cerebral blood flow changes. The assumptions used to derive Equation 6.13 are (1), probe pressure modulation has no effect on cerebral blood flow, and (2), tissue absorption and scattering remain constant. In Appendix 6.10, Equation 6.13 is extended to the more general case wherein tissue absorption and scattering are changing, i.e., Equation 6.34. For accurate measurements of the magnitude of the cerebral blood flow change, knowledge of $d_{F,c}(\tau,\rho_l)$ is also required.

6.3.2.2 Determination of the weighting factor $d_{F,c}(\tau, \rho_l)$

As we described previously [12], the multiplicative weighting factor $d_{F,c}(\tau, \rho_l)$ can be computed by numerically taking the appropriate derivative of the two-layer correlation diffusion solution (G_1) [24, 106]:

$$\begin{aligned} d_{F,c}(\tau, \rho_l) &\equiv \frac{\partial OD_{DCS}^{\text{long},0}}{\partial F_c} = 2\frac{\partial}{\partial F_c}\left(-\log\left[G_1^0(\tau, \rho_l)\right]\right), \\ &\approx \frac{2}{\Delta F_c}\log\left[\frac{G_1(\tau, \rho_l, F_c^0 - \Delta F_c/2, F_{ec}^0, \mu_{a,c}^0, \mu_{a,ec}^0, \mu_{s,c}'^0, \mu_{s,ec}'^0, \ell)}{G_1(\tau, \rho_l, F_c^0 + \Delta F_c/2, F_{ec}^0, \mu_{a,c}^0, \mu_{a,ec}^0, \mu_{s,c}'^0, \mu_{s,ec}'^0, \ell)}\right], \end{aligned} \tag{6.14}$$

where $\Delta F_c/F_c^0 = 10^{-5}$. Evaluating Equation 6.14 requires knowledge of the extra-cerebral layer thickness (ℓ), the baseline flow levels (F_c^0, F_{ec}^0), and baseline tissue optical properties ($\mu_{a,c}^0$, $\mu_{a,ec}^0$, $\mu_{s,c}'^0$, $\mu_{s,ec}'^0$).

Ideally, the extra-cerebral layer thickness is known from *a priori* anatomical information (e.g., MRI scan), and the baseline tissue optical properties are measured with concurrent frequency-domain or time-domain DOS/NIRS [108, 120, 156, 157, 208]. Then, estimates of F_c^0 and F_{ec}^0 are determined from simultaneously fitting the long separation intensity autocorrelation curves measured at two pressures ($g_2^0(\tau, \rho_l)$, $g_2^P(\tau, \rho_l)$) to the two-layer correlation diffusion solution [24, 106]. Important constraints used in this fit are that cerebral blood flow is the same for both probe pressures, i.e., $\Delta F_c^P = 0$, and that the pressure-induced fractional extra-cerebral blood flow change, $\Delta F_{ec}^P/F_{ec}^0$, is determined from the short separation measurements (i.e., $g_2^0(\tau, \rho_s)$, $g_2^P(\tau, \rho_s)$) via semi-infinite methods (Section 6.2). These constraints provided by the pressure calibration data make the nonlinear optimization in the fit more tractable and less sensitive to noise.

Note that if it is not feasible to measure baseline tissue optical properties concurrently, then they need to be assumed based on published cerebral/extra-cerebral measurements in the literature [55, 108, 144, 221]. For some patients, *a priori* anatomical information may also not be available, in which case the extra-cerebral layer thickness, ℓ, could be a third free parameter in the two-layer fit. Although fitting for three free parameters instead of two clearly makes the fit more susceptible to noise and cross-talk, the fitting constraints provided by pressure calibration still enable reasonable estimates of F_c^0, F_{ec}^0, and ℓ.

An alternative approach for using the short separation data is to fit the semi-infinite correlation diffusion solution to $g_2^0(\tau, \rho_s)$ for F_{ec}^0 and to $g_2^P(\tau, \rho_s)$ for F_{ec}^P (see Section 6.2). When using these absolute extra-cerebral flow indices as constraints in the two-layer fit to the long separation data, there are only two free parameters (F_c^0, ℓ) to fit for instead of three (F_c^0, F_{ec}^0, ℓ). However, the absolute extra-cerebral flow indices are sensitive to errors in extra-cerebral tissue optical properties [141], source-detector separation, head curvature, and heterogeneities within the scalp. From our experience, the first approach that utilizes robust fractional extra-cerebral flow change measurements is more reliable.

6.3.3 Summary

Figure 6.3 is a flow chart depicting the steps in the probe pressure modulation algorithm for filtering superficial tissue contamination in cerebral flow monitoring with DCS. In the "calibration stage" of the algorithm, intensity autocorrelation measurements at two probe pressures and two source-detector separations are used to compute the ratio $d_{F,ec}(\tau, \rho_l)/d_{F,ec}(\tau, \rho_s)$ ("calibration term 1") and the long separation weighting factor $d_{F,c}(\tau, \rho_l)$ ("calibration term 2"). These calibration terms are then employed in the "monitoring stage" to permit the rapid estimation of cerebral flow changes (ΔF_c). To obtain the fractional cerebral flow change from baseline, simply divide ΔF_c by the baseline cerebral flow index, F_c^0, obtained in the calibration stage. Although two probe pressures is usually sufficient, acquiring DCS data at more than two probe pressures constrains the nonlinear optimization in the two-layer fit for F_c^0, F_{ec}^0, and ℓ even further. Provided that the probe pressures remain less than the venous pressure in the scalp (i.e., $F_{ec} > 0$), then there is a distinct long separation autocorrelation curve for each probe pressure to simultaneously fit the two-layer model to. Thus, additional probe pressures yield additional data for the two-layer fit in the calibration stage. To determine the ratio $d_{F,ec}(\tau, \rho_l)/d_{F,ec}(\tau, \rho_s)$ with more than two probe pressures ("calibration term 1"), evaluate Equation 6.12 for each probe pressure and then take the average ratio over all pressures.

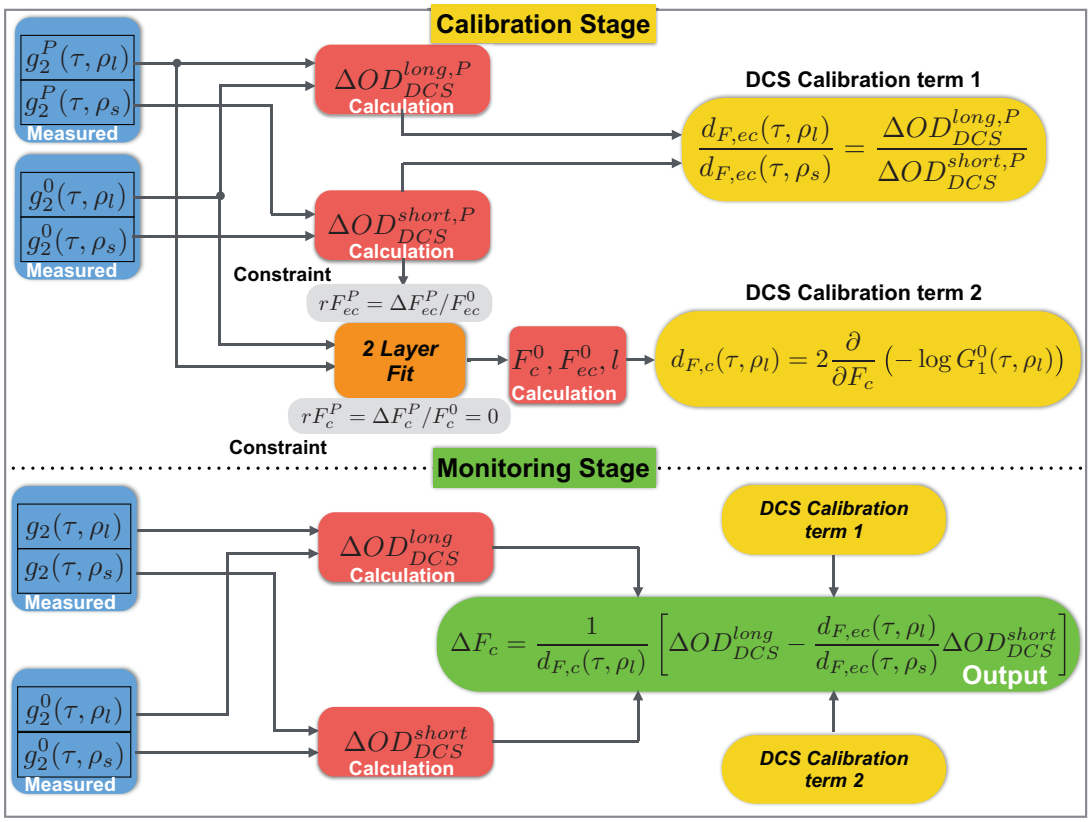

Figure 6.3: Flow chart of probe pressure modulation algorithm for cerebral blood flow monitoring (ΔF_c) with DCS. In the "calibration stage", baseline long and short separation intensity autocorrelation functions measured at probe pressure P^0 ($g_2^0(\tau,\rho_l)$, $g_2^0(\tau,\rho_s)$) and at probe pressure $P \neq P^0$ ($g_2^P(\tau,\rho_l)$, $g_2^P(\tau,\rho_s)$) are used to calculate $\Delta OD_{DCS}^{\text{long},P}$ (Equation 6.10) and $\Delta OD_{DCS}^{\text{short},P}$ (Equation 6.11). These parameters are in turn used to evaluate "calibration term 1" (Equation 6.12). "Calibration term 2" is the numerical evaluation of $d_{F,c}(\tau,\rho_l)$ (Equation 6.14), which requires knowledge of the baseline cerebral and extra-cerebral flow indices (F_c^0,F_{ec}^0) and the extra-cerebral layer thickness (ℓ). F_c^0, F_{ec}^0, and ℓ are extracted from a simultaneous fit of $g_2^0(\tau,\rho_l)$ and $g_2^P(\tau,\rho_l)$ to the two-layer correlation diffusion model given the constraints that pressure modulation does not change cerebral flow ($\Delta F_c^P = 0$) and that the pressure-induced fractional extra-cerebral flow change ($\Delta F_{ec}^P/F_{ec}^0$) is determined from the short separation measurements using semi-infinite methods (Section 6.2). For cases where *a priori* knowledge of the extra-cerebral layer thickness is available, this two-layer fit is even more constrained. In the "monitoring stage", calibration terms 1 and 2 are employed to convert subsequent measurements of differential long and short separation DCS optical density changes, i.e., $\Delta OD_{DCS}^{\text{long}}$ (Equation 6.7) and $\Delta OD_{DCS}^{\text{short}}$ (Equation 6.8), to differential cerebral flow changes via Equation 6.13. Note that the baseline used for the calibration stage and for the monitoring stage is the same. Finally, for this paper, we utilized all of the delay times satisfying the limit $g_2^0(\tau,\rho_l) > 1.25$ to solve Equation 6.13.

6.3.4 Correlation noise sensitivity

The probe pressure modulation scheme depicted in Figure 6.3 is a fast, patient-specific implementation of the two-layer model for cerebral flow monitoring, but a big drawback is a high sensitivity to correlation noise, especially at short delay-times. This sensitivity arises from the fact that correlation noise is largest at short delay-times [276], while the DCS optical density perturbations are typically small. Combined, these opposing trends with decreasing delay-time imply that the measured DCS optical density perturbations can easily be dominated by correlation noise instead of flow changes for non-optimal measurement conditions. Specifically, let's consider a key step in the algorithm wherein calibration term 1 (Equation 6.12) is computed. Compared to longer delay-times, the perturbation $\Delta OD_{DCS}^{\text{long},P}$ at short τ is less sensitive to the superficial blood flow changes induced by probe pressure modulation. This is because the rapid decays of the temporal autocorrelation signal at short τ are mostly due to long light paths that spend less time in superficial tissues than the short light paths contributing to slow decays (long τ) [186, 221]. Therefore, the computation of calibration term 1 at short τ is prone to correlation noise. Substantial noise contamination can lead to a significant systematic error in subsequent cerebral flow monitoring via Equation 6.13.

Another noise-related issue is that the autocorrelation signals at the long and short separations decay at substantially different rates. Thus, at delay-times where the long separation signal has decayed significantly, the short separation signal has decayed much less. At these delay-times, the differences in short separation decays induced by extra-cerebral flow changes are less pronounced than they are at longer delay-times, which means the measurement of $\Delta OD_{DCS}^{\text{short}}$ is also prone to correlation noise.

One way to address the correlation noise issue is to evaluate Equation 6.13 for ΔF_c only using longer delay-times where the DCS optical density perturbations are larger. However, excluding short τ is not desirable because it is the short τ that are most sensitive to cerebral flow. Further, the noise-related improvements associated with longer τ are partially canceled from using fewer delay-times to solve Equation 6.13.

A more robust approach for handling correlation noise is to solve Equation 6.7 directly for

ΔF_c:

$$\Delta F_c = \frac{1}{d_{F,c}(\tau, \rho_l)} \left[\Delta OD_{DCS}^{\text{long}} - d_{F,ec}(\tau, \rho_l) \Delta F_{ec} \right], \tag{6.15}$$

where $d_{F,c}(\tau, \rho_l)$ is given by Equation 6.14, $d_{F,ec}(\tau, \rho_l) \equiv \partial OD_{DCS}^{\text{short},0} / \partial F_{ec}$ is given by the extra-cerebral analogue of Equation 6.14, and ΔF_{ec} is obtained from short separation measurements via semi-infinite techniques (Section 6.2). Pressure variation is still used in the implementation of Equation 6.15 via the two-layer fit for F_c^0, F_{ec}^0, and ℓ (Figure 6.3). These baseline properties are inputs in the evaluation of $d_{F,c}(\tau, \rho_l)$ and $d_{F,ec}(\tau, \rho_l)$. Then, to determine the extra-cerebral flow change, use the relation $\Delta F_{ec} = F_{ec}^0 \times rF_{ec}$, where $rF_{ec} \equiv \Delta F_{ec} / F_{ec}^0$ is the fractional extra-cerebral flow change obtained from fitting the semi-infinite model to the short separation autocorrelation curves. Equation 6.15 is less sensitive to correlation noise, but more reliant on the accuracy of the baseline tissue properties for filtering superficial tissue contamination.

6.4 Probe Pressure Modulation Algorithm for Cerebral Blood Flow Monitoring with DCS: Practical Example

As a practical example for using this pressure modulation algorithm in the clinic, let's consider cerebral blood flow monitoring during head-of-bed (HOB) position changes in stroke patients [86, 97] (Figure 6.4). To maximize perfusion at the stroke site and the surrounding ischemic penumbra, flat head-of-bed positioning (Figure 6.4B) is often used at the clinic. Changing the head-of-bed angle from a baseline position of $30°$ (Figure 6.4A) to a flat position of $0°$ does increase flow in the majority of patients. However, in a significant minority of patients (25%), a paradoxical decrease in flow was observed [86, 97]. Thus, optical cerebral flow monitoring with the probe pressure modulation algorithm has potential for optimizing head-of-bed position in individual patients.

To determine cerebral flow changes induced by HOB position changes, the first step in the calibration stage is to acquire long and short separation intensity autocorrelation measurements at the $30°$ HOB position with a probe pressure P (e.g., $P = 20$ mm Hg) applied against the scalp, i.e., $g_2^P(\tau, \rho_l)$, $g_2^P(\tau, \rho_s)$. Step 2 is to decrease the probe pressure against the scalp to

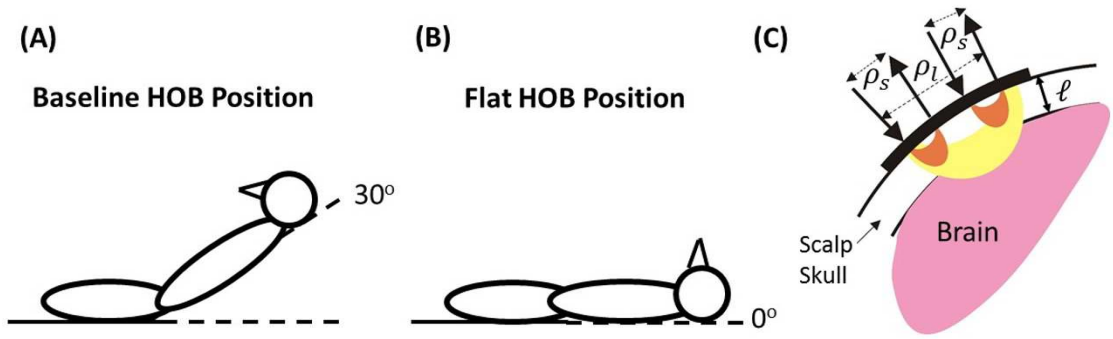

Figure 6.4: Head-of-bed (HOB) positioning at **(A)** the baseline condition of $30°$ and **(B)** the perturbed condition of $0°$ (flat). **(C)** Schematic of two-layer geometry of the head probed with a long separation, ρ_l, and two short separations, ρ_s. The downward and upward pointing arrows indicate DCS source and detector positions, respectively.

P^0 (e.g., $P^0 = 5$ mm Hg). Then, at the new probe pressure P^0 and the $30°$ HOB position, acquire a second set of long and short separation intensity autocorrelation measurements, i.e., $g_2^0(\tau, \rho_l)$, $g_2^0(\tau, \rho_s)$. Using these two sets of measurements, compute calibration terms 1 and 2 from Figure 6.3. These calibration terms are employed in the monitoring stage to determine cerebral flow changes from baseline (Figure 6.3). Continuing with our example, change the HOB position from $30°$ to $0°$, and acquire $g_2(\tau, \rho_l)$ and $g_2(\tau, \rho_s)$, which are the long and short separation autocorrelation measurements at the $0°$ HOB position. The cerebral flow change from the HOB change, i.e., $\Delta F_c \equiv F_c(0°) - F_c^0(30°)$, is given by Equation 6.13.

To the extent that the two-layer model accurately models the head, the cerebral flow changes calculated in this manner will not be contaminated by flow in superficial tissues. The two-layer model approximates the head as a spatially uniform superficial tissue layer above a semi-infinite cerebral layer. In practical measurements of the head, though, interference from superficial tissues in cerebral monitoring is often spatially inhomogeneous across the surface of the scalp [105, 109]. One way to reduce error from these superficial heterogeneities is to probe the superficial tissue volume above the cerebral region of interest with multiple short separations, as shown in Figure 6.4C. As with using more than two probe pressures (Section 6.3.3), it is straightforward to extend the probe pressure modulation algorithm to handle multiple short separations. In our measurements, we followed the steps outlined in Figure 6.3 for each short separation separately to obtain an estimate of the cerebral flow change. We then averaged the two estimates of

ΔF_c obtained from using the two short separations together.

6.5 Probe Pressure Modulation Algorithm for Oxygenation Monitoring with DOS/NIRS

In Section 6.3, we developed a probe pressure modulation paradigm for DCS that filters contamination from superficial tissues in cerebral blood flow measurements. An analogous probe pressure modulation scheme can be used to calibrate continuous wave DOS/NIRS for monitoring of cerebral oxy-hemoglobin (HbO_c) and deoxy-hemoglobin (HbR_c) concentrations. This scheme employs a two-layer Modified Beer-Lambert framework wherein tissue scattering is constant.

6.5.1 Two-layer Modified Beer-Lambert Laws for Absorption at Long and Short Separations

Following analogous steps to those outlined for flow monitoring in Section 6.3, DOS/NIRS measurements of light intensity are made at a long source-detector separation, $I(\rho_l)$, and a short source-detector separation, $I(\rho_s)$. Using a two-layer model of the head, the DOS/NIRS two-layer Modified Beer-Lambert law analogues of Eqs. (6.7) and (6.8) are [91, 130]:

$$\Delta OD^{\text{long}} \equiv -\log\left[\frac{I(\rho_l)}{I^0(\rho_l)}\right] = L_c(\rho_l)\Delta\mu_{a,c} + L_{ec}(\rho_l)\Delta\mu_{a,ec}, \tag{6.16}$$

$$\Delta OD^{\text{short}} \equiv -\log\left[\frac{I(\rho_s)}{I^0(\rho_s)}\right] = L_{ec}(\rho_s)\Delta\mu_{a,ec}. \tag{6.17}$$

The cerebral and extra-cerebral tissue absorption and scattering coefficients that give rise to the measured intensities $I(\rho_l)$ and $I(\rho_s)$ are $\mu_{a,c}$, $\mu_{a,ec}$, $\mu'_{s,c}$, and $\mu'_{s,ec}$, respectively. Similarly, at the baseline measured intensities $I^0(\rho_l)$ and $I^0(\rho_s)$, the baseline cerebral and extra-cerebral tissue absorption and scattering coefficients are $\mu^0_{a,c}$, $\mu^0_{a,ec}$, $\mu'^0_{s,c}$, and $\mu'^0_{s,ec}$, respectively. The differential changes of cerebral and extra-cerebral absorption from baseline are $\Delta\mu_{a,c} \equiv \mu_{a,c} - \mu^0_{a,c}$ and $\Delta\mu_{a,ec} \equiv \mu_{a,ec} - \mu^0_{a,ec}$. Finally, the partial pathlengths $L_c(\rho_l) \equiv \partial OD^{\text{long},0}/\partial\mu_{a,c}$, $L_{ec}(\rho_l) \equiv \partial OD^{\text{long},0}/\partial\mu_{a,ec}$, and $L_{ec}(\rho_s) \equiv \partial OD^{\text{short},0}/\partial\mu_{a,ec}$ are the mean pathlengths that the detected light travels through the cerebral (c) and extra-cerebral (ec) layers [91, 130, 215]. It is assumed that detected light from the short separation does not sample the brain, and consequentially, $L_c(\rho_s) = 0$ and $L_{ec}(\rho_s)$ is approximately the semi-infinite differential pathlength

given by Equation 6.2.

Solving Eqs. (6.16) and (6.17) for $\Delta\mu_{a,c}$, we obtain

$$\Delta\mu_{a,c} = \frac{1}{L_c(\rho_l)}\left[\Delta OD^{\text{long}} - \frac{L_{ec}(\rho_l)}{L_{ec}(\rho_s)}\Delta OD^{\text{short}}\right]. \tag{6.18}$$

The key advantage of using probe pressure modulation with DOS/NIRS is that it enables direct measurement of the ratio $L_{ec}(\rho_l)/L_{ec}(\rho_s)$.

6.5.2 Probe Pressure Calibration of DOS/NIRS for Cerebral Absorption Monitoring

Analogously to Section 6.3.2.1, the ratio $L_{ec}(\rho_l)/L_{ec}(\rho_s)$ can be directly measured from differential short and long separation optical density changes between perturbed and baseline states wherein only the extra-cerebral absorption is different [91]. Probe pressure modulation is a simple way to induce controlled extra-cerebral absorption changes without affecting cerebral absorption. For relating a perturbed state at probe pressure P to the baseline state at probe pressure P^0, Eqs. (6.16) and (6.17) simplify to

$$\Delta OD^{\text{long},P} \equiv -\log\left[\frac{I^P(\rho_l)}{I^0(\rho_l)}\right] = L_{ec}(\rho_l)\Delta\mu^P_{a,ec}, \tag{6.19}$$

$$\Delta OD^{\text{short},P} \equiv -\log\left[\frac{I^P(\rho_s)}{I^0(\rho_s)}\right] = L_{ec}(\rho_s)\Delta\mu^P_{a,ec}, \tag{6.20}$$

where $I^P(\rho_l)$ and $I^P(\rho_s)$ are the measured intensities at probe pressure P, and $\Delta\mu^P_{a,ec} \equiv \mu^P_{a,ec} - \mu^0_{a,ec}$ is the pressure-induced extra-cerebral absorption change.

Dividing Equation 6.19 by Equation 6.20 and then substituting the result into Equation 6.18, we obtain

$$\Delta\mu_{a,c} = \frac{1}{L_c(\rho_l)}\left[\Delta OD^{\text{long}} - \frac{\Delta OD^{\text{long},P}}{\Delta OD^{\text{short},P}}\Delta OD^{\text{short}}\right]. \tag{6.21}$$

Here, intensity measurements at long and short separations along with initial calibration measurements at two probe pressures determines $\Delta\mu_{a,c}$ within a multiplicative proportionality constant, $1/L_c(\rho_l)$. For accurately estimating the magnitude of the cerebral absorption change, $L_c(\rho_l)$ is calculated by numerically computing the derivative of the continuous wave two-layer

photon diffusion Green's function, $\Phi(\rho_l)$ [157,212], evaluated at the baseline tissue optical properties:

$$L_c(\rho_l) = \frac{\partial}{\partial \mu_{a,c}} \left(-\log[\Phi^0(\rho_l)]\right) \approx \frac{1}{\Delta\mu_{a,c}} \log \left[\frac{\Phi(\rho_l, \mu^0_{a,c} - \Delta\mu_{a,c}/2, \mu^0_{a,ec}, \mu'^0_{s,c}, \mu'^0_{s,ec}, \ell)}{\Phi(\rho_l, \mu^0_{a,c} + \Delta\mu_{a,c}/2, \mu^0_{a,ec}, \mu'^0_{s,c}, \mu'^0_{s,ec}, \ell)} \right], \tag{6.22}$$

where $\Delta\mu_{a,c}/\mu^0_{a,c} = 10^{-5}$. The Green's function $\Phi(\rho_l)$ can be evaluated using the analytical two-layer solution, or it can also be evaluated numerically using Monte Carlo techniques [255]. The computation of $L_c(\rho_l)$ requires knowledge of $\mu^0_{a,c}$, $\mu^0_{a,ec}$, $\mu'^0_{s,c}$. $\mu'^0_{s,ec}$, and ℓ. As described in Section 6.3.2.2, ideally the extra-cerebral layer thickness is known *a priori* from anatomical information, and the tissue baseline optical properties are measured (e.g., with time-domain techniques). If *a priori* anatomical information and instrumentation for measuring baseline optical properties is not available, then the baseline optical properties need to be assumed. The extra-cerebral layer thickness can either also be assumed or estimated from the two-layer fit of DCS data at multiple probe pressures (Section 6.3.2.2).

Cerebral absorption determined from Equation 6.21 will not be affected by extra-cerebral absorption changes to the extent that the two-layer model accurately models the head. Figure 6.5 is a flow chart summarizing the DOS pressure modulation algorithm for monitoring cerebral absorption changes. Note that this algorithm can be generalized for calibration with more than two probe pressures and monitoring with multiple short separations in an exactly analogous manner to that described in Sections 6.3.3 and 6.4.

6.5.3 Hemoglobin Monitoring with Multispectral DOS/NIRS

The cerebral tissue absorption coefficient depends linearly on the concentrations of tissue chromophores. With NIR light, changes in cerebral absorption predominantly arise from changes in cerebral oxygenated hemoglobin (HbO_c) and de-oxygenated hemoglobin (HbR_c) concentrations, such that [79]

$$\Delta\mu_{a,c}(\rho_l, \lambda) \approx \varepsilon_{HbO}(\lambda)\Delta HbO_c + \varepsilon_{HbR}(\lambda)\Delta HbR_c. \tag{6.23}$$

Here, $\varepsilon_{HbO}(\lambda)$ and $\varepsilon_{HbR}(\lambda)$ are wavelength-dependent extinction coefficients for oxygenated hemoglobin and de-oxygenated hemoglobin, which are both known and tabulated as a function

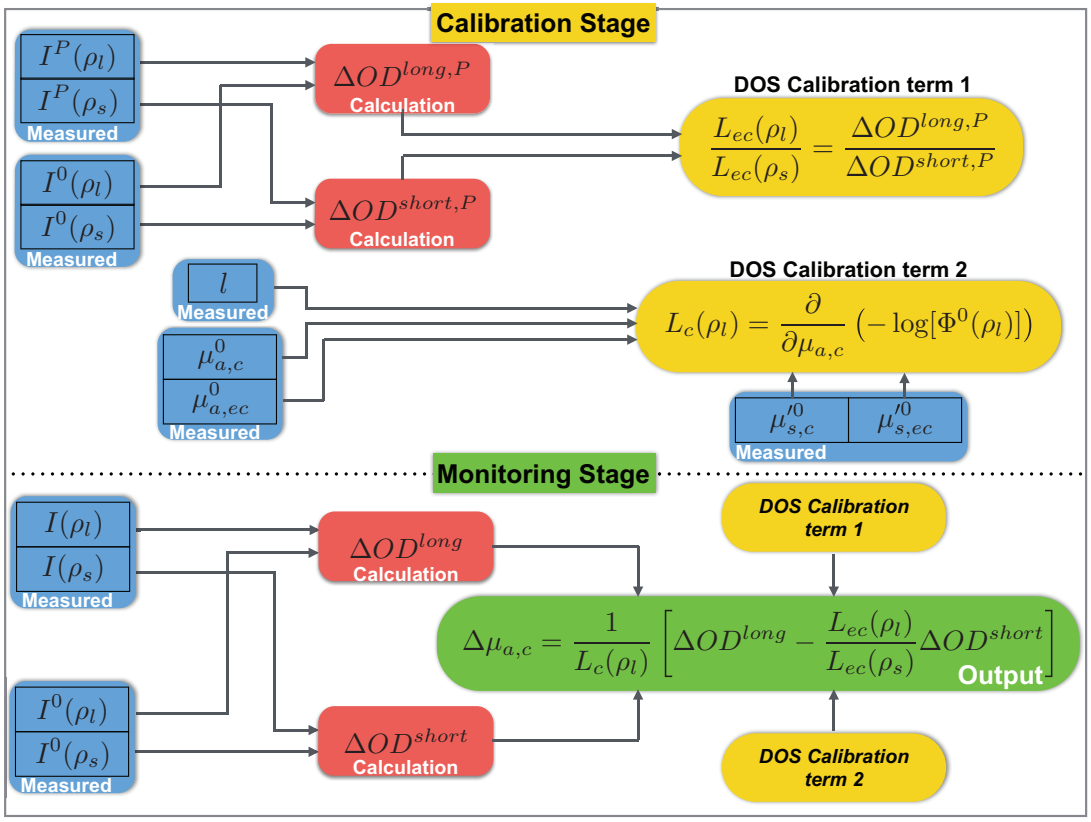

Figure 6.5: Flow chart of probe pressure modulation algorithm for cerebral tissue absorption monitoring ($\Delta\mu_{a,c}$) with DOS/NIRS. In the calibration stage, baseline long and short separation intensities measured at probe pressure P^0 ($I^0(\rho_l)$, $I^0(\rho_s)$) and at probe pressure $P \neq P^0$ ($I^P(\rho_l)$, $I^P(\rho_s)$) are used to calculate $\Delta OD^{\text{long},P}$ (Equation 6.19) and $\Delta OD^{\text{short},P}$ (Equation 6.20), which are then used to estimate $L_{ec}(\rho_l)/L_{ec}(\rho_s)$ ("DOS Calibration term 1). "DOS Calibration term 2" is the numerical evaluation of $L_c(\rho_l)$ (Equation 6.22), which requires knowledge of the baseline tissue optical properties and the extra-cerebral layer thickness (ℓ). Ideally, these baseline tissue properties are measured (see Section 6.5.2). In the monitoring stage, DOS Calibration terms 1 and 2 are employed to convert subsequent measurements of differential long and short separation optical density changes, i.e., ΔOD^{long} (Equation 6.16) and ΔOD^{short} (Equation 6.17), to differential cerebral absorption changes via Equation 6.21. Note that the baseline used for the calibration stage and for the monitoring stage is the same.

of wavelength λ [207], and ΔHbO_c and ΔHbR_c are differential changes in cerebral oxygenated and de-oxygenated hemoglobin concentration from baseline. For multispectral cerebral absorption monitoring with Equation 6.21, Equation 6.23 becomes a system of equations, i.e., one equation for each wavelength, which can then be solved for ΔHbO_c and ΔHbR_c. A minimum of two wavelengths is required to solve for these two chromophores.

Finally, the baseline cerebral hemoglobin concentrations HbO_c^0 and HbR_c^0 can be calculated from multispectral measurements of $\mu_{a,c}^0(\lambda)$, which in turn enables the computation of cerebral tissue oxygen saturation, $StO_{2,c}$ [79]:

$$StO_{2,c} = \frac{HbO_c^0 + \Delta HbO_c}{HbO_c^0 + HbR_c^0 + \Delta HbO_c + \Delta HbR_c}.$$

As many researchers have discussed, combining DOS/NIRS measurements of $StO_{2,c}$ with DCS measurements of cerebral blood flow (F_c) permits monitoring of cerebral oxygen metabolism [28, 62].

6.6 Experimental Methods

The pressure modulation algorithms described above were successfully applied to both simulated data with noise and *in vivo* measurements in healthy adult volunteers to measure cerebral hemodynamic changes. Each of the two adults measured provided written consent, and all protocols/procedures were approved by the Institutional Review Board at the University of Pennsylvania. One adult was asked to do finger tapping, which induces a localized cerebral blood flow increase in the motor cortex along with a more global extra-cerebral flow increase from systemic effects [26, 166, 237]. The other adult sat comfortably while we acquired data at several different probe pressures against the scalp to induce graded scalp ischemia. As discussed above, probe pressure modulation changes extra-cerebral flow while cerebral flow remains constant [184]. The instrumentation used for the *in vivo* measurements are described in Appendix 6.11, and the measurement protocols are explained in Sections 6.6.1 and 6.6.2. We then discuss the generation of simulated data in Section 6.6.3.

6.6.1 Finger Tapping Protocol

Throughout the finger tapping measurement, the subject lay supine on a bed. First, absolute baseline optical properties over the subject's motor cortex (Figure 6.6A) were measured with a multiple-distance frequency domain technique [133,253]. Specifically, a commercial frequency-domain ISS Imagent (ISS Medical, Champaign, IL, USA) was connected to a multiple-distance probe (ISS Medical, $\rho = 2$, 2.5, 3, 3.5 cm). Prior to the motor cortex measurement, the instrument was first calibrated on a solid silicon phantom (ISS Medical) with known optical properties [133, 253]. We used these measurements of the bulk average optical properties over the sampled tissue volume for both the cerebral and extra-cerebral layers.

Then, the cerebral blood flow response to finger tapping was monitored with a DCS optical probe ($\rho_l = 3.0$ cm, $\rho_s = 1.0$ cm) secured over the motor cortex (Figure 6.6A) with double-sided medical tape (3M 1509, Converters Inc., Huntingdon Valley, PA, USA) and an ACE bandage wound around the head. The subject's heart rate was also monitored in parallel with a pulse ox (Radical TM, Masimo, Irvine, CA, USA) attached to his left index finger.

With the probes in place, an initial "pressure calibration" (Figure 6.3) was performed by gently pressing down on the probes with the palm of the hand, as depicted in Figure 6.6B. Then, the subject executed five finger tapping trials consisting of 40-second intervals of finger tapping separated by 60-second rest intervals (Figure 6.6B). During finger tapping, the subject tapped all four fingers of the right hand against the thumb at 3 Hz, in time with an audible cuing signal provided by a metronome.

6.6.2 Graded Scalp Ischemia Protocol

As with the finger tapping measurement (Section 6.6.1), the subject's baseline absolute optical properties over the left forehead were measured first. Then, as the subject sat comfortably, an optical probe (Figure 6.4C) with one long separation ($\rho_l = 3.0$ cm) and two short separations ($\rho_s = 1.0$ cm) was placed on the subject's left forehead and secured with a blood pressure arm cuff (Soma Technology, Bloomfield, CT, USA) wound around the head (Figure 6.7A). The pressure cuff was inflated and maintained at the desired air pressure with a Zimmer ATS-1500 tourniquet system (Soma Technology). DCS measurements were acquired at five different probe

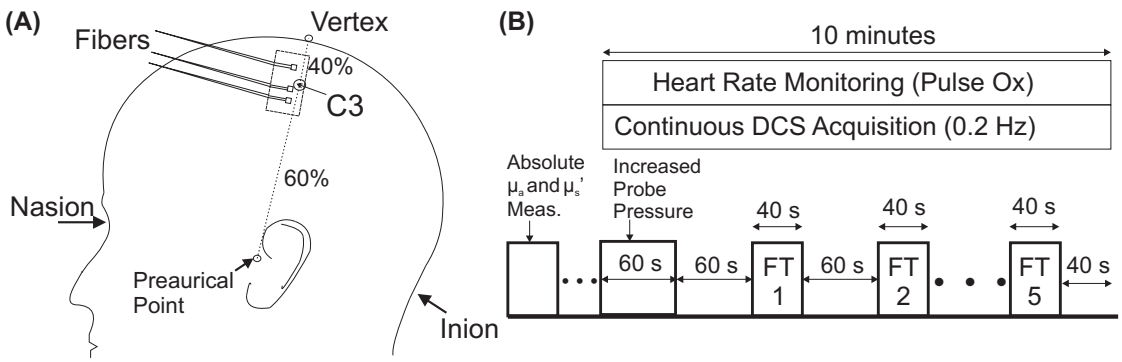

Figure 6.6: **(A)** To measure the cerebral blood flow response to finger tapping, a DCS optical probe ($\rho_l = 3.0$, $\rho_s = 1.0$ cm) was secured over the hand knob area of the motor cortex, which is slightly anterior to the C3 position in the 10-20 EEG coordinate system [150]. The C3 position lies $2/5$ of the distance between the vertex and the preaurical point (i.e., 3-4 cm down from vertex), and the vertex is the halfway point on the curve connecting the nasion to the inion (17-18 cm from nasion). The subject's heart rate was also monitored with a pulse ox. **(B)** Schematic showing the timeline of the finger tapping (FT) measurement. The subject did five blocks of finger tapping (i.e., tapping all four fingers of the right hand against the thumb) at 3 Hz. Prior to finger tapping, baseline absolute optical properties were measured over the measurement location depicted in part (A) (see main text), and the probe pressure was temporarily increased by gently pressing down on the probes with the palm of the hand.

pressures against the scalp (i.e., five different extra-cerebral blood flow levels) ranging from 15 mm Hg to 40 mm Hg (Figure 6.7B). Here, the calculation of cerebral flow involved averaging over the measured signals acquired at both short separations, as described in Section 6.4.

6.6.3 Simulated Data

For light wavelength $\lambda = 785$ nm, we generated simulated intensity autocorrelation functions (DCS) and light intensities (DOS/NIRS) at source-detector separations of $\rho_l = 3$ cm and $\rho_s = 0.7$ cm for two types of hemodynamic perturbations. Simulated DCS data sets were obtained for the special cases of (1), varying cerebral flow while extra-cerebral flow remains constant, and (2), varying extra-cerebral flow while cerebral flow remains constant. Similarly, simulated DOS/NIRS intensity data sets were obtained for the special cases of (1), varying cerebral absorption while extra-cerebral absorption remains constant, and (2), varying extra-cerebral absorption while cerebral absorption remains constant. The simulated intensity autocorrelation

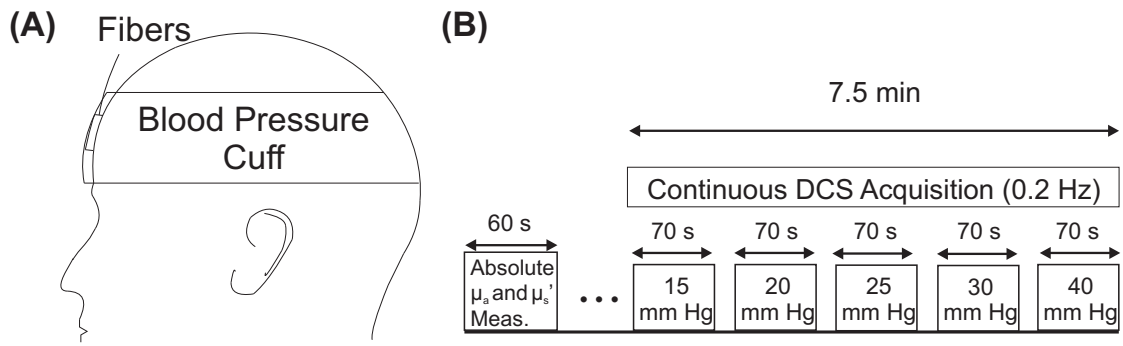

Figure 6.7: **(A)** A blood pressure cuff wound around the head was used to uniformly adjust the pressure of the optical probe against the forehead. **(B)** DCS measurements were made at five different probe pressures against the scalp.

functions were generated from adding correlation noise [276] to 2-layer solutions of the correlation diffusion equation [24, 106], while simulated DOS/NIRS intensities were generated from adding Gaussian noise to 2-layer solutions of the photon diffusion equation [157, 212].

Specifically, baseline tissue optical properties and tissue blood flow levels in the simulated data were chosen to be representative of the head, i.e., $\mu^0_{a,c} = 0.16$, $\mu^0_{a,ec} = 0.12$, $\mu'^0_{s,c} = 6$, $\mu'^0_{s,ec} = 10$ cm^{-1}; $F^0_c = 1.4 \times 10^{-8}$, $F^0_{ec} = 1.4 \times 10^{-9}$ cm^2/s ; $\ell = 1.2$ cm (see Figure 6.2; optical properties from Ref. [55], extra-cerebral flow from Ref. [184], cerebral to extra-cerebral flow ratio from Ref. [250], and the extra-cerebral layer thickness from averaging across MRI measurements in 9 adult volunteers (Durduran *et al*, unpublished)). In the DCS simulations, tissue optical properties remained constant, and the added correlation noise was derived from a correlation noise model [276] evaluated at DCS intensities of $50k$ and $100k$ photons a second for the long and short separations, and an integration time of 2.5 seconds. The DCS signal for each pair of cerebral and extra-cerebral flow levels in the data sets were obtained from averaging across $N = 100$ simulated autocorrelation functions with noise. Finally, to simulate an increased probe pressure during the calibration stage of the measurement (Figure 6.3), the extra-cerebral blood flow was decreased by 30% from baseline.

In the DOS/NIRS simulations, tissue optical scattering remained constant, and the added light intensity noise was derived from a Gaussian noise model ($SNR \equiv \mu/\sigma = 100$). The DOS/NIRS signal for each pair of cerebral and extra-cerebral tissue absorption coefficients in

the data sets were obtained from averaging across $N = 100$ simulated intensities, and the extra-cerebral tissue absorption was decreased by 15% from baseline to simulate the increased probe pressure during the calibration stage (Figure 6.5).

6.7 Results

6.7.1 Validation with simulated data

We tested the pressure modulation algorithms (Figs. 6.3, 6.5) on the simulated data sets described in Section 6.6.3. The cerebral blood flow and tissue absorption changes computed with the pressure modulation algorithms are compared to the semi-infinite blood flow and tissue absorption changes (Section 6.2) in Figure 6.8. Since the short separation measurements predominantly sample the extra-cerebral layer, the semi-infinite hemodynamic changes obtained from the short separation data agree well with the true extra-cerebral hemodynamic changes. The long separation measurements, however, sample both cerebral and extra-cerebral tissues. Substantial signal contamination from the extra-cerebral tissues induced substantial errors in the long separation semi-infinite estimates of cerebral flow and absorption (Figure 6.8). The pressure modulation algorithms, though, successfully filtered much of this extra-cerebral contamination from the measured signals, and consequentially recovered cerebral hemodynamics with higher accuracy (Figure 6.8). Note that in the flow pressure modulation algorithm, we utilized 42 delay-times ranging from $\tau = 0.2$ μs to $\tau = 35$ μs to evaluate Equation 6.13 for ΔF_c. All of these delay-times satisfied the limit $g_2^0(\tau, \rho_l) > 1.25$.

Interestingly, comparing panels (A) and (B) with (C) and (D) in Figure 6.8, it is evident that the semi-infinite DOS/NIRS calculation is less sensitive to the brain than the semi-infinite DCS calculation [12, 221].

6.7.2 Validation with graded scalp ischemia

As described in Section 6.6.2, we acquired DCS measurements on the forehead of a healthy adult volunteer during graded scalp ischemia. The subject's baseline cerebral flow, extra-cerebral flow, and extra-cerebral layer thickness obtained from the calibration stage of the pressure modulation algorithm were $F_c^0 = 4.53 \times 10^{-8}$ cm^2/s, $F_{ec}^0 = 2.23 \times 10^{-9}$ cm^2/s, and $\ell = 1.35$ cm,

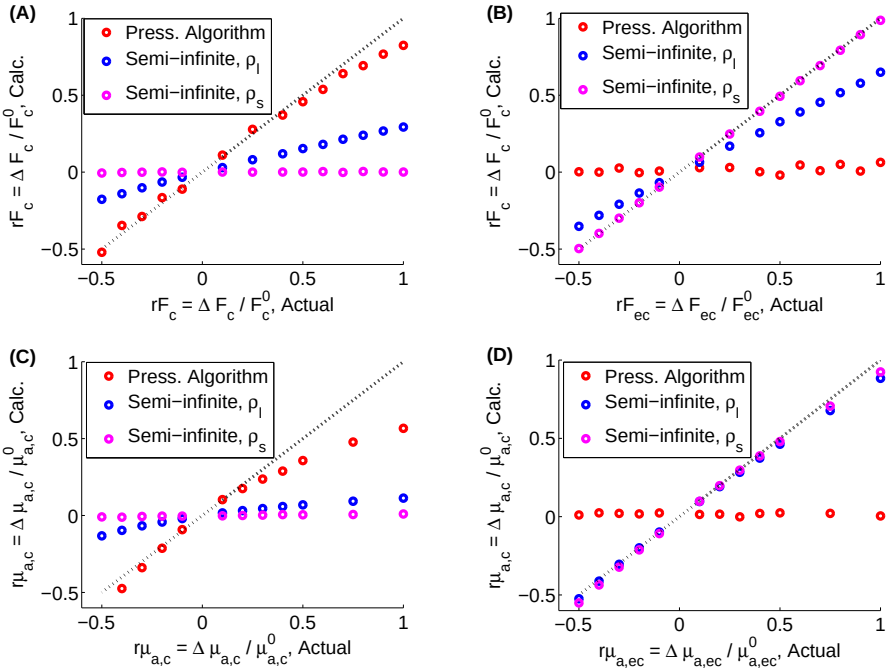

Figure 6.8: The DCS and DOS/NIRS pressure modulation algorithms (Figs. 6.3, 6.5) were utilized to calculate cerebral blood flow and tissue absorption changes from simulated measurements on the head acquired at long and short separations of $\rho_l = 3$ cm and $\rho_s = 0.7$ cm. These pressure algorithm results are then compared with the homogeneous semi-infinite model estimates of blood flow and tissue absorption computed from the long separation data and from the short separation data. The simulated data sets were generated from adding noise to two-layer solutions of the correlation diffusion equation (DCS) and the photon diffusion equation (DOS/NIRS) (see Section 6.6.3). **(A)** Calculated fractional cerebral blood flow changes plotted against the actual cerebral blood flow change in "DCS simulated data set 1" (i.e., extra-cerebral blood flow remains constant). **(B)** Calculated fractional cerebral flow changes plotted against the actual extra-cerebral blood flow change in "DCS simulated data set 2" (i.e., cerebral blood flow remains constant). **(C)** Calculated fractional cerebral absorption changes plotted against the actual cerebral absorption change in "DOS/NIRS data set 1" (i.e., extra-cerebral absorption remains constant). **(D)** Calculated fractional cerebral absorption changes plotted against the actual extra-cerebral absorption change in "DOS/NIRS data set 2" (i.e., cerebral absorption remains constant). Notice that the pressure algorithm calculations of cerebral changes are substantially less sensitive to extra-cerebral hemodynamics than the semi-infinite calculations.

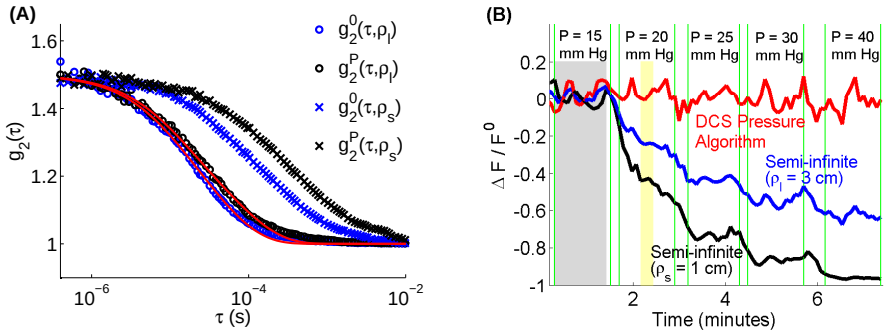

Figure 6.9: DCS measurements were acquired on the forehead of a healthy adult volunteer at multiple probe pressures against the head ($15 - 40$ mm Hg). The optical probe (Figure 6.4C) consisted of one long source-detector separation ($\rho_l = 3$ cm) and two short source-detector separations ($\rho_s = 1$ cm). **(A)** Measured intensity autocorrelation curves employed in the calibration stage of the probe pressure modulation algorithm (Figure 6.3) plotted against delay-time τ. The long separation autocorrelation curves $g_2^0(\tau, \rho_l)$ and $g_2^P(\tau, \rho_l)$ are the temporally averaged signals across the shaded gray and yellow regions of panel (B), respectively. Similarly, the curves $g_2^0(\tau, \rho_s)$ and $g_2^P(\tau, \rho_s)$ are temporally averaged over the same intervals and averaged across both short separations. The solid red lines are the simultaneous two-layer pressure calibration fit (Section 6.3.2.2) to $g_2^0(\tau, \rho_l)$ and $g_2^P(\tau, \rho_l)$ given the constraints that $F_c^P = F_c^0$ and that $F_{ec}^P / F_{ec}^0 = 0.57$. Note that the latter constraint was obtained from the short separation measurements using semi-infinite methods. The extracted baseline parameters from the two-layer fit are $F_c^0 = 4.53 \times 10^{-8}$ cm^2/s, $F_{ec}^0 = 2.23 \times 10^{-9}$ cm^2/s, and $\ell = 1.35$ cm. **(B)** Temporal fractional flow changes computed with the DCS pressure modulation algorithm and computed with semi-infinite techniques. These fractional flow curves are smoothed via a moving average window of size 3 frames (15 seconds). Notice that the cerebral blood flow change computed with the two-layer DCS Modified Beer-Lambert law is not affected by the extra-cerebral changes induced from varying probe pressure.

respectively (Figure 6.9A). Further, the baseline DCS signal intensities for the long and short separations were $35k$ and $170k$ photons a second, and the measured baseline optical properties over the forehead at $\lambda = 785$ nm are $\mu_a^0 = 0.12$ and $\mu_s'^0 = 8$ cm^{-1}. We then monitored cerebral blood flow at several different probe pressures against the head using the DCS pressure modulation algorithm and the semi-infinite model (Figure 6.9B). The extra-cerebral blood flow determined from applying the semi-infinite model to the short separation data decreased steeply with increasing probe pressure, until it was close to zero at $P = 40$ mm Hg. Importantly, the long separation semi-infinite estimate of cerebral blood flow also decreased substantially with increasing probe pressure, though not as severely as the extra-cerebral flow. This apparent change in cerebral flow is due to extra-cerebral contamination in the long separation signal from the pressure-induced extra-cerebral flow changes. The DCS pressure modulation algorithm, though, successfully filtered the extra-cerebral contamination from the long separation signal, and the computed cerebral flow was not affected by probe pressure changes.

Important notes are that the 'robust noise" formulation of the DCS pressure modulation algorithm was used (Section 6.3.4) to obtain the curve in Figure 6.9B. Further, pressure-induced extra-cerebral absorption changes, determined from the short separation signal intensity changes via Equation 6.17, were incorporated into the computation of cerebral flow (e.g., Equation 6.29). Increasing the probe pressure from baseline to 40 mm Hg decreased $\mu_{a,ec}$ by 25%. Cerebral flow monitoring with the DCS pressure modulation algorithm wherein constant absorption is assumed (i.e., Equation 6.15) resulted in an erroneous calculated increase in cerebral flow of 10% at 40 mm Hg.

6.7.3 Validation with in vivo finger tapping data

As another *in vivo* test, we used the DCS pressure modulation algorithm (Figure 6.3) to measure the cerebral flow increase induced by the finger tapping task in a healthy volunteer (Section 6.6.1). The measured baseline optical properties over the motor cortex at $\lambda = 785$ nm were $\mu_a^0 = 0.12$ and $\mu_s'^0 = 8$ cm^{-1}, the baseline DCS signal intensities for the long and short separations were $18k$ and $140k$ photons a second, and the baseline heart rate was 72 bpm. In the calibration stage of this measurement, probe pressure was increased by manually pressing down on the probe with the palm of the hand instead of using a blood pressure cuff wrapped around

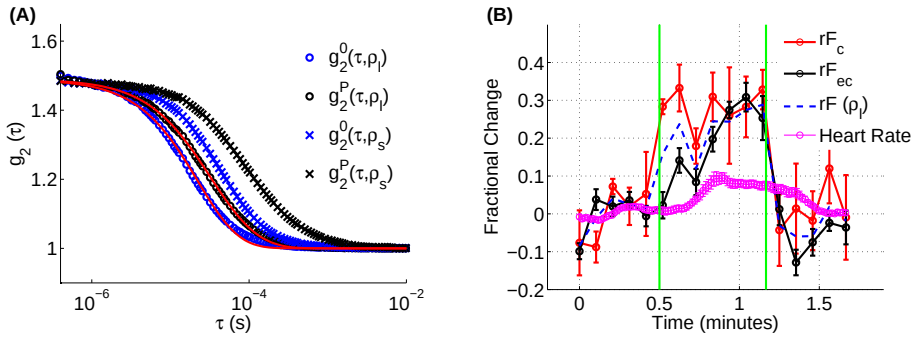

Figure 6.10: DCS measurements at one long source-detector separation ($\rho_l = 3$ cm) and one short source-detector separation ($\rho_s = 1$ cm) were acquired over the motor cortex of a healthy adult volunteer while he performed finger tapping (Figure 6.6A). **(A)** Measured intensity auto-correlation curves employed in the calibration stage of the probe pressure modulation algorithm (Figure 6.3) plotted against delay-time τ. These curves are temporally averaged signals across the 60 second "baseline" and "increased probe pressure" intervals indicated in Figure 6.6B. The solid red lines are the simultaneous two-layer pressure calibration fit (Section 6.3.2.2) to $g_2^0(\tau, \rho_l)$ and $g_2^P(\tau, \rho_l)$ given the constraints that $F_c^P = F_c^0$ and that $F_{ec}^P/F_{ec}^0 = 0.44$, where the extra-cerebral constraint was obtained from $g_2^0(\tau, \rho_s)$ and $g_2^P(\tau, \rho_s)$ via semi-infinite methods. The extracted baseline parameters from the two-layer fit are $F_c^0 = 1.95 \times 10^{-8}$ cm^2/s, $F_{ec}^0 = 3.08 \times 10^{-9}$ cm^2/s, and $\ell = 1.05$ cm. **(B)** Measured finger tapping functional responses (mean $\pm$ SE across $N = 5$ trials) for cerebral blood flow ($rF_c = \Delta F_c/F_c^0$), extra-cerebral blood flow ($rF_{ec} = \Delta F_{ec}/F_{ec}^0$), and heart rate plotted against time. The finger tapping stimulus was between the two green vertical lines. Here, rF_c was computed with the DCS pressure modulation algorithm (Equation 6.15), rF_{ec} was determined from applying semi-infinite methods to the short separation signal (Section 6.2), and the heart rate was measured with a pulse ox on the finger. Further, the blue dashed line ($rF(\rho_l)$) is the mean flow response computed from applying the semi-infinite model to the long-separation signal.

the head. The subject's baseline cerebral flow, extra-cerebral flow, and extra-cerebral layer thickness obtained from the two-layer fit were $F_c^0 = 1.95 \times 10^{-8}$ cm^2/s, $F_{ec}^0 = 3.08 \times 10^{-9}$ cm^2/s, and $\ell = 1.05$ cm, respectively (Figure 6.10A). The average cerebral flow, extra-cerebral flow, and heart rate responses induced by finger tapping ($N = 5$ trials) are plotted against time in Figure 6.10B. For comparison, the average semi-infinite flow response for the long separation is also plotted. Notice that the cerebral flow rapidly increases to a steady state value of 30% within 5 seconds of the start of finger tapping. The extra-cerebral flow increase, though, is more gradual, which roughly corresponds to the delayed heart rate increase from finger tapping. As expected, the long separation semi-infinite flow change is between the cerebral flow change computed with the DCS pressure modulation algorithm (Equation 6.15) and the extra-cerebral flow change computed from the short separation measurements (Figure 6.10B).

6.8 Discussion

Superficial tissue contamination in optical monitoring of cerebral hemodynamics is a well known issue in the DOS/NIRS community, and several methods have been proposed to isolate the cerebral component in the DOS/NIRS signal. Many of these methods assume statistical independence of superficial and cerebral signals, such as adaptive filtering [271], principal component/independent component analysis [26,137,199], state space modeling [107,109], and general linear models [137,161,238]. The justification for this assumption in brain mapping applications is that superficial signals in the scalp arise from systemic effects that are damped by cerebral autoregulation in the brain. Thus, the systemic superficial signals are independent from the local activation signals in the brain. However, as we mentioned in Section 6.1, cerebral autoregulation is impaired in brain diseases such as ischemic stroke. Alternative approaches for filtering superficial tissue contamination include tomographic imaging [68, 89, 114], time-resolved measurements [108, 172, 222, 234], and two-layer models [55, 85, 91, 106, 120, 208, 215].

In the present paper, our main result is a novel implementation of the two-layer model that utilizes two source-detector separations and probe pressure modulation to optically monitor cerebral blood flow (Figure 6.3). The two-layer Modified Beer-Lambert law for flow is employed to

linearly relate DCS signal changes to changes in cerebral and extra-cerebral blood flow (Equation 6.7). Further, a patient-specific "initial" pressure calibration of the measurement substantially improves the tractability of flow monitoring with the two-layer model by reducing the number of free parameters in the model to fit for. *A priori* anatomical information, though helpful, is not required in this pressure modulation algorithm. In our *in vivo* tests of graded scalp ischemia (Figure 6.9) and finger tapping (Figure 6.10), we did not use any *a priori* anatomical information. Unlike with tomographic imaging and principal component analysis, the two-layer model approach does not require a large number of optodes, which permits small area optical probes that are easier to integrate with other monitoring devices in clinical care applications requiring long-term continuous monitoring. Our optical probe for the *in vivo* tests (Figure 6.11) had four optodes. Finally, the linearity of the two-layer Modified Beer-Lambert law greatly facilitates long-term continuous real-time monitoring of cerebral blood flow. An analogous pressure modulation algorithm for cerebral absorption monitoring with DOS/NIRS is depicted in Figure 6.5, which is an extension of Fabbri *et. al.'s* two-layer formulation [91] to include pressure modulation.

The two-layer model is a big simplification of the true head geometry, but it is still effective in filtering extra-cerebral contamination, as we demonstrated in our graded scalp ischemia and finger tapping tests. Cerebral blood flow calculated with the homogeneous semi-infinite model significantly depended on probe pressure, but the two-layer pressure modulation algorithm calculation of cerebral flow (Equation 6.15) did not (Figure 6.9). Further, in our finger tapping test, the pressure modulation algorithm successfully separated the fast cerebral blood flow increase due to brain activation from the more gradual flow increases due to systemic effects (Figure 6.10).

We measured a steady-state increase in cerebral blood flow from finger tapping of 30% (Figure 6.10B). This increase is low compared to other published measurements, but not unreasonable. Durduran *et. al.* measured a mean cerebral blood flow increase of $39 \pm 10\%$ from finger tapping (3 Hz) [85]. Ye *et. al.* measured a $54 \pm 11\%$ cerebral blood flow increase from finger tapping (2 Hz) with arterial spin labeling MRI [265], and Kastrup *et. al.* measured a $101 \pm 24\%$ cerebral blood flow increase from finger tapping (3 Hz) with a FAIR MRI technique [2]. We suspect that our optical probe was not directly centered over the finger tapping hand knob, which is a little less than 2 cm diameter in size [267]. The EEG 10-20 system (Figure 6.6) only roughly

identifies the hand knob location, and we struggled a lot with finding the correct position for probe placement. We obtained assistance with probe placement from a neurosurgeon (David Kung), which was very valuable. If the probe is not exactly over the hand knob area, then only part of the sampled cerebral volume will encompass the hand knob area, inducing a partial volume error in the recovered cerebral flow change not accounted for in the two-layer model. This partial volume error results in an underestimation of the magnitude of the flow increase, which is the likely explanation for our lower than expected measured flow increase.

Also notice that although the extra-cerebral blood flow in the scalp during finger tapping increases gradually with the heart rate, the extra-cerebral blood flow and heart rate finger tapping responses behave qualitatively differently in the post-stimulus interval (Figure 6.10B). Following finger tapping, the heart rate remains elevated and gradually returns to baseline, while the extra-cerebral blood flow rapidly plummets, undershooting and then gradually returning to baseline. There are several factors that can affect superficial tissue blood flow besides the heart rate, such as blood pressure and skin-specific regulation mechanisms [26, 161]. Kirilina *et. al.* investigated the origin of task-evoked hemodynamic changes in the scalp, and found that task-evoked superficial artifacts are co-localized with veins draining the scalp [161]. The post-stimulus undershoot in extra-cerebral blood flow we observed could potentially be explained by an increase in scalp venous pressure induced by arterial vasoconstriction following cessation of finger tapping.

Another aspect of the pressure modulation algorithm is its estimation of the extra-cerebral layer thickness and baseline cerebral and extra-cerebral flow indices (Figs. 6.9A, 6.10A). We regrettably do not have an independent measure of the extra-cerebral layer thickness in the two adult subjects we measured to explicitly validate the extra-cerebral layer thickness estimates. The pressure calibration estimate of the layer thickness at the forehead for the pressure variation measurement was $\ell = 1.35$ cm, while the layer thickness estimate over the motor cortex in the finger tapping measurement for a different subject was $\ell = 1.05$ cm. Both of these estimates are within the range of layer thicknesses measured by Durduran *et. al.* from anatomical MRI scans, i.e., $\ell = 1.20 \pm 0.26$ cm (unpublished). Further, the pressure calibration estimate of the ratio of cerebral to extra-cerebral baseline blood flow in the finger tapping measurement was $F_c^0/F_{ec}^0 = 6.3$, which is consistent with PET measurements in healthy adults [194]. The estimate of this ratio for the graded scalp ischemia measurement was $F_c^0/F_{ec}^0 = 20.3$. This

ratio is high, but is explained by the probe pressure being a non-negligible 15 mm Hg during the baseline state (Figure 6.9B). At a probe pressure of 15 mm Hg, the extra-cerebral blood flow is substantially lower than it would be normally, which is reflected by the higher than normal cerebral to extra-cerebral flow ratio estimate. Importantly, we have demonstrated that pressure calibration can be done successfully through pressing down on the probe with the palm of the hand (Figure 6.10A), facilitating its implementation in a clinical setting. In our pressure algorithm, it is not necessary to know the quantitative pressure being applied to the probe. All that is required is a non-negligible pressure increase to induce an extra-cerebral flow change.

We emphasize that the formulation of the pressure algorithm utlizing Equation 6.13 (Figure 6.3) is sensitive to correlation noise (Section 6.3.4). For high signals and/or long temporal averaging times, this formulation is effective (Figure 6.8), but these luxuries are usually not available for cerebral measurements. In our *in vivo* tests, the correlation noise was too severe for Equation 6.13. Thus, we used Eqs. 6.15 and 6.29 instead, which are more robust to correlation noise. Further, we highly recommend using multiple delay-times in evaluating these equations for the cerebral flow change to reduce sensitivity to noise. In our *in vivo* tests, we utilized all delay-times wherein $g_2^0(\tau, \rho_l) > 1.25$ (~ 40 delay times).

Noise is less of a problem for the DOS/NIRS pressure algorithm formulation (Figure 6.5), though, because multimode detection fibers enable higher signals. During the pressure calibration stage, it is important to ensure that the source-detector separations remain fixed when probe pressure is increased. In our flexible probe, there was a tendency for the source-detector separations to change slightly when pressing down on the probe, and the signal changes were dominated by separation changes rather than extra-cerebral absorption changes. This problem is fixed if a rigid probe is used, but then making good contact with the scalp is harder. Note that the DCS measurement is less sensitive to these small changes in separation.

We finally point out that the DCS pressure modulation algorithm (Figure 6.3) assumes that the coherence of the source laser remains constant over time, i.e., the β coefficient in the Siegert relation (see Section 6.2) does not change. If this is not the case, then the DCS signal will change from varying β in addition to varying flow levels. The pressure algorithm does not account for variations in β. If β is changing, then it is more appropriate to use a DCS Modified Beer-Lambert law for the electric field autocorrelation function, $g_1(\tau) \equiv \langle \mathbf{E}^*(t) \cdot \mathbf{E}(t+\tau) \rangle / \langle I(t) \rangle$, instead of

the intensity autocorrelation function, $g_2(\tau)$. The electric field formulation is exactly analogous to Figure 6.3, except that the DCS optical density $OD_{DCS} \equiv -\log(g_2(\tau) - 1)$ is replaced with the "electric field DCS optical density", $OD_{DCS,g1} \equiv -\log(g_1(\tau))$. In this formulation, the Siegert relation is used to convert the measured g_2 signals to corresponding g_1 signals, wherein the β coefficient for each data frame can be fit for.

6.9 Conclusion

We developed a novel DCS pressure modulation algorithm that successfully isolated cerebral blood flow during graded scalp ischemia and finger tapping without using *a priori* anatomical information. This approach is accurate enough to be useful for filtering superficial tissue contamination in real-time cerebral blood flow monitoring. An analogous pressure modulation algorithm for DOS/NIRS will filter superficial tissue contamination in cerebral blood oxygenation monitoring.

6.10 Cerebral Blood Flow Monitoring Pressure Modulation Algorithm when Tissue Optical Properties Vary

Recall that the results derived in Sections 6.3.1 and 6.3.2 are for the special case of constant tissue absorption and tissue scattering. In this Appendix, we relax the constant optical property assumption and derive more general expressions for cerebral flow monitoring in the pressure modulation algorithm framework. We first focus on the case wherein tissue absorption is changing while tissue scattering remains constant (as in Section 6.5). We then move on to the case wherein both tissue absorption and scattering vary.

6.10.1 Cerebral flow monitoring with varying absorption

The two-layer DCS Modified Beer-Lambert law analogues of Eqs. (6.7) and (6.8) that include absorption components are [12]

$$\Delta OD_{DCS}^{\text{long}} = d_{F,c}(\tau,\rho_l)\Delta F_c + d_{F,ec}(\tau,\rho_l)\Delta F_{ec} + d_{a,c}(\tau,\rho_l)\Delta\mu_{a,c} + d_{a,ec}(\tau,\rho_l)\Delta\mu_{a,ec}, \tag{6.24}$$

$$\Delta OD_{DCS}^{\text{short}} = d_{F,ec}(\tau,\rho_s)\Delta F_{ec} + d_{a,ec}(\tau,\rho_s)\Delta\mu_{a,ec}, \tag{6.25}$$

where the tissue absorption changes $\Delta\mu_{a,c}$ and $\Delta\mu_{a,ec}$ can be estimated from DOS/NIRS measurements via Eqs. (6.21) and (6.17), and the multiplicative weighting factors $d_{a,c}(\tau,\rho_l) \equiv \partial OD_{DCS}^{\text{long},0}/\partial\mu_{a,c}$, $d_{a,ec}(\tau,\rho_l) \equiv \partial OD_{DCS}^{\text{long},0}/\partial\mu_{a,ec}$, and $d_{a,ec}(\tau,\rho_s) \equiv \partial OD_{DCS}^{\text{short},0}/\partial\mu_{a,ec}$ can be numerically determined by evaluating the appropriate derivative of the two-layer correlation diffusion solution at the baseline flow levels, tissue optical properties, and extra-cerebral layer thickness (e.g., Section 6.3.2.2).

For the pressure calibration stage, the analogues of Eqs. (6.10) and (6.11) are

$$\Delta OD_{DCS}^{\text{long},P} = d_{F,ec}(\tau,\rho_l)\Delta F_{ec}^P + d_{a,ec}(\tau,\rho_l)\Delta\mu_{a,ec}^P, \tag{6.26}$$

$$\Delta OD_{DCS}^{\text{short},P} = d_{F,ec}(\tau,\rho_s)\Delta F_{ec}^P + d_{a,ec}(\tau,\rho_s)\Delta\mu_{a,ec}^P, \tag{6.27}$$

where $\Delta\mu_{a,ec}^P \equiv \mu_{a,ec}^P - \mu_{a,ec}^0$ is the pressure induced change in extra-cerebral tissue absorption. Solving Eqs. (6.24), (6.25), (6.26), and (6.27) for the cerebral flow change, we obtain

$$\Delta F_c = \frac{1}{d_{F,c}(\tau,\rho_l)}\Big[\Delta OD_{DCS}^{\text{long}} - d_{a,ec}(\tau,\rho_l)\Delta\mu_{a,ec} - d_{a,c}(\tau,\rho_l)\Delta\mu_{a,c} - \frac{\Delta OD_{DCS}^{\text{long},P} - d_{a,ec}(\tau,\rho_l)\Delta\mu_{a,ec}^P}{\Delta OD_{DCS}^{\text{short},P} - d_{a,ec}(\tau,\rho_s)\Delta\mu_{a,ec}^P}\left(\Delta OD_{DCS}^{\text{short}} - d_{a,ec}(\tau,\rho_s)\Delta\mu_{a,ec}\right)\Big]. \tag{6.28}$$

An alternative approach more robust to correlation noise (see Section 6.3.4) is to solve Equation 6.24 directly for ΔF_c, i.e.,

$$\Delta F_c = \frac{1}{d_{F,c}(\tau,\rho_l)}\Big[\Delta OD_{DCS}^{\text{long}} - d_{F,ec}(\tau,\rho_l)\Delta F_{ec} - d_{a,c}(\tau,\rho_l)\Delta\mu_{a,c} - d_{a,ec}(\tau,\rho_l)\Delta\mu_{a,ec}\Big], \tag{6.29}$$

where ΔF_{ec} is determined from the short separation measurements via semi-infinite methods, as described in Section 6.3.4. As with Equation 6.13, Eqs. (6.28) and (6.29) only require a single τ for monitoring, but multiple delay-times should be used to ameliorate sensitivity to noise.

6.10.2 Cerebral flow monitoring with varying absorption and scattering

If both tissue absorption and scattering vary significantly, then the differential absorption and scattering changes should be directly measured with concurrent frequency-domain or time-domain DOS/NIRS [79, 101, 201]. The extensions of Eqs. (6.24) and (6.25) for varying tissue scattering are [12]

$$\Delta OD_{DCS}^{\text{long}} = d_{F,c}(\tau,\rho_l)\Delta F_c + d_{F,ec}(\tau,\rho_l)\Delta F_{ec} + d_{a,c}(\tau,\rho_l)\Delta\mu_{a,c} + d_{a,ec}(\tau,\rho_l)\Delta\mu_{a,ec} + d_{s,c}(\tau,\rho_l)\Delta\mu'_{s,c} + d_{s,ec}(\tau,\rho_l)\Delta\mu'_{s,ec}, \tag{6.30}$$

$$\Delta OD_{DCS}^{\text{short}} = d_{F,ec}(\tau,\rho_s)\Delta F_{ec} + d_{a,ec}(\tau,\rho_s)\Delta\mu_{a,ec} + d_{s,ec}(\tau,\rho_s)\Delta\mu'_{s,ec}, \tag{6.31}$$

where $\Delta\mu'_{s,c} \equiv \mu'_{s,c} - \mu'^{0}_{s,c}$ and $\Delta\mu'_{s,ec} \equiv \mu'_{s,ec} - \mu'^{0}_{s,ec}$ are the differential changes from baseline of cerebral and extra-cerebral tissue scattering, and the scattering weighting factors $d_{s,c}(\tau,\rho_l) \equiv \partial OD_{DCS}^{\text{long},0}/\partial\mu'_{s,c}$, $d_{s,ec}(\tau,\rho_l) \equiv \partial OD_{DCS}^{\text{long},0}/\partial\mu'_{s,ec}$, and $d_{s,ec}(\tau,\rho_s) \equiv \partial OD_{DCS}^{\text{short},0}/\partial\mu'_{s,ec}$ are determined using the two-layer correlation diffusion solution as described in Section 6.3.2.2. Pressure-induced signal changes from the extra-cerebral layer are given by

$$\Delta OD_{DCS}^{\text{long},P} = d_{F,ec}(\tau,\rho_l)\Delta F_{ec}^{P} + d_{a,ec}(\tau,\rho_l)\Delta\mu_{a,ec}^{P} + d_{s,ec}(\tau,\rho_l)\Delta\mu'^{P}_{s,ec}, \tag{6.32}$$

$$\Delta OD_{DCS}^{\text{short},P} = d_{F,ec}(\tau,\rho_s)\Delta F_{ec}^{P} + d_{a,ec}(\tau,\rho_s)\Delta\mu_{a,ec}^{P} + d_{s,ec}(\tau,\rho_s)\Delta\mu'^{P}_{s,ec}. \tag{6.33}$$

Solving Eqs. (6.30), (6.31), (6.32), and (6.33) for the cerebral flow change, we obtain

$$\Delta F_c = \frac{1}{d_{F,c}(\tau,\rho_l)}\Big[\Delta OD_{DCS}^{\text{long}} - d_{a,ec}(\tau,\rho_l)\Delta\mu_{a,ec} - d_{a,c}(\tau,\rho_l)\Delta\mu_{a,c} - d_{s,ec}(\tau,\rho_l)\Delta\mu'_{s,ec} - d_{s,c}(\tau,\rho_l)\,\Delta\mu'_{s,c} - \frac{d_{F,ec}(\tau,\rho_l)}{d_{F,ec}(\tau,\rho_s)}\left(\Delta OD_{DCS}^{\text{short}} - d_{a,ec}(\tau,\rho_s)\Delta\mu_{a,ec} - d_{s,ec}(\tau,\rho_s)\Delta\mu'_{s,ec}\right)\Big], \tag{6.34}$$

where

$$\frac{d_{F,ec}(\tau,\rho_l)}{d_{F,ec}(\tau,\rho_s)} = \frac{\Delta OD_{DCS}^{\text{long},P} - d_{a,ec}(\tau,\rho_l)\Delta\mu_{a,ec}^{P} - d_{s,ec}(\tau,\rho_l)\Delta\mu'^{P}_{s,ec}}{\Delta OD_{DCS}^{\text{short},P} - d_{a,ec}(\tau,\rho_s)\Delta\mu_{a,ec}^{P} - d_{s,ec}(\tau,\rho_s)\Delta\mu'^{P}_{s,ec}}.$$

Alternatively, the variable scattering extension of Equation 6.29 derived from solving Equation 6.30 for ΔF_c is

$$\Delta F_c = \frac{1}{d_{F,c}(\tau,\rho_l)}\Big[\Delta OD_{DCS}^{\text{long}} - d_{F,ec}(\tau,\rho_l)\Delta F_{ec} - d_{a,c}(\tau,\rho_l)\Delta\mu_{a,c} - d_{a,ec}(\tau,\rho_l)\Delta\mu_{a,ec} - d_{s,c}(\tau,\rho_l)\Delta\mu'_{s,c} - d_{s,ec}(\tau,\rho_l)\Delta\mu'_{s,ec}\Big]. \tag{6.35}$$

Again, ΔF_c is determined from short separation measurements via semi-infinite techniques.

6.11 Instrumentation and Optical Probe

For *in vivo* cerebral blood flow monitoring during finger tapping and probe pressure variation, we used a custom built DCS instrument. Briefly, two continuous wave, long coherence length (> 5 meters) 785 nm lasers (80 mW, DL785-100-3O, CrystaLaser Inc., Reno, NV, USA) deliver source light to tissue via multimode fibers. Single mode detection fibers couple diffusive light emerging from tissue to two arrays of four high sensitivity avalanche photodiodes (SPCM-AQ4C, Excelitas, Quebec, Canada) operating in photon counting mode. The outputs from the detection arrays are connected to a multiple-τ hardware correlator (Correlator.com, Bridgewater, NJ, USA) that computes intensity autocorrelation curves in real time [72].

For interfacing this instrument with the head, we used an optical probe consisting of one long separation, $\rho_l = 3.0$ cm, and two short separations, $\rho_s = 1.0$ cm (Figure 6.11). All four fiber bundles in the probe are terminated with 3 mm dielectric coated right-angle prisms (PS905-E02-SP, custom, Thorlabs, Newton, NJ, USA). The high reflectivity of the prisms (99%) ensures high light throughput at the skin-probe interface. Further, as illustrated in Figure 6.11, the side-firing prism fibers lay in the same plane as the probe head, which facilitates the application of uniform pressure to the top of the probe.

All seven single mode fibers in the "DL" bundle and one attenuated single mode fiber in the "DS" bundle of the optical probe (Figure 6.11) were connected to the 8 detection channels in the DCS instrument. The seven independent measurements of the intensity autocorrelation function acquired in parallel at the DL probe position were subsequently averaged together to improve SNR. For the single mode fiber in the DS bundle, a variable blocking pigtail style fiber optic attenuator (OZ Optics, Ontario, Canada) was employed to avoid detector saturation. Each "S" fiber in the probe was connected to a laser, and the "middle S position fiber" was also attenuated (OZ Optics) to avoid detector saturation. During DCS acquisition, multiplexing of the two S positions was achieved by sequentially switching the two DCS lasers on and off with TTL pulses controlled with Labview software (National Instruments, Austin, TX, USA). For the finger tapping measurement (Section 6.6.1), we only used one laser (i.e., one short separation instead of two) to increase the time resolution.

To manufacture the probe, we utilized 3D printing to produce a mold (template) that securely

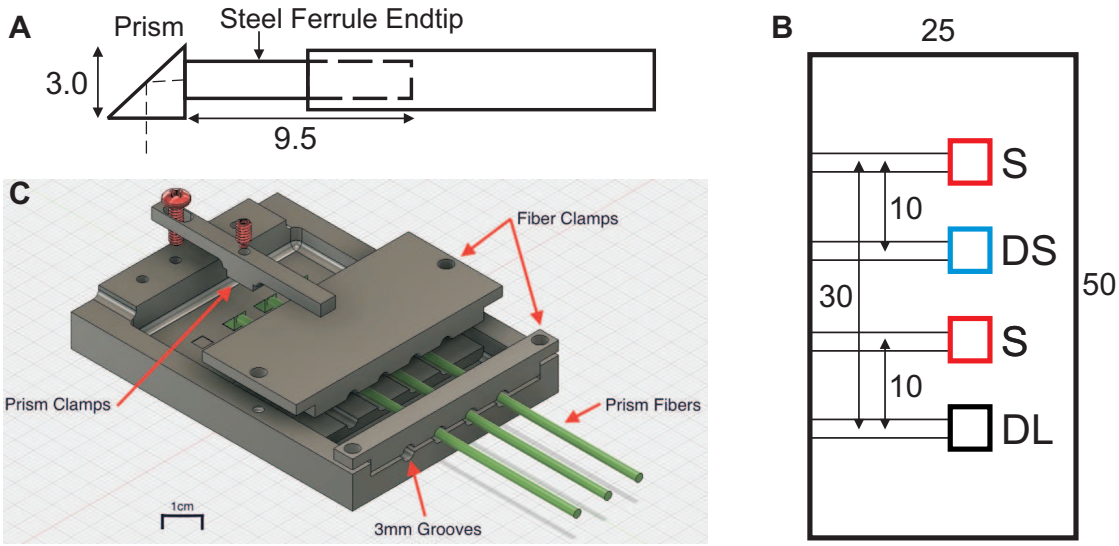

Figure 6.11: Schematic of the optical probe used for co-localized DCS and DOS/NIRS measurements (dimensions in mm). **(A)** For conversion of straight ferrule endtip fiber bundles to side-firing prism-coupled fibers, EPO-TEK 353ND epoxy was utilized to glue right-angle prisms (Thorlabs, E03 dielectric coated) to the ferrule endtips. **(B)** The probe consists of two fused silica multimode source fibers (S; 400μm-core/0.22NA), one long separation detection bundle (DL) of seven single mode fibers (780HP, Thorlabs, 5μm-MFD/0.13NA), and one short separation detection bundle (DS) of three single mode fibers (780HP). The termination and bundling of these optical fibers were done by Fiberoptic Systems, Inc. (Simi Valley, CA, USA). **(C)** Schematic of the 3D printed probe mold used for embedding the prism fibers in silicon elastomer at the positions indicated in panel B (see main text).

holds the prism fibers at the desired probe positions (Figure 6.11C). Specifically, the mold design was made in the Fusion 360 modeling software environment (Autodesk, CA, USA) and then printed with VeroClear material using an Objet 500 printer (Stratasys, MN, USA and Rehovot, Israel). Separately printed prism clamps with integrated set screws secured the prism fibers in place along grooves in the mold (Figure 6.11C). While the fibers remained fixed in place, a two-part silicone elastomer (VytaFlex-30, Smooth-On, PA, USA) was mixed with a black tint (3% volume fraction; SO-Strong Color Tint, Smooth-On), vacuum degassed, and poured into the mold. Cast as a liquid, the elastomer cures over a time period of 24 hours to form a flexible solid probe head with the prism fibers embedded at the desired positions. Notice that this highly flexible technique can be utilized not just for making flat probes, but also probes with "built in" curvature that may facilitate measurements on neonates. Also, the SO black tint we used was not highly absorbing in the near-infrared. For a more absorbing probe head in the NIR, we recommend mixing the elastomer with india ink.

Chapter 7

Neurovascular Coupling Varies with Level of Global Cerebral Ischemia in a Rat Model

This chapter is mostly a verbatim reprint of my paper published in the Journal of Cerebral Blood Flow and Metabolism [13]. However, I have added an Appendix (Section 7.6) wherein the compartment model for computing oxygen metabolism is explicitly derived.

7.1 Introduction

In healthy brains, localized increases in neuronal activity are strongly correlated, both spatially and temporally, to localized increases in cerebral blood flow (CBF) and cerebral metabolic consumption of oxygen ($CMRO_2$) [244]. Thus, quantification of hemodynamics due to increased neuronal activity, i.e., neurovascular coupling, has long been a topic of intense interest. In addition to being critical for the interpretation of techniques such as functional magnetic resonance imaging that use hemodynamic responses to map brain function, neurovascular coupling also plays a role in several diseases, including Alzheimers disease [139] and cerebral ischemia [66]. In this study, the effects of global cerebral ischemia on neurovascular coupling in a rat animal model are investigated.

Specifically, functional CBF, $CMRO_2$, oxy-hemoglobin concentration (HbO), deoxy-hemoglobin concentration (HbR), and total hemoglobin concentration (HbT) responses to forepaw stimulation on rats were measured at several levels of global ischemia from very mild ($CBF \sim 90\%$ of normal supply) to more severe ($CBF \sim 40\%$ of normal supply). The combined optical techniques of laser speckle contrast imaging [27, 76] and optical imaging of intrinsic signals [77, 117] were employed to make these measurements. To characterize neuronal activity, the electrical somatosensory evoked potentials (SEP) were also collected simultaneously with the optical hemodynamic measurements. To our knowledge, this is the first study that examines functional activation during graded ischemia.

This study is also motivated by the notion that functional stimulation can be utilized as a treatment for stroke [38, 164]. Fox and Raichle first reported that localized CBF increases due to functional stimulation vastly exceed the localized $CMRO_2$ increases in healthy humans [102]. This observation suggests that the oxygen delivery increase to the tissue from functional stimulation exceeds the oxygen consumption increase [167]. If the mismatch between the CBF response (surrogate for oxygen delivery) and $CMRO_2$ response persists during ischemia, then repeated application of functional stimulation during ischemia could increase the base level of oxygen in the brain.

For severe ischemia (CBF supply below 40% of normal levels), no hemodynamic response to functional stimulation was observed. For less severe ischemic tissue, though, hemodynamic and electrical responses to stimulation were present. We will show in this paper that at these ischemic levels, $CMRO_2$ and SEP functional responses remained tightly coupled. Importantly, we discovered that as the animals became ischemic, the CBF response was more strongly attenuated than the $CMRO_2$ response. This observation suggests that oxygen delivery and consumption increases due to stimulation become more balanced with graded ischemia. Thus, the mechanism for the neuroprotection of functional stimulation during ischemia observed by others [38, 164] is probably not related to CBF changes. This result also supports the notion that in healthy tissue, oxygen delivery increases from functional stimulation exceed oxygen consumption increases (Leithner et al, 2010; Vazquez et al, 2008). If the oxygen delivery and consumption increases were in balance, then the expectation is the CBF and $CMRO_2$ responses would be attenuated at the same rate by ischemia, which was not observed.

7.2 Materials and Methods

7.2.1 Surgical Preparation

All procedures were in accordance with guidelines established by the National Institutes of Health and approved by the Institutional Animal Care and Use Committee of the University of Pennsylvania (approval # 801100). Adult male Sprague-Dawley rats ($N = 46$, 327 ± 31 g; Charles River, Wilmington, MA, USA) were anesthetized with 4% isoflurane in a bell jar, intubated, and then mechanically ventilated with 1.5% isoflurane in a mixture of oxygen and nitrous oxide (3:7). End-tidal CO_2 was monitored and the ventilation rate was adjusted to maintain an arterial CO_2 pressure close to 40 mm Hg. Polyethylene catheters were placed in the femoral artery for blood pressure monitoring and the femoral vein for drug administration. Throughout the study, body temperature was measured with a rectal probe and maintained at $37.5 \pm 0.2°$ C with a heating pad (ATC1000, World Precision Instruments, Sarasota, FL, U.S.A.). In preparation for hemodynamic imaging, the rats were secured in a stereotaxic head holder. After reflecting their scalps, their skulls were uniformly thinned to translucency over a 5 by 5 mm window encompassing the right forepaw area of the cerebral cortex (center ~ 3.5 mm directly lateral to bregma) (i.e., black square in Figure 7.1A) with a dental drill. To reduce specular reflections, ultrasound gel was applied to the translucent thinned skull and a glass coverslip placed on top. As depicted in Figure 7.1A, two 1 mm burr holes were drilled through the skull down to the dura (~ 3.5 mm lateral and 3 mm anterior of bregma; ~ 2.5 mm directly posterior to lambda) for the placement of electrodes to measure the somatosensory evoked potentials resulting from forepaw stimulation.

To induce global ischemia, animals were held in a supine position while a midline neck incision was made. Both common carotid arteries (CCA) were isolated from the surrounding connective tissue, and loose snares made from a polyethylene catheter (PE-10) were carefully placed around them for later remote occlusion. In order to achieve more severe ischemia, a partial sternotomy was also performed in the last 39 animals in the study. After separating sterno-hyoid muscle, the bifurcation of the right CCA and the right subclavian artery (SCA) from the aorta was carefully dissected and exposed. A snare was then placed around the right subclavian artery between the first and second bifurcation of the right SCA. Finally, to even further increase the

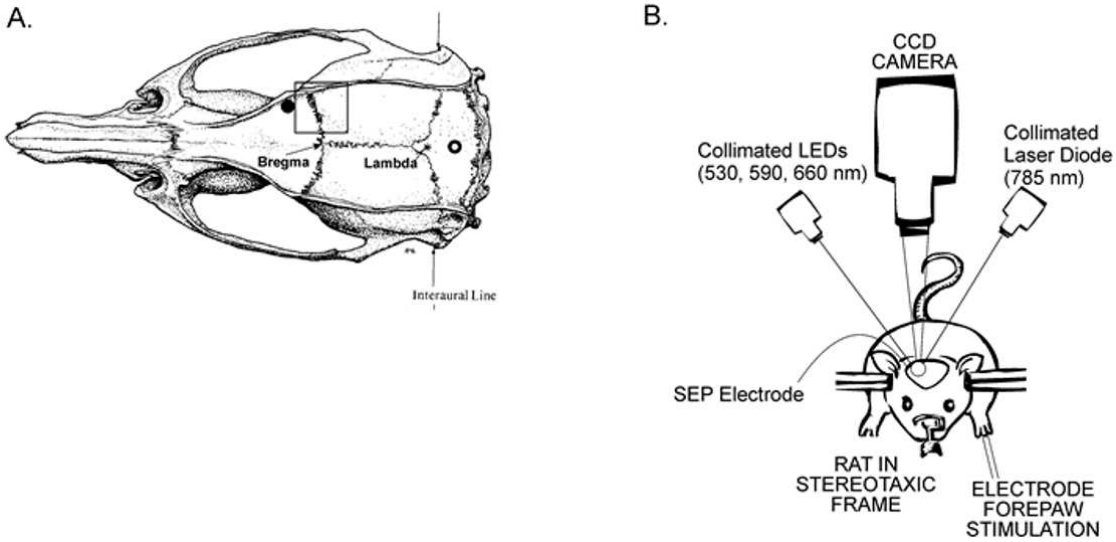

Figure 7.1: **(A)** Diagram of the rat brain showing the 5×5 mm thinned part of the skull over the forepaw area of the cerebral cortex for hemodynamic imaging (black square) and the burr hole locations for electrodes to measure somatosensory evoked potentials (SEP) (filled and open circles). **(B)** Schematic of instrument used for optical imaging of hemodynamics.

degree of ischemia, the lower bodies of the last 17 animals in the study were placed inside a custom-made pressure chamber after the snares were in position. The pressure chamber applied negative pressure to the rats, causing blood to pool in the lower part of the body [71]. The snares were tightened and negative pressure was applied sequentially to create different levels of cerebral ischemia from mild to severe.

For functional stimulation, two needle electrodes were inserted subdermally in the left forepaw of each rat, contra-lateral to the translucent imaging window. Following the surgical preparation, α-chloralose (60 mg/kg) was administered intravenously and the isoflurane was discontinued. Nitrous oxide was also discontinued and replaced with nitrogen gas. Anesthesia was maintained with an intravenous infusion of α-chloralose (30 mg/kg/hr). Upon completion of the study, animals were euthanized with an overdose of barbiturate.

A control group (N = 5) was prepared in the same manner as described above with loose snares placed around both carotid arteries and the right subclavian artery. However, these snares were not tightened to cause ischemia.

7.2.2 Experiment Protocol

Figure 7.2 is a timeline of the study. As described above, the aim of the experiment was to create different levels of global ischemia and measure the hemodynamic and electrical responses to forepaw stimulation. We generated different levels of ischemia by right common carotid artery occlusion (RCCAO), bi-lateral common carotid artery occlusion (RCCAO+LCCAO), bi-lateral common carotid artery occlusion with right subclavian artery occlusion (RCCAO+LCCAO+RSCAO), and three vessel occlusion with lower body negative pressure applied in a pressure chamber. After inducing each condition of ischemia, we waited five minutes to allow flow to stabilize before starting functional stimulation. The control group of animals shared the same timeline except that we did not occlude any arteries or apply lower body negative pressure. After euthanizing the animals, laser speckle images were collected for 5 minutes to obtain a biological zero correction to the CBF measurements [275].

The forepaw stimulation paradigm, which was executed during the time windows marked DA (i.e., data acquisition) in Figure 7.2, consisted of a train of constant current rectangular pulses (amplitude 1.5 mA, duration 300 μs) delivered to the forepaw at 3 Hz for 4 seconds by a commercial high voltage stimulus isolator (A360, World Precision Instruments). The stimulation train was repeated every 30 seconds for a total time period of 8 minutes. After letting the animal rest for four minutes with no stimulation, the stimulation trains were resumed every 30 seconds for another 8 minutes. During these 8 minute periods, laser speckle and spectral images were collected sequentially for hemodynamic imaging, and electrical somatosensory evoked potentials due to the stimulation were recorded. This stimulation paradigm was repeated for every level of ischemia, as indicated in Figure 7.2. Five minutes prior to the first data acquisition, blood was withdrawn from the femoral artery for blood gas analysis.

7.2.3 Optical Instrument

To obtain images of changes in blood flow and oxygenation, the techniques of laser speckle contrast imaging and optical imaging of intrinsic signals were combined [77]. As depicted in Figure 7.1B, a 60-mm lens (Apo-Componon 2.8/40, Schneider-Kreuznach, Bad Kreuznach, Germany) was used to form an image of the 5 by 5 mm forepaw region of the cerebral cortex on a

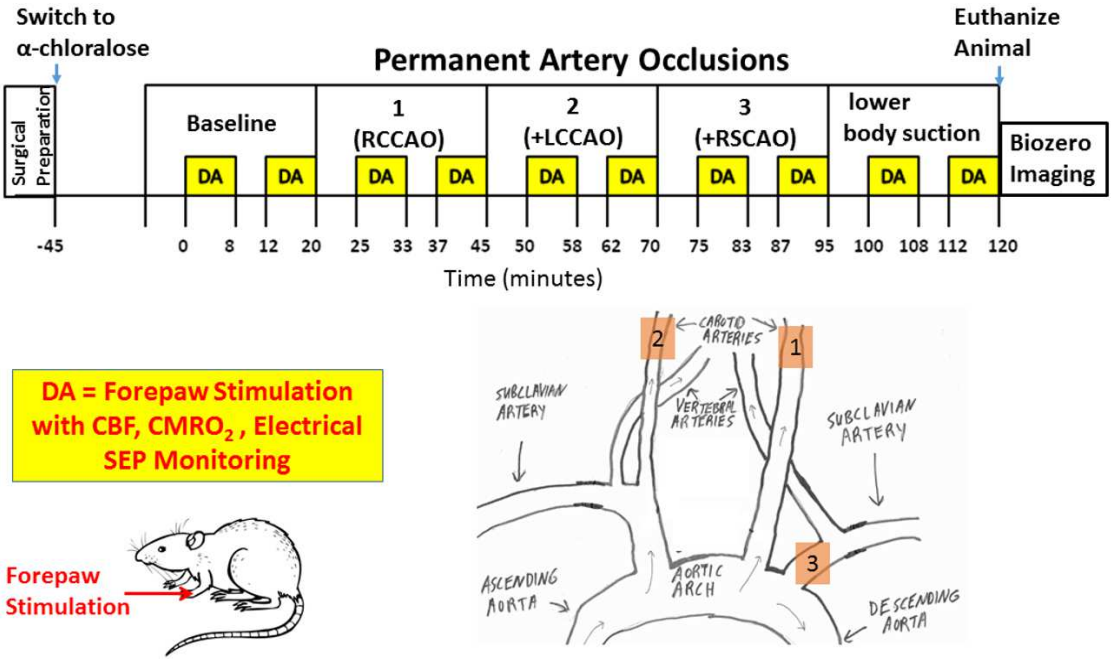

Figure 7.2: Schematic showing the timeline of the study in minutes (time axis not to scale). DA stands for data acquisition, where we collected laser speckle and spectral images and applied forepaw stimulation trains (1.5 mA, 0.3 ms rectangular pulses delivered at 3 Hz for 4 seconds) every 30 seconds as described in the text. The top row of boxes indicate the CBF conditions, which are baseline (i.e., pre-ischemic), right common carotid artery occlusion (RCCAO), right and left common carotid artery occlusion (RCCAO+LCCAO), right and left common carotid artery occlusion with right subclavian artery occlusion (RCCAO+LCCAO+RSCAO), and the occlusion of the previous three arteries with the application of negative lower body pressure.

12-bit TEC cooled CCD camera (UP-680CL-12B, Uniq Vision Inc., Santa Clara, CA, U.S.A.) with unity magnification. Interleaved images (exposure time $T = 4$ ms) under different illumination sources were then captured and recorded using a frame grabber (Grablink Avenue, Euresys Inc., San Juan Capistrano, CA, U.S.A.) and imaging software (StreamPix, NorPix, Montreal, Quebec, Canada).

The illumination source used for laser speckle contrast imaging of CBF was a collimated 785 nm laser diode (Sanyo, DL7140-201S, 785nm, 70 mW, Thorlabs, Newton, NJ, U.S.A.) mounted on a temperature-controlled heat sink (LDM21 Laser Diode Temperature Controlled Mount, Thorlabs) and driven by a commercial driver (LDC 500 Laser Diode Controller, Thorlabs). The illumination sources used for optical imaging of intrinsic signals to measure changes in oxy-hemoglobin (HbO) and deoxy-hemoglobin (HbR) concentrations were three collimated light emitting diodes (LEDs) mounted on heat sinks with central wavelengths of 530, 590, and 660 nm (M530L2-C1, M590L2-C1, M660L2-C1, Thorlabs) driven by commercial drivers (LEDD1B T-Cube LED Driver, Thorlabs).

Commercial software (SciWorks, DataWave Technologies, Boulder, CO, U.S.A.) was employed to program pulse sequences of digital outputs from an A/D board (DataWave Technologies) to control the timing for the interleaved imaging. With this instrument, we acquired 3 spectral images and 4 speckle images/second.

7.2.4 Somatosensory Evoked Potential (SEP) recordings

To measure the SEP response to stimulation, a 1 mm diameter silver/sliver chloride ball electrode and a reference silver screw electrode were placed on the dura in the burr holes indicated by the filled and open black circles in Figure 7.1A, respectively. The recording electrodes were connected to a low-impedance HS4 headstage (World Precision Instruments), which amplified and digitized the voltage difference between the two electrodes before sending the signal to a Digital BioAmp (DB4, World Precision Instruments), where the signal was further amplified and filtered between 5 Hz and 500 Hz. SciWorks software was used to record the SEP signal from the BioAmp for 200 ms after each stimulation pulse was delivered to the animal.

7.2.5 Optical Image Analysis

Laser speckle contrast imaging of CBF has been discussed extensively in previous publications [27], and the specific analysis used in this study to calculate CBF from speckle contrast images is described by Zhou *et al* [275]. It was assumed that the static scattering contribution to the speckle contrast signal from the thinned skull [198] was negligible, since we saw very similar flow responses to studies where the skull was completely removed [82]. Since we were interested in functional CBF responses to stimulation, the CBF images were averaged across stimulation trials for each level of ischemia. A stimulation trial was defined as the 20-second time period that begins 5-seconds before the start of a stimulation pulse train.

Optical imaging of intrinsic signals (or spectral imaging) to determine HbO and HbR is also a well-established technique [78, 163]. As with CBF, the intensity images of each LED were averaged across stimulation trials at each level of ischemia. The averaged spectral intensity images of the three LEDs were converted to images of HbO and HbR via a modified Beer-Lambert law (see Section 7.5).

As many other investigators have done, we employed a compartmental model (Section 7.6) to calculate $CMRO_2$ images from our measurements of CBF, HbO, and HbR [62, 78, 273]:

$$CMRO_2 = \frac{(SaO_2 - HbO/HbT)}{\gamma SaO_2} \times CBF \times C_a. \tag{7.1}$$

Here, HbT is the measured total hemoglobin concentration (i.e., $HbT = HbO + HbR$), SaO_2 is the oxygen saturation in the cerebral arterioles (taken to be 1), γ is the blood volume fraction contained in the venous compartment of the vascular system, and C_a is the blood arteriolar oxygen concentration. There is mounting evidence that oxygen extraction takes place in arteries and arterioles, and as a result, the arterioles directly feeding the cerebral capillary beds may have a lower saturation than the systemic arterial saturation [251, 264]. In the present study, all animals breathed 30% enriched oxygen resulting in high systemic arterial oxygen tensions (~ 120 mm Hg). Thus, even with oxygen extraction in the arteries, the arteriolar saturation will still be close to one throughout the study.

Equation 7.1 is a steady-state model for $CMRO_2$. To estimate the errors in this model when applying it to the dynamic situation of functional stimulation, we followed Vazquezs *et al* [247]

approach of applying a dynamic compartment model to solve for $CMRO_2$ using input measurements from our previous study of cerebral tissue oxygen tension and blood flow in healthy rats during functional stimulation [4]. The increases in $CMRO_2$ during functional activation computed with this dynamic model were then compared to the increases computed with the steady-state model (Equation 7.1). This comparison showed that the calculated peak increases in $CMRO_2$ due to stimulation for the dynamic and steady-state models were within 2% of each other (see Section 7.6). Consequently, and as discussed below, in the present study we use the peak increase from functional stimulation to characterize the response.

Under the assumptions that SaO_2, C_a, and γ remain constant over time, substituting measurements of HbO, HbR, and CBF into Equation 7.1 results in an index that is proportional to $CMRO_2$. Although it is feasible that these assumptions may be violated during ischemia, our group and others have shown the calculated metabolic changes from Equation 7.1 to be relatively insensitive (i.e., $< 5\%$) to most of the likely physiological cases that violate these assumptions [62, 151].

7.2.6 Quantifying Hemodynamic and SEP Responses to Stimulation

Figures 7.3A and 7.3B contain montages of fractional CBF and $CMRO_2$ responses to stimulation for an exemplar animal averaged across all trials during the CBF baseline period of Figure 7.2. To quantify the hemodynamic responses of CBF and $CMRO_2$, as well as the hemoglobin concentrations HbO, HbR, and HbT (image montages not shown), we followed the same approach as Durduran *et al* [82] to select a region of interest (ROI). *A priori* information about the stimulus paradigm was used by computing a temporal correlation coefficient at every image pixel between CBF and the forepaw stimulus [82] during the pre-ischemic baseline period denoted in Figure 7.2.

In order to apply a consistent threshold across all animals for ROI selection, the resulting image of correlation coefficients was normalized by the maximum pixel, resulting in an image of normalized correlation coefficients scaled from 0 to 1 (Figure 7.3C). A ROI to consist of all pixels with normalized correlation coefficients above 0.8 was arbitrarily chosen, and hemodynamic temporal response curves at each level of ischemia were obtained by averaging over all pixels within the ROI. We note here that we did not observe significant changes in our results when

we tried using different correlation coefficient thresholds of 0.9 or 0.7 for the ROI, indicating robustness to the particular ROI threshold.

At ischemic condition i in an animal (e.g., $i =$ RCCAO, RCCAO+LCCAO; see Figure 7.2), the hemodynamic responses were quantitatively characterized by their average peak increases from baseline because of stimulation, i.e., $\langle \Delta x \rangle_i \equiv \langle x_{\text{peak}} - x_0 \rangle_i$, where x refers to the CBF index, $CMRO_2$ index, HbO, HbR, or HbT. The SEP response, in turn, was characterized at condition i by the average difference between the $p1$ and $n1$ peaks of the signal (Figure 7.3D), which is denoted as $\langle \Delta SEP \rangle_i$. To make the quantified responses unitless, which will facilitate comparison between the different response parameters at different ischemic levels, the hemodynamic and SEP responses at each ischemic condition i were normalized by their preischemic baseline responses, $\langle \Delta x \rangle_{BL}$ and $\langle \Delta SEP \rangle_{BL}$:

$$\text{Normalized hemodynamic response} = \langle \Delta x \rangle_i / \langle \Delta x \rangle_{BL}, \tag{7.2}$$

$$\text{Normalized SEP response} = \langle \Delta SEP \rangle_i / \langle \Delta SEP \rangle_{BL}. \tag{7.3}$$

The level of ischemia, or fraction of the normal CBF supply to the brain, reached due to the ith ischemic condition in an animal was determined quantitatively by averaging the prestimulus speckle CBF index during condition i, $\langle CBF_0 \rangle_i$, and dividing this by the same average of CBF during the baseline condition, $\langle CBF_0 \rangle_{BL}$:

$$CBF \text{ level} = \frac{\langle CBF_0 \rangle_i}{\langle CBF_0 \rangle_{BL}}. \tag{7.4}$$

Also of interest is the affect of cerebral ischemia on SEP latency, which we define as the time after stimulus onset of the $p1$ peak in the SEP signal.

7.2.7 Statistical Analysis

Across animals, the degree of ischemia attained following each of the manipulations was quite heterogeneous. Thus, although blood flow was lowered only through three artery occlusions and negative lower body pressure, many different CBF levels ranging from very mild ischemia (i.e., 0.94) to severe ischemia (i.e., 0.36) were achieved in the animals. A major goal of this study was to determine whether there were differences in the mean CBF, $CMRO_2$, and SEP normalized functional responses (Equations 7.2, 7.3) as a function of CBF level (Equation 7.4).

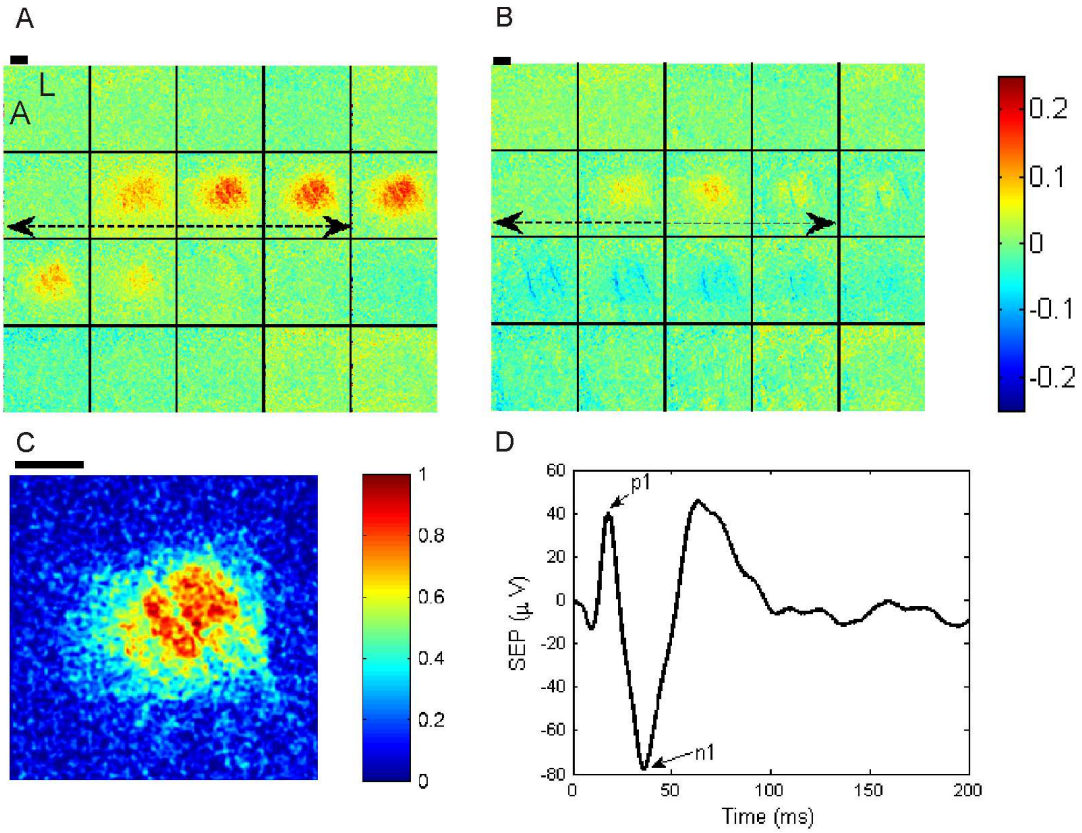

Figure 7.3: Image montages of fractional changes in CBF (**A**) and $CMRO_2$ (**B**) averaged across stimulation trials during the baseline, or pre-ischemic, CBF condition for an exemplar animal. The fractional changes are relative to the mean of the parameters over the 5-second pre-stimulus time windows. Each image in the montages is spaced one second apart when read from left to right and top to bottom. The dashed double arrows indicate the 4-second forepaw stimulus, and the letters L and A within the first image of the CBF montage stand for lateral and anterior, respectively, to indicate image orientation. For ROI selection, a temporal correlation coefficient was computed at every pixel between CBF and the forepaw stimulus during pre-ischemic stimulation, and the resulting correlation coefficient image was then normalized to the maximum pixel [82]. The ROI for the animal in this figure consists of all pixels in the animals normalized correlation coefficient image (**C**) with values greater than 0.8 (see text). The thick black lines in panels (A) through (C) are 1 mm scale bars. (**D**) The SEP signal averaged across stimulation trials during the pre-ischemic baseline condition from the same animal as shown in panels A-C. The difference between the $p1$ and $n1$ peaks in the SEP signal was used to characterize the electrical response to stimulation.

To address this, a mixed effects model was used [205]. This procedure is conceptually similar to repeated measures ANOVA but allows the CBF level to be treated as a continuous variable. Initial graphical procedures suggested that in many cases the association between CBF level and the normalized functional responses was non-linear. Thus, a natural cubic spline was used to model the mean CBF, $CMRO_2$, and SEP normalized functional responses separately at each CBF level.

We additionally fit two natural cubic spline models to these three types of normalized responses (i.e., CBF, $CMRO_2$, and SEP) simultaneously to determine the statistical significance of the differences in patterns over CBF level that we observed between these different types of responses. In one model, these differences were allowed to follow a parallel, albeit non-linear pattern over CBF level. In the second model, the response types were allowed to change differently over CBF level. We applied a likelihood ratio test to these two models to test the null hypothesis that the three functional response types are all affected the same by CBF level. We also determined the significance of the differences between the SEP response and the other two response types by considering the Wald statistics for each of the terms in the spline of the second model. We then repeated this analysis to compare SEP responses with the HbO, HbR, and HbT responses as a function of CBF level.

The analysis described above addresses the global question of whether there were differences in the mean CBF, $CMRO_2$, HbO, HbR, HbT, and SEP responses as a function of CBF level. Another important question is if there are differences in the hemodynamic responses with the SEP response over CBF level, then what are the ranges of CBF levels where these responses are different. To address this, we used individual mixed effects models with a natural cubic spline to model the mean logarithms of the ratios of SEP response with the hemodynamic responses that differed globally from SEP (i.e., $\log(SEP/CBF)$, $\log(SEP/HbO)$, and $\log(SEP/HbR)$) as a function of CBF level. The hemodynamic responses were significantly different from SEP at CBF levels where the 95% CIs from these models did not overlap zero.

Lastly, we used a mixed effects model to test the hypothesis that SEP latency increased with CBF level. As with the normalized responses, a natural cubic spline was employed to model the mean SEP latency as a function of CBF level, and the overall significance was assessed using a likelihood ratio test.

These mixed effects models were implemented with library (nlme) and library (splines) in R 2.13 [241]. A Type I error rate of 0.05 and 95% confidence intervals on the population mean (95% CI) were used.

7.3 Results

Prior to ischemia, the population means and standard deviations of pH, PaO_2, and $PaCO_2$ determined from blood gas analysis were 7.44 ± 0.09, 124 ± 21 mm Hg, and 37 ± 8 mm Hg, respectively, and the arterial blood pressure was 106 ± 6 mm Hg. To aid the visualization of the effects of graded cerebral ischemia in this animal model on blood pressure, hemodynamic responses, and electrical responses, we discretized ischemic CBF levels into bins of width 10 percentage points (i.e., 0.85-0.95, 0.75-0.85, . . ., 0.35-0.45) and determined parameter averages across animals at CBF levels within these bins. The arterial blood pressures (mean $\pm$ SD) at these binned CBF levels were 115 ± 9, 122 ± 12, 112 ± 7, 118 ± 12, 117 ± 15, and 95 ± 19 mm Hg for the CBF levels of $0.85 - 0.95$, $0.75 - 0.85$, $0.65 - 0.75$, $0.55 - 0.65$, $0.45 - 0.55$, and $0.35 - 0.45$, respectively.

Figure 7.4 shows average fractional hemodynamic temporal response curves across animals at each binned CBF level of ischemia. Prior to ischemia (CBF Level 1 panel in Figure 7.4), CBF has the largest response of the hemodynamic parameters, with an average peak increase of 21%, while $CMRO_2$ peaked at 12%. HbO and HbR peaked at 8% and -8%, respectively, while a small 2% peak increase in HbT was observed. All the hemodynamic functional responses were attenuated as the animals became more ischemic, and once the CBF level reached 0.4, the responses essentially disappeared. Also, notice in Figure 7.4 that the peaks of the CBF and $CMRO_2$ responses approach each other as the level of ischemia increases, indicating that global ischemia more strongly attenuates the CBF response.

Corresponding to the average hemodynamic responses in Figure 7.4 are the average electrical SEP responses presented in Figure 7.5. As with the hemodynamic responses, the SEP response is attenuated as the level of ischemia increases. However, the SEP response has not vanished at the CBF level of 0.4, whereas the blood flow response is very much attenuated. Additionally, Figure 7.5 contains the mean SEP latency at each binned CBF level. The observed increase in

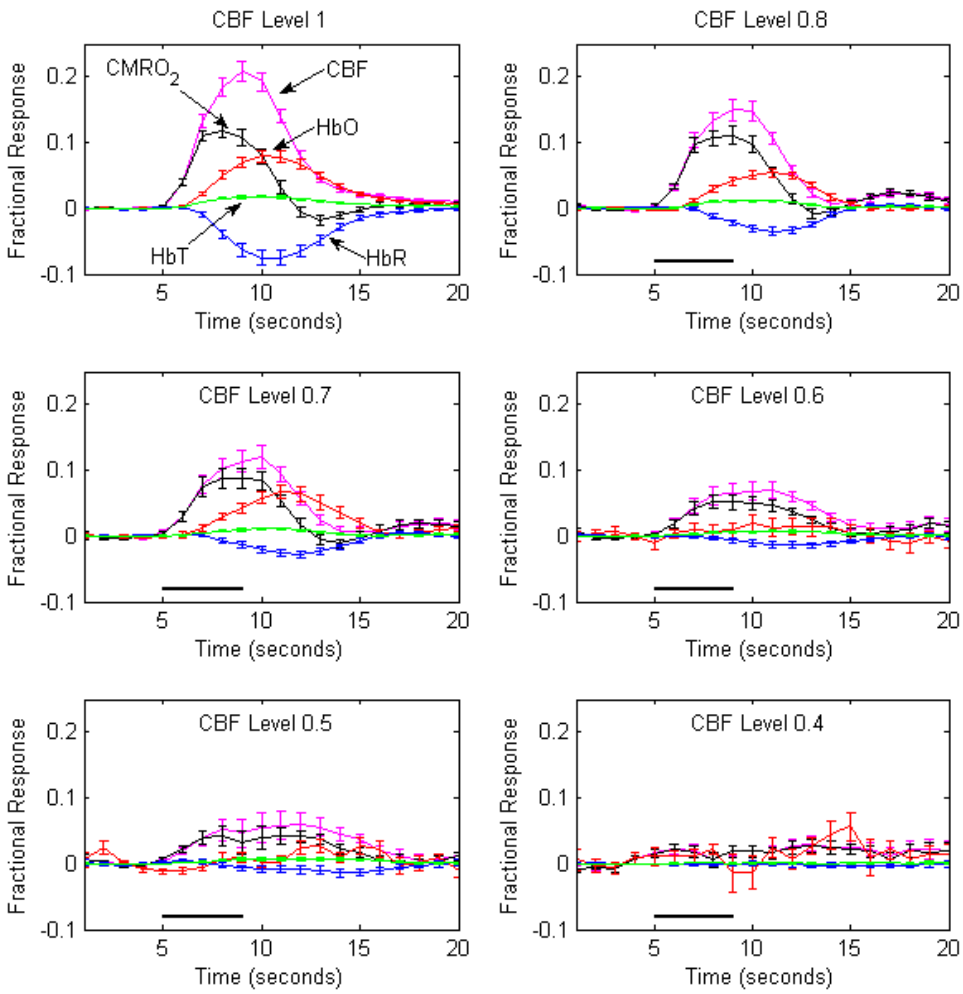

Figure 7.4: The average fractional responses of cerebral blood flow (CBF), cerebral metabolic consumption of oxygen ($CMRO_2$), cerebral oxy-hemoglobin (HbO), cerebral deoxy-hemoglobin (HbR), and cerebral total hemoglobin (HbT) measured at various CBF levels (see Equation 7.4) within the specified bins. The CBF bins are labeled by their central numbers (e.g., CBF level 0.8 spans the range of CBF levels from 0.75 to 0.85), and the CBF level 1 indicates the pre-ischemic responses. Here, the CBF bin 0.9 is omitted since the temporal plots look very similar to the pre-ischemic responses. The error bars indicate the standard errors of these averages, and the 4-second forepaw stimulus is indicated in the panels by a thick black line (omitted from CBF Level 1 panel for readability).

SEP latency with ischemia relative to the pre-ischemic latency is highly significant ($p < 0.0001$).

Interestingly, the CBF response is attenuated more strongly at milder levels of global ischemia than the $CMRO_2$ and SEP responses (Figures 7.6, 7.7). Figure 7.6 is a bar plot showing the mean normalized hemodynamic and SEP responses, as defined by Equations 7.2 and 7.3, at each CBF level bin. Figure 7.6A suggests that the $CMRO_2$ response is tightly coupled to SEP as the animals become more ischemic, whereas the CBF response exhibits a greater attenuation than does SEP. This behavior is confirmed in Figure 7.7, where instead of discretizing the data into bins, a mixed effects model was used to model averages of CBF, $CMRO_2$, and SEP responses at each CBF level. This analysis demonstrates strong evidence of differences among these three response types over the CBF level ($p < 0.0001$) as well as evidence that CBF response differs from SEP ($p < 0.0001$) and from $CMRO_2$ ($p < 0.0001$). However, there was no significant difference between SEP and $CMRO_2$ ($p > 0.1$). The mixed effects model analysis comparing SEP to the hemoglobin concentrations HbO, HbR, and HbT also provides strong evidence of differences among these four response types over CBF level ($p < 0.0001$). As with $CMRO_2$, there was no significant difference between HbT and SEP, but the SEP response did significantly differ from HbO ($p < 0.0001$) and HbR ($p < 0.02$).

We took the logarithms of the ratios of the SEP response with the three hemodynamic responses (CBF, HbO, HbR) that differed from SEP over CBF level, and applied individual mixed effects models to them to determine the range of CBF levels where their means are different from zero ($p < 0.05$). These models predict the mean CBF, HbO, and HbR responses first become different from SEP at CBF levels of 0.86, 0.83, and 0.84, respectively. The mean CBF and HbO responses remain different from SEP at all lower CBF levels in the data set, while the mean HbR response is different from SEP until the CBF level of 0.42. We also note here that in the control group of animals, where no occlusions were made or negative pressure applied, the average normalized hemodynamic and SEP responses across animals did not significantly change (i.e., fluctuations less than 5%) over the two hour time course of data collection (data not shown).

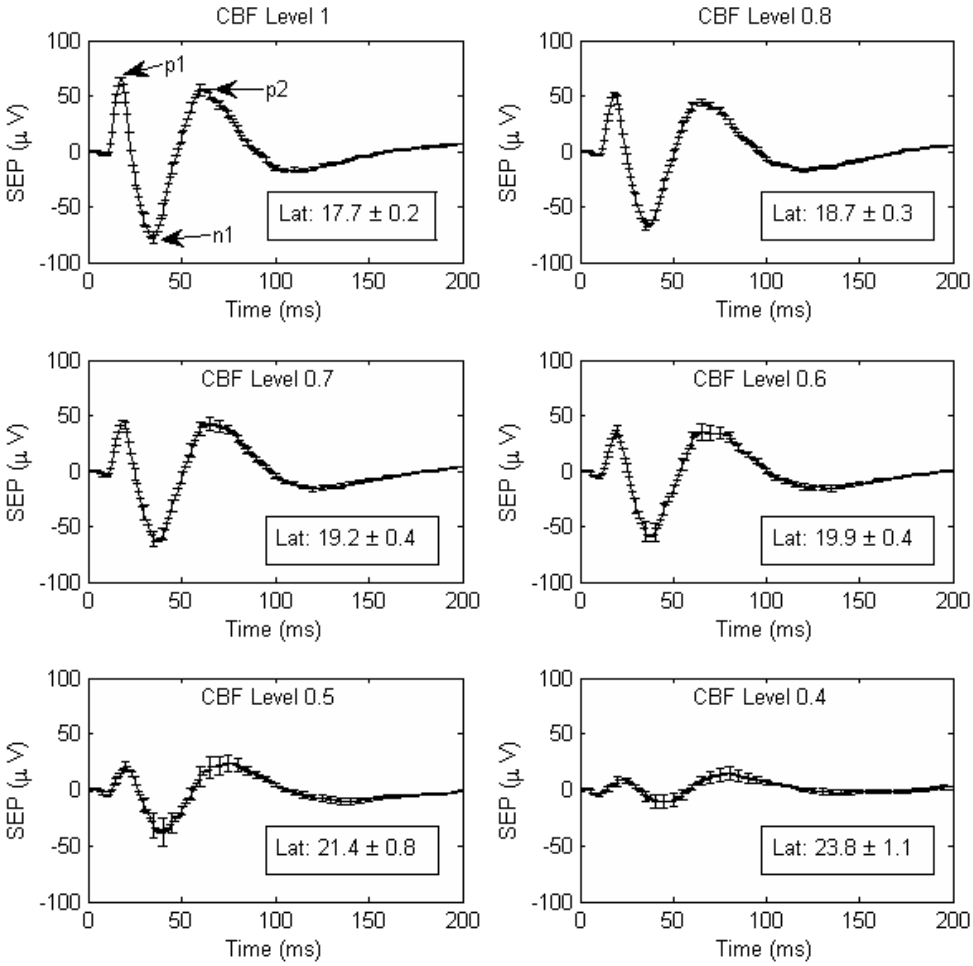

Figure 7.5: The average somatosensory evoked potential (SEP) across animals at each CBF level bin. As with Figure 7.4, the CBF level bins are specified by their central numbers. The error bars indicate the standard errors of these averages, and the time zero here corresponds to the arrival of a stimulation pulse. The boxes in each panel contain the SEP latencies (mean $\pm$ standard error) in milliseconds at each CBF level. The latency is the time from stimulus to the $p1$ peak. SEP latencies are significantly associated with CBF level ($p < 0.0001$).

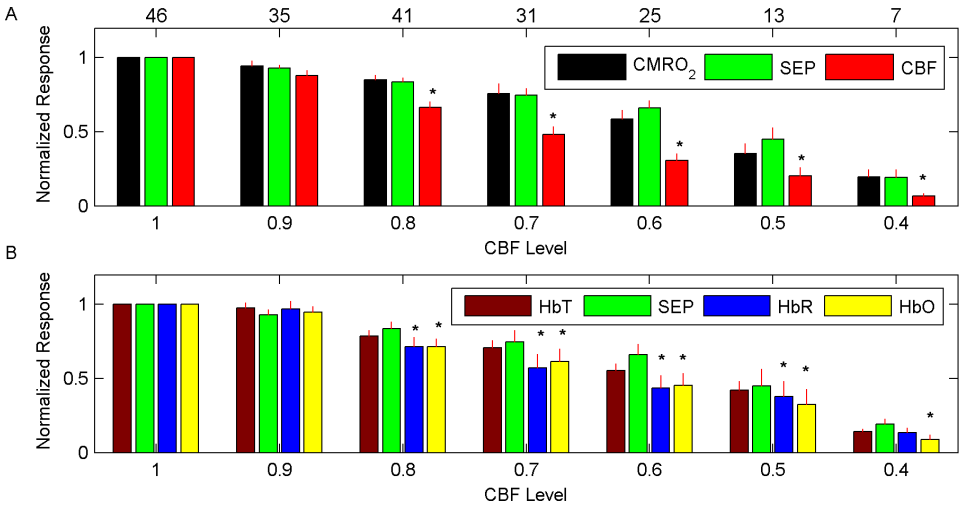

Figure 7.6: Average normalized hemodynamic and SEP responses (Equations 7.2, 7.3) across animals at the binned CBF levels of ischemia (Equation 7.4) specified on the horizontal axis. As with Figures 7.4 and 7.5, the levels of ischemia are discretized into bins with widths of 10 percentage points, such that a CBF level of 0.9 corresponds to the range of CBF levels between 0.85 and 0.95, a CBF level of 0.8 corresponds to the range of CBF levels between 0.75 and 0.85, etc. (**A**) From left to right, the average normalized cerebral metabolic consumption of oxygen ($CMRO_2$), somatosensory evoked potential (SEP), and cerebral blood flow (CBF) responses. (**B**) From left to right, the average normalized cerebral total hemoglobin (HbT), somatosensory evoked potential (SEP), cerebral oxy-hemoglobin (HbO), and cerebral deoxy-hemoglobin (HbR) responses. The top row of numbers in panel (A) indicates the number of animals contributing to the averages for each CBF level. In both panels, the red lines are standard errors to the averages, and the asterisks (*) denote statistically significant differences ($p < 0.05$) with SEP at a given bin, as determined from a mixed effects model of the mean logarithm of the ratio of SEP with the respective hemodynamic parameter (see statistical methods). Recall that by definition, the pre-ischemic response at CBF level 1 is 1, which is why there are no error bars in the first bins of both panels.

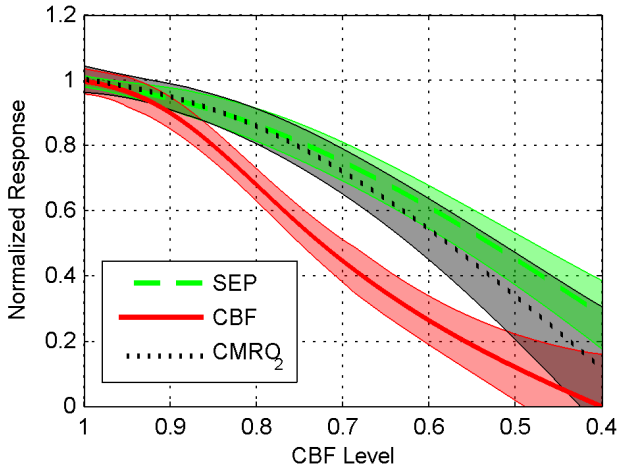

Figure 7.7: Mean normalized response (Equations 7.2, 7.3) across animals (thick lines) of SEP, CBF, and $CMRO_2$ as a function of CBF level (Equation 7.4). Mean values shown are based on individual mixed effects models (see statistical methods) along with their 95% confidence intervals (shaded regions). CBF differed from SEP ($p < 0.0001$) and $CMRO_2$ ($p < 0.0001$), but SEP and $CMRO_2$ were not significantly different ($p > 0.1$).

7.4 Discussion

Fox and Raichle [102] first reported that for healthy humans, the localized CBF increases due to functional stimulation vastly exceed the localized CMRO2 increases, although they were comparable to the increases in localized cerebral glucose metabolism [103]. The compartmental model of Buxton and Frank [41] explained this observation by noting that a large CBF increase could be necessary to support a small $CMRO_2$ increase due to oxygen diffusion limitations. A key assumption of their model is that all of the oxygen leaving the vasculature is metabolized, which results in a tight coupling between CBF and $CMRO_2$. However, the direct measurements of tissue oxygen pressure and CBF in rats by Ances *et al* [4] during functional stimulation provide evidence of an uncoupling between CBF and $CMRO_2$ in that after 1 minute of stimulation, there was a sustained post-stimulus undershoot in tissue oxygen pressure that was not present in CBF. This is similar to the resetting of blood flow and metabolism seen following a more generalized activation (sheltering a rat previously exposed to the environment) [178]. Leithner et al [167] also recently presented data in rats showing that the large CBF response from functional stimulation is not necessary to support small changes in $CMRO_2$. Their interpretation of

these results is that there exists a safety factor wherein the blood flow increase from functional stimulation can deliver more oxygen than is necessary to sustain the increase in neuronal activity.

Our results show an uncoupling between CBF and $CMRO_2$ during functional stimulation at different levels of ischemia that supports the notion of the safety factor described by Leithner et al [167]. As seen from Figures 7.6 and 7.7, the attenuation in functional CBF increases at milder levels of ischemia is stronger than the attenuation in the neuronal activity as measured by SEPs. However, the $CMRO_2$ response does not follow the CBF response at the milder levels of ischemia, but instead remains coupled to SEP. In other words, the effect of global ischemia is to make the safety factor between the increases in oxygen supply and consumption during functional stimulation smaller. Thus, especially for severe ischemia, it is likely that the mechanism for the neuroprotection of functional stimulation during ischemia observed by others [38, 164] is probably not related to CBF changes from stimulation.

As with CBF, oxy-hemoglobin and deoxy-hemoglobin concentrations are also more severely attenuated with moderate ischemia than the electrical SEP response. However, ischemia does not affect the total hemoglobin response significantly differently from the SEP response. The uncoupling between blood flow and total hemoglobin responses with ischemia demonstrates that with functional activation, using total hemoglobin as a surrogate for blood flow via Grubbs relation [119] could lead to inaccurate results for blood flow.

Recall that to characterize the functional hemodynamic responses, we looked at peak increases in the hemodynamic parameters (Equation 7.2). An alternative approach would be to integrate the temporal responses due to functional stimulation (i.e., take the area under the response curves) instead, especially since Figure 7.4 suggests that ischemia broadens the hemodynamic responses in addition to attenuating them. Characterizing the hemodynamic responses this way, we find the same behavior as depicted in Figures 7.6 and 7.7, demonstrating the robustness of our main conclusion on the uncoupling between flow and metabolism increases resulting from ischemia.

Though we are not aware of previously published data on functional hemodynamic responses to an identical stimulation protocol, the pre-ischemic responses we measure are reasonable. For 4 Hz, 4-second, 1.6 mA forepaw stimulation in healthy rats, Royl *et al* [214] observed an average

peak CBF increase of roughly 17% with laser speckle imaging, while Durduran *et al* [82] observed average peak CBF increases with laser speckle imaging of $13.4 \pm 2.5\%$ and $20.0 \pm 3.0\%$ for 5 Hz, 4-second stimulations with amplitudes of 1 mA and 2 mA, respectively. Furthermore, the ratios between the average peak CBF response and the average peak $CMRO_2$, HbO, HbR, and HbT responses in our pre-ischemic data are comparable to functional responses due to a 10-second, 3 Hz, 1 mA forepaw stimulus reported by Dunn *et al* [78]. The small post-stimulus undershoot in $CMRO_2$ present in Figure 7.4, as well as the simultaneous rise of CBF and $CMRO_2$, is likely an artifact of the steady-state model, Equation 7.1 [245].

In regards to somatosensory evoked potentials, experimental work involving a focal ischemia model in baboons showed a sharp CBF threshold for electrical activity in the brain, with complete electrical failure when CBF is approximately 35% of control [33]. A similar CBF threshold was observed for auditory evoked potentials in a global ischemia model in cats [227]. In our study, we did observe severe attenuation in SEPs at a CBF level around 40% (Figures 7.5, 7.6, 7.7), although we did not observe the same sharp CBF threshold for electrical activity seen in these non-rodent ischemia models (Figure 7.7). There is a scarcity of data examining SEPs at milder levels of ischemia. One paper examining SEPs in a hemorrhage ischemia rat model observed SEP amplitudes between $50 - 60\%$ of control when CBF was lowered to approximately 65% of control [230], which is reasonably close to the results in Figure 7.7. In another paper examining the effects of bi-lateral common carotid artery occlusion on SEPs in rats, a steady-state decrease in the SEP $p1$ amplitude to 90% of control is observed, although this decrease was not statistically significant [20]. In the present study, bi-lateral common carotid artery occlusion decreased CBF to $70 \pm 15\%$ (mean $\pm$ SD) of control. Since in the control group, the SEP amplitude remains stable, it is likely that the observed decreases in SEP amplitude during mild ischemia are in fact due to the reduced blood flow levels in the brain. The effect of an increased SEP latency with ischemia (Figure 7.5) has been observed in rodent models of ischemia by others as well [128, 256].

The mechanisms that couple changes in neuronal activity to changes in cerebral blood flow have been under investigation for several decades and involve not only the neurons but also vascular cells and astrocytes encompassing the so-called neurovascular unit [165]. The main mediators for the hemodynamic response to neuronal activation include nitric oxide, adenosine,

glutamate, arachidonic acid metabolites, and epoxyeicosatrienoic acids [139]. During and following cerebral ischemia, the elements that comprise the neurovascular unit may be altered and vascular reactivity depressed [56], with the degree of depression dependent on the degree of ischemia [153]. However, data is lacking on changes to these mediators during graded ischemia. Although a specific mechanism accounting for the decrease in blood flow response as baseline blood flow is decreased cannot be identified, reduction of cerebral blood flow resulting from upstream vascular clamping or hypotension causes the local vasculature to dilate with potential negative implications for further dilation in response to neuronal activation.

To summarize, we have collected a large data set of hemodynamic and electrical functional responses in rats at many different levels of global cerebral ischemia. All of the electrical and hemodynamic responses are attenuated as the global ischemia becomes more severe, but the blood flow, oxy-hemoglobin, and deoxy-hemoglobin responses are more strongly attenuated at milder levels of global ischemia than the electrical or metabolic responses. The observed uncoupling between flow and metabolism at ischemic levels is evidence supporting the notion that during healthy conditions, functional stimulation increases oxygen delivery to brain tissue more than oxygen consumption. During functional stimulation in global ischemia, though, a higher fraction of the oxygen delivered from the vasculature will be consumed.

7.5 Appendix: OIS Modified Beer-Lambert Law with Light Emitting Diodes

A Modified Beer Lambert law for OIS was employed to compute hemoglobin concentration changes from intensity measurements under light emitting diode illumination:

$$-\log\left(\frac{I_{jk}(t)}{I_{0,jk}}\right) = \sum_i w_i \left[\varepsilon_{HbO}(\lambda_i)\Delta HbO_k(t) + \varepsilon_{HbR}(\lambda_i)\Delta HbR_k(t)\right] L(\lambda_i). \tag{7.5}$$

Here, $I_{jk}(t)$ is the measured intensity at time t and $I_{0,jk}$ is the averaged measured pre-stimulus baseline intensity at a given ischemic condition for LED j and pixel k in the CCD camera, $\varepsilon_{HbO}(\lambda)$ and $\varepsilon_{HbR}(\lambda)$ are molar extinction coefficients [207] for HbO and HbR at wavelength λ, respectively, $\Delta HbO_k(t)$ and $\Delta HbR(k)$ are the concentration changes in HbO and HbR from baseline at pixel k and time t, respectively, $L(\lambda)$ is a differential pathlength, w_i are weights

indicating the contribution of wavelength λ_i in the spectra of LED j, and the sum is over all i wavelengths present in the LED spectra. Equation 7.5 assumes that light absorption from tissue chromophores other than HbO and HbR is negligible, and that tissue scattering remains constant over time. The LEDs had a broad spectra (width > 20 nm), which is why it was necessary to measure the emission spectra of the three LEDs used with a spectrophotometer.

The weight w_i in Equation 7.5 is the power of wavelength i emitted by a given LED divided by the total power emitted by the LED over all wavelengths. Using Monte Carlo simulations, the differential pathlengths at each wavelength in the LED spectra were calculated with the procedure described by Kohl *et al* [163] (also see Chapter 3). The mean differential pathlengths for the 530, 590, and 660 nm LEDS we used were 0.063, 0.087, and 0.474 cm, respectively. Equation 7.5 forms a system of 3 equations for each of the 3 LEDs, which was solved for $\Delta HbO_k(t)$ and $\Delta HbR_k(t)$ using a least squares approach.

In addition to using Equation 7.5 to calculate changes in HbO and HbR due to stimulation at a given ischemic condition, Equation 7.5 was also employed to calculate changes in HbO and HbR between adjacent steps of graded ischemia. For example, to measure the changes in HbO and HbR due to unilateral carotid artery occlusion, I_{jk} and $I_{0,jk}$ in the left-hand side of Equation 7.5 are the average pre-stimulus intensities during the uni-lateral carotid artery occlusion and the pre-ischemic baseline periods, respectively, for LED j and pixel k (Fig. 2). HbO and HbR changes between unilateral carotid artery occlusion and bilateral carotid artery occlusion, bilateral carotid artery occlusion and three vessel occlusion, and three vessel occlusion and negative lower-body pressure were calculated the same way. The changes in HbO and HbR between adjacent steps of graded ischemia are small enough that the modified Beer Lambert Law (7.5) is still accurate [152].

It was assumed during the pre-ischemic baseline period for every animal that the cortical tissue under the imaging window is spatially homogeneous with $HbO_0 = 60$ μM, $HbR_0 = 40$ μM, and a reduced scattering coefficient of 10 cm^{-1} for all wavelengths emitted by the LEDs. From this starting point, images of HbO and HbR were then calculated for all subsequent conditions of ischemia.

Table 7.1: Parameters utilized in compartment model (see Equation 7.28 and Figure 7.8).

Quantity	Symbol	Units
Vascular [O_2] (Eq. 7.22)	$C(x,t)$	μmol O_2 / (L blood)
Plasmatic [O_2] (Eq. 7.12)	$C_p(x,t)$	μmol O_2 / (L blood)
Tissue [O_2]	$C_t(t)$	μmol O_2 / L
Arteriole [O_2] ($C(x=0,t)$, Eq. 7.20)	$C_a(t)$	μmol O_2 / (L blood)
Venule [O_2] ($C(x=L,t)$, Eq. 7.16)	$C_v(t)$	μmol O_2 / (L blood)
Vascular cross-section area (Eq. 7.21)	$A_c(x,t)$	cm^2
Arteriole cross-section area (Eq. 7.19)	$A_a(t)$	cm^2
Venule cross-section area (Eq. 7.15)	$A_v(t)$	cm^2
Tissue compartment volume	V_t	mL
Total tissue volume	V_{tissue}	mL
O_2 Permeability (Eq. 7.8)	P	cm / min
surface area O_2 exchange (Eq. 7.11)	$s(x)\mathrm{d}x$	cm^2
Arteriole blood flow (Eq. 7.18)	$CBF_a(t)$	(mL blood) / (min cm^2)
CBF_a, clinical units (Eq. 7.27)	$CBF_{a,c}(t)$	(mL blood) / (min (100 mL tissue))
Venule blood flow (Eq. 7.14)	$CBF_v(t)$	(mL blood) / (min cm^2)
CBF_v, clinical units (Eq. 7.27)	$CBF_{v,c}(t)$	(mL blood) / (min (100 mL tissue))
Tissue [O_2] Metabolism (Eq. 7.26)	$CMRO_2(t)$	μmol O_2 / min
$CMRO_2$, clinical units (Eq. 7.28)	$CMRO_{2,c}(t)$	μmol O_2 / (min (100 mL tissue))

7.6 Appendix: Tissue Compartment Model for $CMRO_2$

The tissue compartment model is essentially a mass balance relation for oxygen that is commonly used to estimate oxygen metabolism (also known as oxygen consumption) from measurements of tissue blood flow and tissue oxygen saturation [41–43,62,104,131,132,136,138,180,187,195, 242,246,273]. The so-called single compartment model approximates the tortuous vasculature in tissue as a single tube embedded in a well-mixed (i.e., spatially homogeneous O_2 concentration) tissue compartment (Figure 7.8) [242]. The parameters used in the compartment model are tabulated in Table 7.1.

7.6.1 Relation of Compartment Model Parameters to Tissue Vasculature

The first step in deriving the compartment model is to calculate the oxygen diffusing from a single blood vessel to the tissue volume at an arbitrary point x along the blood vessel (see dashed box in Figure 7.9). Let w denote the width of the vessel membrane and $c(y)$ denote the concentration of oxygen at a point y within the membrane (Figure 7.9). The oxygen concentration $c(y)$

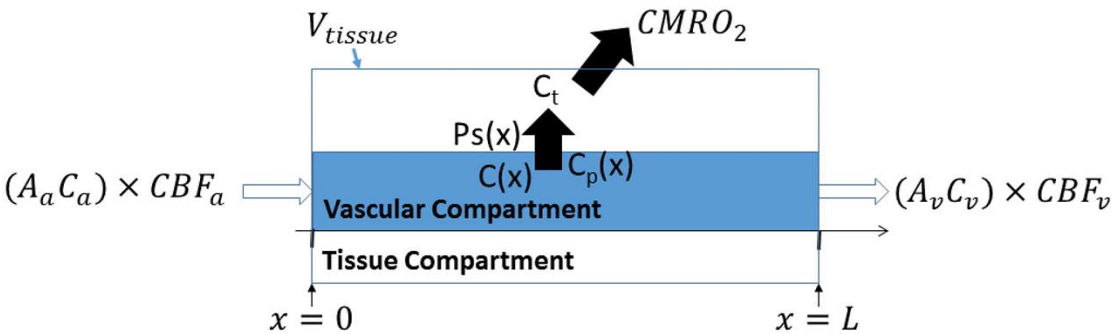

Figure 7.8: An arbitrary tissue volume V_{tissue} is comprised of a vascular compartment of length L and a well-mixed tissue compartment. The total amount of oxygen flowing into the vascular compartment is $(A_aC_a) \times CBF_a$ (Equation 7.17), where C_a is the average arteriole oxygen concentration, A_a is the cross-sectional area of the vascular compartment at $x = 0$, and CBF_a is the blood flow supplying V_{tissue}. Oxygen leaves the vascular compartment via venous drainage ($(A_vC_v) \times CBF_v$ (Equation 7.13); C_v is average venule oxygen concentration, A_v is the cross-sectional area of the vascular compartment at $x = L$, CBF_v is the blood flow draining V_{tissue}) and via oxygen exchange with the tissue compartment (see main text). $C(x)$ is the total concentration of oxygen at position x in the vascular compartment, $C_p(x)$ is the contribution to $C(x)$ from oxygen dissolved in the plasma, P is the oxygen permeability of the vascular compartment (Equation 7.8), $s(x)\mathrm{d}x$ is the infinitesimal surface area of oxygen exchange between the vascular and tissue compartments at x, and C_t is the concentration of oxygen in the well-mixed tissue compartment. The tissue compartment is supplyed by oxygen from the vascular compartment, and "drained" by the consumption of oxygen in V_{tissue} (i.e., $CMRO_2$).

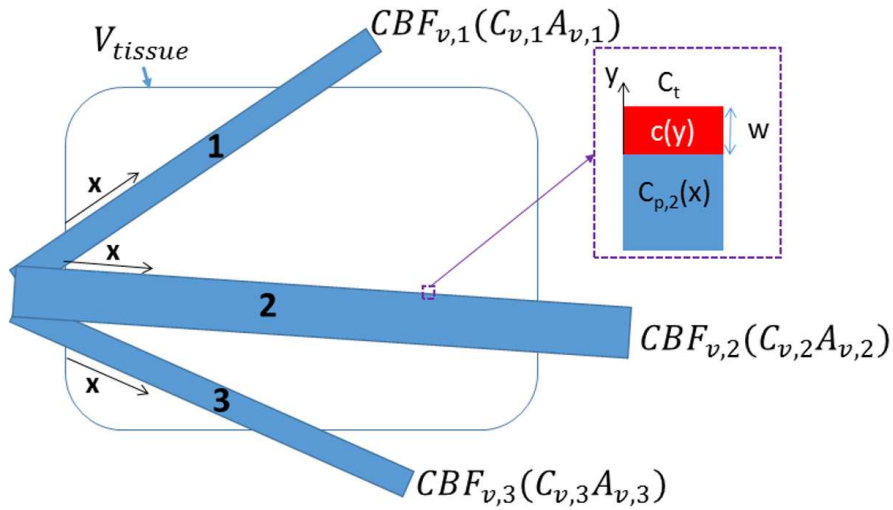

Figure 7.9: Schematic of three vessels spanning the tissue volume V_{tissue} with draining blood flows of $\mathsf{CBF}_{\mathsf{v},1}$, $\mathsf{CBF}_{\mathsf{v},2}$, and $\mathsf{CBF}_{\mathsf{v},3}$. For each vessel, the variable x is understood to be the length along the vessel from its point of entry into the tissue volume. At the "exit points" where the vessels leave V_{tissue}, the oxygen concentrations in the blood are $\mathsf{C}_{\mathsf{v},1}$, $\mathsf{C}_{\mathsf{v},2}$, and $\mathsf{C}_{\mathsf{v},3}$, and the cross-sectional areas of the vessels are $\mathsf{A}_{\mathsf{c},1}$, $\mathsf{A}_{\mathsf{c},2}$, and $\mathsf{A}_{\mathsf{c},3}$. The dashed purple box is a zoomed-in view of a vessel membrane.

is described by the diffusion equation

$$\frac{\partial c}{\partial t} = D_{O2}\frac{\partial^2 c}{\partial y^2}, \tag{7.6}$$

with the boundary conditions $c(y = 0) = \mathsf{C}_\mathsf{p}(x)$ and $c(y = w) = C_t$. D_{O2} is the diffusion coefficient of oxygen in the vessel membrane, $\mathsf{C}_\mathsf{p}(x)$ is the oxygen concentration dissolved in the blood plasma at x, and C_t is the oxygen concentration in the tissue compartment. Assuming steady-state, i.e., $\partial c/\partial t = 0$, the solution to Equation 7.6 is

$$c(y) = \mathsf{C}_\mathsf{p}(x) + [C_t - \mathsf{C}_\mathsf{p}(x)]\frac{y}{w}. \tag{7.7}$$

From Fick's law, the flux of oxygen from the vessel into the tissue at position x, is

$$J_{O2}(x) = -D_{O2}\frac{\partial c}{\partial y} = \frac{D}{w}(\mathsf{C}_\mathsf{p}(x) - C_t) = P(\mathsf{C}_\mathsf{p}(x) - C_t), \tag{7.8}$$

where $P = D_{O2}/w$ [cm / min] is the oxygen permeability of the vessel membrane.

Now, let's consider three vessels flowing through V_{tissue} (Figure 7.9). For a single vessel j, the transport rate of oxygen from vessel to tissue at length x along the vessel is the oxygen flux

given by Equation 7.8 multiplied by the vessel's infinitesimal surface area of oxygen exchange, $\mathsf{s_j}(x)\mathrm{d}x$, i.e., $T_{O2}(x) = P\mathsf{s_j}(x)\mathrm{d}x[\mathsf{C_{p,j}}(x) - C_t]$ [μmol / min]. The total oxygen transport rate is the sum over the rates for each blood vessel, e.g.,

$$\begin{aligned} T_{O2}(x) &= (P\mathsf{s_1}(x)[\mathsf{C_{p,1}}(x) - C_t] + P\mathsf{s_2}(x)[\mathsf{C_{p,2}}(x) - C_t] + P\mathsf{s_3}(x)[\mathsf{C_{p,3}}(x) - C_t])\mathrm{d}x \\ &= Ps(x)\mathrm{d}x[C_p(x) - C_t], \end{aligned} \tag{7.9}$$

where $s(x)\mathrm{d}x = (\mathsf{s_1}(x) + \mathsf{s_2}(x) + \mathsf{s_3}(x))\mathrm{d}x$ is the total surface area of oxygen exchange, and $C_p(x) = [\mathsf{s_1}(x)\mathsf{C_{p,1}}(x) + \mathsf{s_2}(x)\mathsf{C_{p,2}}(x) + \mathsf{s_3}(x)\mathsf{C_{p,3}}(x)]/s(x)$ is a weighted average of the vessel plasmatic oxygen concentrations.

More generally, the total rate of oxygen transport to tissue from N vessels is

$$\begin{aligned} T_{O2}(x) &= \sum_{j=1}^{N} P\mathsf{s_j}(x)\mathrm{d}x[\mathsf{C_{p,j}}(x) - C_t] \\ &= Ps(x)[C_p(x) - C_t], \end{aligned} \tag{7.10}$$

where

$$s(x) = \sum_{j=1}^{N} \mathsf{s_j}(x), \tag{7.11}$$

$$C_p(x) = \frac{1}{s(x)} \sum_{j=1}^{N} \mathsf{s_j}(x)\mathsf{C_{p,j}}(x). \tag{7.12}$$

Also of interest is the "drainage rate" of oxygen from blood flow exiting V_{tissue}, i.e., T^d_{O2} [μmol / min]. The oxygen transport rate out of the tissue from blood flow in an arbitrary vessel j is $\mathsf{CBF_{v,j}}(\mathsf{C_{v,j}}\mathsf{A_{v,j}})$, where $\mathsf{CBF_{v,j}}$, $\mathsf{C_{v,j}}$, and $\mathsf{A_{v,j}}$ are the vessel's blood flow, oxygen concentration, and cross-sectional area, respectively, at the vessel's exit point from V_{tissue}. Therefore, the total drainage rate from N vessels is

$$\begin{aligned} T^d_{O2} &= \sum_{j=1}^{N} \mathsf{CBF_{v,j}}(\mathsf{C_{v,j}}\mathsf{A_{v,j}}) \\ &= CBF_v(A_vC_v). \end{aligned} \tag{7.13}$$

Here,

$$CBF_v = \sum_{j=1}^{N} \mathsf{CBF_{v,j}} \tag{7.14}$$

is the total blood flow exiting V_{tissue},

$$A_v = \sum_{j=1}^{N} \mathsf{A_{v,j}} \tag{7.15}$$

is the total cross-sectional area of the blood vessels at the exit points of V_{tissue}, and

$$C_v = \frac{1}{CBF_v A_v} \sum_{j=1} \mathsf{CBF_{v,j} A_{v,j} C_{v,j}} \tag{7.16}$$

is a weighted average of the vessel oxygen concentrations at their tissue exit points.

Analogously, the "supply rate" of oxygen from blood flow entering V_{tissue} is

$$\begin{aligned} T_{O2}^{s} &= \sum_{j=1}^{N} \mathsf{CBF_{a,j}(C_{a,j} A_{a,j})} \\ &= CBF_a(A_a C_a), \end{aligned} \tag{7.17}$$

where $\mathsf{CBF_{a,j}}$, $\mathsf{C_{a,j}}$, and $\mathsf{A_{a,j}}$ are the jth vessel's blood flow, oxygen concentration, and cross-sectional area, respectively, at the vessel's entry point into V_{tissue}. Further,

$$CBF_a = \sum_{j=1}^{N} \mathsf{CBF_{a,j}} \tag{7.18}$$

is the total blood flow supplying V_{tissue},

$$A_a = \sum_{j=1}^{N} \mathsf{A_{a,j}} \tag{7.19}$$

is the total cross-sectional area of the blood vessels at the entry points of V_{tissue}, and

$$C_a = \frac{1}{CBF_a A_a} \sum_{j=1} \mathsf{CBF_{a,j} A_{a,j} C_{a,j}} \tag{7.20}$$

is a weighted average of the vessel oxygen concentrations at their tissue entry points.

Finally, analogously to Equations 7.19 and 7.20, the vascular compartment cross-sectional area ($A_c(x)$) and oxygen concentration ($C(x)$) at length x in the vascular compartment are

$$A_c(x) = \sum_{j=1}^{N} \mathsf{A_{c,j}(x)}, \tag{7.21}$$

$$C(x) = \frac{1}{CBF(x) A_c} \sum_{j=1} \mathsf{CBF_j}(x) \mathsf{A_{c,j}}(x), \tag{7.22}$$

where $CBF(x) = \sum_{j=1}^{N} \mathsf{CBF_j}(x)$ is the total blood flow at length x.

7.6.2 Oxygen Transport Equations in Vascular and Tissue Compartments

The conservation law [176, Section 1.2] of oxygen in the vascular compartment (see Figure 7.8) is

$$\frac{d}{dt}\int_0^L A_c(x,t)C(x,t)\mathrm{d}x = T_{O2}^s - T_{O2}^d - \int_0^L T_{O2}(x)\mathrm{d}x, \tag{7.23}$$

where the left hand side is the temporal rate of change of oxygen in the vascular compartment, T_{O2}^s is the oxygen supply rate to the vascular compartment, T_{O2}^d is the oxygen drainage rate from vessels exiting the vascular compartment, and the integral on the right-hand side is the diffusive rate of oxygen transport between the vascular and tissue compartments. Substituting Equations 7.10, 7.13, and 7.17 into Equation 7.23, we obtain the vascular compartment oxygen transport equation, i.e.,

$$\frac{d}{dt}\int_0^L A_c(x,t)C(x,t)\mathrm{d}x = CBF_a(t)A_a(t)C_a(t) - CBF_v(t))A_v(t)C_v(t) - \int_0^L Ps(x,t)[C_p(x,t) - C_t(t)]\mathrm{d}x. \tag{7.24}$$

For the tissue compartment, the oxygen transport equation is

$$\frac{d}{dt}\left(V_t(t)C_t(t)\right) = \int_0^L Ps(x)[C_p(x,t) - C_t(t)]\mathrm{d}x - CMRO_2(t), \tag{7.25}$$

where $V_t(t)$ is the volume of the tissue compartment at time t (not to be confused with V_{tissue}, which is the total tissue volume), and $CMRO_2(t)$ [μmol / min] is the tissue oxygen metabolism. In words, Equation 7.25 states that the rate of change in oxygen [μmol/min] in the tissue compartment is the oxygen supply rate diffusing from the vasculature minus the oxygen consumption rate.

Combining Equations 7.24 and 7.25, we find that the compartment model expression for $CMRO_2$ is

$$CMRO_2(t) = CBF_a(t)[A_a(t)C_a(t)] - CBF_v(t)\left[A_v(t)C_v(t)\right] - \frac{d}{dt}\left[V_t(t)C_t(t)\right] - \frac{d}{dt}\left[\int_0^L A_c(x,t)C(x,t)\mathrm{d}x\right]. \tag{7.26}$$

As I discussed in Section 4.9.2, absolute blood flow is reported clinically in units of blood volume per time per tissue volume, e.g., [(mL blood) / (min (100 mL tissue))]. The “clinical”

arterial and venous blood flows, i.e., $CBF_{a,c}$ and $CBF_{v,c}$, relate to CBF_a and CBF_v via

$$CBF_{a,c} = CBF_a \left(\frac{A_a}{V_{\text{tissue}}} \right), \qquad CBF_{v,c} = CBF_v \left(\frac{A_v}{V_{\text{tissue}}} \right). \tag{7.27}$$

Dividing Equation 7.26 by V_{tissue}, we find that the compartment model for $CMRO_2$ in terms of $CBF_{a,c}$ and $CBF_{v,c}$ is

$$CMRO_{2,c}(t) \equiv \frac{CMRO_2(t)}{V_{\text{tissue}}} = CBF_{a,c}(t)C_a(t) - CBF_{v,c}(t)C_v(t) - \frac{1}{V_{\text{tissue}}} \left(\frac{d}{dt}\left[V_t(t)C_t(t)\right] + \frac{d}{dt}\left[\int_0^L A_c(x,t)C(x,t)\right]\right). \tag{7.28}$$

Here, $CMRO_{2,c}(t)$ [μmol / (min (100 mL tissue))] is the tissue oxygen metabolism normalized by the tissue volume.

7.6.3 Steady State Compartment Model

For steady-state conditions wherein the time derivatives are zero and the arterial and venous blood flows are equal, i.e., $CBF_{a,c} = CBF_{v,c} = CBF_c$, Equation 7.28 simplifies substantially to

$$CMRO_{2,c} = CBF_c \left[C_a - C_v\right]. \tag{7.29}$$

Recall that CBF_c is proportional to the DCS blood flow index (i.e., Equation 4.79). Further, if the oxygen dissolved in the plasma is negligible compared to the oxygen bound to hemoglobin, which is usually the case (Figure 7.10), then

$$C_a = 4SaO_2[HbT]_{a,\text{blood}} = 4\upsilon SaO_2 Hct_a, \tag{7.30}$$

$$C_v = 4SvO_2[HbT]_{v,\text{blood}} = 4\upsilon SvO_2 Hct_v. \tag{7.31}$$

Here, SaO_2 and SvO_2 are weighted averages of the oxygen saturation in vessels supplying V_{tissue} (e.g., arterioles) and in vessels draining V_{tissue} (e.g., venules), respectively. Further, $[HbT]_{a,\text{blood}}$ [μmol HbT / L blood] and $[HbT]_{v,\text{blood}}$ are the total hemoglobin concentrations in the blood associated with SaO_2 and SvO_2. Finally, Hct_a and Hct_v are the corresponding hematocrit levels, and υ [μmol HbT / (RBC volume)] is the average amount of total hemoglobin per red blood cell volume. The factor of 4 in Equations 7.30 and 7.31 is present because the concentration of

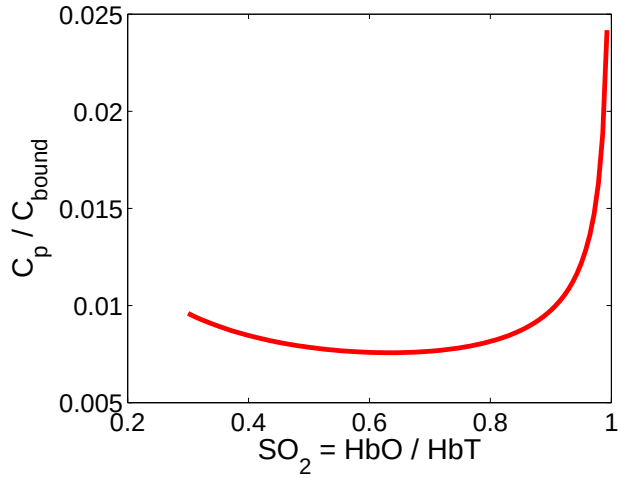

Figure 7.10: Ratio of the dissolved oxygen in plasma over the oxygen bound to hemoglobin (C_p/C_{bound}), plotted as a function of the hemoglobin oxygen saturation ($SO_2 = HbO/HbT$). C_p was calculated from the empirical hemoglobin dissociation curve relating oxygen concentration dissolved in the plasma to oxygen saturation, i.e., $C_p = C_{p,50}(1/SO_2 - 1)^{-1/h}$, with $C_{p,50} = 36.1$ μM and $h = 2.73$ [242]. The bound oxygen is $C_{\text{bound}} = 4SO_2[HbT]_{\text{blood}}$, with $[HbT]_{\text{blood}} \approx 2300$ μM.

bound oxygen is roughly four times that of oxy-hemoglobin (i.e., 4 oxygen molecules are bound to each oxygenated hemoglobin protein).

For constant hematocrit ($Hct_a = Hct_v = Hct$), the steady-state oxygen metabolism obtained from substituting Equations 7.30 and 7.31 into 7.29 is

$$CMRO_{2,c} = (4vHct)CBF_c\,(SaO_2 - SvO_2)\,. \tag{7.32}$$

Optical techniques sensitive to CBF_c include DCS and laser speckle contrast imaging. We know from Chapter 2 that DOS is sensitive to tissue oxygen saturation (StO_2, see Equation 2.139). Thus, to determine $CMRO_{2,c}$ from Equation 7.32, the goal is to estimate the oxygen extraction $SaO_2 - SvO_2$ (or changes in oxygen extraction) from StO_2 measurements. This is a difficult task, though, because the DOS measurement samples a mixture of arteriole, capillary and venule blood oxygen saturation and does not separate venous from arterial saturations.

To proceed, StO_2 is assumed to be a weighted average of arteriole and venule oxygen saturations [62]:

$$StO_2 = (1-\gamma)SaO_2 + \gamma SvO_2, \tag{7.33}$$

where γ is a weighting factor. Substituting Equation 7.33 into Equation 7.32, we obtain

$$CMRO_{2,c} = (4vHct)CBF_c \left(\frac{SaO_2 - StO_2}{\gamma} \right). \tag{7.34}$$

Fractional oxygen metabolism changes relative to a baseline state are in turn given by

$$\frac{CMRO_{2,c}}{CMRO_{2,c}^0} = \left(\frac{CBF_c}{CBF_c^0} \right) \left(\frac{SaO_2 - StO_2}{SaO_2^0 - StO_2^0} \right) \left(\frac{\gamma_0}{\gamma} \right), \tag{7.35}$$

where the superscript "0" denotes baseline. The fractional blood flow change can be directly measured with DCS, and DOS can measure the tissue oxygen saturations. The arteriole oxygen saturations are often assumed to be unity, or else estimated from other techniques such as a pulse ox. Although one could estimate γ from knowledge of the venous blood volume fraction, this estimate is complicated by the non-trivial distribution of detected photon paths in tissue. For example, photons traversing larger vessels have a strong tendency to be absorbed, and therefore even large veins with a high blood volume fraction may contribute little to the DOS signal. However, if the arteriole, capillary, and venule blood volume fractions remain constant between a baseline and perturbed tissue state, then it is reasonable to assume that $\gamma_0/\gamma = 1$.

Alternatively, it is feasible to monitor SvO_2 directly with DOS by looking at hemoglobin changes in sync with the respiration rate [177]. This is a promising approach that can be used to estimate γ. It works best if the respiration rate is regular.

Chapter 8

Conclusions/Future Work

Diffuse correlation spectroscopy (DCS) and diffuse optical spectroscopy (DOS) are noninvasive optical techniques capable of cerebral blood flow (CBF), cerebral blood volume (CBV), and cerebral blood oxygenation (StO_2) monitoring. Further, a tissue compartment model (Section 7.6) can be utilized to estimate cerebral oxygen metabolism ($CMRO_2$) from the optical data. In many applications, such as assessing stroke treatment efficacy and detecting secondary stroke in brain-injured patients, this information provides clinical value.

DOS signals are commonly analyzed either with a photon diffusion approach (Chapter 2) or a Modified Beer-Lambert approach (Chapter 3). Analogously to the DOS photon diffusion approach, DCS signals are analyzed with a correlation diffusion approach (Chapter 4) to extract blood flow. I extended the Modified Beer-Lambert approach for DOS to the DCS measurement, and validated it with both simulated and *in vivo* data (Chapter 5).

The novel DCS Modified Beer-Lambert approach has some useful advantages compared to the correlation diffusion approach. It facilitates real-time flow monitoring in complex tissue geometries, provides a novel route for increasing DCS measurement speed, and can be used to probe tissues wherein light transport is non-diffusive. It also can be used to filter signals from superficial tissues. The latter advantage is especially important, because a well-known drawback of optical cerebral monitoring is its significant sensitivity to superficial tissues above the brain (e.g., scalp and skull). This sensitivity makes the optical techniques prone to extra-cerebral artifacts.

Combining the DCS Modified Beer-Lambert framework with probe pressure modulation is a novel technique that I successfully used to remove extra-cerebral artifacts in *in vivo* cerebral blood flow monitoring during graded scalp ischemia and finger tapping (Chapter 6). This pressure modulation algorithm does not require *a priori* anatomical information, and it can be implemented for real time monitoring. The technique can further be extended to the DOS measurement utilizing the DOS Modified Beer-Lambert framework (Chapter 6).

In another major part of my thesis, I used optical techniques to obtain surface images of CBF and $CMRO_2$ functional responses to forepaw stimulation in rats at many different levels of cerebral ischemia (i.e., conditions of lower than normal CBF) (Chapter 7). Electrical functional responses to the forepaw stimulation were also measured in order to assess neurovascular coupling (Chapter 7) during graded cerebral ischemia. All of the electrical and hemodynamic responses are attenuated as the global ischemia becomes more severe, but the blood flow, oxy-hemoglobin, and deoxy-hemoglobin responses are more strongly attenuated at milder levels of global ischemia than the electrical or metabolic responses. The observed uncoupling between flow and metabolism at ischemic levels is evidence supporting the notion that during healthy conditions, functional stimulation increases oxygen delivery to brain tissue more than oxygen consumption. During functional stimulation in global ischemia, though, a higher fraction of the oxygen delivered from the vasculature is consumed. Another finding is that CBF and CBV were affected differently by ischemia, which demonstrates the importance of using DCS or a related technique to measure CBF directly rather than relying on CBV as a surrogate for CBF.

Future work will include testing the pressure algorithm approach further in clinical settings. Specifically, the non-invasive approach with DCS for monitoring CBF will be compared in traumatic brain-injured patients against the current clinical standard of CBF monitoring with an invasive thermodilution technique. It is further worth exploring the extension of the pressure algorithm to more complex geometries than the two-layer approach, such as geometries that contain non-diffusing domains from cerebral spinal fluid. The interactions of detected light with the vasculature is also not well understood. Monte Carlo simulations with a realistic vasculature would provide useful insights on estimating the γ coefficient in the $CMRO_2$ compartment model calculation (Section 7.6) as well as on relating the DCS blood flow index to absolute blood flow.

Bibliography

[1] Optical fiber tutorial. http://www.fiberoptics4sale.com/Merchant2/optical-fiber.php.

[2] Changes of cerebral blood flow, oxygenation, and oxidative metabolism during graded motor activation. *NeuroImage* **15**(1), 74 – 82 (2002).

[3] B. Ackerson, R. Dougherty, N. Reguigui, and U. Nobbmann. Correlation transfer-application of radiative transfer solution methods to photon correlation problems. *Journal of thermophysics and heat transfer* **6**(4), 577–588 (1992).

[4] B. M. Ances, D. G. Buerk, J. H. Greenberg, and J. A. Detre. Temporal dynamics of the partial pressure of brain tissue oxygen during functional forepaw stimulation in rats. *Neuroscience letters* **306**(1), 106–110 (2001).

[5] L. ANSftSUo. American national standard for the safe use of lasers. *American National Standards Institute. ANSIZ136. New York, NY: American National Standards Institute* (2007).

[6] G. Arfken. *Mathematical Methods for Physicists*. Academic second edition (1970).

[7] R. Aronson. Boundary conditions for diffusion of light. *J. Opt. Soc. Am. A* **12**, 2532–2539 (1995).

[8] S. R. Arridge and W. R. B. Lionheart. Nonuniqueness in diffusion-based optical tomography. *Opt. Lett.* **23**, 882–884 (1998).

[9] S. R. Arridge and J. C. Schotland. Optical tomography: forward and inverse problems. *Inverse Problems* **25**(12), 123010 (2009).

[10] S. R. Arridge, M. Cope, and D. Delpy. The theoretical basis for the determination of optical pathlengths in tissue: temporal and frequency analysis. *Physics in medicine and biology* **37**(7), 1531 (1992).

[11] J. Astrup, B. K. Siesjo, L. Symon, et al. Thresholds in cerebral ischemia-the ischemic penumbra. *Stroke* **12**(6), 723–725 (1981).

[12] W. B. Baker, A. A. Parthasarathy, D. R. Busch, R. C. Mesquita, J. H. Greenberg, and A. G. Yodh. Modified beer-lambert law for blood flow. *Biomedical optics express* , in press (2014).

[13] W. B. Baker, Z. Sun, T. Hiraki, M. E. Putt, T. Durduran, M. Reivich, A. G. Yodh, and J. H. Greenberg. Neurovascular coupling varies with level of global cerebral ischemia in a rat model. *Journal of Cerebral Blood Flow & Metabolism* **33**(1), 97–105 (2013).

[14] R. Bandyopadhyay, A. Gittings, S. Suh, P. Dixon, and D. Durian. Speckle-visibility spectroscopy: A tool to study time-varying dynamics. *Review of Scientific Instruments* **76**(9), 093110 (2005).

[15] G. Barton. *Elements of Green's Functions and Propagation: Potentials, Diffusion, and Waves*. Oxford University Press, USA 7 (1989).

[16] D. A. Benaron, S. R. Hintz, A. , D. Boas, A. Kleinschmidt, J. Frahm, C. Hirth, H. Obrig, J. C. van Houten, E. L. Kermit, W. F. Cheong, and D. K. Stevenson. Noninvasive functional imaging of human brain using light. *J. Cereb. Blood Flow Metab.* **20**(3), 469–477 (2000).

[17] H. C. Berg. *Random Walks in Biology*. Princeton University Press Princeton, N.J. expanded edition edition (1983).

[18] B. J. Berne and R. Pecora. *Dynamic Light Scattering with Applications to Chemistry, Biology, and Physics*. Dover Publications, Inc. Mineola, N.Y. (2000).

[19] D. Bicout and R. Maynard. Diffusing wave spectroscopy in inhomogeneous flows. *Physica A: Statistical Mechanics and its Applications* **199**(3), 387–411 (1993).

[20] F. Block and K.-H. Sontag. Differential effects of transient occlusion of common carotid arteries in normotensive rats on the somatosensory and visual system. *Brain research bulletin* **33**(5), 589–593 (1994).

[21] D. A. Boas. *Diffuse photon probes of structural and dynamical properties of turbid media: theory and biomedical applications*. PhD thesis University of Pennsylvania (1996).

[22] D. A. Boas, M. A. O'Leary, B. Chance, and A. G. Yodh. Scattering of diffuse photon density waves by spherical inhomogeneities within turbid media - analytic solution and applications. *Proceedings of the National Academy of Sciences of the United States of America* **91**(11), 4887–4891 (1994).

[23] D. Boas, L. Campbell, and A. Yodh. Scattering and imaging with diffusing temporal field correlations. *Physical review letters* **75**(9), 1855 (1995).

[24] D. Boas and A. Yodh. Spatially varying dynamical properties of turbid media probed with diffusing temporal light correlation. *JOSA A* **14**(1), 192–215 (1997).

[25] D. Boas, J. Culver, J. Stott, and A. Dunn. Three dimensional monte carlo code for photon migration through complex heterogeneous media including the adult human head. *Optics express* **10**(3), 159–170 (2002).

[26] D. A. Boas, A. M. Dale, and M. A. Franceschini. Diffuse optical imaging of brain activation: approaches to optimizing image sensitivity, resolution, and accuracy. *Neuroimage* **23**, S275–S288 (2004).

[27] D. A. Boas and A. K. Dunn. Laser speckle contrast imaging in biomedical optics. *Journal of biomedical optics* **15**(1), 011109–011109 (2010).

[28] D. A. Boas and M. A. Franceschini. Haemoglobin oxygen saturation as a biomarker: the problem and a solution. *Philosophical Transactions of the Royal Society A: Mathematical, Physical and Engineering Sciences* **369**(1955), 4407–4424 (2011).

[29] F. P. Bolin, L. E. Preuss, R. C. Taylor, and R. J. Ference. Refractive index of some mammalian tissues using a fiber optic cladding method. *Applied Optics* **28**(12), 2297–2303 (1989).

[30] R. Bonner and R. Nossal. Model for laser doppler measurements of blood flow in tissue. *Applied optics* **20**(12), 2097–2107 (1981).

[31] M. Born and E. Wolf. *Principles of Optics: Electromagnetic Theory of Propagation, Interference and Diffraction of Light*. Cambridge University Press 7th edition (1999).

[32] W. F. Boron and E. L. Boulpaep. *Medical Physiology, 2e Updated Edition: with STUDENT CONSULT Online Access*. Elsevier Health Sciences (2012).

[33] N. Branston, L. Symon, H. Crockard, and E. Pasztor. Relationship between the cortical evoked potential and local cortical blood flow following acute middle cerebral artery occlusion in the baboon. *Experimental neurology* **45**(2), 195–208 (1974).

[34] B. Brendel and T. Nielsen. Selection of optimal wavelengths for spectral reconstruction in diffuse optical tomography. *J. Biomed. Opt.* **14**(3), 034041 (2009).

[35] G. Bryan. An application of the method of images to the conduction of heat. *Proc London Math Soc* **22**, 424–430 (1891).

[36] E. M. Buckley. *Cerebral Hemodynamics in High-risk Neonates Probed by Diffuse Optical Spectroscopies (Chapter 4.2)*. PhD thesis University of Pennsylvania (2011).

[37] E. M. Buckley, A. B. Parthasarathy, P. E. Grant, A. G. Yodh, and M. A. Franceschini. Diffuse correlation spectroscopy for measurement of cerebral blood flow: future prospects. *Neurophotonics* **1**(1), 011009–011009 (2014).

[38] M. G. Burnett, T. Shimazu, T. Szabados, H. Muramatsu, J. A. Detre, and J. H. Greenberg. Electrical forepaw stimulation during reversible forebrain ischemia decreases infarct volume. *Stroke* **37**(5), 1327–1331 (2006).

[39] D. R. Busch. *Computer-aided, multi-modal, and compression diffuse optical studies of breat tissue*. PhD thesis University of Pennsylvania (2011).

[40] D. R. Busch, R. Choe, T. Durduran, D. H. Friedman, W. B. Baker, A. D. Maidment, M. A. Rosen, M. D. Schnall, and A. G. Yodh. Blood flow reduction in breast tissue due to mammographic compression. *Academic radiology* **21**(2), 151–161 (2014).

[41] R. B. Buxton and L. R. Frank. A model for the coupling between cerebral blood flow and oxygen metabolism during neural stimulation. *Journal of Cerebral Blood Flow & Metabolism* **17**(1), 64–72 (1997).

[42] R. B. Buxton, K. Uludağ, D. J. Dubowitz, and T. T. Liu. Modeling the hemodynamic response to brain activation. *Neuroimage* **23**, S220–S233 (2004).

[43] R. B. Buxton, E. C. Wong, and L. R. Frank. Dynamics of blood flow and oxygenation changes during brain activation: the balloon model. *Magnetic resonance in medicine* **39**(6), 855–864 (1998).

[44] S. A. Carp, N. Roche-Labarbe, M.-A. Franceschini, V. J. Srinivasan, S. Sakadžić, and D. A. Boas. Due to intravascular multiple sequential scattering, diffuse correlation spectroscopy of tissue primarily measures relative red blood cell motion within vessels. *Biomedical optics express* **2**(7), 2047–2054 (2011).

[45] H. S. Carslaw and J. Jaeger. *Conduction of heat in solids*. Oxford University Press New York (1986).

[46] K. M. Case and P. F. Zweifel. *Linear Transport Theory*. Addison-Wesley Boston (1967).

[47] B. Chance, M. Cope, E. Gratton, N. Ramanujam, and B. Tromberg. Phase measurement of light absorption and scattering in human tissues. *Rev. Sci. Instru.* **689**, 3457–3481 (1998).

[48] B. Chance, M. T. Dait, C. Zhang, T. Hamaoka, and F. Hagerman. Recovery from exercise-induced desaturation in the quadriceps muscles of elite competitive rowers. *Cell Physiology* **262**, C766–C775 (1992).

[49] S. Chandrasekhar. Stochastic problems in physics and astronomy. *Reviews of Modern Physics* **15**(1), 1–89 (1943).

[50] S. Chandrasekhar. Brownian motion, dynamical friction and stellar dynamics. *Dialectica* **3**(1-2), 114–126 (1949).

[51] S. Chandrasekhar. *Radiative Transfer*. Dover (1960).

[52] R. Choe, S. D. Konecky, A. Corlu, K. Lee, T. Durduran, D. R. Busch, S. Pathak, B. J. Czerniecki, J. Tchou, D. L. Fraker, A. DeMichele, B. Chance, S. R. Arridge, M. Schweiger, J. P. Culver, M. D. Schnall, M. E. Putt, M. A. Rosen, and A. G. Yodh. Differentiation of benign and malignant breast tumors by in-vivo three-dimensional parallel-plate diffuse optical tomography. *J. Biomed. Opt.* **14**(2), 024020 (2009).

[53] R. Choe, T. Durduran, G. Yu, M. J. Nijland, B. Chance, A. G. Yodh, and N. Ramanujam. Transabdominal near infrared oximetry of hypoxic stress in fetal sheep brain in utero. *Proceedings of the National Academy of Sciences* **100**(22), 12950–12954 (2003).

[54] R. Choe, M. E. Putt, P. M. Carlile, T. Durduran, J. M. Giammarco, D. R. Busch, K. W. Jung, B. J. Czerniecki, J. Tchou, M. D. Feldman, C. Mies, M. A. Rosen, M. D. Schnall, A. DeMichele, and A. G. Yodh. Optically measured microvascular blood flow contrast of malignant breast tumors. *PloS one* **9**(6), e99683 (2014).

[55] J. Choi, V. Toronov, U. Wolf, D. Hueber, L. P. Safonova, R. Gupta, C. Polzonetti, M. Wolf, A. Michalos, W. Mantulin, and E. Gratton. Noninvasive determination of the optical properties of adult brain: near-infrared spectroscopy approach. *Journal of biomedical optics* **9**(1), 221–229 (2004).

[56] N. Clavier, J. R. Kirsch, P. D. Hurn, and R. Traystman. Effect of postischemic hypoperfusion on vasodilatory mechanisms in cats. *American Journal of Physiology-Heart and Circulatory Physiology* **267**(5), H2012–H2018 (1994).

[57] M. Cope. *The development of a near infrared spectroscopy system and its application for non invasive monitoring of cerebral blood and tissue oxygenation in the newborn infants*. PhD thesis University of London (1991).

[58] A. Corlu, R. Choe, T. Durduran, K. Lee, M. Schweiger, E. M. C. Hillman, S. R. Arridge, and A. G. Yodh. Diffuse optical tomography with spectral constraints and wavelength optimization. *Appl Opt* **44**, 2082–93 (2005).

[59] A. Corlu, R. Choe, T. Durduran, M. A. Rosen, M. Schweiger, S. R. Arridge, M. D. Schnall, and A. G. Yodh. Three-dimensional in vivo fluorescence diffuse optical tomography of breast cancer in humans. *Optics Express* **15**(11), 6696–6716 (2007).

[60] A. Corlu, T. Durduran, R. Choe, M. Schweiger, E. M. C. Hillman, S. R. Arridge, and A. G. Yodh. Uniqueness and wavelength optimization in continous-wave multispectral diffuse optical tomography. *Opt. Lett* **28**, 2339–2341 (2003).

[61] J. P. Culver, R. Choe, M. J. Holboke, L. Zubkov, T. Durduran, A. Slemp, V. Ntziachristos, D. N. Pattanayak, B. Chance, and A. G. Yodh. Three-dimensional diffuse optical tomography in the plane parallel transmission geometry: Evaluation of a hybrid frequency domain/continuous wave clinical system for breast imaging. *Med. Phys.* **30**, 235–247 (2003).

[62] J. P. Culver, T. Durduran, D. Furuya, C. Cheung, J. H. Greenberg, and A. Yodh. Diffuse optical tomography of cerebral blood flow, oxygenation, and metabolism in rat during focal ischemia. *Journal of cerebral blood flow & metabolism* **23**(8), 911–924 (2003).

[63] A. Custo, W. M. Wells Iii, A. H. Barnett, E. Hillman, and D. A. Boas. Effective scattering coefficient of the cerebral spinal fluid in adult head models for diffuse optical imaging. *Applied optics* **45**(19), 4747–4755 (2006).

[64] S. N. Davie and H. P. Grocott. Impact of extracranial contamination on regional cerebral oxygen saturation: a comparison of three cerebral oximetry technologies. *Anesthesiology* **116**(4), 834–840 (2012).

[65] S. L. Dawson, R. B. Panerai, and J. F. Potter. Serial changes in static and dynamic cerebral autoregulation after acute ischaemic stroke. *Cerebrovascular diseases* **16**(1), 69–75 (2003).

[66] G. Del Zoppo. The neurovascular unit in the setting of stroke. *Journal of internal medicine* **267**(2), 156–171 (2010).

[67] D. . T. Delpy, M. Cope, P. Van der Zee, S. Arridge, S. Wray, and J. Wyatt. Estimation of optical pathlength through tissue from direct time of flight measurement. *Physics in medicine and biology* **33**(12), 1433 (1988).

[68] S. G. Diamond, T. J. Huppert, V. Kolehmainen, M. A. Franceschini, J. P. Kaipio, S. R. Arridge, and D. A. Boas. Dynamic physiological modeling for functional diffuse optical tomography. *Neuroimage* **30**(1), 88–101 (2006).

[69] G. Dietsche, M. Ninck, C. Ortolf, J. Li, F. Jaillon, and T. Gisler. Fiber-based multispeckle detection for time-resolved diffusing-wave spectroscopy: characterization and application to blood flow detection in deep tissue. *Applied optics* **46**(35), 8506–8514 (2007).

[70] M. Diop, K. Verdecchia, T.-Y. Lee, and K. St Lawrence. Calibration of diffuse correlation spectroscopy with a time-resolved near-infrared technique to yield absolute cerebral blood flow measurements. *Biomedical optics express* **2**(7), 2068–2081 (2011).

[71] U. Dirnagl, P. Thoren, A. Villringer, G. Sixt, A. Them, and K. Einhäupl. Global forebrain ischaemia in the rat: controlled reduction of cerebral blood flow by hypobaric hypotension and two-vessel occlusion. *Neurological research* **15**(2), 128–130 (1993).

[72] J. Dong, R. Bi, J. H. Ho, P. S. Thong, K.-C. Soo, and K. Lee. Diffuse correlation spectroscopy with a fast fourier transform-based software autocorrelator. *Journal of biomedical optics* **17**(9), 0970041–0970049 (2012).

[73] R. Dougherty, B. Ackerson, N. Reguigui, F. Dorri-Nowkoorani, and U. Nobbmann. Correlation transfer: development and application. *Journal of Quantitative Spectroscopy and Radiative Transfer* **52**(6), 713–727 (1994).

[74] R. Drezek, M. Guillaud, T. Collier, I. Boiko, A. Malpica, C. Macaulay, M. Follen, and R. Richards-Kortum. Light scattering from cervical cells throughout neoplastic progression: influence of nuclear morphology, dna content, and chromatin texture. *J. Biomed. Opt.* **8**(1), 7–16 (2003).

[75] A. Duncan, J. H. Meek, M. Clemence, C. E. Elwell, L. Tyszczuk, M. Cope, and D. T. Delpy. Optical pathlength measurements on adult head, calf and forearm and the head

of the newborn infant using phase resolved optical spectroscopy. *Phys. Med. Biol.* **40**(2), 295–304. (1995).

[76] A. K. Dunn, H. Bolay, M. A. Moskowitz, and D. A. Boas. Dynamic imaging of cerebral blood flow using laser speckle. *Journal of Cerebral Blood Flow & Metabolism* **21**(3), 195–201 (2001).

[77] A. K. Dunn, A. Devor, H. Bolay, M. L. Andermann, M. A. Moskowitz, A. M. Dale, and D. A. Boas. Simultaneous imaging of total cerebral hemoglobin concentration, oxygenation, and blood flow during functional activation. *Optics letters* **28**(1), 28–30 (2003).

[78] A. K. Dunn, A. Devor, A. M. Dale, and D. A. Boas. Spatial extent of oxygen metabolism and hemodynamic changes during functional activation of the rat somatosensory cortex. *Neuroimage* **27**(2), 279–290 (2005).

[79] T. Durduran, R. Choe, W. B. Baker, and A. G. Yodh. Diffuse optics for tissue monitoring and tomography. *Reports on Progress in Physics* **73**(7), 076701 June (2010).

[80] T. Durduran, R. Choe, J. P. Culver, L. Zubkov, M. J. Holboke, J. Giammarco, B. Chance, and A. G. Yodh. Bulk optical properties of healthy female breast tissue. *Phys. Med. Biol.* **47**, 2847–2861 (2002).

[81] T. Durduran. *Non-invasive measurements of tissue hemodynamics with hybrid diffuse optical methods*. PhD thesis University of Pennsylvania (2004).

[82] T. Durduran, M. G. Burnett, G. Yu, C. Zhou, D. Furuya, A. G. Yodh, J. A. Detre, and J. H. Greenberg. Spatiotemporal quantification of cerebral blood flow during functional activation in rat somatosensory cortex using laser-speckle flowmetry. *Journal of Cerebral Blood Flow & Metabolism* **24**(5), 518–525 (2004).

[83] T. Durduran, R. Choe, G. Yu, C. Zhou, J. C. Tchou, B. J. Czerniecki, and A. G. Yodh. Diffuse optical measurement of blood flow in breast tumors. *Optics letters* **30**(21), 2915–2917 (2005).

[84] T. Durduran and A. G. Yodh. Diffuse correlation spectroscopy for non-invasive, microvascular cerebral blood flow measurement. *NeuroImage* **85**, 51–63 (2014).

[85] T. Durduran, G. Yu, M. G. Burnett, J. A. Detre, J. H. Greenberg, J. Wang, C. Zhou, and A. G. Yodh. Diffuse optical measurement of blood flow, blood oxygenation, and metabolism in a human brain during sensorimotor cortex activation. *Optics letters* **29**(15), 1766–1768 (2004).

[86] T. Durduran, C. Zhou, B. L. Edlow, G. Yu, R. Choe, M. N. Kim, B. L. Cucchiara, M. E. Putt, Q. Shah, S. E. Kasner, J. H. Greenberg, A. G. Yodh, and J. A. Detre. Transcranial optical monitoring of cerebrovascular hemodynamics in acute stroke patients. *Optics express* **17**(5), 3884–3902 (2009).

[87] M. E. Eames, J. Wange, B. W. Pogue, and H. Dehghani. Wavelength band optimization in spectral near-infrared optical tomography improves accuracy while reducing data acquisition and computational burden. *J. Biomed. Opt.* **13**(5), 054037 (2008).

[88] W. G. Egan and T. W. Hilgeman. *Optical Properties of Inhomogeneous Materials: Applications to Geology, Astronomy, Chemistry, and Engineering*. Academic Press New York (1979).

[89] A. T. Eggebrecht, S. L. Ferradal, A. Robichaux-Viehoever, M. S. Hassanpour, H. Dehghani, A. Z. Snyder, T. Hershey, and J. P. Culver. Mapping distributed brain function and networks with diffuse optical tomography. *Nature Photonics* (2014).

[90] S. B. Erdoğan, M. A. Yücel, and A. Akın. Analysis of task-evoked systemic interference in fnirs measurements: Insights from fmri. *NeuroImage* **87**, 490–504 (2014).

[91] F. Fabbri, A. Sassaroli, M. E. Henry, and S. Fantini. Optical measurements of absorption changes in two-layered diffusive media. *Physics in medicine and biology* **49**(7), 1183 (2004).

[92] Q. Fang and D. A. Boas. Monte carlo simulation of photon migration in 3d turbid media accelerated by graphics processing units. *Opt. Express* **17**(22), 20178–20190 Oct (2009).

[93] S. Fantini, M. A. Franceschini, J. B. Fishkin, B. Barbieri, and E. Gratton. Quantitative determination of the absorption spectra of chromophores in strongly scattering media: a light-emitting diode based technique. *Appl. Opt.* **33**(22), 5204–5213 (1994).

[94] S. Fantini, D. Hueber, M. A. Franceschini, E. Gratton, W. Rosenfeld, P. G. Stubblefield, D. Maulik, and M. R. Stankovic. Non-invasive optical monitoring of the newborn piglet brain using continuous-wave and frequency-domain spectroscopy. *Physics in medicine and biology* **44**(6), 1543 (1999).

[95] T. J. Farrell, M. S. Patterson, and M. Essenpreis. Influence of layered tissue architecture on estimates of tissue optical properties obtained from spatially resolved diffuse reflectometry. *Applied optics* **37**(10), 1958–1972 (1998).

[96] T. J. Farrell, M. S. Patterson, and B. Wilson. A diffusion theory model of spatially resolved, steady-state diffuse reflectance for the noninvasive determination of tissue optical properties invivo. *Medical physics* **19**(4), 879–888 (1992).

[97] C. G. Favilla, R. C. Mesquita, M. Mullen, T. Durduran, X. Lu, M. N. Kim, D. L. Minkoff, S. E. Kasner, J. H. Greenberg, A. G. Yodh, and J. A. Detre. Optical bedside monitoring of cerebral blood flow in acute ischemic stroke patients during head-of-bed manipulation. *Stroke* **45**(5), 1269–1274 (2014).

[98] M. Ferrari, M. Muthalib, and V. Quaresima. The use of near-infrared spectroscopy in understanding skeletal muscle physiology: recent developments. *Philosophical Transactions of the Royal Society A: Mathematical, Physical and Engineering Sciences* **369**(1955), 4577–4590 (2011).

[99] M. Ferrari and V. Quaresima. A brief review on the history of human functional near-infrared spectroscopy (fnirs) development and fields of application. *Neuroimage* **63**(2), 921–935 (2012).

[100] R. P. Feynman, R. B. Leighton, and M. Sands. *The Feynman Lectures on Physics* volume I. Addison-Wesley Publishing Company (1963).

[101] J. B. Fishkin and E. Gratton. Propagation of photon-density waves in strongly scattering media containing an absorbing semi-infinite plane bounded by a straight edge. *JOSA A* **10**(1), 127–140 (1993).

[102] P. T. Fox and M. E. Raichle. Focal physiological uncoupling of cerebral blood flow and oxidative metabolism during somatosensory stimulation in human subjects. *Proceedings of the National Academy of Sciences* **83**(4), 1140–1144 (1986).

[103] P. T. Fox, M. E. Raichle, M. A. Mintun, and C. Dence. Nonoxidative glucose consumption during focal physiologic neural activity. *Science* **241**(4864), 462–464 (1988).

[104] K. J. Friston, A. Mechelli, R. Turner, and C. J. Price. Nonlinear responses in fmri: the balloon model, volterra kernels, and other hemodynamics. *NeuroImage* **12**(4), 466–477 (2000).

[105] L. Gagnon, R. J. Cooper, M. A. Yücel, K. L. Perdue, D. N. Greve, and D. A. Boas. Short separation channel location impacts the performance of short channel regression in nirs. *Neuroimage* **59**(3), 2518–2528 (2012).

[106] L. Gagnon, M. Desjardins, J. Jehanne-Lacasse, L. Bherer, and F. Lesage. Investigation of diffuse correlation spectroscopy in multi-layered media including the human head. *Optics express* **16**(20), 15514–15530 (2008).

[107] L. Gagnon, K. Perdue, D. N. Greve, D. Goldenholz, G. Kaskhedikar, and D. A. Boas. Improved recovery of the hemodynamic response in diffuse optical imaging using short optode separations and state-space modeling. *Neuroimage* **56**(3), 1362–1371 (2011).

[108] L. Gagnon, J. Selb, D. A. Boas, C. Gauthier, R. D. Hoge, and F. Lesage. Double-layer estimation of intra-and extracerebral hemoglobin concentration with a time-resolved system. *Journal of biomedical optics* **13**(5), 054019–054019 (2008).

[109] L. Gagnon, M. A. Yücel, D. A. Boas, and R. J. Cooper. Further improvement in reducing superficial contamination in nirs using double short separation measurements. *Neuroimage* **85**, 127–135 (2014).

[110] A. Go, D. Mozaffarian, V. Roger, E. Benjamin, J. Berry, W. Borden, D. Bravata, S. Dai, E. Ford, C. Fox, et al. On behalf of the american heart association statistics committee and stroke statistics subcommittee. *Heart disease and stroke statistics2013 update: a report from the American Heart Association. Circulation* **127**(1), e1–e240 (2013).

[111] L. B. Goldstein. Should antihypertensive therapies be given to patients with acute ischaemic stroke? *Drug safety* **22**(1), 13–18 (2000).

[112] J. W. Goodman. *Speckle phenomena in optics: theory and applications* volume 1. (2007).

[113] E. Gratton, W. Mantulin, M. J. Ven, M. van de Ven, J. Fishkin, M. Maris, and B. Chance. *The possibility of a near-infrared imaging system using frequency-domain methods* pages 183–189. Hamamatsu, Japan (1990).

[114] N. M. Gregg, B. R. White, B. W. Zeff, A. J. Berger, and J. P. Culver. Brain specificity of diffuse optical imaging: improvements from superficial signal regression and tomography. *Frontiers in neuroenergetics* **2** (2010).

[115] G. Greisen, T. Leung, and M. Wolf. Has the time come to use near-infrared spectroscopy as a routine clinical tool in preterm infants undergoing intensive care? *Philosophical Transactions of the Royal Society A: Mathematical, Physical and Engineering Sciences* **369**(1955), 4440–4451 (2011).

[116] D. J. Griffiths. *Introduction to Electrodynamics*. Prentice Hall 3rd edition (1999).

[117] A. Grinvald, E. Lieke, R. D. Frostig, C. D. Gilbert, and T. N. Wiesel. Functional architecture of cortex revealed by optical imaging of intrinsic signals. (1986).

[118] R. A. J. Groenhuis, H. A. Ferwerda, and T. J. J. Bosch. Scattering and absorption of turbid materials determined from reflection measurements, I. theory. *Appl. Opt.* **22**, 2456–2462 (1983).

[119] R. L. GRUBB, M. E. Raichle, J. O. Eichling, and M. M. Ter-Pogossian. The effects of changes in paco2 cerebral blood volume, blood flow, and vascular mean transit time. *Stroke* **5**(5), 630–639 (1974).

[120] B. Hallacoglu, A. Sassaroli, and S. Fantini. Optical characterization of two-layered turbid media for non-invasive, absolute oximetry in cerebral and extracerebral tissue. *PloS one* **8**(5), e64095 (2013).

[121] B. Hallacoglu, A. Sassaroli, M. Wysocki, E. Guerrero-Berroa, M. S. Beeri, V. Haroutunian, M. Shaul, I. H. Rosenberg, A. M. Troen, and S. Fantini. Absolute measurement of cerebral optical coefficients, hemoglobin concentration and oxygen saturation in old and young adults with near-infrared spectroscopy. *Journal of biomedical optics* **17**(8), 0814061–0814068 (2012).

[122] T. Hamaoka, K. K. McCully, M. Niwayama, and B. Chance. The use of muscle near-infrared spectroscopy in sport, health and medical sciences: recent developments. *Philosophical Transactions of the Royal Society A: Mathematical, Physical and Engineering Sciences* **369**(1955), 4591–4604 (2011).

[123] R. C. Haskell, L. O. Svaasand, T.-T. Tsay, T.-C. Feng, M. S. McAdams, and B. J. Tromberg. Boundary conditions for the diffusion equation in radiative transfer. *JOSA A* **11**(10), 2727–2741 (1994).

[124] T. Hayashi, Y. Kashio, and E. Okada. Hybrid monte carlo-diffusion method for light propagation in tissue with a low-scattering region. *Appl. Opt.* **42**(16), 2888–2896 (2003).

[125] L. He, Y. Lin, Y. Shang, B. J. Shelton, and G. Yu. Using optical fibers with different modes to improve the signal-to-noise ratio of diffuse correlation spectroscopy flow-oximeter measurements. *Journal of biomedical optics* **18**(3), 037001–037001 (2013).

[126] J. Heino, S. Arridge, J. Sikora, and E. Somersalo. Anisotropic effects in highly scattering media. *Phys. Rev. E* **68**, 031908 (2003).

[127] W.-D. Heiss. The ischemic penumbra: how does tissue injury evolve? *Annals of the New York Academy of Sciences* **1268**(1), 26–34 (2012).

[128] N. Henninger, A. Heimann, and O. Kempski. Electrophysiology and neuronal integrity following systemic arterial hypotension in a rat model of unilateral carotid artery occlusion. *Brain research* **1163**, 119–129 (2007).

[129] A. H. Hielscher, H. L. Liu, B. Chance, F. K. Tittel, and S. L. Jacques. Time-resolved photon emission from layered turbid media. *Appl Opt* **35**(4), 719–728 (1996).

[130] M. Hiraoka, M. Firbank, M. Essenpreis, M. Cope, S. Arridge, P. Van Der Zee, and D. Delpy. A monte carlo investigation of optical pathlength in inhomogeneous tissue and its application to near-infrared spectroscopy. *Physics in medicine and biology* **38**(12), 1859 (1993).

[131] R. Hoge, M. Franceschini, R. Covolan, T. Huppert, J. Mandeville, and D. Boas. Simultaneous recording of task-induced changes in blood oxygenation, volume, and flow using diffuse optical imaging and arterial spin-labeling mri. *Neuroimage* **25**(3), 701–707 (2005).

[132] R. D. Hoge, J. Atkinson, B. Gill, G. R. Crelier, S. Marrett, and G. B. Pike. Investigation of bold signal dependence on cerebral blood flow and oxygen consumption: the deoxyhemoglobin dilution model. *Magnetic resonance in medicine* **42**(5), 849–863 (1999).

[133] D. Hueber, M. Franceschini, H. Ma, Q. Zhang, J. Ballesteros, S. Fantini, D. Wallace, V. Ntziachristos, and B. Chance. Non-invasive and quantitative near-infrared haemoglobin spectrometry in the piglet brain during hypoxic stress, using a frequency-domain multi-distance instrument. *Physics in medicine and biology* **46**(1), 41 (2001).

[134] E. L. Hull. *Quantitative broadband near-infrared spectroscopy of tissue-simulating phantoms containing erythrocytes*. PhD thesis University of Rochester (1999).

[135] E. L. Hull and T. H. Foster. Steady-state reflectance spectrsocopy in the P_3 approximation. *J. Opt. Soc. Am. A* **18**(3), 584–599 (2001).

[136] T. J. Huppert, M. S. Allen, H. Benav, P. B. Jones, and D. A. Boas. A multicompartment vascular model for inferring baseline and functional changes in cerebral oxygen metabolism and arterial dilation. *Journal of Cerebral Blood Flow & Metabolism* **27**(6), 1262–1279 (2007).

[137] T. J. Huppert, S. G. Diamond, M. A. Franceschini, and D. A. Boas. Homer: a review of time-series analysis methods for near-infrared spectroscopy of the brain. *Applied optics* **48**(10), D280–D298 (2009).

[138] F. Hyder, R. G. Shulman, and D. L. Rothman. A model for the regulation of cerebral oxygen delivery. *Journal of applied physiology* **85**(2), 554–564 (1998).

[139] C. Iadecola. Neurovascular regulation in the normal brain and in alzheimer's disease. *Nature Reviews Neuroscience* **5**(5), 347–360 (2004).

[140] S. Ijichi, T. Kusaka, K. Isobe, K. Kawada, T. Imai, S. Itoh, F. Islam, K. Okubo, H. Okada, and M. Namba. Quantification of cerebral hemoglobin as a function of oxygenation using near-infrared time-resolved spectroscopy in a piglet model of hypoxia. *Journal of biomedical optics* **10**(2), 024026–0240269 (2005).

[141] D. Irwin, L. Dong, Y. Shang, R. Cheng, M. Kudrimoti, S. D. Stevens, and G. Yu. Influences of tissue absorption and scattering on diffuse correlation spectroscopy blood flow measurements. *Biomedical optics express* **2**(7), 1969–1985 (2011).

[142] A. Ishimaru. *Wave Propagation and Scattering in Random Media*. Academic Press, Inc. San Diego (1978).

[143] S. L. Jacques. Time-resolved reflectance spectroscopy in turbid tissues. *IEEE Transactions on Biomedical Engineering* **36**, 1155–1161 (1989).

[144] S. L. Jacques. Optical properties of biological tissues: a review. *Physics in medicine and biology* **58**(11), R37 (2013).

[145] S. L. Jacques. Coupling 3d monte carlo light transport in optically heterogeneous tissues to photoacoustic signal generation. *Photoacoustics* **2**(4), 137 – 142 (2014).

[146] S. L. Jacques and B. W. Pogue. Tutorial on diffuse light transport. *Journal of Biomedical Optics* **13**(4), 041302–041302 (2008).

[147] F. Jaillon, J. Li, G. Dietsche, T. Elbert, and T. Gisler. Activity of the human visual cortex measured non-invasively by diffusing-wave spectroscopy. *Optics Express* **15**(11), 6643–6650 (2007).

[148] F. Jaillon, S. E. Skipetrov, J. Li, G. Dietsche, G. Maret, and T. Gisler. Diffusing-wave spectroscopy from head-like tissue phantoms: influence of a non-scattering layer. *Optics express* **14**(22), 10181–10194 (2006).

[149] V. Jain, E. M. Buckley, D. J. Licht, J. M. Lynch, P. J. Schwab, M. Y. Naim, N. A. Lavin, S. C. Nicolson, L. M. Montenegro, A. G. Yodh, and F. W. Wehrli. Cerebral oxygen metabolism in neonates with congenital heart disease quantified by mri and optics. *Journal of Cerebral Blood Flow & Metabolism* (2013).

[150] H. Jasper. Report of the committee on methods of clinical examination in electroencephalography. *Electroenceph. Clin. Neurophysiol.* **10**, 370–375 (1958).

[151] M. Jones, J. Berwick, D. Johnston, and J. Mayhew. Concurrent optical imaging spectroscopy and laser-doppler flowmetry: the relationship between blood flow, oxygenation, and volume in rodent barrel cortex. *Neuroimage* **13**(6), 1002–1015 (2001).

[152] P. B. Jones, H. K. Shin, D. A. Boas, B. T. Hyman, M. A. Moskowitz, C. Ayata, and A. K. Dunn. Simultaneous multispectral reflectance imaging and laser speckle flowmetry of cerebral blood flow and oxygen metabolism in focal cerebral ischemia. *Journal of biomedical optics* **13**(4), 044007–044007 (2008).

[153] S. Jones, B. Bose, A. Furlan, H. Friel, K. Easley, M. Meredith, and J. Little. Co2 reactivity and heterogeneity of cerebral blood flow in ischemic, border zone, and normal cortex. *American Journal of Physiology-Heart and Circulatory Physiology* **257**(2), H473–H482 (1989).

[154] P. D. Kaplan, M. H. Kao, A. G. Yodh, and D. J. Pine. Geometric constraints for the design of diffusing-wave spectroscopy experiments. *Appl. Opt.* **32**(21), 3828–3836 (1993).

[155] T. A. Kent, V. M. Soukup, and R. H. Fabian. Heterogeneity affecting outcome from acute stroke therapy making reperfusion worse. *Stroke* **32**(10), 2318–2327 (2001).

[156] A. Kienle and T. Glanzmann. In vivo determination of the optical properties of muscle with time-resolved reflectance using a layered model. *Physics in medicine and biology* **44**(11), 2689 (1999).

[157] A. Kienle, M. S. Patterson, N. Dögnitz, R. Bays, G. Wagnieres, H. van Den Bergh, et al. Noninvasive determination of the optical properties of two-layered turbid media. *Applied optics* **37**(4), 779–791 (1998).

[158] M. N. Kim. *Applications of hybrid diffuse optics for clinical management of adults after brain injury (Chapter 3)*. PhD thesis University of Pennsylvania (2013).

[159] M. N. Kim, T. Durduran, S. Frangos, B. L. Edlow, E. M. Buckley, H. E. Moss, C. Zhou, G. Yu, R. Choe, E. Maloney-Wilensky, R. L. Wolf, M. S. Grady, J. H. Greenberg, J. M. Levine, A. G. Yodh, J. A. Detre, and W. A. Kofke. Noninvasive measurement of cerebral blood flow and blood oxygenation using near-infrared and diffuse correlation spectroscopies in critically brain-injured adults. *Neurocritical care* **12**(2), 173–180 (2010).

[160] M. N. Kim, B. L. Edlow, T. Durduran, S. Frangos, R. C. Mesquita, J. M. Levine, J. H. Greenberg, A. G. Yodh, and J. A. Detre. Continuous optical monitoring of cerebral hemodynamics during head-of-bed manipulation in brain-injured adults. *Neurocritical care* **20**(3), 443–453 (2014).

[161] E. Kirilina, A. Jelzow, A. Heine, M. Niessing, H. Wabnitz, R. Brühl, B. Ittermann, A. M. Jacobs, and I. Tachtsidis. The physiological origin of task-evoked systemic artefacts in functional near infrared spectroscopy. *Neuroimage* **61**(1), 70–81 (2012).

[162] A. D. Klose and A. H. Hielscher. Optical tomography with the equation of radiative transfer. *Methods for Heat and Fluid Flow* **18**, 443–464 (2008).

[163] M. Kohl, U. Lindauer, G. Royl, M. Kuhl, L. Gold, A. Villringer, and U. Dirnagl. Physical model for the spectroscopic analysis of cortical intrinsic optical signals. *Phys. Med. Biol.* **45**, 3749–3764 (2000).

[164] C. C. Lay, M. F. Davis, C. H. Chen-Bee, and R. D. Frostig. Mild sensory stimulation completely protects the adult rodent cortex from ischemic stroke. *PloS one* **5**(6), e11270 (2010).

[165] C. Lecrux and E. Hamel. The neurovascular unit in brain function and disease. *Acta Physiologica* **203**(1), 47–59 (2011).

[166] D. R. Leff, F. Orihuela-Espina, C. E. Elwell, T. Athanasiou, D. T. Delpy, A. W. Darzi, and G.-Z. Yang. Assessment of the cerebral cortex during motor task behaviours in adults: a systematic review of functional near infrared spectroscopy (fnirs) studies. *NeuroImage* **54**(4), 2922–2936 (2011).

[167] C. Leithner, G. Royl, N. Offenhauser, M. Füchtemeier, M. Kohl-Bareis, A. Villringer, U. Dirnagl, and U. Lindauer. Pharmacological uncoupling of activation induced increases in cbf and cmro2. *Journal of Cerebral Blood Flow & Metabolism* **30**(2), 311–322 (2010).

[168] P.-A. Lemieux and D. Durian. Investigating non-gaussian scattering processes by using nth-order intensity correlation functions. *JOSA A* **16**(7), 1651–1664 (1999).

[169] J. Li, M. Ninck, L. Koban, T. Elbert, J. Kissler, and T. Gisler. Transient functional blood flow change in the human brain measured noninvasively by diffusing-wave spectroscopy. *Optics letters* **33**(19), 2233–2235 (2008).

[170] X. Li. *Fluorescence and diffusive wave diffraction tomographic probes in turbid media*. PhD thesis University of Pennsylvania (1998).

[171] Y.-K. Liao and S.-H. Tseng. Reliable recovery of the optical properties of multi-layer turbid media by iteratively using a layered diffusion model at multiple source-detector separations. *Biomedical optics express* **5**(3), 975–989 (2014).

[172] A. Liebert, H. Wabnitz, J. Steinbrink, H. Obrig, M. Möller, R. Macdonald, A. Villringer, and H. Rinneberg. Time-resolved multidistance near-infrared spectroscopy of the adult head: intracerebral and extracerebral absorption changes from moments of distribution of times of flight of photons. *Applied Optics* **43**(15), 3037–3047 (2004).

[173] A. Liemert and A. Kienle. Light diffusion in n-layered turbid media: frequency and time domains. *Journal of biomedical optics* **15**(2), 025002–025002 (2010).

[174] Q. Liu and N. Ramanujam. Scaling method for fast monte carlo simulation of diffuse reflectance spectra from multilayered turbid media. *JOSA A* **24**(4), 1011–1025 (2007).

[175] S. Lloyd-Fox, A. Blasi, and C. Elwell. Illuminating the developing brain: the past, present and future of functional near infrared spectroscopy. *Neuroscience & Biobehavioral Reviews* **34**(3), 269–284 (2010).

[176] J. D. Logan. *Applied partial differential equations*. Springer Science & Business Media (2004).

[177] J. M. Lynch, E. M. Buckley, P. J. Schwab, D. R. Busch, B. D. Hanna, M. E. Putt, D. J. Licht, and A. G. Yodh. Noninvasive optical quantification of cerebral venous oxygen saturation in humans. *Academic radiology* **21**(2), 162–167 (2014).

[178] P. L. Madsen, R. Linde, S. G. Hasselbalch, O. B. Paulson, and N. A. Lassen. Activation-induced resetting of cerebral oxygen and glucose uptake in the rat. *Journal of Cerebral Blood Flow & Metabolism* **18**(7), 742–748 (1998).

[179] G. Maret and P. Wolf. Multiple light scattering from disordered media. the effect of brownian motion of scatterers. *Zeitschrift für Physik B Condensed Matter* **65**(4), 409–413 (1987).

[180] J. Mayhew, D. Johnston, J. Martindale, M. Jones, J. Berwick, and Y. Zheng. Increased oxygen consumption following activation of brain: theoretical footnotes using spectroscopic data from barrel cortex. *Neuroimage* **13**(6), 975–987 (2001).

[181] E. A. Mellon, R. S. Beesam, M. A. Elliott, and R. Reddy. Mapping of cerebral oxidative metabolism with mri. *Proceedings of the National Academy of Sciences* **107**(26), 11787–11792 (2010).

[182] R. Mesquita, T. Durduran, G. Yu, E. Buckley, M. Kim, C. Zhou, R. Choe, U. Sunar, and A. Yodh. Direct measurement of tissue blood flow and metabolism with diffuse optics. *Philos. T. Roy. Soc. A* **369**(1955), 4390–4406 (2011).

[183] R. C. Mesquita, M. Putt, M. Chandra, G. Yu, X. Xing, S. W. Han, G. Lech, Y. Shang, T. Durduran, C. Zhou, A. G. Yodh, and E. R. Mohler. Diffuse optical characterization of an exercising patient group with peripheral artery disease. *Journal of biomedical optics* **18**(5), 057007–057007 (2013).

[184] R. C. Mesquita, S. S. Schenkel, D. L. Minkoff, X. Lu, C. G. Favilla, P. M. Vora, D. R. Busch, M. Chandra, J. H. Greenberg, J. A. Detre, and A. G. Yodh. Influence of probe pressure on the diffuse correlation spectroscopy blood flow signal: extra-cerebral contributions. *Biomedical optics express* **4**(7), 978–994 (2013).

[185] R. C. Mesquita, N. Skuli, M. N. Kim, J. Liang, S. Schenkel, A. J. Majmundar, M. C. Simon, and A. G. Yodh. Hemodynamic and metabolic diffuse optical monitoring in a mouse model of hindlimb ischemia. *Biomedical optics express* **1**(4), 1173–1187 (2010).

[186] A. A. Middleton and D. S. Fisher. Discrete scatterers and autocorrelations of multiply scattered light. *Physical Review B* **43**(7), 5934 (1991).

[187] M. Mintun, M. Raichle, W. Martin, and P. Herscovitch. Brain oxygen utilization measured with o-15 radiotracers and positron emission tomography. *Journal of nuclear medicine: official publication, Society of Nuclear Medicine* **25**(2), 177–187 (1984).

[188] M. I. Mishchenko. The poyntingstokes tensor and radiative transfer in discrete random media: the microphysical paradigm. *Optics Express* **18**(19), 19770–19791 (2010).

[189] J. R. Mourant, J. P. Freyer, A. H. Hielscher, A. A. Eick, D. Shen, and T. M. Johnson. Mechanisms of light scattering from biological cells relevant to noninvasive optical-tissue diagnostics. *Applied Optics* **37**(16), 3586–3593 (1998).

[190] M. Ninck, M. Untenberger, and T. Gisler. Diffusing-wave spectroscopy with dynamic contrast variation: disentangling the effects of blood flow and extravascular tissue shearing on signals from deep tissue. *Biomedical optics express* **1**(5), 1502–1513 (2010).

[191] V. Ntziachristos and B. Chance. Accuracy limits in the determination of absolute optical properties using time-resolved nir spectroscopy. *Medical Physics* **28**(6), 1115–1124 (2001).

[192] H. Obrig and J. Steinbrink. Non-invasive optical imaging of stroke. *Philosophical Transactions of the Royal Society A: Mathematical, Physical and Engineering Sciences* **369**(1955), 4470–4494 (2011).

[193] H. Obrig and A. Villringer. Beyond the visibleimaging the human brain with light. *Journal of Cerebral Blood Flow & Metabolism* **23**(1), 1–18 (2003).

[194] E. Ohmae, Y. Ouchi, M. Oda, T. Suzuki, S. Nobesawa, T. Kanno, E. Yoshikawa, M. Futatsubashi, Y. Ueda, H. Okada, et al. Cerebral hemodynamics evaluation by near-infrared time-resolved spectroscopy: correlation with simultaneous positron emission tomography measurements. *Neuroimage* **29**(3), 697–705 (2006).

[195] S. Ohta, E. Meyer, C. J. Thompson, and A. Gjedde. Oxygen consumption of the living human brain measured after a single inhalation of positron emitting oxygen. *Journal of Cerebral Blood Flow & Metabolism* **12**(2), 179–192 (1992).

[196] E. Okada and D. T. Delpy. Near-infrared light propagation in an adult head model. i. modeling of low-level scattering in the cerebrospinal fluid layer. *Applied optics* **42**(16), 2906–2914 (2003).

[197] E. Okada and D. T. Delpy. Near-infrared light propagation in an adult head model. ii. effect of superficial tissue thickness on the sensitivity of the near-infrared spectroscopy signal. *Applied optics* **42**(16), 2915–2922 (2003).

[198] A. B. Parthasarathy, S. Kazmi, and A. K. Dunn. Quantitative imaging of ischemic stroke through thinned skull in mice with multi exposure speckle imaging. *Biomedical optics express* **1**(1), 246–259 (2010).

[199] S. Patel, T. Katura, A. Maki, and I. Tachtsidis. Quantification of systemic interference in optical topography data during frontal lobe and motor cortex activation: an independent component analysis. In *Oxygen Transport to Tissue XXXII* pages 45–51. Springer (2011).

[200] M. S. Patterson, S. Andersson-Engels, B. C. Wilson, and E. K. Osei. Absorption spectroscopy in tissue-simulating materials: a theoretical and experimental study of photon paths. *Applied Optics* **34**(1), 22–30 (1995).

[201] M. S. Patterson, B. Chance, and B. C. Wilson. Time resolved reflectance and transmittance for the non-invasive measurement of tissue optical properties. *Applied optics* **28**(12), 2331–2336 (1989).

[202] F. L. Pedrotti, L. S. Pedrotti, and L. M. Pedrotti. Introduction to optics third edition. *Introduction to Optics 2nd Edition by Frank L. Pedrotti, SJ, Leno S. Pedrotti New Jersey: Prentice Hall, 1993* **1** (1993).

[203] A. Pifferi, J. Swartling, E. Chikoidze, S. Andersson-Engels, R. Cubeddu, A. Torricelli, P. Taroni, and A. Bassi. Spectroscopic time-resolved diffuse reflectance and transmittance measurements of the female breast at different interfiber distances. *J. Biomed. Opt.* **9**(6), 1143–1151 (2004).

[204] D. Pine, D. Weitz, P. Chaikin, and E. Herbolzheimer. Diffusing wave spectroscopy. *Physical Review Letters* **60**(12), 1134 (1988).

[205] J. C. Pinheiro and D. M. Bates. *Mixed-effects models in S and S-PLUS*. Springer Science & Business Media (2000).

[206] G. L. Pollack and D. R. Stump. *Electromagnetism*. Addison-Wesley (2002).

[207] S. A. Prahl and S. L. Jacques. Optical properties spectra. http://omlc.ogi.edu/spectra/ (2012).

[208] O. Pucci, V. Toronov, and K. St Lawrence. Measurement of the optical properties of a two-layer model of the human head using broadband near-infrared spectroscopy. *Applied optics* **49**(32), 6324–6332 (2010).

[209] E. M. Purcell. Life at low reynolds number. *Am. J. Phys* **45**(1), 3–11 (1977).

[210] J. Ripoll. *Light diffusion in turbid media with biomedical applications*. PhD thesis Universidad Autonoma de Madrid (2000).

[211] J. Ripoll. Derivation of the scalar radiative transfer equation from energy conservation of maxwells equations in the far field. *J. Opt. Soc. Am. A* **28**(8), 1765–1775 (2011).

[212] J. Ripoll, V. Ntziachristos, J. P. Culver, D. N. Pattanayak, A. G. Yodh, and M. Nieto-Vesperinas. Recovery of optical parameters in multiple-layered diffusive media: theory and experiments. *JOSA A* **18**(4), 821–830 (2001).

[213] N. Roche-Labarbe, A. Fenoglio, H. Radhakrishnan, M. Kocienski-Filip, S. A. Carp, J. Dubb, D. A. Boas, P. E. Grant, and M. A. Franceschini. Somatosensory evoked changes in cerebral oxygen consumption measured non-invasively in premature neonates. *Neuroimage* **85**, 279–286 (2014).

[214] G. Royl, C. Leithner, H. Sellien, J. P. Müller, D. Megow, N. Offenhauser, J. Steinbrink, M. Kohl-Bareis, U. Dirnagl, and U. Lindauer. Functional imaging with laser speckle contrast analysis: vascular compartment analysis and correlation with laser doppler flowmetry and somatosensory evoked potentials. *Brain research* **1121**(1), 95–103 (2006).

[215] R. B. Saager and A. J. Berger. Direct characterization and removal of interfering absorption trends in two-layer turbid media. *JOSA A* **22**(9), 1874–1882 (2005).

[216] R. B. Saager, N. L. Telleri, and A. J. Berger. Two-detector corrected near infrared spectroscopy (c-nirs) detects hemodynamic activation responses more robustly than single-detector nirs. *Neuroimage* **55**(4), 1679–1685 (2011).

[217] A. Sassaroli, F. Martelli, and S. Fantini. Perturbation theory for the diffusion equation by use of the moments of the generalized temporal point-spread function. i. theory. *JOSA A* **23**(9), 2105–2118 (2006).

[218] K. Schatzel. *Dynamic light scattering: the method and some applications* volume 49 chapter Single photon correlation techniques. Oxford University Press, USA (1993).

[219] F. Scholkmann, S. Kleiser, A. J. Metz, R. Zimmermann, J. Mata Pavia, U. Wolf, and M. Wolf. A review on continuous wave functional near-infrared spectroscopy and imaging instrumentation and methodology. *Neuroimage* **85**, 6–27 (2014).

[220] F. Scholkmann and M. Wolf. General equation for the differential pathlength factor of the frontal human head depending on wavelength and age. *Journal of biomedical optics* **18**(10), 105004–105004 (2013).

[221] J. Selb, D. A. Boas, S.-T. Chan, K. C. Evans, E. M. Buckley, and S. A. Carp. Sensitivity of near-infrared spectroscopy and diffuse correlation spectroscopy to brain hemodynamics: simulations and experimental findings during hypercapnia. *Neurophotonics* **1**(1), 015005–015005 (2014).

[222] J. Selb, D. K. Joseph, and D. A. Boas. Time-gated optical system for depth-resolved functional brain imaging. *Journal of biomedical optics* **11**(4), 044008–044008 (2006).

[223] I. Seo, J. S. You, C. K. Hayakawa, and V. Venugopalan. Perturbation and differential monte carlo methods for measurement of optical properties in a layered epithelial tissue model. *Journal of biomedical optics* **12**(1), 014030–014030 (2007).

[224] Y. Shang, L. Chen, M. Toborek, and G. Yu. Diffuse optical monitoring of repeated cerebral ischemia in mice. *Optics express* **19**(21), 20301–20315 (2011).

[225] Y. Shang, K. Gurley, and G. Yu. Diffuse correlation spectroscopy (dcs) for assessment of tissue blood flow in skeletal muscle: Recent progress. *Anatomy & physiology: current research* **3**(2), 128 (2013).

[226] Y. Shang, T. Symons, T. Durduran, A. G. Yodh, and G. Yu. Effects of muscle fiber motion on diffuse correlation spectroscopy blood flow measurements during exercise. *Biomedical optics express* **1**(2), 500–511 (2010).

[227] N. Shimada, R. Graf, G. Rosner, and W.-D. Heiss. Differences in ischemia-induced accumulation of amino acids in the cat cortex. *Stroke* **21**(10), 1445–1451 (1990).

[228] A. M. Siegel, J. A. Marota, and D. A. Boas. Design and evaluation of a continuous-wave diffuse optical tomography system. *Optics Express* **4**, 287–298 (1999).

[229] B. K. Siesjö. Pathophysiology and treatment of focal cerebral ischemia: Part i: Pathophysiology. *Journal of neurosurgery* **77**(2), 169–184 (1992).

[230] J. Skarphedinsson, M. Delle, S. Carlsson, and S. Bealer. The effects of hexamethonium on cerebral blood flow and cerebral function during relative cerebral ischaemia in rats. *Acta physiologica scandinavica* **158**(1), 21–28 (1996).

[231] M. Smith. Shedding light on the adult brain: a review of the clinical applications of near-infrared spectroscopy. *Philosophical Transactions of the Royal Society A: Mathematical, Physical and Engineering Sciences* **369**(1955), 4452–4469 (2011).

[232] S. Srinivasan, B. W. Pogue, S. Jiang, H. Dehghani, and K. D. Paulsen. Spectrally constrained chromophore and scattering near-infrared tomography provides quantitative and robust reconstruction. *Appl. Opt.* **44**(10), 1858–1869 (2005).

[233] K. St. Lawrence, K. Verdecchia, J. Elliott, and M. Diop. Measuring cerebral hemodynamics and energy metabolism by near-infrared spectroscopy. In J. Hirrlinger and H. S. Waagepetersen, editors, *Brain Energy Metabolism* volume 90 of *Neuromethods* pages 265–292. Springer New York (2014).

[234] J. Steinbrink, H. Wabnitz, H. Obrig, A. Villringer, and H. Rinneberg. Determining changes in nir absorption using a layered model of the human head. *Physics in medicine and biology* **46**(3), 879 (2001).

[235] G. Strangman, M. A. Franceschini, and D. A. Boas. Factors affecting the accuracy of near-infrared spectroscopy concentration calculations for focal changes in oxygenation parameters. *Neuroimage* **18**(4), 865–879 (2003).

[236] U. Sunar, D. Rohrbach, N. Rigual, E. Tracy, K. Keymel, M. T. Cooper, H. Baumann, and B. H. Henderson. Monitoring photobleaching and hemodynamic responses to hpph-mediated photodynamic therapy of head and neck cancer: a case report. *Optics express* **18**(14), 14969–14978 (2010).

[237] I. Tachtsidis, T. S. Leung, A. Chopra, P. H. Koh, C. B. Reid, and C. E. Elwell. False positives in functional nearinfrared topography. In *Oxygen Transport to Tissue XXX* pages 307–314. Springer (2009).

[238] S. Tak and J. C. Ye. Statistical analysis of fnirs data: a comprehensive review. *Neuroimage* **85**, 72–91 (2014).

[239] T. Takahashi, Y. Takikawa, R. Kawagoe, S. Shibuya, T. Iwano, and S. Kitazawa. Influence of skin blood flow on near-infrared spectroscopy signals measured on the forehead during a verbal fluency task. *Neuroimage* **57**(3), 991–1002 (2011).

[240] J. R. Taylor. *Classical Mechanics*. University Science Books United States of America (2005).

[241] R. C. Team. R: A language and environment for statistical computing. r foundation for statistical computing, vienna, austria, 2012 (2012).

[242] R. Valabrègue, A. Aubert, J. Burger, J. Bittoun, and R. Costalat. Relation between cerebral blood flow and metabolism explained by a model of oxygen exchange. *Journal of Cerebral Blood Flow & Metabolism* **23**(5), 536–545 (2003).

[243] P. van der Zee, M. Cope, S. R. Arridge, M. Essenpreis, L. A. Potter, A. D. Edwards, J. S. Wyatt, D. C. McCormick, S. C. Toth, E. O. R. Reynolds, and D. T. Delpy. Experimentally measured optical pathlengths for the adult's head, calf and forearm and the head of the newborn infant asa function of interoptode spacing. *Adv. Exp. Med. Biol.* **316**, 143–153 (1992).

[244] I. Vanzetta and A. Grinvald. Coupling between neuronal activity and microcirculation: implications for functional brain imaging. *HFSP journal* **2**(2), 79–98 (2008).

[245] A. L. Vazquez, M. Fukuda, and S.-G. Kim. Evolution of the dynamic changes in functional cerebral oxidative metabolism from tissue mitochondria to blood oxygen. *Journal of Cerebral Blood Flow & Metabolism* **32**(4), 745–758 (2012).

[246] A. L. Vazquez, K. Masamoto, M. Fukuda, and S.-G. Kim. Cerebral oxygen delivery and consumption during evoked neural activity. *Frontiers in neuroenergetics* **2** (2010).

[247] A. L. Vazquez, K. Masamoto, and S.-G. Kim. Dynamics of oxygen delivery and consumption during evoked neural stimulation using a compartment model and cbf and tissue p o2 measurements. *Neuroimage* **42**(1), 49–59 (2008).

[248] A. Villringer and B. Chance. Non-invasive optical spectroscopy and imaging of human brain function. *Trends in neurosciences* **20**(10), 435–442 (1997).

[249] A. Villringer, A. Them, U. Lindauer, K. Einhäupl, and U. Dirnagl. Capillary perfusion of the rat brain cortex. an in vivo confocal microscopy study. *Circulation research* **75**(1), 55–62 (1994).

[250] I. Vogiatzis, Z. Louvaris, H. Habazettl, D. Athanasopoulos, V. Andrianopoulos, E. Cherouveim, H. Wagner, C. Roussos, P. D. Wagner, and S. Zakynthinos. Frontal cerebral cortex blood flow, oxygen delivery and oxygenation during normoxic and hypoxic exercise in athletes. *The Journal of physiology* **589**(16), 4027–4039 (2011).

[251] E. Vovenko. Distribution of oxygen tension on the surface of arterioles, capillaries and venules of brain cortex and in tissue in normoxia: an experimental study on rats. *Pflügers Archiv* **437**(4), 617–623 (1999).

[252] S. A. Walker, D. A. Boas, and E. Gratton. Photon density waves scattered from cylindrical inhomogeneities: Theory and experiments. *Appl Opt* **37**, 1935–1944 (1998).

[253] D. J. Wallace, B. Michener, D. Choudhury, M. Levi, P. Fennelly, D. M. Hueber, and B. B. Barbieri. Results of a 95-subject human clinical trial for the diagnosis of peripheral vascular disease using a near-infrared frequency domain hemoglobin spectrometer. In *BiOS'99 International Biomedical Optics Symposium* pages 300–316. International Society for Optics and Photonics (1999).

[254] L. V. Wang and S. L. Jacques. Hybrid model of Monte Carlo simulation diffusion theory for light reflectance by turbid media. *J. Opt. Soc. Am. A* **10**, 1746–1752 (1993).

[255] L. Wang, S. L. Jacques, and L. Zheng. Mcmlmonte carlo modeling of light transport in multi-layered tissues. *Computer methods and programs in biomedicine* **47**(2), 131–146 (1995).

[256] Y. Wang, Y. Shiraishi, Y. Kawai, and K. Nakashima. Ligation of lateral carotid artery attenuates disturbance of brain function caused by subsequent cerebral ischemia in rabbits. *Neuroscience letters* **218**(2), 119–122 (1996).

[257] D. A. Weitz and D. J. Pine. *Dynamic light scattering: the method and some applications* volume 49 chapter Diffusing-wave spectroscopy. Oxford University Press, USA (1993).

[258] B. R. White and J. P. Culver. Phase-encoded retinotopy as an evaluation of diffuse optical neuroimaging. *Neuroimage* **49**(1), 568–577 (2010).

[259] A. J. Wood, T. Brott, and J. Bogousslavsky. Treatment of acute ischemic stroke. *New England Journal of Medicine* **343**(10), 710–722 (2000).

[260] X. Wu, D. Pine, P. Chaikin, J. Huang, and D. Weitz. Diffusing-wave spectroscopy in a shear flow. *JOSA B* **7**(1), 15–20 (1990).

[261] T. Yamada, S. Umeyama, and K. Matsuda. Multidistance probe arrangement to eliminate artifacts in functional near-infrared spectroscopy. *Journal of biomedical optics* **14**(6), 064034–064034 (2009).

[262] T. Yamada, S. Umeyama, and K. Matsuda. Separation of fnirs signals into functional and systemic components based on differences in hemodynamic modalities. *PloS one* **7**(11), e50271 (2012).

[263] Y. Yamashita, A. Maki, and H. Koizumi. Wavelength dependence of the precision of noninvasive optical measurement of oxy-, deoxy-, and total-hemoglobin concentration. *Med Phys* **28**(6), 1108–14. (2001).

[264] M. A. Yaseen, V. J. Srinivasan, S. Sakadžić, H. Radhakrishnan, I. Gorczynska, W. Wu, J. G. Fujimoto, and D. A. Boas. Microvascular oxygen tension and flow measurements in rodent cerebral cortex during baseline conditions and functional activation. *Journal of Cerebral Blood Flow & Metabolism* **31**(4), 1051–1063 (2011).

[265] F. Q. Ye, Y. Yang, J. Duyn, V. S. Mattay, J. A. Frank, D. R. Weinberger, and A. C. McLaughlin. Quantitation of regional cerebral blood flow increases during motor activation: A multislice, steady-state, arterial spin tagging study. *Magnetic resonance in medicine* **42**(2), 404–407 (1999).

[266] A. Yodh and B. Chance. Spectroscopy and imaging with diffusing light. *Physics Today* **48**(3), 34–41 (1995).

[267] T. Yousry, U. Schmid, H. Alkadhi, D. Schmidt, A. Peraud, A. Buettner, and P. Winkler. Localization of the motor hand area to a knob on the precentral gyrus. a new landmark. *Brain* **120**(1), 141–157 (1997).

[268] G. Yu, T. Durduran, G. Lech, C. Zhou, B. Chance, E. R. Mohler, and A. G. Yodh. Time-dependent blood flow and oxygenation in human skeletal muscle measured with noninvasive near-infrared diffuse optical spectroscopies. *J Biomed Opt* **10**(3), 024027–1–12 (2005).

[269] G. Yu. Diffuse correlation spectroscopy (dcs): a diagnostic tool for assessing tissue blood flow in vascular-related diseases and therapies. *Current Medical Imaging Reviews* **8**(3), 194–210 (2012).

[270] G. Yu. Near-infrared diffuse correlation spectroscopy in cancer diagnosis and therapy monitoring. *Journal of biomedical optics* **17**(1), 0109011–0109019 (2012).

[271] Q. Zhang, G. E. Strangman, and G. Ganis. Adaptive filtering to reduce global interference in non-invasive nirs measures of brain activation: how well and when does it work? *Neuroimage* **45**(3), 788–794 (2009).

[272] H. Zhao, Y. Tanikawa, F. Gao, Y. Onodera, A. Sassaroli, K. Tanaka, and Y. Yamada. Maps of optical differential pathlength factor of human adult forehead, somatosensory motor and occipital regions at multi-wavelengths in nir. *Physics in medicine and biology* **47**(12), 2075 (2002).

[273] Y. Zheng, J. Martindale, D. Johnston, M. Jones, J. Berwick, and J. Mayhew. A model of the hemodynamic response and oxygen delivery to brain. *Neuroimage* **16**(3), 617–637 (2002).

[274] C. Zhou. *In-vivo optical imaging and spectroscopy of cerebral hemodynamics*. PhD thesis University of Pennsylvania (2007).

[275] C. Zhou, T. Shimazu, T. Durduran, J. Luckl, D. Y. Kimberg, G. Yu, X.-H. Chen, J. A. Detre, A. G. Yodh, and J. H. Greenberg. Acute functional recovery of cerebral blood

flow after forebrain ischemia in rat. *Journal of Cerebral Blood Flow & Metabolism* **28**(7), 1275–1284 (2008).

[276] C. Zhou, G. Yu, D. Furuya, J. Greenberg, A. Yodh, and T. Durduran. Diffuse optical correlation tomography of cerebral blood flow during cortical spreading depression in rat brain. *Optics express* **14**(3), 1125–1144 (2006).

[277] P. Zirak, R. Delgado-Mederos, L. Dinia, D. Carrera, J. Mart-Fbregas, and T. Durduran. Transcranial diffuse optical monitoring of microvascular cerebral hemodynamics after thrombolysis in ischemic stroke. *Journal of Biomedical Optics* **19**(1), 018002 (2014).